Study of Protein-Cofactor Interaction and Electron Transfer Properties in Modified Photosystem I Complexes by Multifrequency Time Resolved Electron Paramagnetic Resonance

Inaugural Dissertation

zur Erlangung der Doktorwürde

vorgelegt dem Fachbereich Physik
der Freien Universität Berlin

von
Irina V. Karyagina
aus Kazan, Russland

Juni 2007

1. Gutachter: Prof. Dr. D. Stehlik

2. Gutachter: Prof. Dr. H. H. Limbach

Tag der mündlichen Prüfung: 17. Juli 2007

In memory of my Doktorvater Prof. Dr. Dietmar Stehlik

Zusammenfassung

Ziel der vorliegenden Arbeit ist die Charakterisierung von Protein-Kofaktor-Wechselwirkungen in Photosystem I der Photosynthese, besonders soweit dadurch wichtige Funktionsmerkmale der lichtinduzierten Ladungstrennung durch transmembranen Elektronentransfer bestimmt werden. Hierzu wurde zeitauflösende Multifrequenz-Elektronspinresonanz Spektroskopie eingesetzt, womit funktionelle paramagnetische Zwischenzustände als Radikalionen-Paare ($P_{700}^{\bullet+}A_1^{\bullet-}$ und $P_{700}^{\bullet+}F_X^-$) in Echtzeit verfolgt werden können, wie sie im Verlauf der lichtinduzierten Elektrontransfer-Prozesse entstehen.

Zwei Ansätze wurden verfolgt, um systematische Modifizierung von Protein-Kofaktor Wechselwirkungen vorzunehmen und Einzelbeiträge der funktionsbestimmenden Eigenschaften zu identifizieren: A) Ersetzen des nativen Chinon-Kofaktors in der A_1-Bindungstasche durch geeignet modifizierte synthetische und auch andere Chinone. Zur Entfernung/Rekonstitution von Kofaktoren standen neben „harschen“ Extraktionsmethoden auch „sanfte“ Unterbrechungsmutanten im biosynthetischen Aufbauprozess der Kofaktoren zur Verfügung. B) Gezielte Veränderung der Proteinumgebung von Kofaktoren, insbesondere durch geeignete Punktmutation einzelner Aminosäuren in der Protein-Primärsequenz.

Mit dem Einbau vom ^{13}C-Isotopen markierten Chinon in der A_1-Bindungstasche von Photosystem I (Kapitel 5) wurde die stark asymmetrische Spindichteverteilung für den funktionellen Radikalpaar-Zustand $P_{700}^{\bullet+}A_1^{\bullet-}$ bestätigt, insbesondere da die C–O Gruppe (mit oder ohne Wasserstoff-Brücke) ausgedehnt werden konnten. Die im Röntgen-Strukturmodell für den Grundzustand geforderte stark asymmetrische Wasserstoff-Brückenbindung wurde so für den funktionellen ladungsseparierten Zustand nachgewiesen.

Die Ergebnisse an Photosystem I Komplexen der *menB rubA* Doppelmutante zeigen: (i) Trotz der Abwesenheit der Eisen-Schwefel-Komplexe und der “stromalen” Protein-Untereinheiten (PsaC, PsaE und PsaD) bleiben alle ESR-zugänglichen strukturellen Eigenschaften, wie Lage, Orientierung des Chinons sowie wesentliche Protein-Kofaktor-Wechselwirkungen erhalten (Kapitel 6). (ii) Das eingebaute schwächer gebundene Ersatz-Chinon (Plastochinone-9) lässt sich einfach durch eine Reihe anderer Chinone ersetzen. Anthraquinone, wegen noch negativerem Redoxpotential als natives Phyllochinon besonders interessant ist, konnte in PS I mit und ohne [4Fe-4S]-Cluster eingebaut werden (Kapitel 7). Entsprechend der veränderten Energetik wird die Kinetik aufeinander folgender Elektronentransferprozesse komplementär modifiziert: der erste Prozess von $A_0^{\bullet-}$ zu A_1 ist verlangsamt, während der Nachfolgeprozess von $A_1^{\bullet-}$ zu F_X gegenüber Wildtyp beschleunigt abläuft. Erstmals konnte der Einfluss der partiellen negativen Ladung eines [4Fe-4S]-Clusters auf die Kinetik eines Elektronentransferprozesses nachgewiesen werden.

Die Untersuchungen von Punkt-Mutanten in der Proteinumgebung von einem der beiden A_1-Bindungstaschen bzw. vom ersten [4Fe-4S]-Cluster F_X fokussierten auf den Einfluss von spezifischen Aminosäuren Aspartat mit negativ geladener Seitenkette (Kapitel 8) auf die Elektronentransfer-Kinetik. Die Veränderung der Seitenkettenladung von negativ zu neutral und zu positiv führt zu sehr kleinen, aber systematischen Änderungen der Elektronentransfer-Kinetik von $A_1^{\bullet-}$ zu F_X, konsistent mit den erwarteten Redoxpotenzial-Differenzen, je nachdem ob sich das mutierte Aspartat beim Chinon-A_1-Bindungsplatz oder beim ersten [4Fe-4S]-Cluster befindet.

Weiter wurde Methionin als Ligand zum A_0-Kofaktor zur Mutation ausgewählt (Kapitel 9). Sowohl bei der Mutation zu Leuzin als auch zu Asparagin wird gegenüber dem Wildtyp verlangsamter Elektrontransfer von $A_0^{\bullet-}$ zu A_1 beobachtet. Die Ergebnisse stimmen sehr gut mit komplementären optischen Untersuchungen überein und belegen einen deutlich

asymmetrischen Elektronentransfer entlang der PsaA-Seite der quasi-C_2 symmetrischen räumlichen Anordnung der Elektronen-Akzeptoren.

Abstract

The goal of this thesis is the characterization of specific protein-cofactor interactions which control transmembrane electron transfer processes in Photosystem I of the cyanobacterial photosynthesis apparatus. Multifrequency Time Resolved Electron Paramagnetic Resonance (TR EPR) spectroscopy is applied to detect the sequential $P_{700}^{\bullet+}A_1^{\bullet-}$ and $P_{700}^{\bullet+}F_X^-$ radical pair states created by light induced charge separation.

Systematic variation of functionally relevant properties of protein-cofactor interactions is carried out in two ways: A) substitution of the native phylloquinone in the A_1-binding site of Photosystem I complex by suitably modified synthetic or various other quinones. For the extraction/reconstitution procedure two methods were available for comparison: a “harsh” one, extraction of native phylloquinone by organic solvents, and a “soft” one, use of native quinone biosynthetic pathway deletion mutants with a more weakly bound rescue quinone (plastoquinone-9) in the A_1-binding site; in each case reconstitution/replacement followed by offering the wanted quinone in excess. B) Selective variation of the protein environment in the cofactor site by site-directed mutation.

In Part A the first incorporation concerns 2-methyl-1,4-naphthoquinones selectively labelled with a ^{13}C isotope at one of the carbon positions (Chapter 5). A highly asymmetric spin density distribution is observed for the functional $P_{700}^{\bullet+}A_1^{\bullet-}$ RP state. It provides solid evidence for a highly asymmetric (single-sided) hydrogen bond scheme between the protein environment and the quinone as it was suggested in the X-ray structure model for the ground state.

The results on PS I complexes isolated from the *menB rubA* double mutant show: i) In spite of the absence of the [4Fe-4S] clusters F_X, F_A, F_B and all stromal subunits PsaC, PsaD, PsaE the TR EPR detectable structural and essential protein-cofactor interaction features remain the same as observed for phylloquinone in the wild type. ii) Because plastoquinone-9 is more weakly bound into the A_1-binding site of PS I it can be exchanged easily by a number of quinones (Chapter 6). In particular, 9,10-anthraquinone with a more negative redox potential than native phylloquinone was chosen for incorporation into the A_1-binding site of Photosystem I both, in the presence and absence of the [4Fe-4S] clusters. Corresponding to the altered energetics the kinetics of consecutive electron transfer processes from $A_0^{\bullet-}$ to AQ to F_X are changed in a complementary way (Chapter 7). The first ET kinetics from $A_0^{\bullet-}$ to AQ slows down, the second one from $AQ^{\bullet-}$ to F_X speeds up. Moreover, for the first time, the effect of the formal negative charge $[Fe_4S_4(SCH_3)_4]^{2-}$ associated with F_X on an electron transfer step from $A_0^{\bullet-}$ to A_1 could be demonstrated.

In part B first the influence of the specific aspartate residues on electron transfer from $A_1^{\bullet-}$ to F_X was studied by site-directed mutants in either the environment of the phylloquinone or the first iron-sulphur F_X cofactor (Chapter 8). Changing from a negatively charged side chain to a neutral and to a positively charged one results in very small but systematic changes of the electron transfer kinetics from $A_1^{\bullet-}$ to F_X, consistent with the expected redox potential shifts depending whether the aspartate mutation concerns more the vicinity of A_1 or F_X.

Furthermore, the axial methionine ligand to the central Mg atoms of the first acceptor A_0 was chosen for mutation, either to asparagine (N) or leucine (L), selectively in the PsaA- or PsaB-branch (Chapter 9). In comparison to the wild type both PsaA-branch mutants show a decrease in the electron transfer rate from $A_0^{\bullet-}$ to A_1. These results agree well with those from complementary optical studies. They confirm asymmetric electron transfer, predominantly along the PsaA-branch. Extended conclusions are presented in the final Chapter 10.

Contents

Part A: Characterisation of the A_1-Binding Site of Photosystem I

Part B: Site-Directed Mutants in Photosystem I

1. Introduction

Photosynthesis is the main process on earth that converts light energy into chemical bond energy. The initial steps of oxygenic photosynthesis are catalyzed in two large protein-pigment complexes, Photosystem I (PS I) and Photosystem II (PS II), embedded in the thylakoid membrane of the chloroplasts in higher plants, algae and cyanobacteria.

With 2.5 Å/3.2 Å resolution achieved for the X-ray structure of Photosystem I /Photosystem II from *Thermosynechococcus elongatus*, the knowledge of the structural details increased dramatically. However, understanding details of fundamental processes such as light-induced charge separation along a chain of cofactors remains one of the most challenging aspects of research. For example, how does the protein environment adjust the redox potential of cofactors like quinone to act as highly reducing/oxidizing agent in Photosystem I/Photosystem II?

The primary task of my thesis is to determine detailed properties of the specific protein-cofactor interactions which control the light-induced transmembrane electron transfer processes in Photosystem I.

The electron transfer in Photosystem I is initiated by capture of light energy by antenna chlorophylls. Their excitation energy is guided to a primary donor P_{700}. The excited $^*P_{700}$ gives an electron to a primary electron acceptor A_0 (charge separation). Then the electron is further transferred along a chain of electron cofactors A_1, F_X, F_A, F_B arranged across the membrane. Therefore, during these primary events, short-lived radical-ion pairs are created. Time Resolved Electron Paramagnetic Resonance (TR EPR) is one of the methods by which the time course of these intermediate paramagnetic states (second $P_{700}^{\bullet +}A_1^{\bullet -}$ and third $P_{700}^{\bullet +}F_X^{\bullet -}$ radical pairs) can be followed. The concept of spin correlated radical pairs (SCRP) described in Chapter 3 and Appendix I is applied for the numerical simulation of the observed spin polarisation patterns of the sequential radical pairs. Chapter 4 completes the description of the background materials.

The main approach chosen in my thesis is based on the systematic variation of functionally relevant properties of protein-cofactor interactions by incorporation of various quinones in the A_1-binding site of Photosystem I (Part A) or by modification of the protein environment by site-directed mutations (Part B).

In Part A, specific properties of the A_1-binding site of Photosystem I are characterized. The X-ray structure model revealed two specific protein-cofactor interactions for phylloquinone in the A_1-binding site. The phylloquinone is π-stacked with a tryptophan residue and is connected to the protein backbone by one dominant hydrogen bond to one of its two carbonyl groups. The latter H-bonding scheme is unique among other well characterized quinone sites, e.g. in purple bacterial reaction centers and the quinol oxidase, where the quinones have at least one or more hydrogen bonds to each of the carbonyl groups. In order to probe the single-sided hydrogen bond motif in the functional charge-separated state of Photosystem I, 2-methyl-1,4-naphthoquinones with selective ^{13}C isotope labelled in each carbon ring positions of the quinone carbonyl groups were incorporated into the A_1-binding site. The effect of asymmetric hydrogen bonding as reflected in the spin density distribution over the quinone ring is the object of investigation in Chapter 5.

Three iron-sulphur clusters constitute the terminal electron acceptors of Photosystem I, the latter two are bound by the PsaC protein subunit of the “stromal ridge” in PS I structural model. It is expected that these iron-sulphur clusters contribute significantly to the redox potential of quinone. This can be tested with suitable mutants modifying the biosynthesis of the native phylloquinone and iron sulphur cofactors. A specific *menB rubA* double mutant has been studied for this purpose in Chapter 6 and Chapter 7. First, the identity of the quinone cofactor and the integrity of the A_1-binding site are investigated in the double mutant. How does the lack of the stromal PsaC, PsaD and PsaC subunits influence the quinone binding affinity and make ease a quinone substitution protocol for the A_1-binding site?

Incorporation of the three ring 9,10-anthraquinone into the A_1-binding site is of particular interest because it introduces a more negative redox potential than the native phylloquinone. The altered energetics are expected to influence the electron transfer steps from $A_0^{\bullet-}$ to A_1 and $A_1^{\bullet-}$ to F_X in a way that it slows down the first and accelerates the second step. The ability to incorporate 9,10-anthraquinone in the presence (extracted Photosystem I) and in the absence (*menB rubA* double mutant) of iron-sulphur clusters opens a new way to study the influence of the negative charge $[Fe_4S_4(SCH_3)_4]^{2-}$ associated with F_X on the electron transfer step from $A_0^{\bullet-}$ to A_1.

The main issue studied in Part B is identification and characterisation of the specific amino acid residues that control the redox potential of the cofactors in Photosystem I. With the availibility of the 2.5 Å X-ray structure model it has become possible to investigate theoretically individual contributions by using electrostatic calculations. For example, it was proposed that the partial negative charges associated with the particular aspartate residues $D575_{PsaB}$ and $D566_{PsaB}$ play a significant role in modulating the redox potentials of A_1 and F_X. Alternative method to test this prediction is the point mutational change of these specific aspartate residues. It is expected that the point mutations will change the electron transfer rate from $A_1^{\bullet-}$ to F_X which can be evaluated by TR EPR, as shown Chapter 8.

The work in Part B deals also with the directionality of electron transfer in Photosystem I. The presence of two symmetric branches (PsaA and PsaB) of the identical electron acceptors in Photosystem I raises the question whether the forward electron transfer proceeds through one or two branches? There are a lot of speculations to suggest that both branches might be active in electron transfer or it may be even possible to redirect it by suitable alternation of the protein environment. However, many aspects of the directionality of electron transfer in Photosystem I still remain unclear. Site-directed mutagenesis is often used for selectively influencing the branches of cofactors. Most of the initial site-directed mutation concerns the change in the environment of A_1. These results indicate that electron transfer occurs predominantly along the PsaA-branch. In order to probe directionality at an earlier step of electron transfer from $A_0^{\bullet-}$ to A_1 the methionine residue which is an axial ligand to Mg^{2+} of the primary electron acceptor A_0 was targeted for mutation to the asparagine or leucine either in the PsaA or PsaB-branch. Alteration of this residue is expected to change the redox potential of A_0 in the branch carrying this mutation. As a consequence electron transfer from $A_0^{\bullet-}$ to A_1 will be changed, as described in Chapter 9.

The conclusions are collected in Chapter 10.

2. Basics

2.1. Photosynthesis

Photosynthesis is a process by which light energy is converted into chemical energy. This process occurs in higher plants, algae and some bacteria. The overall conversion equation for photosynthesis can be formulated as:

$$6\ CO_2 + 6\ H_2O \xrightarrow{\text{light}} 6\ \underset{\text{glucose}}{(CH_2O)} + 6\ O_2\uparrow$$

Photosynthesis occurs in two stages. In the first phase, called *photosynthetic* or *light-induced primary reactions*, light energy is captured, converted to electric energy via charge separation and to chemical energy by production of high-energy molecules. During the second phase, called as *light-independent* or *dark* reactions, the high-energy molecules capture carbon dioxide (CO_2) and synthesize the precursors of glucose.

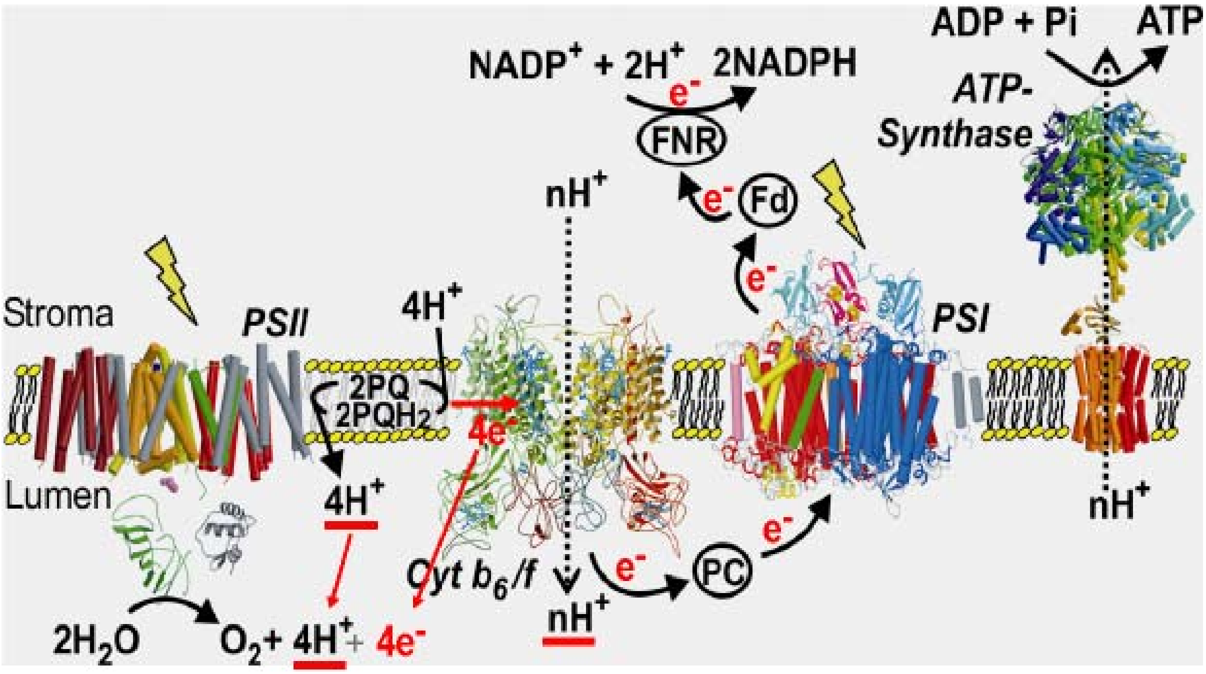

Figure 2.1. Schematic overview of light-induced reactions in the thylakoid membrane of cyanobacteria. (Figure kindly provided by Prof. Wolfram Saenger).

2.2.1. Photosynthetic apparatus

The primary process of light energy conversion takes place in the membrane bound pigment-protein complexes, known as reaction centers (RCs). In the thylakoid membrane of plants and cyanobacteria, two types of RCs are found: photosystem II (PS II) and photosystem I (PS I). PS II is the complex where water splitting and oxygen evolution occurs. PS I catalyzes the $NADP^+$ reduction. In both RCs, under illumination with light of approximately 680/700 nm,excitation energy is captured by a core-antenna systems (light harvesting complexes in PS II) and passed to the centre of the PS II/PS I complex, where charge separation occurs. In PS II the primary donor P_{680} looses an electron which is transported along a chain of sequential intermediate electron acceptors (Phe_A, Q_A, Q_B) and further to the cytochrome b_6f complex. Oxidised $P_{680}^{\bullet+}$ gets an electron from a nearby tyrosine radical, which in turn receives an electron from the water splitting complex. In PS I similar transmembrane ET occurs. The light-driven transmembrane electron transfer (ET) proceeds from the primary electron donor P_{700} along a chain of sequential intermediate electron acceptors (A_0, A_1) to the terminal [4Fe-4S] clusters (F_X, F_A and F_B). On the stromal side of membrane the reduced terminal acceptor F_B passes the electron to soluble ferrodoxin Fd (or flavodoxin) and the reduced ferredoxin transports the electron to the enzyme ferrodoxin:NADP$^+$-reductase, which catalyzes the reduction of NADP$^+$ to NADPH on the stromal side of the photosynthetic membrane. $P_{700}^{\bullet+}$ receives an electron from PS II via the cytochrome b_6f complex. Water soluble plastocyanin (or cytochrome) PC serves as a carrier on the luminal side of the photosynthetic membrane. Therefore, ET through PS II and PS I results in water oxidation and NADP$^+$ reduction. The proton gradient generated by the action of PS II and the b_6f complex drives ATP synthesis. In the subsequent dark reactions NADPH and ATP are used to convert CO_2 to carbohydrates. A schematic overview of these processes is provided in Figure 2.1.

2.2. Photosystem I

2.2.1 Structure of PS I

Detailed structural information of PS I is available from the X-ray structure model of the core complex of cyanobacterial PS I from the thermophilic cyanobacteria *Thermosynechococcus elongatus* at 2.5 Å resolution (pdb entry code 1JB0) [2-4] and of plant PS II (with a ring of light harvesting units) from the high plant *Pisum sativum* var. *alaska* at 4.4 Å resolution [5].

Cyanobacterial PS I exists in trimeric as well as in monomeric form. The trimer has a molecular weight of 1056 kDa. Each monomeric unit consist of 12 different protein subunits (PsaA, PsaB, PsaC, PsaD, PsaE, PsaF, PsaI, PsaJ, PsaK, PsaL, PsaM, and PsaX), to which 127 cofactors (96 chlorophylls, 22 carotenoids, 3 [4Fe-4S] clusters, 2 phylloquinones, and 4 lipids) are non-covalently bound [2-4]. Figure 2.2 shows the organisation of all subunits of the monomeric unit of trimeric PS I. The two largest protein subunits PsaA and PsaB form a heterodimeric core and bind all cofactors of ET chain from P_{700} to the first [4Fe-4S] cluster F_X and most of the antenna system (most of the chlorophylls and carotenoids). The other subunits are located in the periphery of the PsaA/PsaB heterodimer. The PsaC subunit binds over F_X at the stromal side and carries the two terminal [4Fe-4S] clusters F_A and F_B. Together with PsaD and PsaE subunits it constitutes the “stromal ridge” of PS I complex.

Antenna system

The core antenna system consists of 90 Chl *a* molecules and 22 carotenoids. Most of antenna chlorophylls are organised in a double disc shaped cluster-arrangement near the stromal and luminal membrane surface [3, 4, 6]. The function of the antenna chlorophylls is to capture light energy and transfer the excitation energy to a special pair of Chl *a* molecules, the primary electron donor P_{700}, of PS I complex from which directly the transmembrane ET occurs [2, 6, 7]. Carotenoids can serve as triplet traps preventing formation of poisonous singlet oxygen.

2.2.2. Electron transfer chain of PS I

Figure 2.3 represents the structural arrangement of the cofactors of RC with two quasi C_2 symmetric branches, PsaA- and PsaB-branch, named in accordance with cofactors binding to the relative protein subunits PsaA and PsaB. The cofactor branches separate at the primary electron donor P_{700}, which is a heterodimer (Chl *a*/Chl *a'*). Each branch contains an equal sequence of electron acceptors: accessory chlorophyll A_{-1}, chlorophyll A_0 and phylloquinone A_1. The two branches re-converge on the first [4Fe-4S] cluster F_X. The terminal electron acceptors F_A and F_B bound to the extrinsic protein subunit PsaC on the stromal side of PS I complete the ET transfer chain.

Primary electron donor P_{700}

According to the X-ray structure model three sets of chlorophylls are present in the ET chain: P_{700}, A_{-1}, A_0. The primary donor P_{700} is a pair of inequivalent chlorophylls located close to the lumenal side of PS I (pdb entry 1JB0) [2-4]. The two chemically different chlorophyll molecules are Chl *a* and Chl *a'* molecule. The latter is a $C13^2$-epimer of Chl *a*. The Chl *a* is in the PsaB-branch, axially coordinated to histidine $H660_{PsaB}$ and does not form any hydrogen bonds with the surrounding protein. In contrast, Chl *a'* in the PsaA-branch is axially coordinated to histidine $H680_{PsaA}$ and forms three hydrogen bonds to the side chains of transmembrane α-helices A-**i** and A-**k** and a water molecule. The distance between the Mg^{2+} ions of these two Chl *a* and Chl *a'* molecules is 6.3 Å. Their planes are oriented perpendicular to the membrane plane and parallel to each other with an interplanar distance of 3.6 Å.

Magnetic resonance and infrared spectroscopy of the triplet state $^3P_{700}$ and cation state P_{700}^+ indicate that it has dimeric nature [2, 8-13]. ENDOR studies on single crystals of

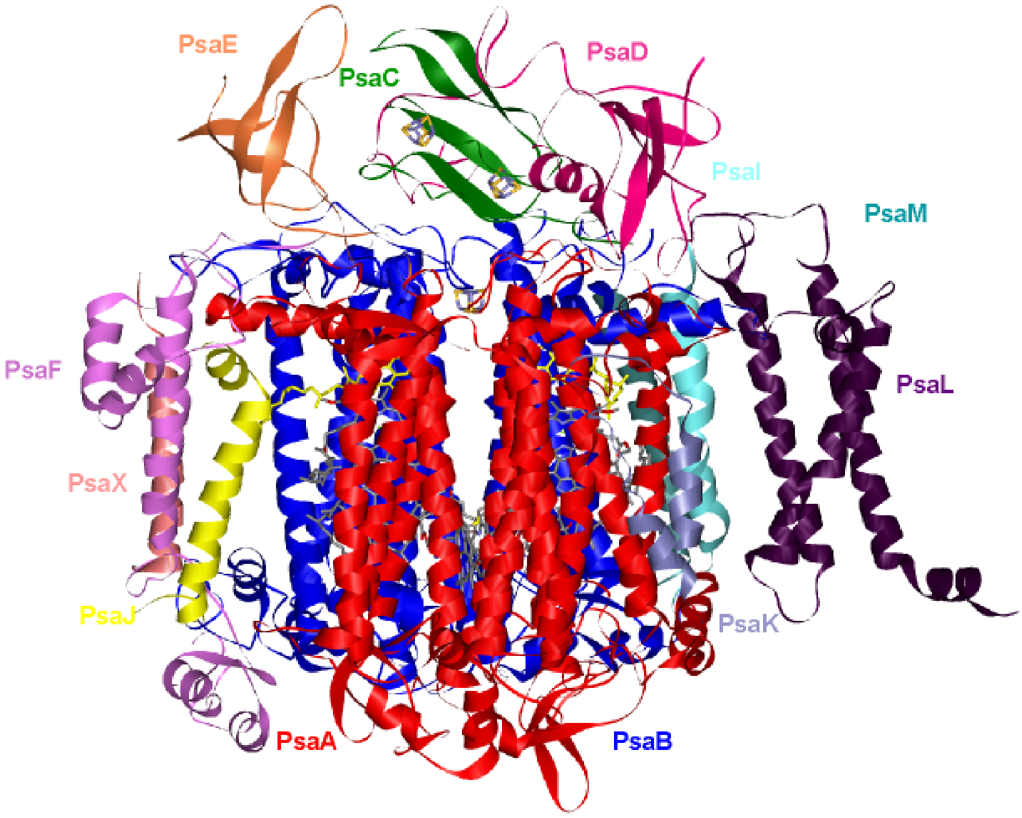

Figure 2.2. Monomeric structure of cyanobacterial PS I viewed parallel to the membrane plane. The twelve proteins are shown in a backbone representation.

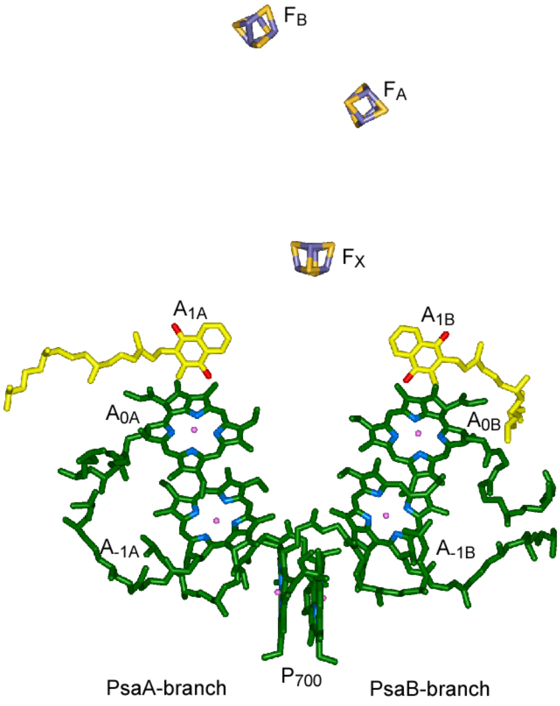

Figure 2.3. Arrangement of the ET cofactors in PS I. The approximate C_2 symmetry axis is perpendicular to the membrane plane and passes through F_X.

PS I showed that the spin density of the oxidised P_{700}^{+} is asymmetrically distributed with 85 % of the spin density being located on the Chl *a* ligated by $H660_{PsaB}$ of the PsaB-branch [2, 10, 11]. TR FTIR results indicate that the charge density over two Chl *a* and Chl *a'* of P_{700}^{+} state is distributed relative equally. From semi-empirical calculations it has been concluded that due to spin polarisation effects the spin asymmetry is significantly larger than the charge distribution [14]. Recent analysis of zero-field parameters (D, E) of the triplet $^{3}P_{700}$ and monomeric ^{3}Chl *a* showed that the triplet excitation is delocalised over the two chlorophylls of the heterodimer P_{700} at higher temperature, but localised on one chlorophyll at cryogenic temperature. This is in line with TR FTIR data at low temperature where localisation of spin density of triplet $^{3}P_{700}$ on the Chl *a'* (PsaA-branch) was found [8].

Accessory Chlorophyll A_{-1}

The chlorophylls A_{-1A}/A_{-1B} of the second set are named as accessory chlorophylls. The center to center distance to the chlorophylls of P_{700} is approximately 12 Å [2-4]. These two chlorophylls are the only cofactors of the ET chain for which the coordinated subunit of A_{-1A} is PsaB and *vice versa*. In both branches, a binding water molecule provides the fifth ligand to the central Mg^{2+} ion of the chlorophyll.

Primary electron acceptor A_0

The chlorophylls A_{0A}/A_{0B} (third set of Chl's) are located in the middle of membrane and spectroscopically identified as a primary electron acceptor A_0, which is a Chl *a* monomer. The second and the third set of chlorophylls are located in close vicinity to each other with plane-to-plane distance of approximately 3.8 Å. The chlorine rings of A_{-1A}/A_{0A} and A_{-1B}/A_{0B} are nearly parallel to each other [2-4]. Each of the chlorophylls A_{0A}/A_{0B} is hydrogen bonded to the side chain of tyrosine $Y696_{PsaA}/Y676_{PsaB}$. Only the chlorophyll A_{0A} in PsaA-branch has a second hydrogen bond to serine $S429_{PsaB}$. For each chlorophyll A_{0A}/A_{0B}, the sulphur atom of methionine $M688_{PsaA}/M668_{PsaB}$ residue provides the fifth ligand to Mg^{2+} ion. Ligation of the hard acid Mg^{2+} ion by the soft base sulphur of the methionine is very unusual and predicts weak interaction between Mg^{2+} and sulphur. These methionine residues are also hydrogen bonded via their backbone oxygen to serine $S692_{PsaA}/S672_{PsaB}$, whose side chain oxygen forms a hydrogen bond with the side chain nitrogen of tryptophan $W697_{PsaA}/W677_{PsaB}$. These tryptophan residues are π-stacked with phylloquinones A_{1A}/A_{1B}, respectively [2].

Secondary electron acceptor A_1

Spectroscopic and biochemical analysis has identified the secondary electron acceptor A_1 in the ET chain as a phylloquinone (PhQ). The two PhQs, marked as A_{1A}/A_{1B}, are located near the stromal side of the membrane. Each quinone A_{1A}/A_{1B} is π-stacked with tryptophan $W697_{PsaA}/W677_{PsaB}$ [2-4]. Only one of two oxygen atoms of each quinone forms a hydrogen bond with the backbone NH group of leucine $L722_{PsaA}/L702_{PsaB}$, respectively. The second oxygen atom of each quinone is not involved in any hydrogen bonds. This leads to an asymmetric spin density distribution of the unpaired electron over the quinone ring in the reduced $A_1^{\bullet -}$ state. In addition, the backbone oxygen of the $L722_{PsaA}/L706_{PsaB}$ residue is hydrogen bonded to the F_X binding loop through arginine $R694_{PsaA}/R674_{PsaB}$.

Third electron acceptor F_X

The third electron acceptor F_X embedded in the stromal interface of the PsaA and PsaB subunits is a [4Fe-4S] cluster ligated by four cysteine residues $C578_{PsaA}$, $C587_{PsaA}$ and $C565_{PsaB}$, $C574_{PsaB}$. The ligands are located in the loop connecting helices A-**h** and A-**i** or B-**h** and B-**i**. Both these loops sections are highly conserved among each other and in all PS I from plants, algae and cyanobacteria.

Terminal electron acceptors F_A, F_B

The two terminal electron acceptors F_A and F_B are [4Fe-4S] clusters are bound to the extrinsic subunit PsaC. F_A is coordinated by cysteine residues $C21_{PsaC}$, $C48_{PsaC}$, $C51_{PsaC}$, and $C54_{PsaC}$. F_B is coordinated by cysteine residues $C11_{PsaC}$, $C14_{PsaC}$, $C17_{PsaC}$, and $C58_{PsaC}$. Center-to-center distance between F_X and F_A/F_B is 14.9 Å/22 Å, respectively [2-4, 6].

2.2.3. Charge separation in PS I

Light energy conversion to chemical energy begins with light absorption by antenna pigments (Ant) on the surface of membrane. Electronic excitation is transferred to the primary electron donor P_{700} in the membrane. Then charge separation occurs in the RC: the excited primary donor P_{700}^* gives one electron to the primary acceptor A_0 and the electron is transferred along a chain of electron acceptors (A_0, A_1, F_X, F_A, F_B) with generation of intermediate RP states. The initial steps of charge separation in the photosynthetic RC could be written in the following scheme:

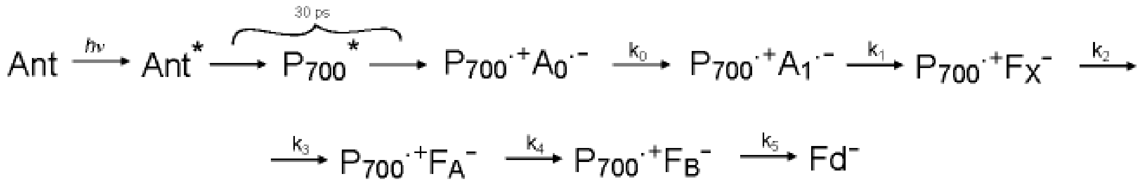

$$\mathrm{Ant} \xrightarrow{h\nu} \mathrm{Ant}^{*} \overbrace{\longrightarrow P_{700}^{*} \longrightarrow}^{30\ \mathrm{ps}} P_{700}^{\cdot+}A_0^{\cdot-} \xrightarrow{k_0} P_{700}^{\cdot+}A_1^{\cdot-} \xrightarrow{k_1} P_{700}^{\cdot+}F_X^{-} \xrightarrow{k_2}$$

$$\xrightarrow{k_3} P_{700}^{\cdot+}F_A^{-} \xrightarrow{k_4} P_{700}^{\cdot+}F_B^{-} \xrightarrow{k_5} \mathrm{Fd}^{-}$$

where Ant*, P_{700}^* are the excited singlet states of the antenna pigment, primary donor P_{700}, respectively. k_1, k_2, k_3, k_4, k_5 are rate constants of subsequent forward ET processes.

First step of charge separation: ET from P_{700}^* to A_0

The primary $P_{700}^{\bullet+}A_0^{\bullet-}$ RP appears in ~ 30 ps after light excitation [15, 16]. According to the kinetic model for time resolved absorption and fluorescence data the intrinsic rate constant for ET from P_{700}^* to A_0 is less than 3 ps [15, 17, 18].

There are two main mechanisms proposed in the literature for the primary charge separation. i) From the excited primary donor P_{700}^* an electron is transferred sequentially to the first stable electron acceptor A_{0A}/A_{0B} via the accessory chlorophylls A_{-1A}/A_{-1B} [19, 20]. ii) Charge separation starts from the accessory chlorophyll (even predominantly on A_{-1B}) to A_{0A}/A_{0B}, only in the second step a hole is transferred to P_{700} [21].

Note that the initial ET steps are difficult to observe by optical spectroscopy because the excitation energy transfer with a time constant of about 30 ps occurs on the same or longer time scale as the first charge separation events. In addition, spectroscopic features of the antenna pigments (90 chlorophylls) also overlap with those of chlorophylls involved in the charge separation events.

Second step of charge separation: ET from $A_0^{\bullet-}$ to A_1

The time constant of ET from $A_0^{\bullet-}$ to A_1 has been determined to be ~ 50 ps by various techniques [15, 20, 22-24]. There is some variation in the values as a result of different data analysis and techniques used.

Third step of charge separation: ET from $A_1^{\bullet-}$ to F_X

Pathway, kinetics and energetics of ET from $A_1^{\bullet-}$ to F_X are still a matter of debate. The re-oxidation of $A_1^{\bullet-}$ has been measured by a number of different techniques and two life times of ~ 20 ns (“fast” phase) and ~ 200 ns (“slow” phase) have been found at room temperature [1, 25-29]. Below the glass transition temperature (180 K) of PS I in glycerol/water solution, forward ET from past $A_1^{\bullet-}$ is blocked in approximately one third of RCs with the consequence of recombination from the second $P_{700}^{\bullet+}A_1^{\bullet-}$ RP state. Stable formation of the $P_{700}^{\bullet+}(\mathrm{FeS})^-$

state occurs in the other two thirds [1]. Possible explanation of this behaviour is given as a result of two different frozen conformational substates. When the [4Fe-4S] clusters are absent, charge recombination from $A_1^{\bullet-}$ takes place with two lifetimes of ~ 20 μs and ~ 200 μs [29]. At present it is unknown whether a correlation exists between the two fractions, two phase kinetics of forward ET and two recombination rates.

Several models have been proposed to rationalise the biphasic $A_1^{\bullet-}$ oxidation kinetics. They are divided in two limiting cases [30]: i) bidirectional and ii) unidirectional ET. i) In the bidirectional model, both the PsaA and PsaB-branches are active in the forward ET: the slow k_{1A} and fast phase k_{1B} are assigned to ET from $A_{1A}^{\bullet-}$ to F_X and $A_{1B}^{\bullet-}$ to F_X, respectively (Scheme 2.1, a).

Scheme 2.1.

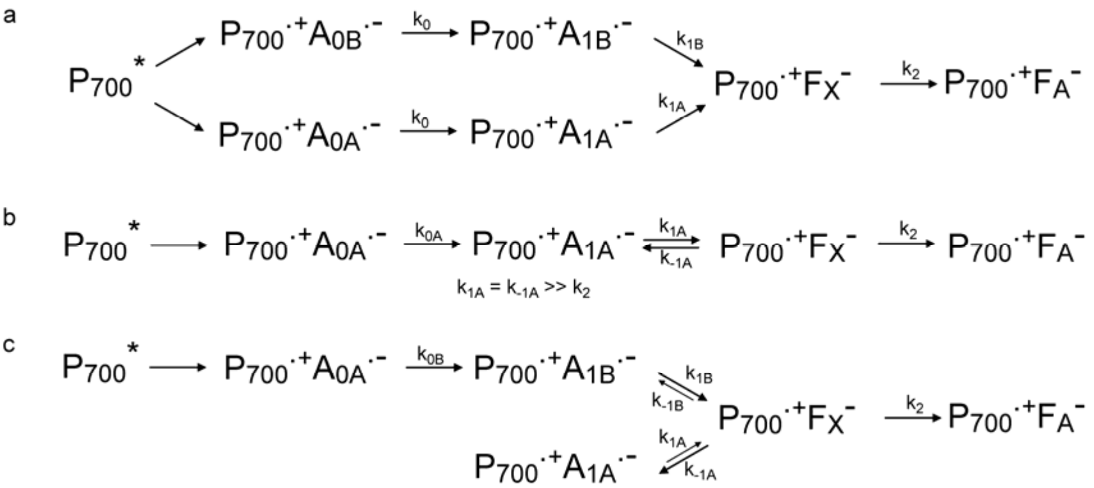

iia) Two possibilities are based on thermal equilibration among populations of energetically close lying states. The first model assumes ET along the PsaA-branch only and similar energies for the second $P_{700}^{\bullet+}$ $A_{1A}^{\bullet-}$ and third $P_{700}^{\bullet+}$ F_X^{-} states. If the back reaction rate k_{1A} (from F_X^{-} to A_{1A}) and the forward ET rate k_{-1A} (from $A_{1A}^{\bullet-}$ to F_X) are comparable, the observed reoxidation of $A_1^{\bullet-}$ may be bi-exponential. Establishment of thermal-equilibrium between the $P_{700}^{\bullet+}A_{1A}^{\bullet-}$ and $P_{700}^{\bullet+}F_X^{-}$ RP states would give rise to the “fast” phase and depopulation of this quasi-equilibrium state by forward ET from F_X^{-} to F_A/F_B with rate constant k_2 would give rise to the “slow” phase (Scheme 2.1, b).

A second scenario implies that only the PsaB-branch is active in the forward ET. It is further assumed that ET from $A_{1B}^{\bullet-}$ to F_X is downhill while $A_{1A}^{\bullet-}$ to F_X is uphill. Following

ET from $A_{1B}^{\bullet-}$ to F_X and population equilibration, the electron on F_X^- may transfer further to either A_1 or F_A. The establishment of equilibrium population for the $P_{700}^{\bullet+}A_{1B}^{\bullet-}$, $P_{700}^{\bullet+}F_X^-$ and $P_{700}^{\bullet+}F_A^-$ states could be assigned to the “fast” phase and reoxidation of $A_{1A}^{\bullet-}$ via F_X to F_A could give rise to the “slow” phase (Scheme 2.1, c).

It is worth to emphasize that both equilibrium models are not consistent with observed spin polarisation pattern of the secondary $P_{700}^{\bullet+}A_{1A}^{\bullet-}$ RP state, if the thermal equilibration rates are fast compared to the observation time window. Thermal hopping between spin states with different orientations to the magnetic field would alter the spin polarisation pattern significantly which was not observed.

iib) As another possibility, structural diversity in a single active branch may occur. Thus, structural, conformational or other environmental variation in the A_1/F_X vicinity may be responsible for different sets or a distribution of the $A_1^{\bullet-}$ to F_X ET rates.

TR EPR is widely used to investigate the second $P_{700}^{\bullet+}A_1^{\bullet-}$ and third $P_{700}^{\bullet+}$ F_X^- RP states. At time resolution of about 50 ns the “slow” phase can be resolved [26, 31]. Based on branch specific mutation studies this “slow” phase could be assigned to ET along the PsaA-branch [32-35]. Distance measurement by out-of-phase ESEEM combined with TR EPR spin polarisation pattern data on single crystal at low temperature showed that the $P_{700}^{\bullet+}$ $A_1^{\bullet-}$ RP state is formed by interaction of unpaired spins localized on the PhQ in PsaA-branch and the Chl *a* part of P_{700} ligated with the PsaB-branch [2, 36, 37].

ET past F_X

A number of mostly structural evidence shows that F_B is the terminal acceptor and forward ET proceeds from F_X^- to F_A and to F_B [38-40]. However, the ET kinetics of each of these sequential steps is not resolved yet. Photovoltage measurements and studies of reduction of ferredoxin suggest that the overall time constant for forward ET from P_{700}^* to F_B is less than 500 ns [30].

Energetics of charge separation in PS I

Figure 2.4 shows a simplified energetics scheme for PS I with the ET time constants and decay processes based on experimental data from [15]. P_{700}^* has a highly negative redox potential of about -1300 meV [15]. The primary ET steps (from P_{700}^* to A_0 to A_1) has a considerable driving force (free energy difference). The free energy difference for the initial ET step from P_{700}^* to A_0 was estimated to be ΔG = 250 meV [15]. From the kinetic data of ultrafast difference absorption measurements the free energy gap for ET from $A_0^{\bullet-}$ to A_1 is in

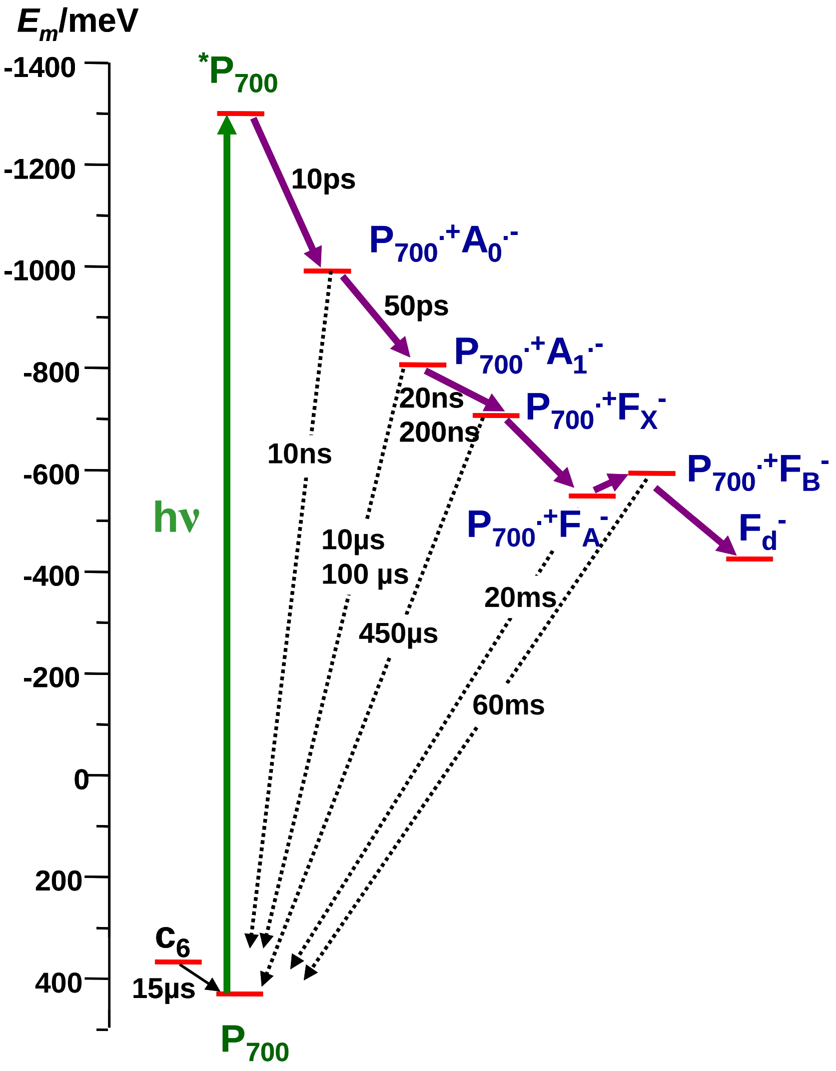

Figure 2.4. Approximate redox potentials and ET time constants between cofactor states in PS I. The figure was adapted from the literature data.

the order of 340 meV and assumed to be the optimal condition for rapid ET from $A_0^{\bullet-}$ to A_1, $\Delta G = -\lambda$, [41, 42]. ET from $A_1^{\bullet-}$ to F_X to Fto F_B involves lower energy gaps. The redox potential of PhQ is not well established yet and estimated to be in the range from -750 meV to -810 meV. Note that such negative redox compared to PhQ in solution (170 meV in water and -570 meV in dimethyl formamide (DMF)) or to quinone sites in type II RCs (- 130 meV for Q_A in PS II) is the most negative one of all known quinone binding sites [15]. From the biochemical study on PS I complexes, depleted of the extrinsic subunits or with the pre-reduced terminal electron acceptor F_A, F_B, the redox potential of F_X was estimated to be ~ -710 meV [2]. The redox potentials of F_A and F_B were estimated to be about ~ -540 meV and ~ -590 meV in titration experiments [15].

2.3. Principles of EPR Spectroscopy

In this part a brief introduction is given to Electron Paramagnetic Resonance. Electron Paramagnetic Resonance (EPR), first detected by Evgeniy Zavoisky in Kazan in 1945 [43], is a powerful method to study the systems having an electron magnetic momentum, e.g. free radicals, transition metal ions, triplet states and biradicals. Classically, the Larmor precession of the electronic magnetic momentum occurs about the direction of externally applied static magnetic field. Quantum mechanically, the resonance occurs when the Zeeman splitting of energy levels is equal the energy of a photon.

2.3.1. Free electron in a magnetic field

The magnetic dipole moment $\boldsymbol{\mu}_S$ of a free electron is defined as:

$$\boldsymbol{\mu}_S = g_e \beta_e \hat{\boldsymbol{S}} \tag{2.1}$$

where g_e is the g-factor of the free electron (g_e = 2.002319304386(20) [44]), $\hat{\boldsymbol{S}}$ is the operator of spin angular momentum and $\beta_e = \frac{e\hbar}{2m_e}$ is the Bohr magneton.

The interaction of the magnetic dipole moment with a magnetic field $\boldsymbol{B_0}$ is expressed as:

$$E = \boldsymbol{\mu}_S \boldsymbol{B_0} \tag{2.2}$$

This produces the spin Hamiltonian operator $\hat{H}_Z$, also called Hamiltonian operator of the Zeeman Interaction:

$$\hat{H}_Z = -\boldsymbol{\mu}_S \boldsymbol{B_0} = -g_e \beta_e \hat{\boldsymbol{S}} \boldsymbol{B_0} \tag{2.3}$$

If magnetic field $\boldsymbol{B_0}$ is applied along z axis then:

$$\hat{H}_Z = g_e \beta_e \hat{S}_z B_0$$

For the electron spin with $S = \frac{1}{2}$ the spin magnetic moment can become aligned with or against the applied magnetic field $\boldsymbol{B_0}$ $(0, 0, B_0)$, giving rise to $2S + 1 = 2$ states of different energy. The two states are characterized by a quantum number m_S which can take values $-\frac{1}{2}$ or $+\frac{1}{2}$. The states with low and high energy are denoted as:

$$|\beta\rangle\ (m_S = -\frac{1}{2}) \qquad E_{-\frac{1}{2}} = -\frac{1}{2} g_e\, \beta_e\, B_0$$

$$|\alpha\rangle\ (m_S = +\frac{1}{2}) \qquad E_{+\frac{1}{2}} = +\frac{1}{2} g_e\, \beta_e\, B_0 \tag{2.4}$$

Transition between two states may be induced by an electromagnetic field $\boldsymbol{B_1}$ applied perpendicular to the field $\boldsymbol{B_0}$ at resonance frequency ω such that the photon energy matches the energy difference:

$$\hbar\omega = \Delta E = E_{+\frac{1}{2}} - E_{-\frac{1}{2}} = g_e\, \beta_e\, B_0 \tag{2.5}$$

For magnetic field strengths of 0.3 - 6 Tesla, usually applied in EPR spectroscopy, the resonance frequency of the radiation is in the range of 9 - 180 GHz and belongs to the microwave region. In an actual EPR experiment, one usually leaves the microwave frequency fixed and sweeps through the resonance by varying the strength of magnetic field $\boldsymbol{B_0}$.

2.3.2. Unpaired electron spin

In general g-factor is a matrix, then the Hamiltonian of Zeeman interaction of an unpaired electron spin with external magnetic field $\boldsymbol{B_0}$ is given by [44-46]:

$$\hat{H}_Z = \beta_e\, \boldsymbol{B_0}\, g\, \hat{\boldsymbol{S}} \tag{2.6}$$

where $\hat{S} = (S_x, S_y, S_z)$ is the spin operator, g denotes the g-tensor of the electron which accounts for the deviation of the measured g-value from the g-factor of the free electron (g_e).

The deviation arises from the coupling between the electron spin and orbital magnetic moment. The orbital magnetic moment is given by:

$$\boldsymbol{\mu}_L = -\frac{e}{2m_e}\hat{\boldsymbol{L}} \tag{2.7}$$

where $\hat{\boldsymbol{L}}$ is the operator of angular orbital momentum and associated with motaion of electron about nucleus. The coupling energy of $\hat{\boldsymbol{L}}$ and $\hat{\boldsymbol{S}}$ is:

$$\hat{H}_{LS} = \zeta \hat{\boldsymbol{L}} \hat{\boldsymbol{S}} \tag{2.8}$$

here ζ is the spin-orbit coupling constant.

The shift of resonance frequency due to this interaction is included in the g-values. In solid state, g-factor becomes orientation dependent and thus is conveniently described by a second rank matrix. For organic radicals the deviation of the measured g-factor from g_e is small $| g - g_e | / g_e < 1$ % but can be significant in complexes with metal ions.

The g-tensor of an organic π-radical is an integral property of the electronic wave functions. The principal values of the g-tensor and orientation of its principal axes with respect to the molecular axes frame is determined by spatial distribution of the orbitals carrying the unpaired spin. This distribution can be influenced by interaction with other molecules, e.g. due to hydrogen bond, π-stacking interaction.

When the magnetic field $\boldsymbol{B_0}$ is along an arbitrary direction, described by the vector $\boldsymbol{n}$, the effective g-value measured along this direction can be evaluated as [44]:

$$g_{eff}(\theta,\varphi) = \sqrt{\boldsymbol{n}^T g g^T \boldsymbol{n}} \text{ with } \boldsymbol{n}(\theta,\varphi) = \frac{\boldsymbol{B_0}}{B_0} = \begin{pmatrix} \sin\theta\cos\varphi \\ \sin\theta\sin\varphi \\ \cos\theta \end{pmatrix} \tag{2.9}$$

where θ and φ are the polar and azimuthal angles describing the orientation of $\boldsymbol{n}$ with respect to principal axis system**.**

2.3.3. Hyperfine interaction

The interaction between an electron spin $\boldsymbol{S}$ and a nucleus spin $\boldsymbol{I}$, which has also a spin moment, is described by the Hamiltonian of the hyperfine interaction (hfc):

$$\hat{H}_{hfs} = \hat{\boldsymbol{S}} A \hat{\boldsymbol{I}} \tag{2.10}$$

where A is the hfc tensor, $\hat{\boldsymbol{I}}$ is the nuclear spin operator.

The hfc A tensor components can be separated into its isotropic a_{iso} (spherically symmetric) and anisotropic A' components:

$$A = a_{iso} + A' \tag{2.11}$$

a_{iso} describes the Fermi contact interaction and is proportional to the probability density $|\varphi(0)|^2$ of electron at the position of nucleus [44, 46]:

$$a_{iso} = \frac{2}{3}\mu_0 \beta_e \beta_N g_e g_N \, |\varphi(0)|^2 \qquad (2.12)$$

where g_N is the g-value of the nucleus.

The anisotropic components are derived from the classical expression of interacting magnetic dipoles [44, 47]:

$$A' = \frac{g_e \beta_e g_N \beta_N}{hr^3} \rho_\pi (3\cos^2\vartheta - 1), \qquad (2.13)$$

where ρ_π is the unpaired π electron spin density, ϑ is the angle between the applied magnetic field and distance r between dipoles.

Since the $Tr(A')$ is equal zero, a_{iso} is determined as $a_{iso} = \frac{1}{3} TrA$.

The isotropic hfc a_{iso} constant in the planar π electron radicals is linearly related to the π electron spin density. For isotropic hfc constant a_{iso} of proton bonded directly to the carbon atom (aromatic C-H fragment) the McConnell assumption can be applied [44, 47, 48]:

$$a_{iso}(H) = Q_{CH} \rho_\pi (C), \qquad (2.14)$$

where ρ_C^π is the π electron spin density at carbon atom, Q_{CH} is the spin polarisation constant of C-H bound.

However, the isotropic ^{13}C hfc constant a_{iso}(C) is not simply proportional to the π electron spin density on the same carbon atom as in case of proton hfc splitting in C-H fragment. Thus, in this case the famous McConnell assumption cannot be applied. For nucleus such as ^{13}C, the prediction of isotropic hfc a_{iso} constant becomes considerably complicated. According to the Karplus-Fraenkel assumption, the isotropic $a_{iso}(C)$ constant for an sp^2 hybridised carbon atom C bound to three atoms, Xj (j = 1,2,3), can be written as [44, 49, 50]:

$$a_{iso}(C) = (Q_S^C + \sum_{j=1}^{3} Q_{CXj}^C)\rho_\pi(C) + \sum_{j=1}^{3} Q_{XjC}^C \rho_\pi(Xj), \qquad (2.15)$$

where $\rho_\pi(C)$ and $\rho_\pi(Xj)$ are the π electron spin densities on carbon atom C and Xj, respectively; Q_S^C is the spin polarisation contribution from the *1s* electrons of carbon atom C, Q_{CXj}^C represents the spin polarisation contribution from the *2s* electrons and Q_{XjC}^C is the spin polarisation contribution arising from the interaction between bond *C-Xj* and π electron spin densities on atom *Xj*. Correspondingly, the spin polarisation parameters Q_S^C, Q_{XjC}^C are negative and Q_{CXj}^C is positive.

The anisotropic A' hfc ^{13}C depends mainly on the unpaired π spin density of corresponding carbon atoms and has an axially symmetric form:

$$A'_{xx}=A'_{yy}=-A'_{zz}/2. \qquad (2.16)$$

Moreover, the largest and positive A'_{zz} component is usually collinear with p_z orbital carrying unpaired π spin density and A'_{xx}, A'_{yy} lie perpendicular to A'_{zz}, respectively. Although, some deviation of the anisotropic ^{13}C hfc tensors from the axial symmetry can be due to the presence of unpaired π spin density on the neighbouring atoms (oxygen, carbon).

Thus, measurement of the hfc tensor provides information on the spin densities at certain positions of the molecule.

3. Spin Correlated Radical Pair Mechanism

Spin-correlated radical pair (RP) is a pair of radicals whose electron spins do not have random relative orientation. Spin-correlated RP can be created, for example, by photolysis, radiolysis, and thermolysis and, in a few cases, enzymolysis [51-53]. In photosynthetic RC spin-correlated RPs are formed by photoexcitation and charge separation.

The initial spin state is conserved during excitation energy transfer and primary charge separation. Formation time of the primary RP is shorter compared to the time scale of all spin magnetic interaction. Hence, the first elementary step of ET from P_{700}^{*} to A_0 to A_1 has to be considered as a non-adiabatic process with respect to the electron spins. The first $P_{700}^{\bullet+}A_0^{\bullet-}$ RP is generated in the pure singlet state. In good approximation, spin dynamics can be neglected in the short-lived RP. Thus, at the moment of ET from $A_0^{\bullet-}$ to A_1, the first $P_{700}^{\bullet+}A_0^{\bullet-}$ RP stays in the singlet state and the second $P_{700}^{\bullet+}A_1^{\bullet-}$ RP inherits this spin state. The life time of the second $P_{700}^{\bullet+}A_1^{\bullet-}$ RP is long enough for spin dynamic development. As a consequence the subsequent RP acquires the spin state of the previous RP. Thus, during ET in RC a sequence of spin correlated RP is formed. This chapter characterises the appearance of EPR spectrum of the second $P_{700}^{\bullet+}A_1^{\bullet-}$ RP.

3.1. EPR spectrum of spin correlated RP

To characterize the appearance of EPR spectrum of a spin correlated RP the spin Hamiltonian, energy levels, population of the energy levels and transition probabilities must be considered. The spin Hamiltonian and values of energy levels will be given in frequency units (rad/s).

3.1.1. Spin Hamiltonian of spin correlated RP

The spin Hamiltonian $\hat{H}_0$ of a pair of coupled electron spins ($S = \frac{1}{2}$) in external static magnetic field includes the following terms [54-56]:

$$\hat{H}_0 = \hat{H}_{ZA} + \hat{H}_{ZP} + \hat{H}_{dd} + \hat{H}_j + \hat{H}_{hfs} \tag{3.1}$$

The first two items $\hat{H}_{ZA}$ and $\hat{H}_{ZP}$ represent the Zeeman interaction of each electron spin $\boldsymbol{S_A}$ (acceptor) and $\boldsymbol{S_P}$ (donor) with an external static magnetic field $\boldsymbol{B_0}$ applied along z axis:

$$\hat{H}_{ZA} + \hat{H}_{ZP} = g_A \beta B_0 \hat{S}_{Az} + g_P \beta B_0 \hat{S}_{Pz} \tag{3.2}$$

g_A, g_P are g-factors of the electron spins $\boldsymbol{S_A}$ and $\boldsymbol{S_P}$, respectively.

$\hat{H}_{dd}$ is the dipole-dipole interaction between the electron spins $\boldsymbol{S_A}$ and $\boldsymbol{S_P}$. In point-dipole approximation (distant radicals) the dipole-dipole coupling can be considered to be axially symmetric. Its secular part in high magnetic field approximation has the form:

$$\hat{H}_{dd} = 2d \hat{S}_{Az} \hat{S}_{Pz} - d(\hat{S}_{Ax} \hat{S}_{Px} + \hat{S}_{Ay} \hat{S}_{Py}) \tag{3.3}$$

where d is the dipole coupling constant.

$\hat{H}_j$ is the spin exchange interaction of two spins $\boldsymbol{S_A}$ and $\boldsymbol{S_P}$:

$$\hat{H}_j = -J(\frac{1}{2} + 2\hat{\mathbf{S}}_{\mathbf{A}} \hat{\mathbf{S}}_{\mathbf{P}}) \tag{3.4}$$

where J is the exchange coupling constant.

$\hat{H}_{hfs}$ is the hfc interaction with nuclear spins. In the high field approximation, neglecting all non-secular terms one obtains:

$$\hat{H}_{hfs} = \hat{S}_{Az} \sum_l A_{Al} \hat{I}_{lz} + \hat{S}_{Pz} \sum_m A_{Pm} \hat{I}_{mz} \tag{3.5}$$

where A_{Ap}, A_{Pr} are their hfc constants with nuclear spins $\hat{I}_l$, $\hat{I}_m$ for acceptor and donor, respectively.

The EPR transitions are induced by a microwave magnetic field with vector components $\boldsymbol{B_1} = (B_1 \cos\omega_{mw}t; B_1 \sin\omega_{mw}t; 0)$. The Hamiltonian of Zeeman interaction of electron spins $\boldsymbol{S_A}$ and $\boldsymbol{S_P}$ with a microwave magnetic field $\boldsymbol{B_1}$ is defined in the following way [46]:

$$\hat{H}(t)_{mw} = g_A\beta\boldsymbol{B_1}\hat{\boldsymbol{S}}_{\boldsymbol{A}} + g_P\beta\boldsymbol{B_1}\hat{\boldsymbol{S}}_{\boldsymbol{P}} \tag{3.6}$$

Then the total Hamiltonian $\hat{H}$ of a pair of coupled electron spins is time-dependent:

$$\hat{H} = \hat{H}_0 + \hat{H}_{mw}(t) \tag{3.7}$$

In order to get rid of the time dependence in the Hamiltonian given by Eqn. 3.7 a standard approach is to transform the total Hamiltonian $\hat{H}$ into a frame of reference system rotating with an angular velocity ω_{mw}, the frequency of microwave field, around the static magnetic field $\boldsymbol{B_0}$, axis z. Assuming the same g-factor for the pair of coupled electron spins (g_A = g_P) in Eqn. 3.6 the Hamiltonian $\hat{H}_{mw}$ of interaction of electron spins with the microwave magnetic field in the rotating coordinate system becomes:

$$\hat{H}_{mw} = g_A\beta B_{1x}(\hat{S}_{Ax} + \hat{S}_{Px}) \tag{3.8}$$

Then the Hamiltonian $\hat{H}_0$, in the rotating frame can be expressed in the following way:

$$\begin{aligned} \hat{H}_0' = {} & g_A\beta B_0\hat{S}_{Az} + g_P\beta B_0\hat{S}_{Pz} + \hat{S}_{Az}\sum_l A_{Al}\hat{I}_{lz} + \hat{S}_{Pz}\sum_m A_{Pm}\hat{I}_{mz} + \\ & + 2d\hat{S}_{Az}\hat{S}_{Pz} - d(\hat{S}_{Ax}\hat{S}_{Px} + \hat{S}_{Ay}\hat{S}_{Py}) - J\left(\frac{1}{2} + 2\hat{\boldsymbol{S}}_{\boldsymbol{A}}\hat{\boldsymbol{S}}_{\boldsymbol{P}}\right) - \omega_{mw} \end{aligned} \tag{3.9}$$

The presence of the last term in Eqn. 3.9 does not change the eigenstates of the Hamiltonian $\hat{H}_0$ and shifts equally only their eigenvalues by ω_{mw}.

3.1.2. Eigenvectors and eigenvalues of spin Hamiltonian

There are four eigenstates of the system consisting of a pair of coupled electron spins with $S=\frac{1}{2}$. In the basis of the eigenstates of spin operator $\hat{\boldsymbol{S}}^2=(\hat{\boldsymbol{S}}_A+\hat{\boldsymbol{S}}_P)^2$ (singlet-triplet basis) they can be written as:

$$\begin{aligned}
&|T_+\rangle=|\alpha\alpha\rangle, S=1, S_z=+1\\
&|S\rangle=\frac{1}{\sqrt{2}}(|\alpha\beta\rangle-|\beta\alpha\rangle), S=0, S_z=0\\
&|T_0\rangle=\frac{1}{\sqrt{2}}(|\alpha\beta\rangle+|\beta\alpha\rangle), S=1, S_z=0\\
&|T_-\rangle=|\beta\beta\rangle, S=1, S_z=-1
\end{aligned} \tag{3.10}$$

where $|\alpha\rangle$ and $|\beta\rangle$ are the single spin Zeeman Hamiltonian eigenstates.

Therefore, in the singlet-triplet basis set, the above mentioned Hamiltonian $\hat{H}_0'$ can be expressed in matrix form as shown below [56-61]:

$$\hat{H}_0'=\begin{pmatrix}
\langle T_+|\hat{H}_0'|T_+\rangle & \langle T_+|\hat{H}_0'|S\rangle & \langle T_+|\hat{H}_0'|T_0\rangle & \langle T_+|\hat{H}_0'|T_-\rangle\\
\langle S|\hat{H}_0'|T_+\rangle & \langle S|\hat{H}_0'|S\rangle & \langle S|\hat{H}_0'|T_0\rangle & \langle S|\hat{H}_0'|T_-\rangle\\
\langle T_0|\hat{H}_0'|T_+\rangle & \langle T_0|\hat{H}_0'|S\rangle & \langle T_0|\hat{H}_0'|T_0\rangle & \langle T_0|\hat{H}_0'|T_-\rangle\\
\langle T_-|\hat{H}_0'|T_+\rangle & \langle T_-|\hat{H}_0'|S\rangle & \langle T_-|\hat{H}_0'|T_0\rangle & \langle T_-|\hat{H}_0'|T_-\rangle
\end{pmatrix}=$$

$$=\begin{pmatrix}
\omega_0-J/2+d/2 & 0 & 0 & 0\\
0 & J & \Delta\omega & 0\\
0 & \Delta\omega & -J-d & 0\\
0 & 0 & 0 & -\omega_0-J/2+d/2
\end{pmatrix} \tag{3.11}$$

with

$$\Delta\omega=\frac{1}{2}\beta B_0(g_A-g_P)-\frac{1}{2}\sum_j(A_{Aj}-A_{Pj})m_j \tag{3.12}$$

$$\omega_0=\frac{1}{2}\beta B_0(g_A+g_P)+\frac{1}{2}\sum_l A_{Al}\hat{I}_{lz}+\frac{1}{2}\sum_m A_{Pm}\hat{I}_{mz}-\omega_{mw} \tag{3.13}$$

It is easily seen that the triplet states $|T_+\rangle$ and $|T_-\rangle$ are eigenvectors of $\hat{H}_0'$. Two remaining eigenvectors $|2\rangle$ and $|3\rangle$ can be presented as a linear superposition of states $|S\rangle$ and $|T_0\rangle$:

$$\begin{aligned} &|1\rangle = |T_+\rangle \\ &|2\rangle = c_{22}\,|S\rangle + c_{23}\,|T_0\rangle \\ &|3\rangle = c_{32}\,|S\rangle + c_{33}\,|T_0\rangle \\ &|4\rangle = |T_-\rangle \end{aligned} \tag{3.14}$$

or written in matrix form:

$$\begin{pmatrix} |1\rangle \\ |2\rangle \\ |3\rangle \\ |4\rangle \end{pmatrix} = \begin{pmatrix} 1 & 0 & 0 & 0 \\ 0 & c_{22} & c_{23} & 0 \\ 0 & c_{31} & c_{33} & 0 \\ 0 & 0 & 0 & 1 \end{pmatrix} \begin{pmatrix} |T_+\rangle \\ |S\rangle \\ |T_0\rangle \\ |T_-\rangle \end{pmatrix} = U \begin{pmatrix} |T_+\rangle \\ |S\rangle \\ |T_0\rangle \\ |T_-\rangle \end{pmatrix} \tag{3.15}$$

where matrix U contains the coefficients c_{ij} and is an unitary matrix ($UU^T = 1$). The matrix elements can be expressed as sines or cosines of the *mixing angle* φ (or *mixing angle* of $|S\rangle$ and $|T_0\rangle$ states) [44]:

$$U = \begin{pmatrix} 1 & 0 & 0 & 0 \\ 0 & c_{22} & c_{23} & 0 \\ 0 & c_{31} & c_{33} & 0 \\ 0 & 0 & 0 & 1 \end{pmatrix} = \begin{pmatrix} 1 & 0 & 0 & 0 \\ 0 & \cos\varphi & \sin\varphi & 0 \\ 0 & -\sin\varphi & \cos\varphi & 0 \\ 0 & 0 & 0 & 1 \end{pmatrix} \tag{3.16}$$

U also transforms the Hamiltonian $\hat{H}_0'$ into its diagonal form by a simple rotation of the basis functions with angle φ [44]:

$$\hat{H}_0'^{\,diag} = U\,\hat{H}_0'\,U^T = \begin{pmatrix} E_1 & 0 & 0 & 0 \\ 0 & E_2 & 0 & 0 \\ 0 & 0 & E_3 & 0 \\ 0 & 0 & 0 & E_4 \end{pmatrix} \tag{3.17}$$

The eigenvalues and eigenvectors (or eigenstates) of $\hat{H}_0'$ are [44, 55, 57-62]:

$$\begin{aligned} E_1 &= \omega_0 - \frac{(2J-d)}{2} \\ E_2 &= -\frac{d}{2} + \Omega \\ E_3 &= -\frac{d}{2} - \Omega \\ E_4 &= -\omega_0 - \frac{(2J-d)}{2} \end{aligned} \qquad \begin{aligned} &|1\rangle = |T_+\rangle \\ &|2\rangle = \cos\varphi\,|S\rangle + \sin\varphi\,|T_0\rangle \\ &|3\rangle = -\sin\varphi\,|S\rangle + \cos\varphi\,|T_0\rangle \\ &|4\rangle = |T_-\rangle \end{aligned} \tag{3.18}$$

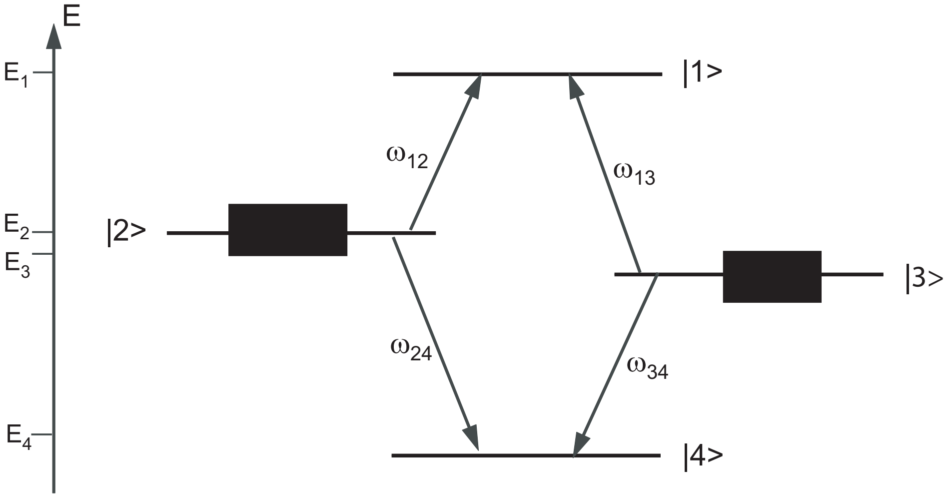

Figure 3.1. Energetic scheme for a pair of coupled electron spins in the presence of a static magnetic field. The arrows denote the allowed single quantum transition between the energy levels for a pair born in the singlet precursor state.

where 2Ω is the energy difference between states E_2 and E_3:

$$\Omega = \sqrt{(J+\frac{d}{2})^2+\Delta\omega^2} \tag{3.19}$$

Angle φ is defined as:

$$\sin 2\varphi = \frac{\Delta\omega}{\Omega}; \quad \cos 2\varphi = \frac{J+\frac{d}{2}}{\Omega}; \quad \tan 2\varphi = \frac{\Delta\omega}{J+\frac{d}{2}} \tag{3.20}$$

The scheme of energy levels is shown in Figure 3.1. Note that, for simplicity, the hfc interactions of both electron spins are neglected.

3.1.3. EPR transitios and intensities

EPR transitions are induced by the Hamiltonian $\hat{H}_{mw}$ and their efficiency is proportional to the squared transition matrix elements $|\langle i | H_{mw} | j \rangle|^2$, where $|i\rangle$ and $|j\rangle$ are the eigenstates of $\hat{H}_0'$.

Since the matrix element $\langle S | \hat{H}_{mw} | T_0 \rangle = 0$, only the transition between the triplet states of Hamiltonian $\hat{H}_0'$ of RP can be induced by the perturbation of $\hat{H}_{mw}$. Non-zero matrix elements of the allowed transitions give [55]:

$$\begin{aligned} &|\langle 1 | H_{mw} | 2 \rangle|^2 \propto \frac{1}{2}\sin^2\varphi \quad && |\langle 4 | H_{mw} | 2 \rangle|^2 \propto \frac{1}{2}\sin^2\varphi \\ &|\langle 1 | H_{mw} | 3 \rangle|^2 \propto \frac{1}{2}\cos^2\varphi \quad && |\langle 4 | H_{mw} | 3 \rangle|^2 \propto \frac{1}{2}\cos^2\varphi \end{aligned} \tag{3.21}$$

The transition intensities can be determined if the initial conditions are specified. The RP is born in a pure singlet state. The singlet state can be presented as a linear superposition of eigenvectors of Hamiltonian $\hat{H}_0'$:

$$| S \rangle = \cos\varphi | 2 \rangle - \sin\varphi | 3 \rangle \tag{3.22}$$

Therefore, only the two states $|2\rangle$ and $|3\rangle$ are populated:

$$n_2 = \cos^2\varphi; \quad n_3 = \sin^2\varphi \tag{3.23}$$

populations of states $|1\rangle$ and $|4\rangle$ are $n_1 = n_4 = 0$.

Intensities I_{ij} of a resonance EPR transition $i \rightarrow j$ $(|\Delta m| = 1)$ are determined by the product of the transition probability $\langle i | H_{mw} | j \rangle^2$ with the population differences of states *i* and *j* involved in this transition, $(n_i - n_j)$, [45, 46, 63]:

$$I_{ij} \propto (n_i - n_j) |\langle i | H_{mw} | j \rangle|^2 \tag{3.24}$$

According to the populations of the energy levels the polarized EPR spectrum is expected to consist of four lines with the same absolute intensities. Indeed, by putting the population of the energy levels and transition probabilities for the EPR lines intensities one obtains [55, 57, 60]:

$$\begin{aligned}
I_{12} &\propto (n_2 - n_1)\,|\langle 1|H_{mw}|2\rangle|^2 = \frac{1}{8}\sin^2 2\varphi = \frac{1}{8}\left(\frac{\Delta\omega}{\Omega}\right)^2 \\
I_{42} &\propto (n_4 - n_2)\,|\langle 4|H_{mw}|2\rangle|^2 = \frac{1}{8}\sin^2 2\varphi = -\frac{1}{8}\left(\frac{\Delta\omega}{\Omega}\right)^2 \\
I_{31} &\propto (n_3 - n_1)\,|\langle 3|H_{mw}|1\rangle|^2 = \frac{1}{8}\sin^2 2\varphi = -\frac{1}{8}\left(\frac{\Delta\omega}{\Omega}\right)^2 \\
I_{43} &\propto (n_4 - n_3)\,|\langle 4|H_{mw}|3\rangle|^2 = \frac{1}{8}\sin^2 2\varphi = \frac{1}{8}\left(\frac{\Delta\omega}{\Omega}\right)^2
\end{aligned} \tag{3.25}$$

Four possible transitions with the following frequencies are expected (Figure 3.1):

$$\begin{aligned}
\omega_{12} &= \frac{E_1 - E_2}{h} = \frac{\omega_0 - (J-d) - \Omega}{h} \\
\omega_{34} &= \frac{E_3 - E_4}{h} = \frac{\omega_0 + (J-d) - \Omega}{h} \\
\omega_{13} &= \frac{E_1 - E_3}{h} = \frac{\omega_0 - (J-d) + \Omega}{h} \\
\omega_{24} &= \frac{E_2 - E_4}{h} = \frac{\omega_0 + (J-d) + \Omega}{h}
\end{aligned} \tag{3.26}$$

Thus, the polarized spectrum of the spin correlated RP consists of two “antiphase” doublets centred at the *g*-factors of the individual electron spins, g_A and g_P with emission/absorption (E/A) polarisation pattern. The stick spectrum corresponding to transitions given by Eqn. 3.25 and 3.26 is shown in Figure 3.2. Transitions $1 \rightarrow 2$ and $1 \rightarrow 3$ correspond to absorption (A) and transitions $2 \rightarrow 4$ and $3 \rightarrow 4$ to emission (E). All intensities of the RP spectrum are at their maximum when $|\Delta\omega| >> |J + \frac{d}{2}|$ (*weak coupling case*). The EPR intensities are expected to be very weak when $|\Delta\omega| << |J + \frac{d}{2}|$ (φ~0, *strong coupling case*), in which case, then transitions $1 \rightarrow 2$ and $2 \rightarrow 4$ are almost forbidden and for the transitions $1 \rightarrow 3$ and $3 \rightarrow 4$ the population differences are very small.

For the weakly coupled RP, whether the doublets are EA (i.e. E for the low-field component and A for the high-field component) or AE (*vice-versa*) depends on the sign of the splitting, *2(J- d)*, and hence on the angle ϑ between the dipole-dipole coupling vector and the magnetic field direction. The dipole-dipole constant is defined as $d = \frac{1}{6}D(3\cos^2\vartheta - 1)$, where $D = -\frac{\mu_0 h g_A g_B}{4\pi r^3}$. The angle $\vartheta \approx 54.7°$ is the “magic” angle for which the effective

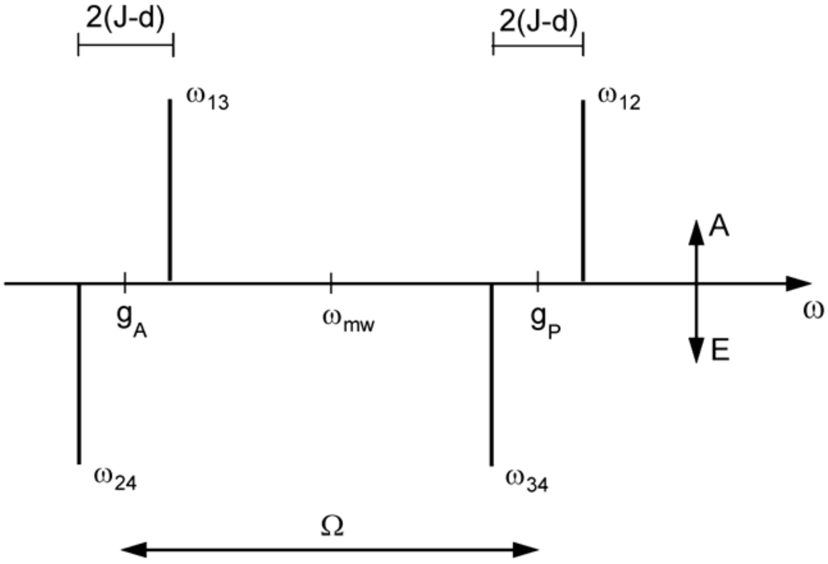

Figure 3.2. Stick spectrum for the pair originated from the corresponding transition denoted above. The separation between the line pairs is determined by the g-shift between two spins. The difference within each line pair is given by $2(J+d)$. The polarisation pattern characterised as E/A/E/A (E-emission, A-absorption) is expected for orientation $\vartheta < 54.7°$ and negligible J coupling.

dipolar coupling changes its sign. For a pair of interacting electron spins the dipolar coupling is expected to be negative when ($d < 0$) for $\vartheta < 54.7°$ and positive ($d > 0$) for $\vartheta > 54.7°$. If exchange coupling is neglected an E/A/E/A polarisation pattern is expected for the case $\vartheta < 54.7°$. Radical pairs with $\vartheta = 54.7°$ do not contribute to the spectrum and the two lines within doublet cancel each other. For $\vartheta > 54.7°$ the polarisation changes to A/E/A/E [57, 60, 61].

3.2. Time evolution of the RP spin density matrix

If the spin density matrix operator is described in the singlet-triplet basis set for a singlet-born RP all elements of $\hat{\rho}_{ST}(0)$ are equal to zero except only $\hat{\rho}_{ss}(0) = 1$:

$$\hat{\rho}_{ST}(0) = \begin{pmatrix} 0 & 0 & 0 & 0 \\ 0 & 1 & 0 & 0 \\ 0 & 0 & 0 & 0 \\ 0 & 0 & 0 & 0 \end{pmatrix} \tag{3.27}$$

In the eigenbasis of $\hat{H}_0$ [57, 64-66]:

$$\hat{\rho}(0) = U\hat{\rho}_{ST}(0)U^{+} = \begin{pmatrix} 0 & 0 & 0 & 0 \\ 0 & \cos^2\varphi & -\frac{1}{2}\sin 2\varphi & 0 \\ 0 & -\frac{1}{2}\sin 2\varphi & \sin^2\varphi & 0 \\ 0 & 0 & 0 & 0 \end{pmatrix} \tag{3.28}$$

where the diagonal elements $\rho_{22} = \cos^2\varphi$ and $\rho_{33} = \sin^2\varphi$ represent populations of the states $|2\rangle$ and $|3\rangle$ and off-diagonal elements $\rho_{32} = -\rho_{23} = -\sin\varphi\cos\varphi$ represent the initial coherence between them.

At $t = 0$ the net polarisation is zero. Due to the spin coupling and Zeeman interaction together with the hfc interaction (or so called *spin-dynamics*) the spin polarisation across RP spectrum evolves.

In general, time evolution of the spin density matrix can be obtained by solving of von-Neumann equation:

$$\frac{\delta\hat{\rho}(t)}{\delta t} = -i\left[\hat{H}_0^{'}, \hat{\rho}(t)\right] \tag{3.29}$$

Note that $\hat{H}_0^{'}$ is given in frequency units.

The solution of the Eqn. 3.29 for the spin density matrix $\hat{\rho}(t)$ in the singlet-triplet basis set is straightforwardly given by:

$$\hat{\rho}_{ST}(t) = U^{+}\exp(-i\hat{H}_0^{'\,diag}t)U\hat{\rho}(0)U^{+}\exp(i\hat{H}_0^{'\,diag}t)U =$$
$$U^{+}\begin{pmatrix} \exp(-iE_1t) & 0 & 0 & 0 \\ 0 & \exp(-iE_2t) & 0 & 0 \\ 0 & 0 & \exp(-iE_3t) & 0 \\ 0 & 0 & 0 & \exp(-iE_4t) \end{pmatrix} \times \tag{3.30}$$
$$U\begin{pmatrix} 0 & 0 & 0 & 0 \\ 0 & 1 & 0 & 0 \\ 0 & 0 & 0 & 0 \\ 0 & 0 & 0 & 0 \end{pmatrix}U^{+}\begin{pmatrix} \exp(iE_1t) & 0 & 0 & 0 \\ 0 & \exp(iE_2t) & 0 & 0 \\ 0 & 0 & \exp(iE_3t) & 0 \\ 0 & 0 & 0 & \exp(iE_4t) \end{pmatrix}U$$

Matrix multiplication yields:

$$\hat{\rho}_{ST}(t) = \begin{pmatrix} 0 & 0 & 0 & 0 \\ 0 & 1-\sin^2 2\varphi\sin^2\Omega t & \sin^2 2\varphi(\cos 2\varphi\sin^2\Omega t + \frac{i}{2}\sin 2\Omega t) & 0 \\ 0 & \sin^2 2\varphi(\cos 2\varphi\sin^2\Omega t - \frac{i}{2}\sin 2\Omega t) & \sin^2 2\varphi\sin^2\Omega t & 0 \\ 0 & 0 & 0 & 0 \end{pmatrix} \tag{3.31}$$

with $\rho_{ST}(t) = \rho_{TS}^{*}(t)$.

In the eigenbasis of $\hat{H}_0'$ the spin density matrix is given by [56]:

$$\hat{\rho}(t) = \exp(-i\hat{H}_0'^{\,diag} t)\,\hat{\rho}(0)\exp(i\hat{H}_0'^{\,diag} t) = U\hat{\rho}_{ST}(t)U^{+}$$
$$\begin{pmatrix} 0 & 0 & 0 & 0 \\ 0 & \cos^2\varphi & -\frac{1}{2}\sin 2\varphi\exp(-2i\Omega t) & 0 \\ 0 & -\frac{1}{2}\sin 2\varphi\exp(+2i\Omega t) & \sin^2\varphi & 0 \\ 0 & 0 & 0 & 0 \end{pmatrix} \tag{3.32}$$

where $\rho_{32}(t) = \rho_{23}^{*}(t)$.

In the eigenbasis of $\hat{H}_0'$ populations of the levels, $n_2 = \rho_{22}$ and $n_3 = \rho_{33}$, are time-independent while off-diagonal elements oscillate with frequency $E_2 - E_3 = 2\Omega$:

$$\rho_{32}(t) = \rho_{23}^{*}(t) = -\frac{1}{2}\sin 2\varphi\exp(+i2\Omega t) \tag{3.33}$$

They represent the coherent superposition of states $|2\rangle$ and $|3\rangle$, so called *zero-quantum coherence* [54, 55, 65].

Therefore, in accordance with theory the intensity of each of the four allowed EPR transition will beat at 2Ω frequency (called as *zero-quantum beat frequency*) [55]:

$$I(t) = \frac{1}{2}\sin^2 2\varphi\sin^2(2\Omega t) \tag{3.34}$$

There are two contributions which can damp these beats: spin-spin relaxation and inhomogeneous distribution of transition frequencies [57]. The latter is due to the g-tensor anisotropy and hfc interactions and is responsible for fast damping of the *zero-quantum beats*. Because of that the *zero-quantum beats* can be detected in TR EPR only in a narrow time range, which is determined by $T_2^{*} << t < T_2$, where $\frac{1}{T_2^{*}} = \frac{1}{T_2} + \Delta\Omega$, $\frac{1}{T_2}$ is the rate of spin-spin relaxation and $\Delta\Omega$ is the inhomogeneous broadening. The effect of the *zero* q*uantum beats* at frequency ~ 20 MHz (as it was predicted for the weekly coupled RP) has been revealed in the fully deuterated sample by narrow band excitation detected EPR at times up to t = 130 ns after laser flash [66-68].

However, approximately 130 ns after the laser flash, the conditions $\Omega t >> 1$ are satisfied and all terms in (3.31) and (3.32) tend to their average:

$\sin^2(2\Omega t) \to \frac{1}{2}, \sin(2\Omega t) \to 0$ and $\exp(\pm 2i\Omega t) \to 0$. Then spin density matrix takes the form in the singlet-triplet basis set [57]:

$$\hat{\rho}_{ST}(t) = \begin{pmatrix} 0 & 0 & 0 & 0 \\ 0 & 1-\frac{1}{2}\sin^2 2\varphi & -\frac{1}{2}\sin 2\varphi\cos 2\varphi & 0 \\ 0 & -\frac{1}{2}\sin 2\varphi\cos 2\varphi & \frac{1}{2}\sin^2 2\varphi & 0 \\ 0 & 0 & 0 & 0 \end{pmatrix} \tag{3.35}$$

or, in the eigenbasis set of $\hat{H}_0'$:

$$\hat{\rho}(t) = \begin{pmatrix} 0 & 0 & 0 & 0 \\ 0 & \cos^2\varphi & 0 & 0 \\ 0 & 0 & \sin^2\varphi & 0 \\ 0 & 0 & 0 & 0 \end{pmatrix} \tag{3.36}$$

It is easily seen, that after damping of the *zero quantum coherence*, line intensities of the RP spectrum can be described by population according to the singlet character since the populations of the states $|2\rangle$ and $|3\rangle$ are the same as in Eqn. 3.23.

Thus, as the spin dynamics changes the initial coherence the triplet state with zero projection on the z axis, $|T_0\rangle$ acquires population from the singlet state $|S\rangle$, because in the eigenstates of $\hat{H}_0'$ $|T_0\rangle$ and $|S\rangle$ states are mixed. As a result, microwave field can induce four EPR transitions between energy levels of RP and polarised EPR spectrum appears. In accordance with the populations of energy levels the polarized spectrum of RP consisting of two antiphase doublets appears with the exception of the initial time after laser flash when the *zero quantum beats* have taken place.

4. Materials and Methods

4.1. Materials

All external redox agents such as NaAsc (sodium ascorbate), PMS (phenazine methosulfate), and reagents for preparation of buffers were purchased from Aldrich. Following buffers were used:

1. 50 mM Tris (α, α, α, α-Tris-(hydroxymethyl)-methylamine) with 0.02 % ß-DM (n- dodecyl-ß-D-maltoside), pH = 8.3;
2. 50 mM Tricine with 10 % glycerol, 0.2 % Triton X-100, pH =8 .3.

4.2. Quinones

9,10-anthraquinone (AQ) was purchased from Aldrich and purified by column chromatography on aluminium. 2-methyl-1,4-naphtoquinone (2-methyl-1,4-NQ), 2-methyl-4-^{13}C-1,4-naphtoquinone (2-methyl-4-^{13}C-1,4-NQ), 2-methyl-1-^{13}C-1,4-naphtoquinone (2-methyl-1-^{13}C-1,4-NQ) were synthesized by Dr. Herbert Zimmermann (MPImF Heidelberg).

Synthesis of isotope-labelled 2-methyl-4-^{13}C-1,4-NQ

The starting material for the synthesis of 2-methyl-4-^{13}C-NQ was 2-methylcynamic acid, prepared according to [69] by modified Perkin reaction from benzaldehyde and propionic anhydride. 2-methylcynamic acid was reduced to 2-methylcinnamylalcohol with LiH_4 in ether. Catalytic hydrogenation to 2-benzyl-1-propanol was accomplished with fresh reduced Adam's catalyst in methanol. Conversion to the 2-benzylpropylbromide with $SOCl_2$ was followed by carboxylation of the corresponding Grignard reagent with $^{13}CO_2$ (from $Ba^{13}C0_3$, -30 °C, ether) to 3-benzylbutyric acid-1-^{13}C. Cyclisation to 2-methyl-4-^{13}C-tetralone was made via the acidchloride ($SOCl_2$, room temperature) with polyphosphoric acid as described for tetralone [70]. Clemmensen reduction of 2-methyl-4-^{13}C-tetralone resulted in 2-methyl-4-^{13}C-tetraline, followed by dehydrogenation with palladium on charcoal to 2-methyl-4-^{13}C-napthalene. Oxidation with CrO_3 in the usual way yielded 2-methyl-4-^{13}C-1,4-naphtoquinone.

Synthesis of isotope-labelled 2-methyl-1-^{13}C-1,4-NQ

4-Phenyl-2-butanol was converted to 2-bromo-4-phenyl-butane with PBr_3. The corresponding Grignard reagent was carboxylated with $^{13}CO_2$ (from $BaCO_3$, -30 °C, ether) to 1-^{13}C-2-methyl-4-phenyl-butanoic acid. The cyclization to 1-^{13}C-2-methyl-1-tetralone was accomplished with methane-sulfonic acid instead of using the polyphosphoric acid cyclization reaction of the acid chloride [71]. The usual Clemmensen reduction to the tetraline, followed by dehydrogenation and oxidation was avoided by introducing the surprising one step dehydrogenation and oxidation of the 1-^{13}C-2-methyl-1-tetralone to the wanted 1-^{13}C-2-methyl-1,4-naphthoquinone with $CrO_3/CH_3COOH/ H_2SO_4$:

Oxidation solution: 14 g CrO_3 dissolved in 9 ml conc. CH_3COOH was diluted with 14 ml H_2O and acidified with 1.4 ml conc. H_2SO_4.

Oxidation: 3 g of 1-^{13}C-2-methyl-1-tetralone was mixed with 14 ml conc. CH_3COOH. To the stirred solution the chromium reagent was dropwise added at 5 °C within 30 min. After the addition the mixture was stirred at 50 °C for two hours, warmed up to room temperature and diluted with water in an ice bath until crystals appeared. Yield = 1.5 g (VI). TLC, Silica, hexane/ether 8 : 2, one spot. Fp = 103.5 - 104.5 °C.

The precise labelling of 2-methyl-4-^{13}C-1,4-naphtoquinone and 2-methyl-1-^{13}C-1,4-naphtoquinone, the percentage of ^{13}C, as well as the chemical purity, were checked by ^{13}C, ^{1}H NMR and mass-spectrometry, and were found to be better than 99 %.

4.3. Preparation of PS I with other quinones

4.3.1. AQ reconstitution into PS I complex after organic solvent extraction of PhQ

Organic solvent extraction of PS I was performed in the lab of Prof. Art van der Est (Brock University, Canada).

PS I isolated from *Synechocystis* PCC 6803 was prepared by the method of Biggins and Mathis [72]. The isolated PS I was lyophilized and the PhQ (2-methyl-3-phytyl-1,4-naphthoquinone) was removed by solvent extraction as described also in [13] using hexane (99 %, Aldrich) containing 0.3 % methanol (Caledon). The extraction of PhQ was monitored at X-band by measuring the disappearance of the spin polarized EPR signal due to the second $P_{700}^{\bullet+}A_1^{\bullet-}$ RP state and the accompanying appearance of the characteristic polarization pattern of the triplet $^3P_{700}$ formed by recombination from the first $P_{700}^{\bullet+}A_0^{\bullet-}$ RP. The loss of other pigments was monitored using the visible absorption spectrum of the supernatant recorded with a Unicam UV/Vis spectrometer. Samples for EPR analysis were prepared by suspending 15 mg of extracted PS I in 150 µl of buffer containing 50 mM Tricine, 10 % glycerol and 0.2 % Triton X-100. A homogenizer was used to ensure complete resuspension. AQ was introduced into the A_1-binding site by adding ~ 5 µL of a ~ 150 mM solution of AQ in dimethylsulfoxide (DMSO) to the PS I sample and in the dark at 4 °C for several hours. The incorporation of quinone into the A_1-binding site was monitored by observing the appearance of a spin polarized EPR spectrum due to the $P_{700}^{\bullet+}AQ^{\bullet-}$ RP state accompanied by a decrease in the intensity of the triplet $^3P_{700}$ spectrum. A control experiment using a blank of the solvent containing no quinone was also performed and no change in the TR EPR spectra was observed. For TR EPR measurements 10 µL of 0.8 M NaAsc and 10 µL of 0.08 M PMS were added as external redox agents and the samples were dark adapted and frozen in liquid nitrogen.

4.3.2. Quinone replacement of PQ-9 in PS I complexes isolated from the *menB* mutant and double *menB rubA* mutant (^{13}C labelled NQs and AQ)

A hundred fold molar excess of 2-methyl-1,4-NQ, 2-methyl-4-^{13}C-1,4-NQ, 2-methyl-1-^{13}C-1,4-NQ (10 µL of 0.019 M solution of quinone in ethanol) and AQ (10 µl of 0.034 M solution in dimethylsulfoxide, DMSO) was added to trimer PS I complex in buffer (50 mM Tris-HCl buffer pH = 8.3 containing 0.2 % Triton X-100) isolated from the *menB* mutant and *menB rubA* double mutant strains of *Synechocystis* sp. PCC 6803, respectively [73, 74]. Incubation was carried out at room temperature with intensive stirring about 2 - 4 hours at room temperature. The PS I particles were washed twice with 150 µl buffer (50 mM Tris buffer containing 0.02 % β-MD, pH = 8.3) to remove the excess of quinone. To the final solution 100 µL of sample 10 µL of 0.8 M NaAsc was added. The sample was dark adapted with sequential freezing in liquid nitrogen.

4.4. Selective point mutants

All mutants were grown up in the lab of Prof. J. H. Golbeck (Pennsylvania State University, USA)

4.4.1. Preparation of PS I complexes isolated from the M688N$_{\text{PsaA}}$, M668N$_{\text{PsaB}}$ mutants

The M688N$_{\text{PsaA}}$ and M668N$_{\text{PsaB}}$ variants of *Synechocystis sp.* PCC 6803 were constructed as described in [75].

For low temperature TR EPR experiment, to a solution of PS I, 140 µL, 10 µL of 0.8 M NaAsc was added and the sample was dark adapted and frozen in liquid nitrogen. For high temperature TR EPR experiment, to a solution of sample, 50 µL, 10 µL of 0.8 M NaAsc and 10 µL of 0.08 M PMS were added. The sample was dark adapted and sequentially frozen in liquid nitrogen.

4.4.2. Preparation of PS I complexes isolated from the D566A$_{PsaB}$, D566K$_{PsaB}$, D557A$_{PsaB}$, D557K$_{PsaB}$ mutants

The D566K$_{PsaB}$, D566A$_{PsaB}$, D557K$_{PsaB}$, D557A$_{PsaB}$ variants of *Synechocystis sp.* PCC 6803 were constructed as described in [76]. These variants correspond to D575K$_{PsaB}$, D575A$_{PsaB}$, D566K$_{PsaB}$, D566A$_{PsaB}$ in *Thermosynechococcus elongatus*. PS I complexes are identical to those used in ref. [76] were thawed from long-term storage at -80 °C, and used for this study. Briefly, the growth of the D566K$_{PsaB}$ mutant was impaired under low light and the chlorophyll content per cell was lower than the wild-type, but other growth and chlorophyll content of the other four mutants were identical to the wild-type. PS I complexes isolated form all of the mutants, including D566K$_{PsaB}$, showed rates of NADP$^+$ reduction no less than 75 % of the wild type, and the kinetics of the back reaction with $P_{700}{}^+$ on a single turnover flash showed efficient ET to the terminal [4Fe-4S] clusters, F_A/F_B [76]. Thus, these PS I variants efficiently converted light to a stable charge-separated state.

For low temperature TR EPR experiments, 10 µL of 0.8 M NaAsc was added to 150 µL of sample and the sample was dark adapted and frozen in liquid nitrogen. For high temperature TR EPR experiments, 10 µL of 0.08 M PMS was added to 60 µL of sample with NaAsc and the sample was dark adapted and frozen in liquid nitrogen.

4.5. Multifrequency TR EPR spectroscopy

4.5.1. TR EPR experiment

TR EPR experiment is based on the conventional CW-EPR spectroscopy: the spin system is continuously irradiated by low-power microwave inside the microwave cavity [59]. The RP states are created by pulsed laser flash and TR EPR signal is detected at a fixed magnetic filed as function of time *t* after amplification of signal. The experimental scheme of TR EPR experiment is depicted in Figure 4.1.

TR EPR spectra is measured in the direct-detection mode and observed directly at the out-put of the pre-amplifier without field modulation and lock-in amplification. TR EPR taken in this mode provides fast time resolution (50 ns). EPR spectra are observed in the direct A or E mode but not in the usual derivative form. The need of the broad bandwidth

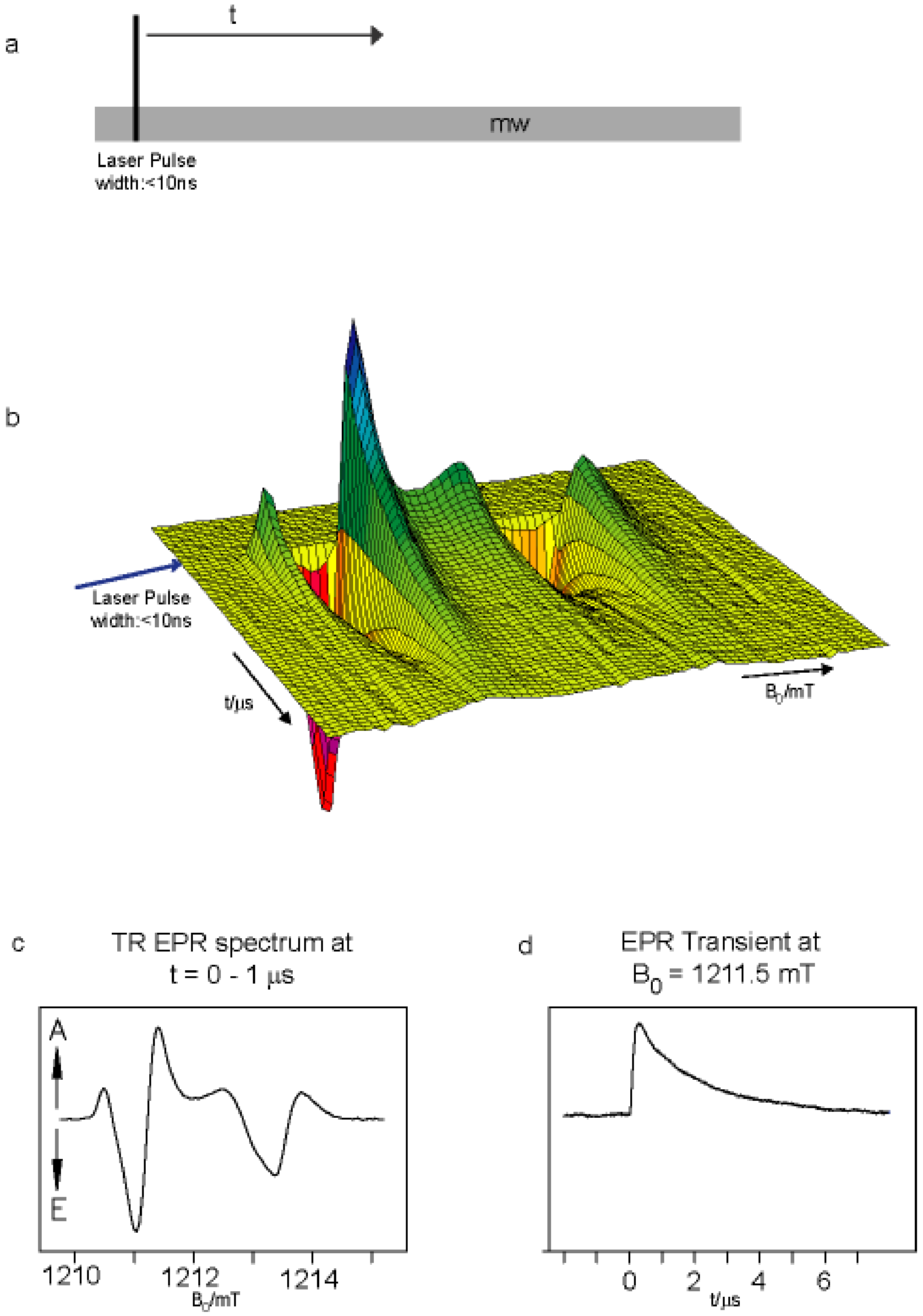

Figure 4.1. a) Experimental scheme of TR EPR experiment.
b) Two dimensional representation of time and magnetic field dependence of EPR signal assigned to the second $P_{700}^{\bullet+}A_1^{\bullet-}$ RP state in PS I complex reconstituted with deuterated 1,4-NQ at Q-band.
c) TR EPR spectrum extracted from the two-dimensional data set by integration of the time-signal between 0 - 1 µs after the laser flash.
d) Time development of the EPR signal at $B_0 = 1211.5$ mT.

of pre-amplifier is to reach a high time resolution and causes a decrease of signal-to-noise ratio. However, spin polarisation leads to much stronger signal due to the selective populations of energy levels which differ significantly from the Boltzman distribution. The TR EPR signal following the laser flash at a fixed magnetic field was stored by a LeCroy 9450 350 MHz digital oscilloscope and averaged over repetitive optical pumping cycles. Complete data sets correspond to the TR EPR signals measured at equidistant magnetic field points as shown in Figure 4.1. The control of the whole experiment was carried out by a home-written acquisition module. Complete 2-D data sets (time/magnetic field) were acquired and after experiment were passed to a personal computer. The data were treated with a self-written data analysis program.

Corrections of raw data sets were carried out in two ways: i) Baseline shifts are taken into account by subtracting a normalized background signal within the time window [t'_1, t'_2] immediately before the laser flash. ii) To get rid of laser background (caused by photo-induced effect inside the cavity) an average of off-resonance transients is subtracted from each transient.

In order to obtain TR EPR spectra digital boxcar integration procedure of the time signal was used. It integrates the signal in a specified integration gate [t_1, t_2] according to the following relation:

$$I(B_0) = \frac{\int_{t_1}^{t_2} I(B_0, t)dt}{t_2 - t_1} \tag{4.1}$$

TR EPR experiment at X-band (9.6 GHz) was carried out as described in [26] using a Bruker ER046 XK-T microwave bridge equipped with a dielectric ring resonator ER 4118 X-MD-5W1 and an Oxford liquid helium gas-flow cryostat (Oxford CF935). The loaded *Q*-value for this dielectric ring resonator with a 4 mm quartz was about Q = 3000, equivalent to a rise time of $\tau_r = Q/(2\pi * \nu_{mw}) \approx 50$ ns. This is in order of the upper bandwidth limit (6.5 MHz) of pre-amplifier.

TR EPR experiment at Q-band (35 GHz) were performed on the same set-up except that a Bruker ER 056 QMV microwave bridge equipped with a home built cylindrical resonator TE_{011} with light access was used. The loaded *Q*-value for this dielectric ring resonator with a 3 mm quartz was about Q = 2500, equivalent to a rise time of

$\tau_r = Q/(2\pi * \nu_{mw}) \approx 50$ ns. The overall time resolution in TR EPR at Q-band was achieved by about 100 ns, limited by the upper bandwidth (1 MHz) of pre-amplifier.

The samples were illuminated using a Spectra Physics Nd:YAG laser (Spectra Physics GCR 130) operating in Q-switch with a pulse width about 8 ns, at 10 Hz, at the 2nd harmonic 532 nm. The light energy at the sample was about 1 - 2 mJ per pulse.

Low temperature experiments were carried out at 80 K. High temperature experiments for the kinetic studies were performed at temperatures between 230 and 260 K. The available microwave power of about 200 mW was reduced to 25 or 35 dB for X-band and to 25 dB for Q-band in order to obtain the transients free from nutation distortion.

4.5.2. Analysis of ET kinetics from $A_1^{\bullet -}$ to F_X

The program for the analysis of ET kinetics was developed and written by Prof. Art van der Est [26].

The TR EPR measurements at high temperature give access to the ET kinetics from the second acceptor $A_1^{\bullet -}$ to the [4Fe-4S] cluster. The accessible time window is limited by the instrumental rise time about 50 ns and spin relaxation of the spin polarisation at longer times (several μs). If the ET kinetics fall into this range, two sequential RP spectra can be observed in the TR EPR data set as demonstrated for native PS I [77]. Global spectral analysis allows the rate constants of the various processes to be extracted from the complete time-field data set.

In general, the transient EPR signal of a sample with several consecutive light-induced paramagnetic species is observed as a function of the magnetic field strength, B_0, and the delay time, t, after the laser flash. It can be described by a sum of signal contributions:

$$S(t,B_0) = \sum_i S_i(t,B_0) \tag{4.3}$$

The signal of a given species $S_i(t, B_0)$ depends on the evolution of its concentration and spin polarisation with time. For the electron transfer reaction $A^{\bullet -} + B \rightarrow A + B^{\bullet -}$, it is modelled as [77]:

$$\begin{aligned} S_A(t,B_0) &= \alpha(B_0) e^{-(k+w_A)t} \\ S_B(t,B_0) &= \beta(B_0) \frac{k}{k+w_A-w_B} \left\{ e^{-w_B t} - e^{-(k+w_A)t} \right\} \end{aligned} \tag{4.4}$$

where k is the first-order reaction rate constant, w_A and w_B are the decay rates of the spin polarisation in species $A^{\bullet -}$ and $B^{\bullet -}$, respectively, and $\alpha(B_0)$ and $\beta(B_0)$ are their spin-polarized EPR spectra in the absence of relaxation. The decay of the spin polarised signal is given by spin-lattice relaxation rate as obtained by extrapolating the microwave power to zero [78]. For finite values of microwave power w_A and w_B are effective relaxation rates which are generally faster than the true spin-lattice relaxation rates. Additionally, the bandwidth of the spectrometer is taken into account and $S(t, B_0)$ is convoluted with a single exponential instrumental rise time.

5. PS I with Selective ^{13}C Isotope Labelled 2-methyl-1,4-Naphthoquinones in the A_1-Binding Site

In this chapter, 2-methyl-1,4-NQs selectively labelled with ^{13}C isotope were incorporated into the A_1-binding site of PS I in order to probe the highly asymmetric spin density distribution over the quinone ring induced by one dominant H-bond between the protein environment and only one of the two carbonyl groups of quinone. According to the asymmetric H-bond scheme the position with increased spin density compared with symmetric H-bonding is predicted for the ring carbon C_4 of the carbonyl group which is H-bonded to the protein environment. Correspondingly, decreased spin density is predicted for the ring carbon C_1 position of the other carbonyl group without the H-bond. In order to test this prediction each of the C_4 and C_1 carbon positions was selectively labelled with the spin 1/2 ^{13}C isotope in the synthesized 2-methyl-1,4-NQ.

5.1. Background

Quinone incorporation into the A_1-binding site of PS I can be carried out in two ways: i) quinone reconstitution in PS I complex after organic solvent extraction of native PhQ (extracted PS I) [41]; ii) quinone replacement in the PhQ biosynthetic pathway mutants

[79, 80]. The method to extract PhQ from lyophilised PS I with diethyl ether or hexane is a very harsh one. It causes additional loss of about 90 % of the antenna chlorophyll molecules as well as carotenoids [41]. In the other method, which is most favourable for PS I integrity, the gene which codes for one of the enzymes in the PhQ biosynthetic pathway in *Synechococcus* sp. PCC 6803 was interrupted. For example, interruption of the *menG* gene, which encodes for a methyltransferase responsible for the last step in the biosynthetic pathway, for transferring the methyl group to 2-phytyl-1,4-NQ, leads to the accumulation of 2-phytyl-1,4-NQ in the A_1-binding site of PS I [81]. Interruption of *menB* or *menA* gene encoding for the quinone ring closure or phytyltransferase, respectively, leads to a complete interruption of PhQ biosynthesis. However, the A_1-binding site of PS I is not empty but PQ-9 is rescued as a substituent [73, 74]. Normally PQ-9 serves in PS II as an one-electron gate quinone acceptor in the Q_A-binding site and as an exchangeable two-electron/two proton acceptor in the Q_B-binding site. Because PQ-9 is more weakly bound to the A_1-binding site of PS I it can be exchanged *in vivo* or *in vitro* by a number of 1,4-NQ derivatives [79, 80]. In this study the *menB* mutant was chosen for the quinone-replacement protocol.

5.2. General strategy and significance

According to the X-ray structure model at 2.5 Å resolution (1JB0) two specific properties have been identified for the A_1-binding site of PS I. Each PhQ is π-stacked with tryptophan residue ($W696_{PsaA}$ and $W676_{PsaB}$) which is located in the first turn of the stromal surface **jk** helix of the PsaA and PsaB heterodimer, respectively. Each PhQ is hydrogen bonded in a highly asymmetric manner to the NH backbone group of leucine residue ($L722_{PsaA}$ and $L702_{PsaB}$) [3, 4, 6]. Despite the fact that the X-ray model describes the structure only in the ground state, all mentioned features are highly conserved in the functional charge-separated state as was confirmed in several spectroscopic studies [34, 35, 82-85].

The X-ray structure model (pdb entry 1JB0) of the A_{1A}-binding site with native PhQ is shown in Figure 5.1 (a). The carbonyl group in the ortho position to the phytyl tail of PhQ forms a H-bond with the backbone NH of the leucine $L722_{PsaA}$ whereas the second carbonyl group in the ortho-position to the methyl group is not H-bonded. Instead, a H-bond network is formed. It involves the carbonyl side chain of serine $S692_{PsaA}$ residue that is H-bonded to the NH group of the π-stacked tryphtophan $W697_{PsaA}$ residue and to the backbone carbonyl group of the methionine $M688_{PsaA}$ residue. This H-bond network may also be a part of the ET pathway between A_0 and F_X [34, 35]. A valence bond model has been suggested for the quinone radical anion with a single H-bond [3] and has been adapted in Figure 5.1 (b). It rationalizes the asymmetric and alternating π spin density distribution over quinone ring as an average of three resonance structures for the unpaired π-electron due to the single H-bond. In other words, electrostatic interaction of the partial positive charge of the proton of the H-bond leads to electron withdrawal from O_4. As a consequence, increased spin density of the unpaired electron is predicted at the alternating ring carbons C_4, C_2 and at the oxygen atom O_1 of the carbonyl group without H-bond and decreased spin density for the positions in between, i.e. C_1, C_3 as well as O_4.

Correspondingly, by somewhat smaller changes due to anisotropic H-bonding, i.e. an anisotropic and alternating π spin density distribution as indicated in the hfc values of the quinone radical-ion, have been already observed for the Q_A-binding site of the type II RC of purple bacteria (pbRC) [86, 87] and for the Q_H-binding site of quinol oxidase (*bo*$_3$-QOX) [88, 89]. The reduced asymmetries correlate well with the expectation that the number of H-bonds per quinone increases in those cases: two H-bonds of different strength and geometry, one to each of the carbonyl oxygens O_1 and O_4 are confirmed for Q_A in pbRC [86, 87, 90]; for Q_H two H-bonds to O_4 and one H-bond to O_1 have been suggested to explain best the experimental results [89]. Thus, the A_1-binding site of PS I with only one dominant H-bond to the quinone radical-ion is unique among the well-studied quinone binding sites. The fact of a single predominant H-bond is also expected to provide a critical test of advanced DFT calculations.

According to the valence bond model the two carbonyl groups of quinone are predicted to carry most of the total unpaired electron spin density (DFT calculations quantify about 70 %, with the larger portion located at the oxygen nuclei). The goal of this work is to determine the spin density distribution at the two carbon position of the carbonyl groups.

For 2-methyl-1,4-NQ labelled with ^{17}O the hfc tensor values of the ^{17}O nuclei turn out to be quite high in agreement with a high spin density at the oxygen atoms, but the asymmetry for two oxygen atoms was observed to be very small [91]. However, it was known that the ^{17}O hfc tensor elements are rather insensitive to the H-bonding strength (and thus also asymmetry) consistent with previous experimental results comparing radical-ion spectra in polar and non-polar solutions [92]. Therefore, although the oxygen positions carry the largest spin density they are not suited for a detailed study of asymmetry in H-bonding. The next best candidates are the carbons of the carbonyl groups, which are characterized in detail in this thesis.

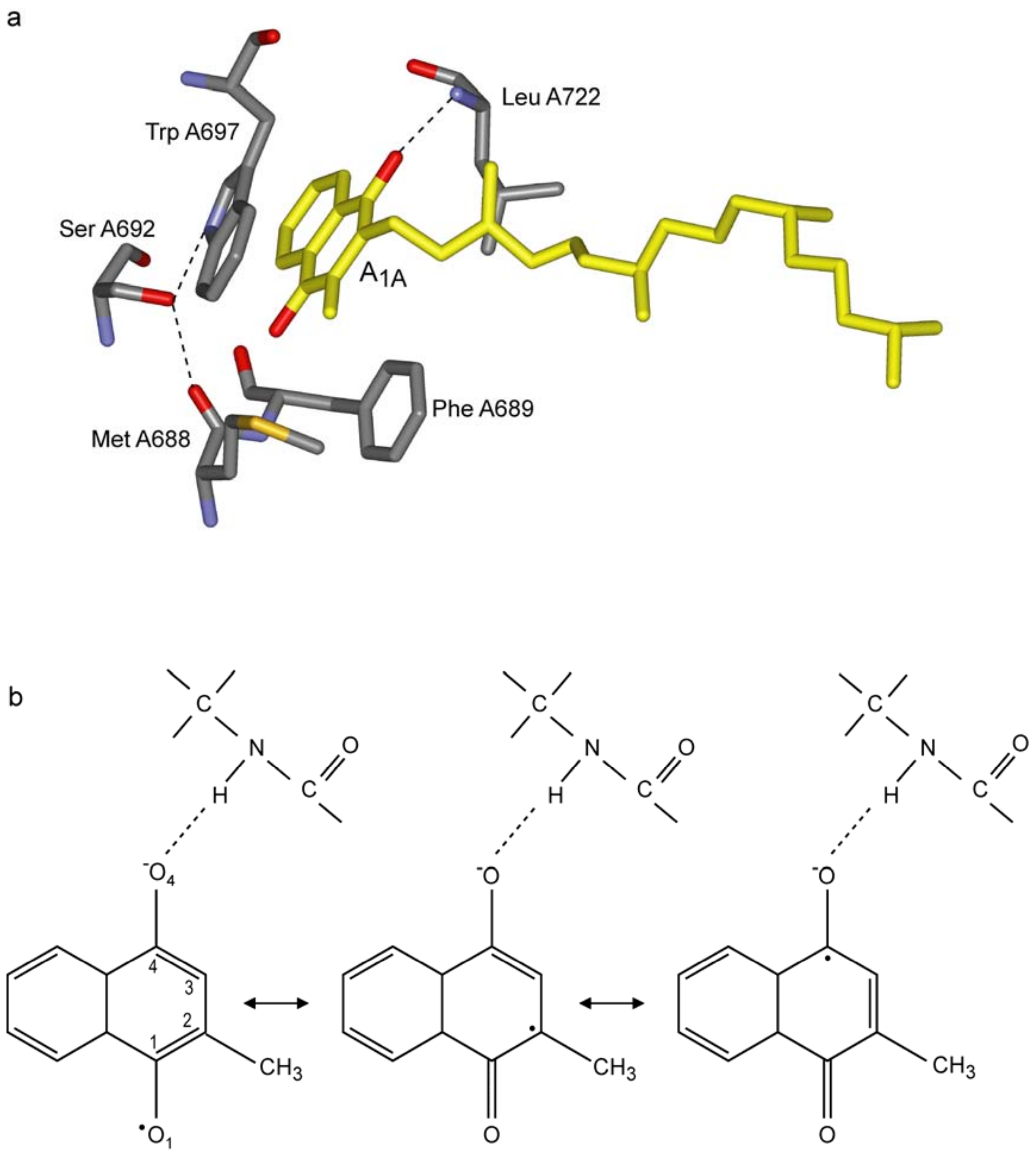

Figure 5.1. a) Structural model of the A_{1A}-binding site according to the X-ray structure at 2.5 Å resolution (pdb entry 1JB0). Amino acids involved in identified protein-quinone interactions are included explicitly. H-bonds are indicated by broken lines. The quinone carbonyl group in ortho position to the phytyl tail is H-bonded to the backbone NH of $L722_{PsaA}$. The second quinone carbonyl group is modelled without a H-bond. Instead, a H-bond network involves the carbonyl side chain of $S692_{PsaA}$ with H-bonds to the NH group of π-stacking $W697_{PsaA}$ and to the backbone carbonyl of $M688_{PsaA}$. The $M688_{PsaA}$ side chain provides the central ligand to the A_{0A} cofactor.

b) A valence bond scheme is depicted for the semiquinone π-radical anion part of the charge separated state based on the single H-bond structural model. Three resonance structures are shown with the unpaired π-electron spin located at quinone ring positions: C_4, C_2 and O_1 (right to left). The superposition of the equivalent structures results in increased spin densities at ring positions C_4, C_2, O_1 and decreased in between compared to symmetric H-bonding.

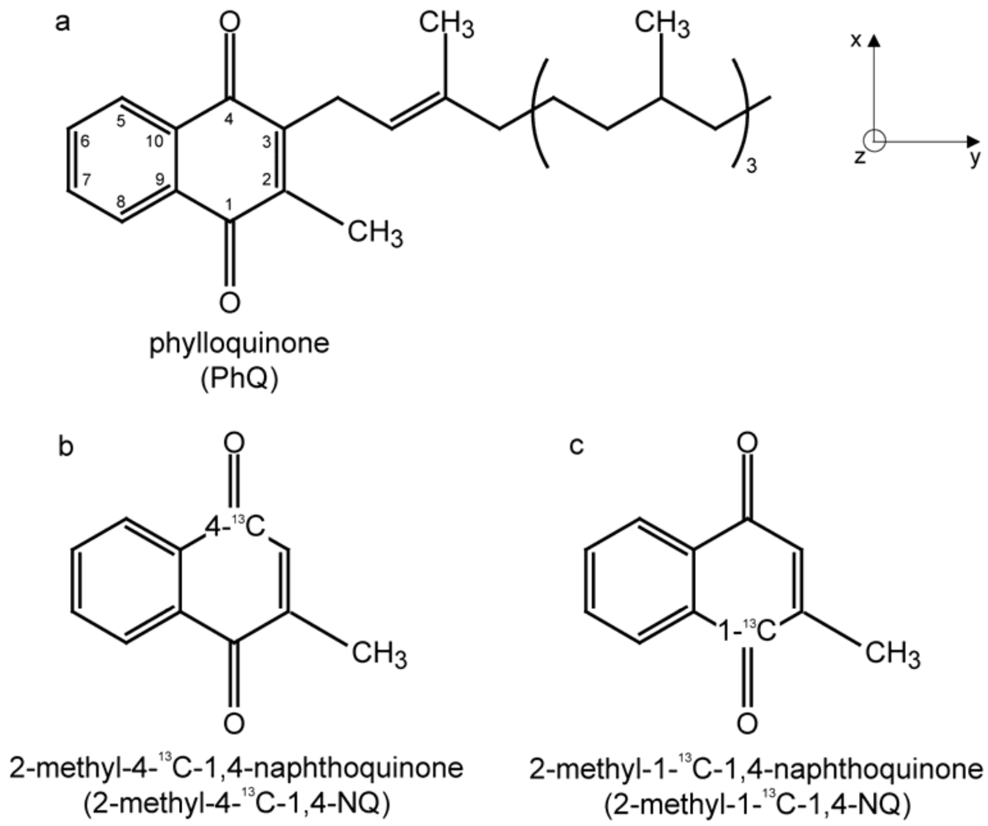

phylloquinone
(PhQ)

2-methyl-4-^{13}C-1,4-naphthoquinone
(2-methyl-4-^{13}C-1,4-NQ)

2-methyl-1-^{13}C-1,4-naphthoquinone
(2-methyl-1-^{13}C-1,4-NQ)

Figure 5.2. Molecular structure of native (a) PhQ, of 2-methyl-1,4-NQ selectively ^{13}C isotope labelled in ring carbon position (b) C_4 and (c) C_1. The g-tensor principal axes of the quinone anion are nearly collinear with the molecular axes shown on the right.

2-methyl-1,4-NQ is available as synthesized by Dr. Herbert Zimmermann (MPImF Heidelberg), selectively labelled with ^{13}C isotope in either of the two carbon carbonyl positions. They are named: 2-methyl-4-^{13}C-1,4-NQ and 2-methyl-1-^{13}C-1,4-NQ. The molecular structures are shown in Figure 5.2. They were incorporated into the A_1-binding site of PS I isolated from the *menB* mutant. The TR EPR powder spectra of the second $P_{700}^{\bullet+}A_1^{\bullet-}$ RP state provide sufficient detail to evaluate the essential parameters of the ^{13}C hfc tensor for each of the two selectively ^{13}C labelled carbon positions. A suitable reference for the asymmetry in hfc parameters and spin density is available with the case of symmetric H-bonding, hence symmetric spin density distribution, which is realised in isotropic solution (polar or non-polar). In addition, density functional theory (DFT) calculations are available at various levels of complexity and can be compared with the experimentally determined ^{13}C hfc tensors for each carbon position.

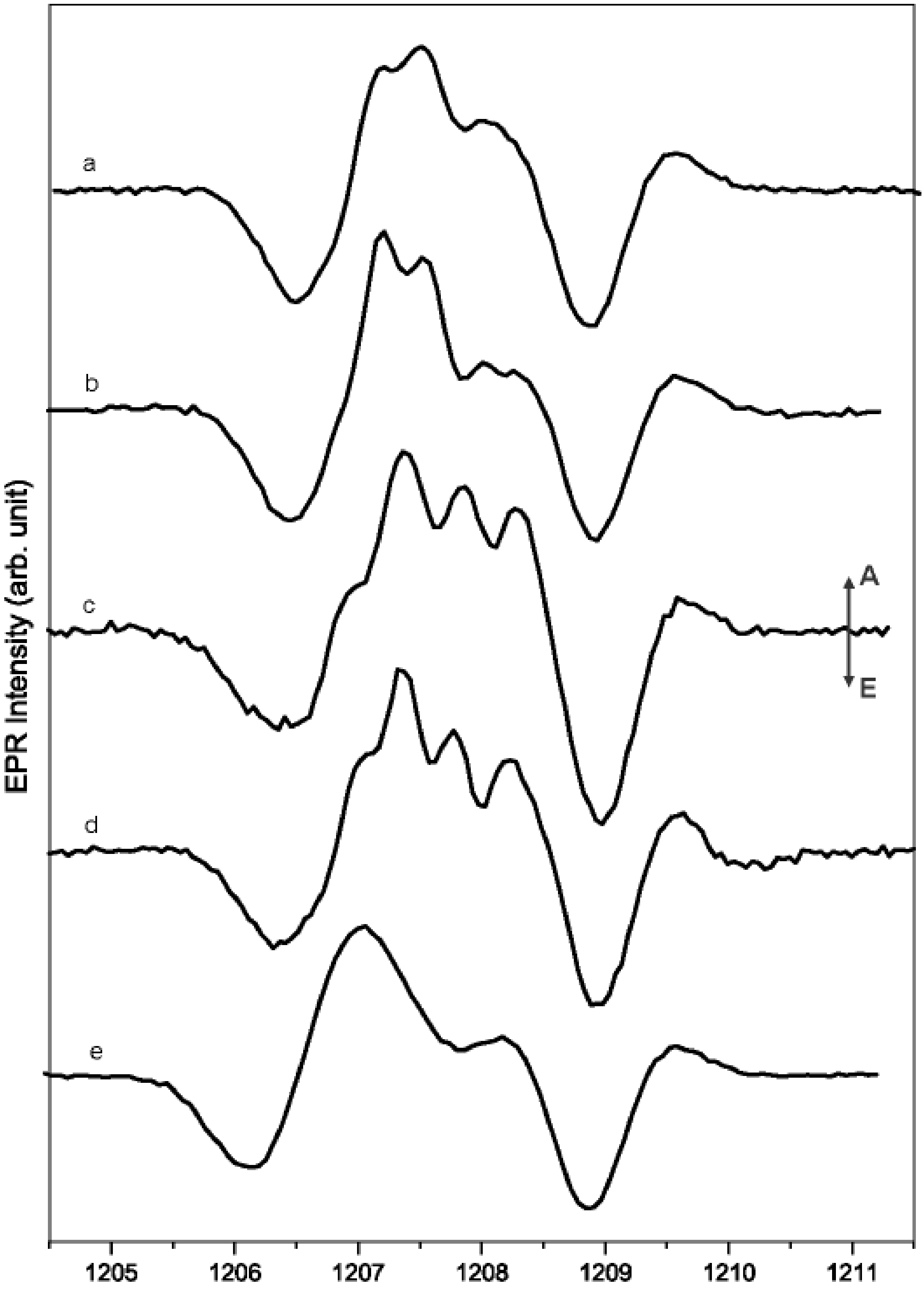

Figure 5.3. Q-band TR EPR spectra of the second $P_{700}^{\bullet+}A_1^{\bullet-}$ RP state in PS I complexes at 80 K. Comparison of spectra with (a) native PhQ (wild type), (b) 2-methyl-1,4-NQ, (c) 2-methyl-1-^{13}C-1,4-NQ, (d) 2-methyl-4-^{13}C-1,4-NQ, (e) PQ-9 (*menB* mutant) in the A_1-binding site of PS I isolated from the *menB* mutant. The spectra have been extracted from the full time/field data set by integrating the signal intensity in a time window from 500 to 2000 ns following the laser flash.

5.3. Results

5.3.1. Q- and X-band TR EPR study of PS I with selectively ^{13}C labelled 2-methyl-1,4-NQ in the A$_1$-binding site at 80 K

Efficiency of substitution and orientation of replaced quinones in the A_1-binding site of PS I

Q-band spin polarized TR EPR spectra of the second $P_{700}{}^{\bullet+}A_1{}^{\bullet-}$ RP state of PS I isolated from the wild type with PhQ (a) and from the *menB* mutant (e) with unlabelled 2-methyl-1,4-NQ (b), 2-methyl-1-^{13}C-1,4-NQ (c), and 2-methyl-4-^{13}C-1,4-NQ (d) in the A$_1$-binding site are represented in Figure 5.1. Neglecting for the moment the spectral details related to the methyl proton and ^{13}C hfc splittings, all TR EPR spectra exhibit the same overall polarization pattern, showing polarization maxima from the low to high field side as E/A/A/E/A. This pattern is known to be specifically sensitive to the orientation of the A$_1$ molecular axes with respect to vector joining the spin density centers of $P_{700}{}^{\bullet+}$ and $A_1{}^{\bullet-}$ [37] and can be taken as a signature of the quinone orientation in the A$_{1A}$-binding site for the charge separated state. The spin polarization pattern in Figure 3 confirms that within experimental accuracy, the substituted 2-methyl-1,4-NQs in the *menB* mutants are oriented in the same manner as PhQ in the wild type [37] and PQ-9 in the *menB* mutant [73] (for more details see Chapter 6).

Since the position of the low field minimum is related to the g_{xx} value of the quinone g-tensor, the efficiency of PQ-9 to 2-methyl-1,4-NQ substitution can be analysed from the spectra by the contribution of the respectively shifted emission peaks. In comparison with PhQ (or 2-methyl-1,4-NQ) the low field minimum of PQ-9 is shifted more down field, corresponding to a larger g_{xx} value of PQ-9 versus NQ derivatives [73] (for more details see Chapter 6). Within experimental accuracy (< 5 %) it can be concluded that complete substitution has been achieved, i.e. nearly all A$_1$-binding sites are filled with 2-methyl-1,4-NQs in PS I from the *menB* mutant.

Hyperfine induced spectral differences

Nevertheless, in spite of their overall similar polarization patterns, the spectra in Figure 5.3 differ significantly with respect to the partially-resolved hfc splittings. A well understood quartet due to the protons of the methyl group with relative intensities 1:3:3:1 is centered at a g_{eff} spectral position near the g_{yy} component of the NQ g-tensor. It is better resolved for 2-methyl-1,4-NQ (Figure 5.3, b) than PhQ (a) due to the lack of unresolved hfc contribution to the linewidth by the protons of the phytyl tail [93]. For methyl groups with fast tunnelling-

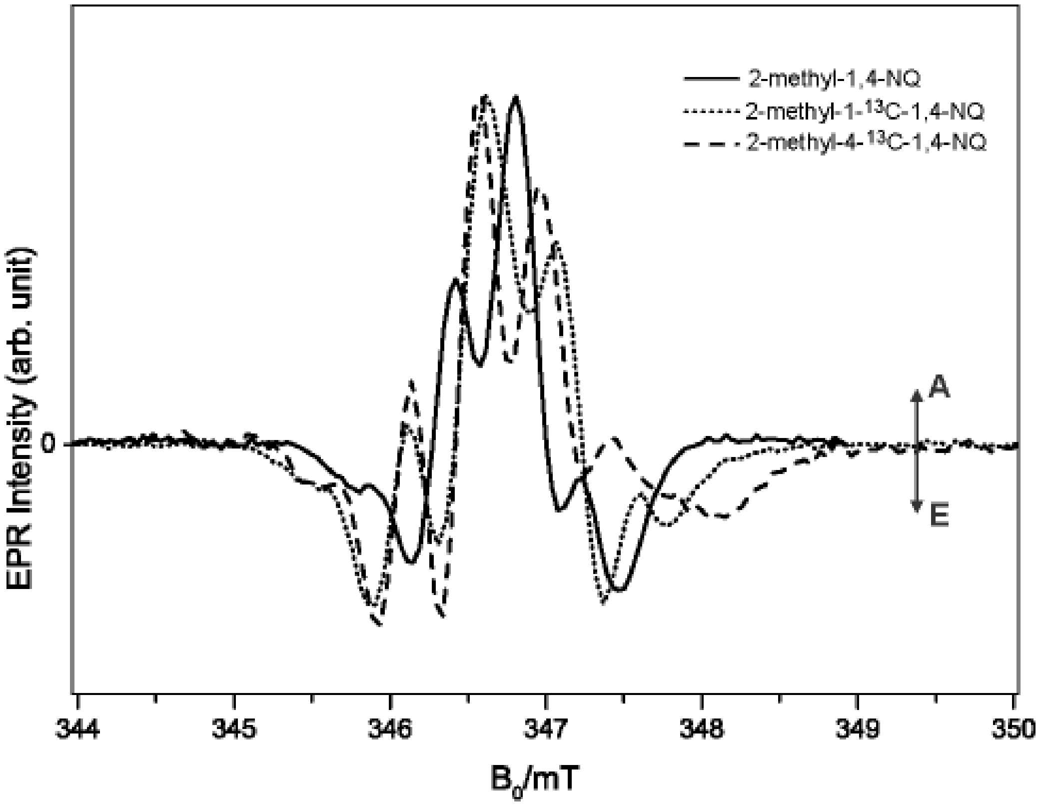

Figure 5.4. Comparison of X-band TR EPR spectra of the second $P_{700}^{\bullet+}A_1^{\bullet-}$ RP state in PS I complexes isolated from the *menB* mutant at 80 K. The PQ-9 recruited into the A_1-binding site of the *menB* mutant is exchanged with unlabelled 2-methyl-1,4-NQ (solid line), 2-methyl-1-^{13}C-1,4-NQ (dotted line) and 2-methyl-4-^{13}C-1,4-NQ (broken line). The spectra have been extracted from the full time/field data sets by integrating the signal intensity in a time window from 500 to 1500 ns following the laser flash.

hopping, the proton hfc tensor is nearly axially symmetric as it is confirmed by CW ENDOR for the photoaccumulated $A_1^{\bullet-}$ anion [94] and by pulsed ENDOR for the second $P_{700}^{\bullet+}A_1^{\bullet-}$ RP state [85] (Table 5.1). Obviously, additional ^{13}C hfc splittings over the whole spectral range contribute to the spectra c and d of Figure 5.3.

X-band TR EPR spectra of the three 2-methyl-1,4-NQs (unlabelled, 1-^{13}C and 4-^{13}C labelled) are superimposed in Figure 5.4 for a more detailed comparison of the ^{13}C hfc induced differences. The following qualitative features are apparent:

i) The overall spectra width is clearly wider in case of both ^{13}C labelled 2-methyl-1,4-NQs than for the unlabelled 2-methyl-1,4-NQ.

ii) The spectral patterns differ for the two 1-^{13}C and 4-^{13}C labelled 2-methyl-1,4-NQs, reflecting the expected asymmetric spin density distribution that arises from the asymmetric H-bonding. The 4-^{13}C pattern (broken line) extends further than the 1-^{13}C (dotted line) pattern, most clearly at the high-field side of the spectrum. It is mostly influenced by the out-of-NQ-plane component (A_{zz}) of the ^{13}C hfc tensor in the up-field part and the in-NQ-plane components (A_{xx}, A_{yy}) in the central and down-field part.

iii) The field positions of the absorptive and emissive polarisation maximum vary considerably over the whole spectrum between the three samples. This indicates that all components (A_{xx}, A_{yy}, A_{zz}) of the ^{13}C hfc tensor must be involved in the observed spectral differences.

5.3.2. Determination of ^{13}C hyperfine tensor parameters from spectra simulation

For a more quantitative evaluation of ^{13}C hfc tensor components, simulations of the spin polarisation patterns of the second $P_{700}{}^{\bullet +}A_1{}^{\bullet -}$ RP spectra were carried out. The concept of spin correlated RP was used, as described in Appendix I and extensively tested in previous studies [2, 95]. The algorithm accounts for selective spin state population, spin dynamics during the lifetime of the observed RP states, charge recombination and relaxation processes. It includes a large number of magnetic interactions and structural parameters, collected in Table 2. Fortunately, most of them are known from independent experimental data. It is important to emphasise that in all simulations isotropic linewidth parameters for $P_{700}{}^{\bullet +}$ and $A_1{}^{\bullet -}$ are used. As it will be shown, this leads to a very good simulation of the EPR line positions, but not of the EPR relative intensities. Usually the latter is fixed by introducing additional anisotropic linewidth parameters. However, lacking a good physical model for the anisotropic linewidth parameters, it corresponds to introducing unjustified the free-floating fit parameters. In order to avoid such strategy only isotropic line width parameter is applied in the simulations.

The spin polarized TR EPR spectrum of the second $P_{700}{}^{\bullet +}A_1{}^{\bullet -}$ RP state of the unlabelled 2-methyl-1,4-NQ has been resimulated [93]. In Figure 5.5, the simulated spectrum is compared to the experimental spectrum of the *menB* mutant with 2-methyl-1,4-NQ. The partially resolved hfc splitting in the experimental spectra is attributed to the methyl group as described for the Q-band spectrum in Figure 5.4. In addition, the spin polarisation pattern at Q-band indicates that orientation of 2-methyl-1,4-NQ is indistinguishable from that of PhQ in the wild type. In order to simulate the spectrum with 2-methyl-1,4-NQ in the A_1-binding site of PS I, the same structural and magnetic resonance parameters for $P_{700}{}^{\bullet +}$ and $A_1{}^{\bullet -}$ are used as determined for the wild type [37, 96]. Only the inhomogeneous linewidth was slightly reduced for $A_1{}^{\bullet -}$ compared to native PhQ as a result of the lack of the proton hfc splitting from phytyl tail of 2-methyl-1,4-NQ [93]. Usually the proton hfc splittings from the phytyl

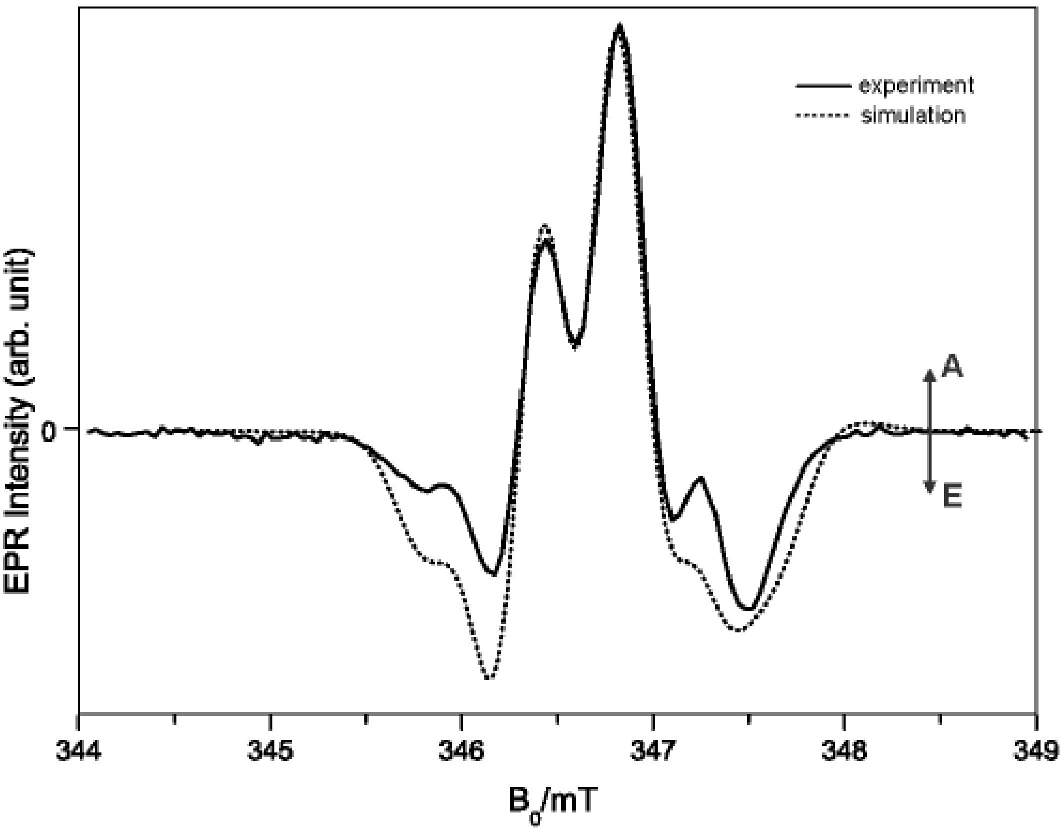

Figure 5.5. X-band experimental TR EPR spectrum (solid line) of the second $P_{700}^{\bullet+}A_1^{\bullet-}$ RP state in PS I complexes with 2-methyl-1,4-NQ in the A_1-binding site at 80 K is compared with simulation (dotted line). The structural and magnetic parameters used for the simulations are collected in Table 5.1.

tail of PhQ are small but contribute to an additional inhomogeneous line broadening of $A_1^{\bullet-}$. The spectral positions of the partially resolved methyl hfc splitting are simulated quite well. A certain discrepancy between experimental and simulated spectra is evident in the relative intensities, particularly in the down-field and up-field spectral region. Note that the spectra in Figure 5.5 are normalised at the mild-field A maximum. It indicates the requirement of extra anisotropic line broadening of the residual linewidth of $A_1^{\bullet-}$. For further study I ignore the effect of the anisotropic line broadening and concentrate on the line positions due to the hfc parameters only. Therefore, the simulated spectrum of 2-methy-1,4-NQ will be used as a reference spectrum. For subsequent simulations of the spectra with ^{13}C labelled 2-methyl-1,4-NQs, all parameters related to the structure, relative orientation, inhomogeneous linewidth broadening of $A_1^{\bullet-}$ and hfc tensor of methyl group were kept unchanged. In order to simulate X-band TR EPR spectra for ^{13}C labelled 2-methy-1,4-NQs, the components of the hfc ^{13}C tensor were considered as adjustable parameters.

Table 5.1. Structural and magnetic interaction parameters used for the simulation of TR EPR spectra of the second $P_{700}^{\bullet+}A_1^{\bullet-}$ RP state.

g-tensor						
	g_{xx}	g_{yy}	g_{zz}			
$P_{700}^{\bullet+}$	2.00308	2.00264	2.00226			
$A_{1A}^{\bullet-}$	2.00622	2.00507	2.00218			
	Euler angles relating g-tensors			dipolar axes in $g(A_{1A}^{\bullet-})$		
	α	β	γ	θ	φ	
$P_{700}^{\bullet+}A_{1A}^{\bullet-}$	81°	126°	182°	90°	0°	
	methyl hfc tensor (MHz)			Euler angles between $g(A_{1A}^{\bullet-})$ and methyl hfc		
A_{xx}	A_{yy}	A_{zz}		α	β	γ
9.1	12.8	9.1		25°	0°	0°
spin-spin coupling						
	D					
$P_{700}^{\bullet+}A_{1A}^{\bullet-}$	-170 μT					
relaxation and recombination						
$T_1 = 100$ μs				$K_S = (220\ \mu s)^{-1}$		
$T_2 = 1.3$ μs				$K_T = (1\ ms)^{-1}$		
residual inhomogeneous isotropic linewidth						
$\Delta B(P_{700}^{\bullet+}) = 0.50$ mT						
$\Delta B(A_1^{\bullet-}) = 0.30$ mT						

There is plenty of independent experimental evidence to assume in the case of quinone ring carbon positions that the principal axis orientations of the principal axis of the ^{13}C hfc tensor coincide with those of the quinone molecular axes which in turn coincide well with the principal g-tensor axes. By analogy with basic theoretical concepts and previous experimental investigations, it is expected that the dipolar part of ^{13}C hfc tensor is nearly axially symmetric [47, 86]. The parallel and largest positive A_{zz} component is associated with the out-of-NQ-plane axis z. The perpendicular and usually smaller A_{xx}, A_{yy} components are associated with in-NQ-plane axis x and y (Figure 5.2). However, the sign of the ^{13}C tensor component cannot be determined from our experimental and simulated spectra, but can be assigned by analogy to cases where ^{13}C hfc tensors have been determined including the signs for aromatic carbon positions by Triple ENDOR [86] and by comparison with theoretical predictions.

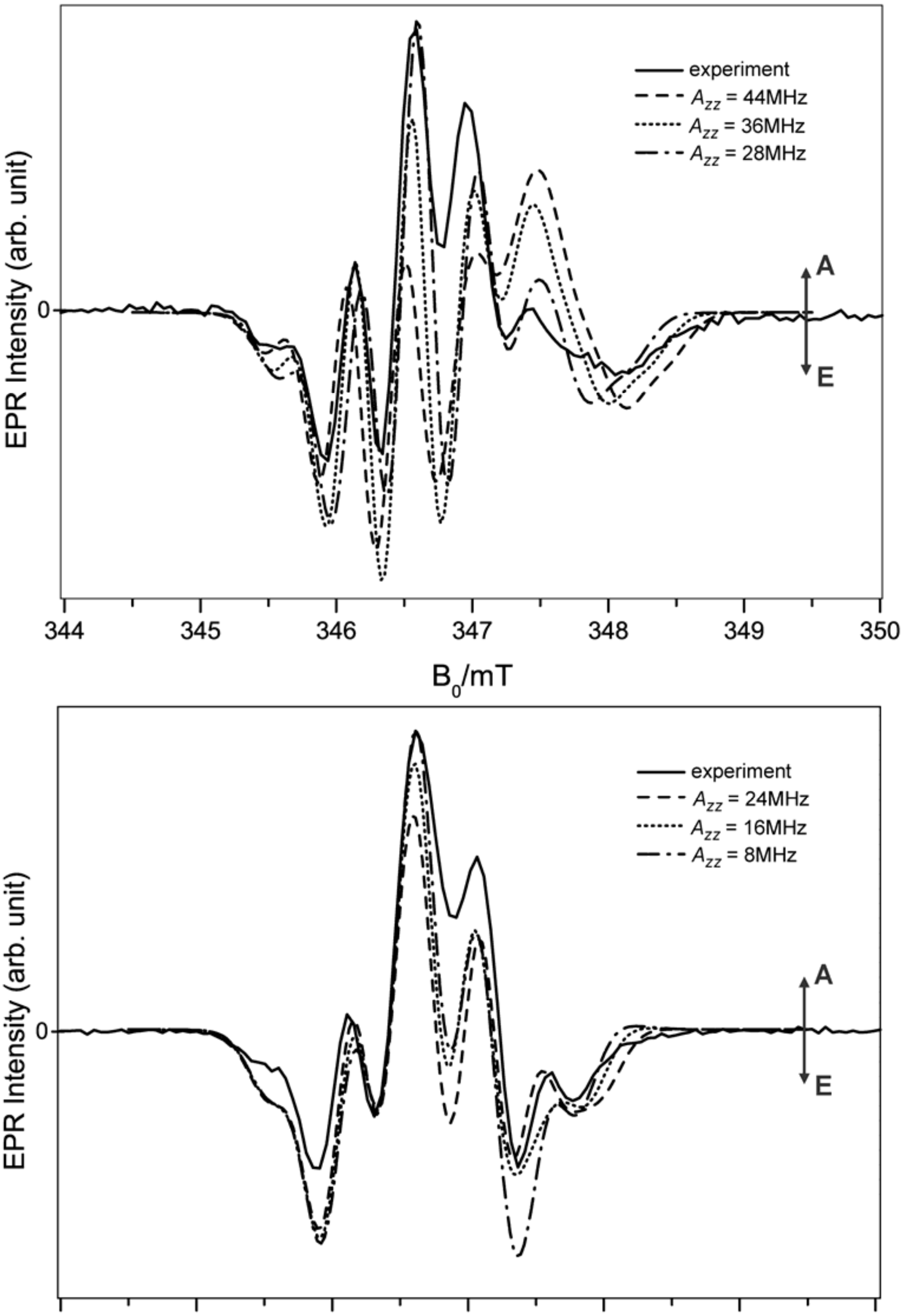

Figure 5.6. Experimental X-band spin-polarization patterns (solid line) of the second $P_{700}^{\bullet+}A_1^{\bullet-}$ RP state in PS I complexes with labelled 2-methyl-1,4-NQ in the A_1-binding site are compared with simulations.

Top: A_1-binding site with 2-methyl-4-^{13}C-1,4-NQ The A_{zz} value of the ^{13}C hfc tensor is varied as indicated while the perpendicular components are fixed at $|A_{xx}| = |A_{yy}|$ = 10.5 MHz.
Bottom: A_1-binding site with 2-methyl-1-^{13}C-1,4-NQ. The A_{zz} value of ^{13}C hfc tensor is varied as indicated and the perpendicular components are fixed at $|A_{xx}| = |A_{yy}|$ = 15 MHz.

Variation of out-of-NQ-plane hyperfine A_{zz} component

The influence of each individual ^{13}C hfc tensor component on the spin polarisation pattern can be demonstrated by varying each hfc component separately. Figure 5.6 presents simulations at X-band in which the out-of-NQ-plane A_{zz} component is systematically varied. The perpendicular A_{xx} and A_{yy} components are set equal, however, at different values for the top and bottom spectra (see Figure captions).

In the case of 4-^{13}C labelled 2-methyl-1,4-NQ in Figure 5.6 (top) a large ^{13}C hfc A_{zz} component is required for an acceptable simulation. It was varied from 44 to 28 MHz. This parameter produces a prominent shift of the peak/edge/shoulder of the broad up-field emissive feature. In addition, the variation of this A_{zz} component induces specific but smaller changes over the whole spectral range. The value of 10.5 MHz for the smaller perpendicular A_{xx}, A_{yy} components of 4-^{13}C labelled 2-methyl-1,4-NQ was chosen from separate simulations concerning variation of this perpendicular component.

Even large perpendicular components (fixed at $|A_{xx}| = |A_{yy}| = 15$ MHz) are required to reproduce the spectral properties in the low-field region for 1-^{13}C labelled 2-methyl-1,4-NQ. For this case, the A_{zz} tensor component was varied from 18 to 6 MHz (Figure 5.6, bottom). In this range, the high-field edge is still sensitive to the variation of the A_{zz} component, but the inward shift of the up-field edge essentially is found to approach zero below $A_{zz} \sim 8$ MHz. Note that the $A_{zz} = 6$ MHz spectra represents the limiting case.

Variation of in-plane A_{xx} and A_{yy} hyperfine tensor components

In order to justify the chosen perpendicular components ($A_{xx}| = |A_{yy}| = 15$ MHz) for the simulation of the experimental spectrum of 1-^{13}C labelled 2-methyl-1,4-NQ (Figure 5.5, bottom) the influence of each of the A_{xx} and A_{yy} components was investigated separately. Figure 5.7 presents simulations at X-band when the in-NQ-plane hfc tensor A_{xx} (top) or the A_{yy} (bottom) components were varied from 18 to 12 MHz. The in-plane A_{xx} component induces more prominent changes in the low-field region while variation of A_{yy} contributes more to the mid-field region. Note that even the high-field edge features are influenced to some extent (provided A_{zz} is kept small).

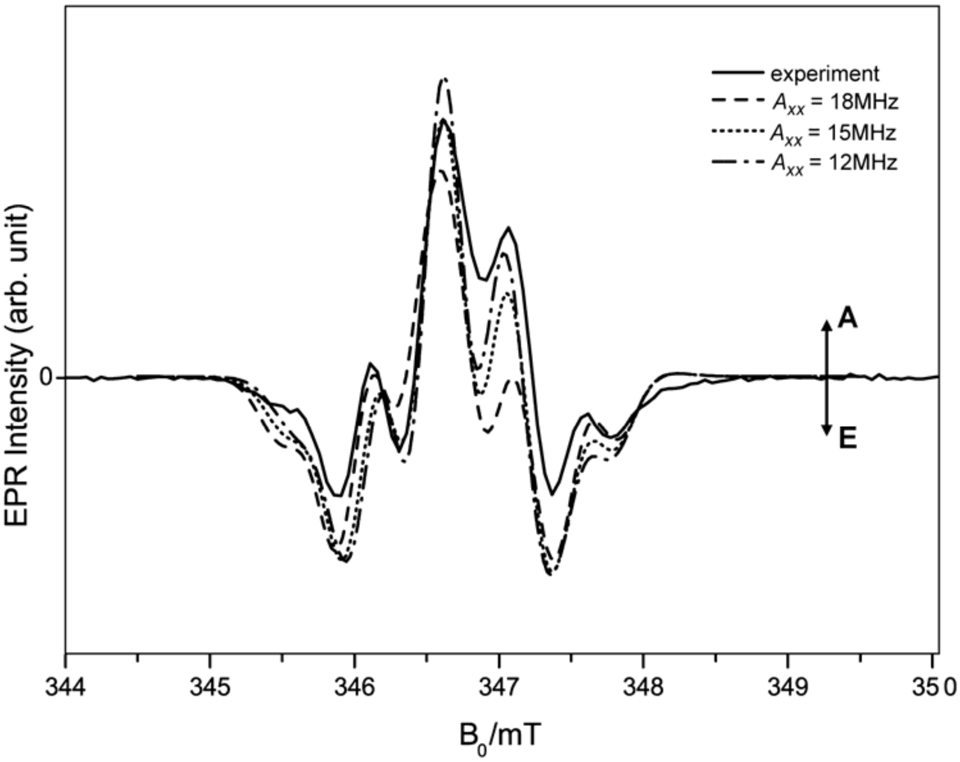

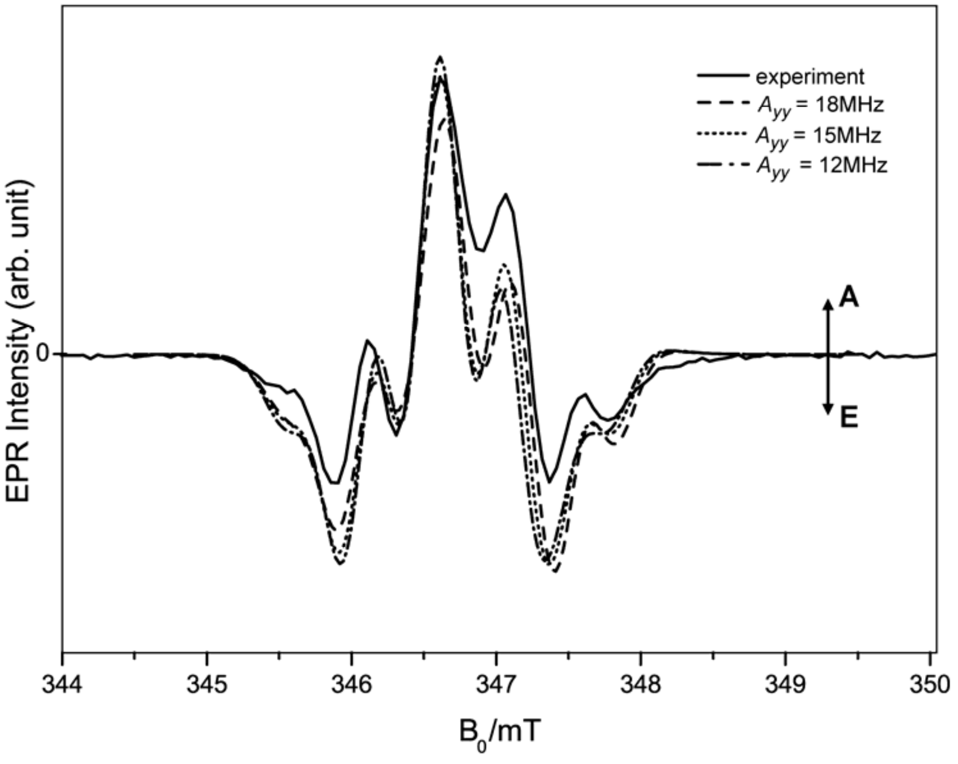

Figure 5.7. Experimental X-band spin polarisation pattern of the second $P_{700}{}^{\bullet+}A_1{}^{\bullet-}$ RP state in PS I complexes with 2-methyl-1-^{13}C-1,4-NQ in the A_1-binding site is compared with simulations concerning separate variation of each of the two in-NQ-plane principal ^{13}C hfc tensor parameters.

Top: Variation of the A_{xx} value of ^{13}C hfs tensor as indicated. The other hfc tensor components are fixed to $|A_{yy}|$ = 15 MHz and $|A_{zz}|$ = 6 MHz.
Bottom: Variation of the A_{yy} value of ^{13}C hfc tensor as indicated. The other hfc tensor components are fixed to $|A_{xx}|$ = 15 MHz and $|A_{zz}|$ = 6 MHz.

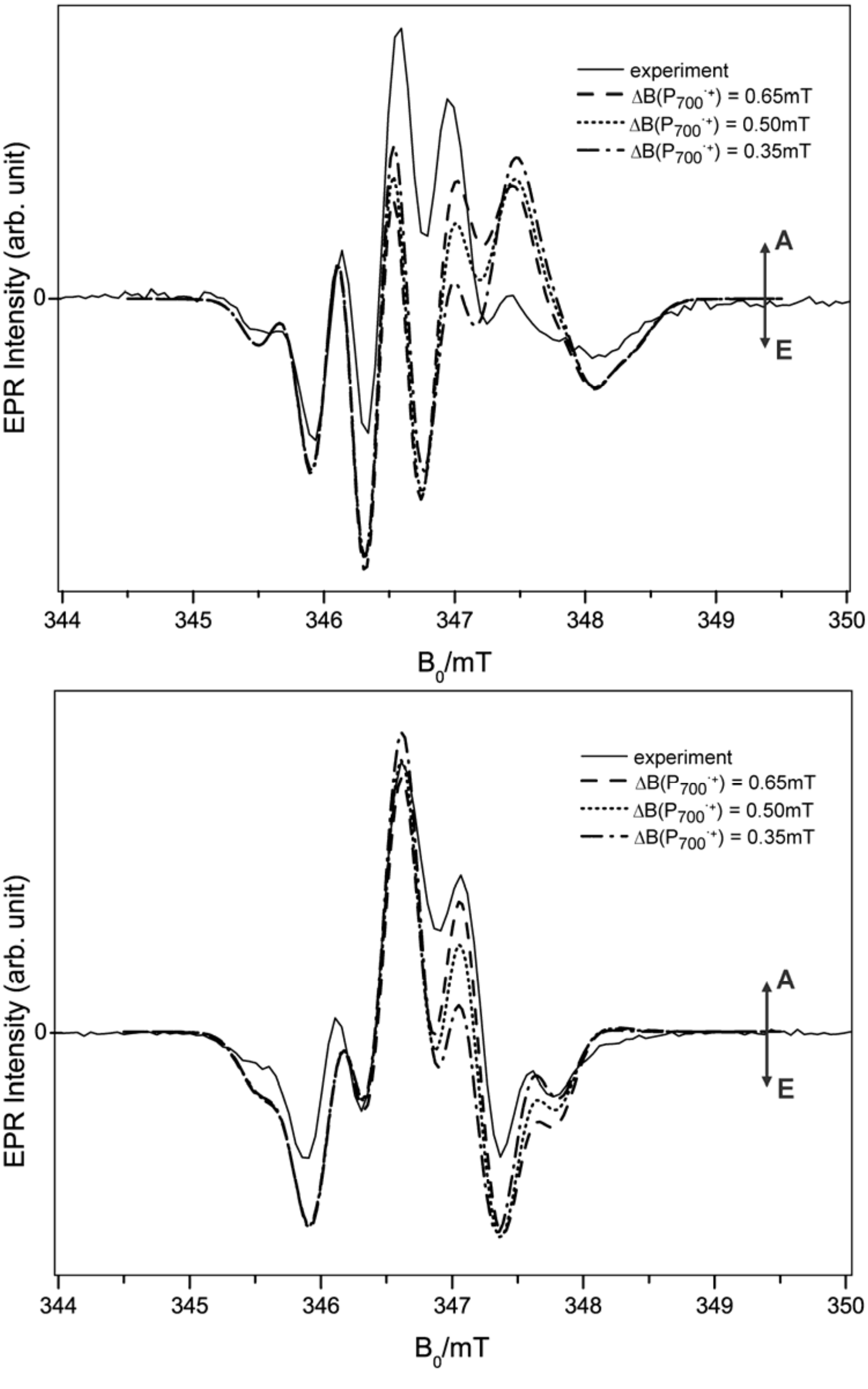

Figure 5.8. X-band experimental spin polarisation pattern of the second $P_{700}^{\bullet+}A_1^{\bullet-}$ RP state in PS I complexes with 2-methyl-1-^{13}C-1,4-NQ (top) and 2-methyl-4-^{13}C-1,4-NQ (bottom) in the A_1-binding site is compared with simulations. The hfc tensor parameters are taken from the best simulation in Figures 5.6 and 5.7, respectively. Only the isotropic Gaussian line width parameter $\Delta B(P_{700}^{\bullet+})$ is varied in step of 0.15 mT from 0.35 to 0.65 mT. The residual linewidth $\Delta B(A_1^{\bullet-})$ is fixed to 0.30 mT.

Effect of residual Gaussian line width parameters

The simulation results indicate that while the spectral positions of the partly resolved hfc lines can be reproduced quite well, the relative line intensities are not reproducible. It is common practice to adjust calculated intensities to measured intensities by introducing anisotropic line-broadening parameters, e.g. [87]. In addition to an isotropic linewidth parameter (chosen here) this adds two additional freely variable parameters per radical-ion, unless they would be available from independent experimental evidence or based on specific physical models (e.g. anisotropic cofactor motion). For the cofactor sites of PS I, the simulations are restricted to one residual Gaussian line-broadening parameter per radical-ion. The two chosen parameters agree with independent experimental evidence: $P_{700}^{\bullet+}$ (ΔB = 0.50 mT) and $A_1^{\bullet-}$ (ΔB = 0.30 mT) [37, 93](Table 5.1). The main reason for this limitation is that the correct spectral position of the observed unresolved hfc lines should only depend on the evaluated hfc tensor parameters. Additional freely adjustable anisotropic line width parameters yield better line intensities. In contrast, they may cause an unwanted interplay with the choice of the hyperfine parameters. Figure 5.8 shows simulations at X-band when the Gaussian line-broadening parameter of $P_{700}^{\bullet+}$ was systematically varied from 0.65 to 0.35 mT for 2-methyl-4-^{13}C-1,4-NQ and 2-methyl-1-^{13}C-1,4-NQ in the A_1-binding site of PS I. As expected, the variation of the line width parameter of $P_{700}^{\bullet+}$ has essentially no influence on the spectral line positions, may be not fully if A_{zz} is smaller than the linewidth parameter (Figure 5.8). Note that the ^{13}C hfc induced high-field emissive feature in the experimental spectrum is also not affected by the choice of the linewidth parameter of $P_{700}^{\bullet+}$. Nevertheless, the necessity of additional line-broadening of the experimental high field emissive peak is obvious. This is a clear indication of the extra anisotropic line-broadening of $A_1^{\bullet-}$ when the magnetic field is oriented along the molecular z axis. Indeed, simulations (not shown) with variation of $\Delta B(A^{\bullet-})$ demonstrate that the high field part can be simulated with an increased linewidth parameter.

5.4. Conclusion of TR EPR study of PS I with selective ^{13}C isotope labelled 2-methyl-1,4-NQs in the A_1-binding site

Table 5.2 collects the best simulation values for the full ^{13}C hfc tensor parameters of the two carbon ring positions C_1 and C_4. Comparison of the value of the ^{13}C hfc tensor components for the decreased C_1 and increased C_4 spin density position allows us to draw a few tentative conclusions:

i) The ^{13}C hfc tensor parameters of the quinone in the A_{1A}-binding site of PS I give direct and clear evidence of a large asymmetry with respect to the two carbonyl groups. It is consistent with the single-sided H-bond to quinone as suggested in the valence bond model.

ii) The asymmetry is most pronounced for the out-of-NQ-plane principal $|A_{zz}|$ component, with a value of 40(2) MHz for the H-bonded C_4-O group versus 8(2) MHz for the C_1-O group without the H-bond. The respective in-NQ-plane principal $|A_{xx}|$ and $|A_{yy}|$ components are 10.5(2.0) and 15(2) MHz, respectively.

iii) By comparison with nearly equivalent ^{13}C hfc tensor parameters for the 1-^{13}C and 4-^{13}C labelled 2-methyl-1,4-NQ in isotropic frozen isopropanol (IP) solution, the amount of increase/decrease of the $|A_{zz}|$ component is quite unequal.

For further consideration it is necessary to analyse the components of the ^{13}C hfc tensor for the increased C_4 and decreased C_1 spin density position.

5.5. Interpretation of ^{13}C hyperfine tensor for increased C_4 and decreased C_1 spin density positions of 2-methyl-1,4-NQ

According to the valence bond model the C_4 carbon position is predicted to have increased spin density, whereas the neighbour carbon positions C_3 and C_{10} have correspondingly reduced spin density and their contribution to the hfc tensor (isotropic scalar constant and dipolar tensor) of $^{13}C_4$ can be neglected. In other words, the only significant contributions to the ^{13}C hfc tensor are due to unpaired π spin density ρ_π in the p_z orbital at the C_4 and O_4 atoms. In full analogy to textbook arguments for example, in case of the malonic acid radical it can be argued: i) the dipolar hfc interaction between unpaired π electron spin density in the p_z orbital of C_4 and the ^{13}C nucleus located in the orbital center results in a large positive $\rho_\pi(C_4)$ contribution to the ^{13}C A_{zz} component ($\rho_\pi \sim A_{zz}$) [47]; and ii) dipolar contribution of $\rho_\pi(O_4)$ to the out-of-plane dipolar ^{13}C A_{zz} component is close to zero (by analogy with the McConnell-Strathdee consideration for an aromatic C — H fragment [47, 62]). As a side, the respective contributions to isotropic hfc scalar constant has opposite sign which argues for a largely dipolar character for $p_z(C_4)$ as indeed observed for the ^{13}C hfc tensor in the increased C_4 spin density position (Table 5.2). In contrast, the C_1 position is surrounded by positions

Table 5.2. ^{13}C hfc tensor data for selectively isotope labelled quinones in the A_1-binding site of PS I. Comparison to data for other quinone binding sites in protein-cofactor systems and to results from DFT calculations. (Experimental values have approx. errors in parentheses behind.)

	system	^{13}C in **C_1-position**				^{13}C in **C_4-position**		
site	quinone as cofactor	ref.	A_{xx}	A_{yy}	A_{zz}	A_{xx}	A_{yy}	A_{zz}
A_1 in PS I	2-CH_3- (^{13}C)-1,4-NQ also named: (^{13}C)-VK_3	[79] this work	[-]15.0(2.0)	[-]15.0(2.0)	[+]8.0(2.0)	[-]10.5(1.5)	[-]10.5(1.5)	[+]40.0(2.0)
		[99] [89] [99]	-16.6 -13.4 -15.3	-20.4 -16.8 -19.0	+1.5 +9.9 +1.8	-12.2 -10.5 -9.7	-15.1 -13.3 -12.2	+22.2 +26.0 +32.7
	^{13}C-VK_3 in IP	[79]	C_1 and C_4 equivalent in cw-EPR			[-]10.0(2.0)	[-]10.0(2.0)	[+]30.0(2.0)
	^{13}C-VK_3 in IP	[99]	-10.9	-13.3	+29.0	-10.5	-12.8	+30.3
Q_A in pbRC	^{13}C UQ-3 ^{13}C UQ-10	[86] [100]	[-]9.2(1.7) [-]7.0(1.4)	[-]9.8(1.7) [-]7.0(1.4)	[+]35.0(0.6) [+]35.6(0.8)	[-]12.6(1.7) [-]15.4(1.4)	[-]14.6(1.7) [-]18.2(1.4)	[+]22.7(0.6) [+]22.4(0.8)
		[89, 101]	-10.0 -10.2	-12.6 -13.1	+28.0 +26.4	-14.5 -13.6	-17.9 -17.0	+16.0 +15.5
	^{13}C UQ-3 in IP	[86]	-11.2	- 9.8	+32.2	-12.1	-10.4	+30.6
Q_H bo_3- QOX	^{13}C UQ-2	[88]	[-]7.0(1.4)	[-]10.4(1.4)	[+]20. (0.8)	[-]4.2(1.4)	[-]12.6(1.4)	[+]30.8(0.8)
model (2/1) 4HO-4HN-1HO 4HN-4HN-1HN		[89]	-12.0 -12.0	-15.0 -15.0	+20.8 +20.8	-11.2 -11.6	-14 -14.4	+27.9 +27.9
(1/0) 4HN 4HO		[89]	-13.7 -14.4	-17.4 -18.1	+10.1 +9.4	-11.4 -10.5	-14.4 -13.4	+24.3 +25.6

with increased spin density (O_1, C_2 and C_9) and this leads to equally relevant hfc contributions to the ^{13}C hfc tensor from all these neighbour positions. Thus, it explains the low ^{13}C A_{zz} value of the decreased C_1 position as a sum of competing contributions from $p_z(O_1)$, $p_z(C_2)$ and $p_z(C_9)$ of the neighbour atoms.

5.6. Comparison of π spin density distribution in different quinone binding sides

The degree of asymmetry of ρ_π over the quinone ring induced by H-bonds can be compared with other relevant quinone systems such as the Q_A-binding site in pbRC and for the Q_H-binding site in *bo₃*-QOX. Table 5.2 includes experimental values for the ^{13}C hfc tensor components of the analogous carbon ring position associated with quinone carbonyl groups in these systems. By comparison the following characteristics are revealed:

i) All listed values of ^{13}C hfc tensor components are highly anisotropic with nearly cylindrical symmetry.

ii) The largest component (the smallest in case of the C_1 position in the A_1-binding site of PS I) is associated with the out-of-plane component; the nearly equal (negative) components with the in-plane A_{xx} and A_{yy} components. This corresponds to a common structure of the ^{13}C hfc tensor for aromatic carbon positions. Although the sign (in brackets) of the ^{13}C hfc tensor components has not been determined in all experiments, they can be assigned by analogy with ^{13}C hfc tensor determined for aromatic carbon positions [86].

Different degrees of asymmetry in the ρ_π distribution are revealed by comparing of the A_{zz} components in the various quinone binding sites to the fully symmetric case realized in isotropic solution. As suitable asymmetry parameter is noted as $|\Delta A_{zz}|$ may be used.

For example, compared to the double-sided H-bonds for ubiquinone (UQ-3) in the Q_A-binding site of pbRC, the asymmetry parameter ΔA_{zz} is increased about by nearly a factor of two in favour of the case of single-sided H-bond to 2-methyl-1,4-NQ in the A_1-binding site of PS I. The ratio for the increased spin density positions is $|\Delta A_{zz}(A_1 \text{ in PS I})|/|\Delta A_{zz}(Q_A \text{ in bRC})| \sim 1.9$. Note that only the high spin density position C_4 of quinone in the A_1-binding site and correspondingly C_1 in the Q_A-binding site in bRC of PS I should be compared because $A_{zz} \sim \rho_\pi$ holds.

5.7. Comparison of measured ^{13}C hyperfine tensor with DFT data

Independent sets of calculated data have been presented in the last decade for magnetic resonance parameters of different quinone anion radical in their quinone binding sites [89, 97, 100, 102, 103] (Table 5.2). Most of the DFT calculations had been performed prior to the experimental results for the ^{13}C and ^{17}O hfc tensors, in particular for the A_1-binding site in PS I. In the case of *bo₃*-QOX, the DFT results have been applied to predict suitable structural models for the Q_H-site binding site involve several distinctly H-bond schemes to quinone [100]. In this context, the A_1-binding site in PS I reveals uniqueness as it is the only example with a single-sided H-bond to a quinone among all well-studied quinone systems. Hence, DFT calculations for the A_1-binding site of PS I should be the most sensitive test system for asymmetry in the ρ_π distribution due to asymmetric H-bonding.

In general, the DFT-calculated and measured values of ^{13}C hfc tensor components correlate quite well (Table 5.2). The value of the out-of-NQ-plane ^{13}C hfc A_{zz} component is largest for the C_4 and smallest for the C_1 positions and also the high asymmetry C_4/C_1 is obvious in the DFT calculations. The values for the in-NQ-plane ^{13}C hfc A_{xx} and A_{yy} components are in good agreement within experimental and calculated accuracy; the same (opposite) asymmetry C_1/C_4 (compared to asymmetry in the $|A_{zz}|$ values) appears in both experimental and DFT-calculated data. However, the most prominent and experimentally accessible value of the $A_{zz}(^{13}C_4)$ component is clearly underestimated in the DFT calculations. Also the discrepancy between experimental and DFT calculated value of the A_{zz} component is observed for the other quinone systems listed in Table 5.2, but to a lesser extent as a result of reduced asymmetries due to the compensating effects by multiple H-bonds to one or both carbonyl groups of quinone.

In particular, the discrepancy between measured and calculated values of the ^{13}C hfc A_{zz} components becomes evident if the value of this component in isotropic frozen solution is taken as reference for symmetric H-bonding. The calculated values for the A_{zz} component $|A_{zz}(^{13}C_1)| = 29.0$ MHz and $|A_{zz}(^{13}C_1)| = 30.3$ MHz agree very well within experimental accuracy with measured $|A_{zz}(^{13}C)| = 30(2)$ MHz for both labelled 1-^{13}C and 4-^{13}C labelled 2-methyl-1,4-NQ measured in IP. The calculated value of the ^{13}C hfc $A_{zz}(C_4)$ component in isotropic solution is increased only in one case when compared to the same quinone in the A_1-binding site from 30.3 MHz to 32.7 MHz. In other cases it turns out to be even smaller than in isotropic solution. However, the experimental value of the $A_{zz}(C_4)$ component in IP is increased considerably for 2-methy-1,4-NQ in the A$_1$-binding site from 30(2) MHz to 40(2) MHz in accordance with the valence-bond model in Figure 5.2. The same tendency is also observed in comparison of experimental and calculated values of the ^{13}C A_{zz} component for UQ-3 in isotropic solution and in the Q$_A$-binding site of pbRC. In all sets of DFT calculation, the values of the A_{zz} components are decreased for both the C$_4$ and C$_1$ positions of UQ-3 in the Q$_A$-binding site of pbRC in comparison to that of the isotropic solution. This is not a case for the experimental values, not even, for the C$_1$ position where increased spin density position is predicted in accordance with the stronger H-bond to the carbonyl group C$_1$ — O$_1$ than to the carbonyl group C$_4$ — O$_4$ [86, 90].

The discrepancy in the calculated value of the ^{13}C A_{zz}(C$_4$) components reflects a discrepancy in the respective spin density population ρ_π(C$_4$), as expected from a direct proportionality between the two quantities. At least for the large A$_{zz}$(C$_4$) value (dipolar character), the $A_{zz}(C_4) \sim \rho_\pi(C_4)$ proportionality can be applied in an analogous way as the famous McConnell relation for the isotropic hfc constant in a C — H fragment: $a_{iso}(H) = Q\rho_\pi(C)$. Indeed, in case for the increased C$_4$ spin density position, the A_{zz}(C$_4$) ~ ρ_π(C$_4$) proportionality correlates quite well with the DFT calculations. In isotropic solution the spin densities are calculated to be 0.14 for both the C$_1$ and C$_4$ positions [98, 101] (Figure 5.9). In the A$_1$-binding site of PS I they are calculated to increase to 0.16 in the C$_4$ and to reduce to 0.05 in the C$_1$ positions (Figure 5.8). The increase of ρ_π(C$_4$) from 0.14 to 0.16 corresponds to the calculated increase in the value of the ^{13}C A_{zz}(C$_4$) component from 30.3 MHz to 32.7 MHz consistent with the A_{zz}(C$_4$) ~ ρ_π(C$_4$) proportionality. On the basis of this proportionality and with the calculated and measured ρ_π(C$_4$) = 0.14 in IP, the experimentally observed value of A_{zz}(C$_4$) = 40(2) MHz in the A$_1$-binding site of PS I corresponds to ρ_π(C$_4$) ~ 0.19(1). This large spin density increase may be compared with the other increased C$_2$ spin density position, to which a methyl group is attached. For this methyl group, the spin density ρ_π(C$_2$) increases from 0.11(1) in IP to 0.15(1) in A$_1$-binding site of PS I in agreement with the DFT calculated values 0.11 and 0.16 [85, 93]. The ratios of the respective densities (in the A$_1$-binding site and in IP solution) at C$_4$ and C$_2$ positions are almost the same (0.19/0.14 and 0.15/0.11) in agreement with the asymmetric H-bond scheme (Figure 5.2).

According to Figure 5.9 adapted from the DFT calculated values, the summed spin density of the C$_1$ and C$_4$ position reduces from 2 * 0.14 = 0.28 in IP solution to 0.16 + 0.15 = 0.21 in the A$_1$-binding site. This reflects relocation of spin density from the C$_1$/C$_4$ positions to other positions of quinone. Indeed, the calculated spin densities correspond to relocation of

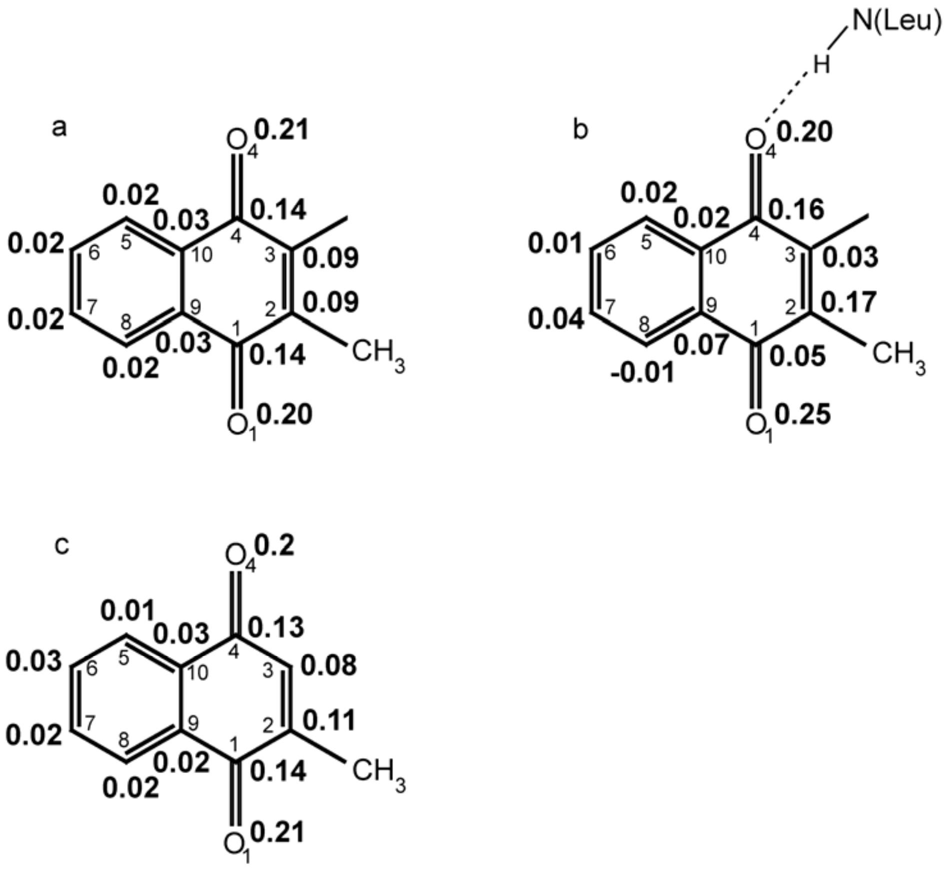

Figure 5.9. Distribution of ρ_π spin densities according to DTF calculations as described in [114] for isotropic solution model (4IP) in IP with two H-bond to each of carbonyl groups of the semequinone redical anion: (a) PhQ radical anion in the PhQ/4IP (phytyl truncated), (b) PhQ/Leu in the A_1-binding site (phytyl truncated), (c) 2-methy-1,4-NQ in the 2-methy-1,4-NQ/4IP model.

spin density from C_1/C_4 mainly to O_1/O_4 and C_2/C_3 and slightly to the second aromatic ring. Therefore, the small calculated increase of $\rho_\pi(C_4) = 0.16$ in the A_1-binding site is traceable to relocation of spin density to other ring position of quinone molecule, also to the C_2 position. As a consequence, the long established good agreement between experimental and calculated hfc tensor components of the methyl group attached to the C_2 position may also be a result of relocation of spin density from C_4 to C_2 positions. The present ^{13}C hfc tensor based date would require for the A_1-binding site no spin density removal from the C_1/C_4 positions (with maintained slight increased for the C_2/C_3 positions). This spin density relocation could come from the oxygen carbonyl groups eventhough this is not an agreement with the presented DFT calculations.

Note all ^{13}C hfc tensor values were calculated for native PhQ (with truncated phytyl tail) and compared with the values measured for 1-^{13}C and 4-^{13}C labelled 2-methyl-1,4-NQ

(Figure 5.9). Small deviation in the values of the hfc tensor of methyl group and H-bonds have been already observed for 2-methyl-1,4-NQ in IP solution from that of PhQ [98]. Also the DFT calculation in IP solution indicates small but noticeable increase in the asymmetry of the spin density distribution for 2-methyl-1,4-NQ compared to that for PhQ, as a result of the asymmetric single substituent:

$\rho_\pi(C_4)/\rho_\pi(C_1) = 0.13/0.14$ and $\rho_\pi(C_3)/\rho_\pi(C_2) = 0.08/0.11$ for 2-methyl-1,4-NQ;
$\rho_\pi(C_4)/\rho_\pi(C_1) = 0.14/0.14$ and $\rho_\pi(C_3)/\rho_\pi(C_2) = 0.09/0.09$ for PhQ.

Intuitively, the same kind (sign) of asymmetry introduced by the single methyl group can be rationalized in accordance with the valence-bond model. The asymmetric methyl group attached at the C_2 position is likely to weaken the H-bond(s) to the $C_1 - O_1$ carbonyl group due to steric hindrance more than the H-bond(s) to the $C_4 - O_4$ group. In the A_1-binding site the strongly H-bonds to the $C_4 - O_4$ group would result in a slight increase in the asymmetry of spin density distribution in 2-methyl-1,4-NQ.

The reason for disagreement between the experimentally determined and calculated values could be also the over-simplification of the A_1-binding site of PS I, where only leucine residue with backbone H-bond to the $C_4 - O_4$ was taken into account [89]. Indeed, significant influences of the specific protein-cofactor interactions on the EPR parameters have been noted for the A_1-binding site of PS I [104, 105] and in the Q_A-binding site of pbRC [102]. However, extended DFT calculations are still needed to complete the experimental spin density map (including many lower spin density positions, also in the second NQ ring) for quinone in the A_1-binding site of PS I.

5.8. Physical models for orientation dependent line broadening effects

By comparison of experimental and simulated spectra in Figure 5.7, satisfactory agreement was found with respect to the spectral line positions. However, the intensities of the spectral features deviate substantially between experiment and simulation, in particular at the up- and down-field side. Freely adjustable, orientation-dependent line width parameters are not deemed an acceptable procedure, as they do not provide for physical insight. On the other hand, the experimental polarisation patterns indicate quite obvious orientation-dependent broadening effects, most clearly at the up-field end of the spectra. This spectral region is dominated by the g_{zz} tensor components, which happens to have nearly equal contributions from $P_{700}^{\bullet+}$ and $A_1^{\bullet-}$ for the observed RP. As it was shown, variation of the line width of

$\Delta B(P_{700}^{\bullet +})$ does not affect the up-field emissive feature (Figure 5.7, top) and the high-field edge (Figure 5.7, bottom). Both results confirm nicely the expectation that these extreme up-field features are exclusively due to the ^{13}C hfc-induced effects of $g_{zz}(NQ^{\bullet -})$. What are the possible mechanisms for selective broadening in this region (and to a lesser extent at the low-field end of the spectra associated exclusively with the $g_{xx}(NQ)$ component)?

Orientation dependent transverse T_2 spin-spin relaxation effects have been studied extensively for the Q_A- and Q_B-binding site of pbRC using high-field pulsed EPR technique [106, 107]. The measured anisotropy in the relaxation time ($T_{2,eff}(B)$) was related to anisotropic stochastic fluctuations of the quinones in their binding pockets and two motional models have been distinguished: i) anisotropic slow librational motion of quinone around specific H-bonds to the amino acid residues of protein environment; and ii) essentially isotropic motion due to collective vibrational motion in the protein environment. The latter process is observed to dominate at temperatures higher than 160 K. In both cases, the longest relaxation times are observed when the field is oriented along the quinone molecular axes identical with the g-tensor, furthermore $T_{2,eff}^{X} > T_{2,eff}^{Y}, T_{2,eff}^{Z}$. It is important to stress that all characteristic powder pattern features, in particular the edges, remain unchanged over the full time regime of the pulse experiment. In addition, any $T_{2,eff}(B)$ induced line width contributions would necessarily result in narrowing at the edges of powder pattern. Therefore, these convincing and highly informative models of stochastic motion can be excluded for quinone in the A_1-binding site of PS I as the origin of the broadening mechanism is likely to be effective only for hfc induced features in the TR EPR spectra.

In addition, an anisotropic distribution of quinone orientations, which in the first instance associated with the H-bond to the protein environment and length of this H-bond, does not seem a likely case to explain the observed broadening effect. The well-resolved ^{13}C hfc features associated with the in-NQ-plane $A_{xx}(^{13}C)$ and $A_{yy}(^{13}C)$ components (also applicable to the partially resolved methyl hfc coupling) can not require a selective distribution of the $A_{zz}(^{13}C)$ values. This cannot be visualized within a simple molecular model and would certainly require rather involved molecular dynamics. Hence, due to the lack of reasonable physical model till now, simulations performed did not include the freely adjustable anisotropic line width parameters.

5.9. Effect of H-bond on structural and functional properties of quinone in the A_1-binding site of PS I

Particular emphasis of this study was on the better understanding of how magnetic interaction properties are related to structural and functional properties of the relevant biological process. The latter consists of sequential ET process through quinone acceptor during light-induced charge separation.

The most remarkable feature of quinone in the A_1-binding site of PS I among all very well-known quinone systems is its very negative redox potential (ca. -750 to 810 meV [15, 30]) required for ET from $A_0^{\bullet-}$ to A_1 to F_X. As was shown in the quinone substituted study [74] and will be shown in Chapter 7 and Chapter 8, the essential contributions to the quinone redox potential in the A_1-binding site of PS I come from the protein environment. Therefore, H-bond can be considered as one of the many significant contributors to the specific quinone redox potential in PS I. It is very well known that with increasing the numbers of H-bonds to quinone its redox potential shifts by an average positive amount [103, 108, 109]. Higher values of up to 250 meV estimated for one H-bond suggested in the literature are clearly overestimated. Recent assessment based on the electrostatic calculation by modelling of additional H-bond to quinone in the A_1-binding site of PS I suggests a small up-contribution of about 50 meV per one H-bond to quinone redox potential, by cannot explain the large difference about 700 meV in the redox potential for a similar quinone in the Q_A-binding site of bRC [110]. Thus, formation of a single H-bond to the quinone in the A_1-binding site of PS I makes only a minor positive contribution to the highly negative redox potential of quinone.

Some attempt to explain the large negative redox potential of quinone was made by correlation of quinone binding pocket with non-polar or polar environment [105]. Note that the difference in the quinone redox potential in polar versus non-polar solvent is estimated to be ~ 400 meV (-170 meV in water and -570 in DMF) [104]. By comparison of values of g-tensor component for PhQ in the A_1-binding site with the respective model systems *in vitro* (PhQ in DMF) it was suggested that the quinone in the A_1-binding site is situated in a highly hydrophobic protein environment [104, 105]. Then by the same analogy a highly hydrophilic

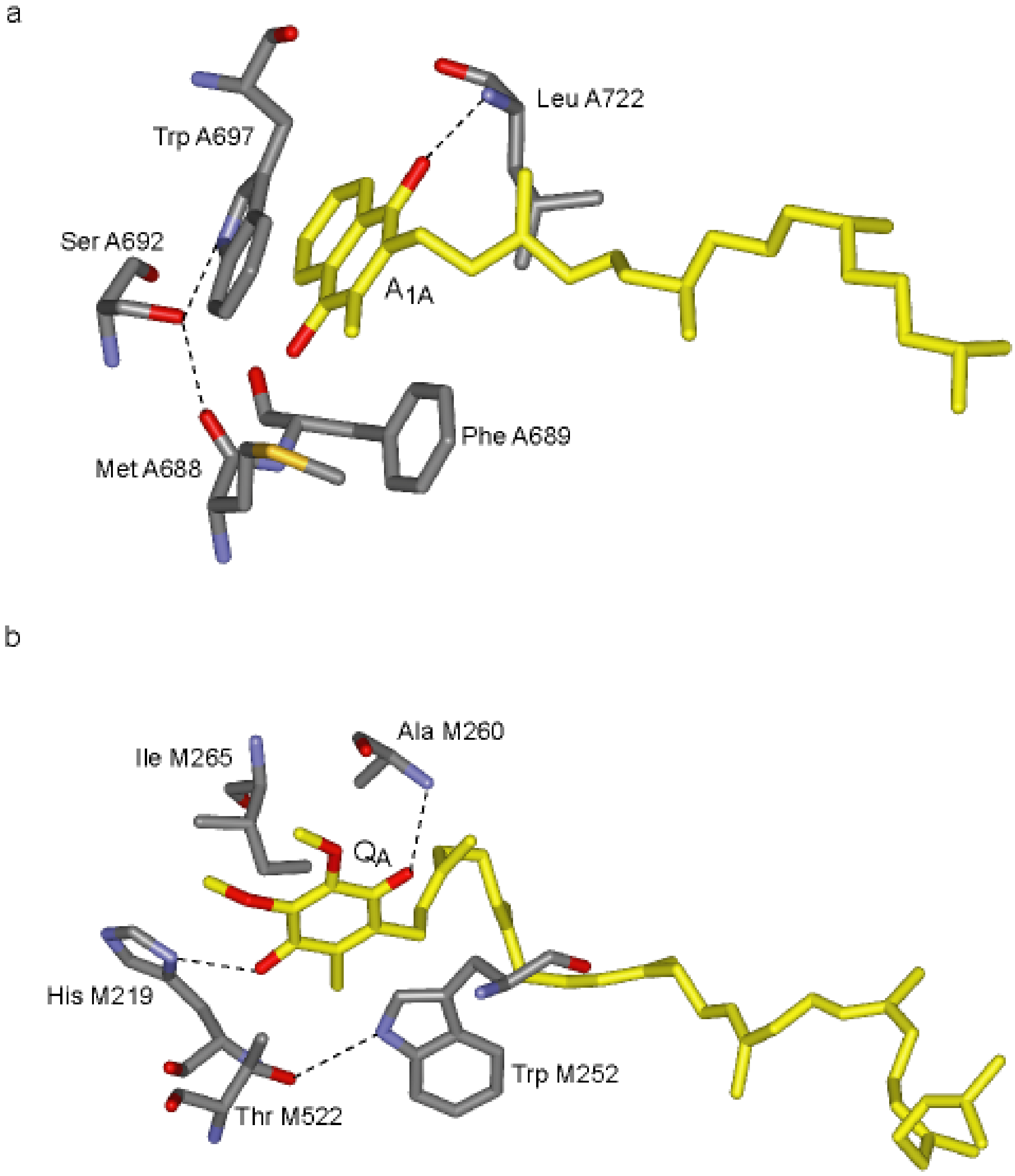

Figure 5.10. Comparison of quinone binding sites in (a) PS I (as in Figure 5.1) and (b) bRC according to the X-ray structure model (pdb entry 1JBC and 1IPCR, respectively). The amino residues which are involved in essential protein-cofactor interactions are depicted with H-bond (broken line) and π-stacking with tryptophan residue.

protein environment has to be realized for the quinone in the Q_A-binding site of bRC. Nevertheless, it is not clear how this polarity can be related to the respective atomic structure model and the distribution of local (partial) charges, dipoles and protonable groups.

A difficulty in interpretation of this result arises already from detailed structural inspection of the quinone binding sites (A_1-binding site of PS I and Q_A-binding site of bRC) (Figure 5.10). Both quinone binding sites based on the X-ray structure model indicate several similarities besides the common function as one-electron gate during ET:

i) In each binding site the quinones is in π-stacked configuration with tryphtophan residue ($W697_{PsaA}$ for the A_{1A}-binding site of PS I [3, 4] and $W252_M$ for the Q_A-binding site of bRC [111]) with most favourable overlap for quinone in the A_1-binding site. (In the Q_A-binding site of bRC $W252_M$ is shifted to a side of quinone and slightly titled from the parallel alignment with quinone.)

ii) The quinone in each site is H-bonded to one quinone carbonyl group from the NH backbone group of the protein ($L722_{PsaA}$ for the A_{1A}-binding site of PS I and $A260_M$ for the Q_A-binding site of bRC).

iii) The backbone H-bond involves the carbonyl group which is in ortho-position to the extended hydrocarbon tail.

iv) The backbone H-bond is in close vicinity of the bound water network identified in the respective X-ray structures model [4, 111].

The main difference apart from a different overall quinone orientation with respect to the common C_2-symmetry axis is that the Q_A-binding site of bRC includes one more H-bond between the second quinone carbonyl group and the NH group of the side chain of a residue, which ligates the non-heme Fe (as one of four histidine ligands). A comparison of the ^{13}C hfc tensors of the individually ^{13}C labelled C_1 and C_4 ring positions, listed in Table 5.1, shows a fairly strong C_1/C_4 asymmetry for the Q_A-binding site. As expected, due to double-sided H-bonds to the quinone, it is smaller than that for the A_1-binding site. Note that the asymmetry has the opposite sign with respect to quinone ring position for the quinone in the A_1-bindind site of PS I. This inverted asymmetry reflects a dominant strong H-bond to the C_1-O_1 carbonyl group from the side chain of $H219_M$ compared to the weaker H-bond to the C_4-O_4 carbonyl group from the back bone of $A260_M$ [87, 90, 102]. Indeed, a detailed orientation-selective ^{1}H and ^{2}H ENDOR results clearly demonstrates the inequivalence of the H-bonds in the Q_A- binding site of bRC [90] (Table 5.3).

Again a comparison of ENDOR data for the respective backbone H-bond in both quinone binding site shows similar hfc tensor and geometry. Both H-bond proton hfc tensors

Table 5.3. Comparison of ^{1}H-ENDOR hfc tensor components (average values in [MHz]) for protons in H-bonds to quinone as: $A_1^{\bullet-}$ in PS I and $Q_A^{\bullet-}$ in pbRC

H-bond	Ref.	observed hfc tensor components		dipolar hfc components		spin density	H-bond distance
		$A_\perp$	$A_\parallel$	$A'_\perp$	$A'_\parallel$	$\rho_\pi(O)$	$r_{O...H}$ [Å]
$A_1^{\bullet-}$ in PS I	[90]	(-)4.9	n.e.	-4.9	-	0.19 (0.20)	1.45 (1.48)
N-H....O_4 (Leu A722)	[112]	(-)4.9[a]	(+)7.7	-	+7.7	0.20	1.68
	[113]	(-)3.5[b]	(+)7.3	-	+7.3	0.20	1.71
$Q_A^{\bullet-}$ in pbRC N-H.....$O_{(1)}$ (Ala M266) N_δ-H....$O_{(4)}$ (His M219)	[99]	(-)4.82 (-)6.43	(+)9.07 (+)9.07	-4.63 -5.17	+9.26 +10.34	0.21 0.15	1.53 1.32

Remarks

H-bond distances $r_{O...H}$ are evaluated according to the dipolar approximation:

$A'_{dip}(\delta) = \frac{g_e \beta_e g_N \beta_N}{h r^3} \rho_\pi(O)(3\cos^2\delta - 1)$; δ is the angle between the H-bond direction and the external magnetic field B_0; for $\delta = 0°$: $A'_\parallel = 2|A'_\perp|$ and for $\delta = 90°$: $A'_\perp$ [MHz] $= -\frac{79.2}{r^3} \rho_\pi(O)$.

The spin density at the H-bonded carbonyl oxygen $\rho_\pi(O)$ is taken from DFT calculations. Hfc components are uncertain; [a] identified later as possible $A_0^{\bullet-}$ contaminant; [b] tentative because of overlap with other lines in the same spectral region. In both cases only the $A'_\parallel$ dipolar hfc component is used for H-bond distance evaluation.

have dipolar character and both H-bonds exhibit a comparable deviation of the O -- - H — N bond direction from the quinone ring plane [90, 112, 114] (Table 5.3). However, the back bone H-bond appears to be weaker in the A_1-binding site of PS I than in the Q_A-binding site of bRC. Combined with the fact that the second H-bond to quinone from side chain of protein surrounding is even stronger in the Q_A-binding site of bRC, quinone in the in the Q_A-binding site of bRC appears to be more tightly bound than the quinone in the A_1-binding site of PS I, at least with respect to the H-bonds.

The main goal in the next chapter is to investigate the quinone binding affinity feature into the A_1-binding site of PS I.

6. Characterisation of PS I Complex from the *menB rubA* Double Mutant with Plastoquinone-9 in the A_1-Binding Site of PS I

The main issue of this chapter is to further investigate the functional features of the A_1-binding site of PS I. This can be achieved by identifying structural properties of the protein environment and the quinone cofactor itself to function as an efficient electron acceptor in the A_1-binding site of PS I. TR EPR is applied to characterize PS I complex isolated from the *menB rubA* double mutant with a quinone rescued or substituted into the A_1-binding site with different structural and kinetic (thermodynamic) properties.

6.1. General strategy

In this chapter I present results of PS I complexes isolated from the *menB rubA* double mutant. In this mutant, two genes *menB* and *rubA* are interrupted. The interruption of *menB* genes results in PQ-9 occupying the A_1-bindig site of PS I [73, 74]. Inactivation of *rubA* gene, coding the membrane-bound protein rubredoxin, which is essential for the assembly of the [4Fe-4S] clusters, causes the lack of F_X, F_A, F_B [32]. The PsaC subunit cannot bind to PsaA and PsaB heterodimer of the PS I complex without F_A and F_B. Also, without the PsaC subunit, the PsaD and PsaE subunits don't bind to PS I [115].

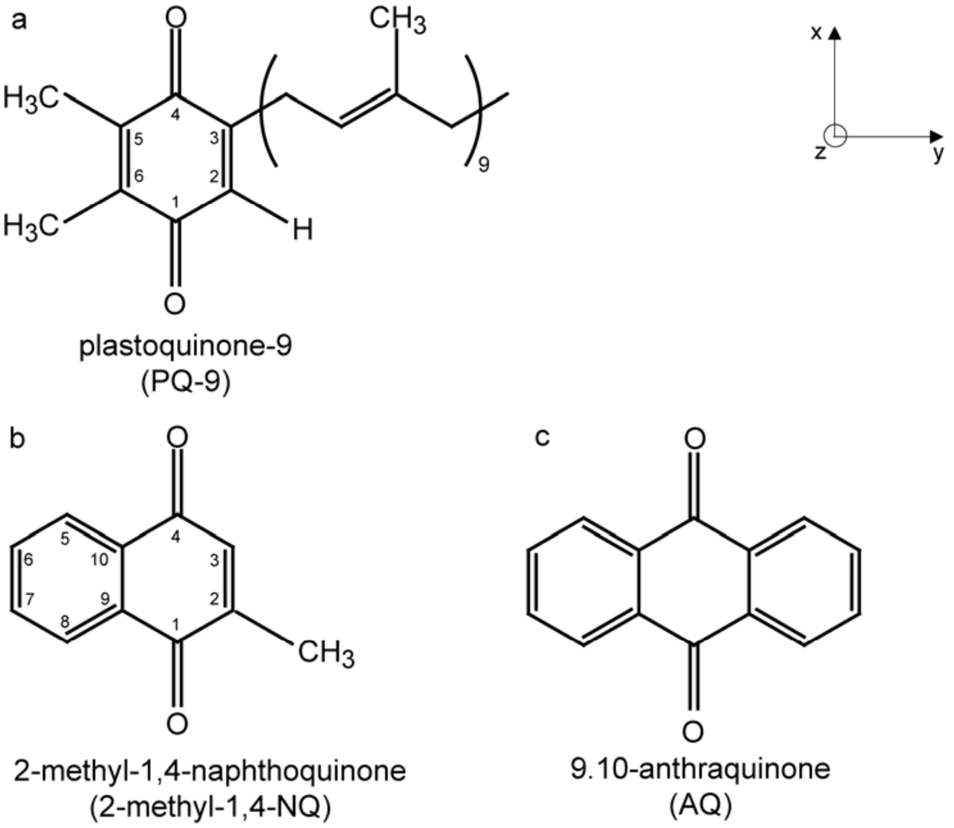

Figure 6.1. Molecular structure of (a) PQ-9, (b) 2-methyl-1,4-NQ and (c) AQ. The g-tensor principal axes of the quinone anion are nearly collinear with the molecular axes shown on the right.

Absence of the [4Fe-4S] clusters and stromal subunits opens a new possibility to study the role of specific cofactors and protein subunits for the quinone binding properties in the A_1-binding site of PS I. The first goal is to investigate the functional properties of PQ-9 in the A_1-binding site of PS I complexes isolated from the *menB rubA* double mutant and to compare them with results of the well studied *menB* and *rubA* single mutants. The next goal is to find particular features of this double mutant for subsequent quinone replacement. It was expected that the more weakly bound PQ-9 in the *menB rubA* double mutant can be easily substituted by different quinones. Two quinones of substantially different molecular structures, 2-methyl-1,4-NQ and AQ, were chosen for in *vitro* incorporation into the *menB rubA* double mutant to probe their binding affinity in the A_1-binding site of PS I. The molecular structures of these quinones are shown in Figure 6.1.

6.2. Results

6.2.1. Characterisation of spin polarised TR EPR spectra of the second $P_{700}^{\bullet +}A_1^{\bullet -}$ RP state in the *menB rubA* double mutant at 80 K

X-band (top) and Q-band (bottom) spectra of the second $P_{700}^{\bullet +}A_1^{\bullet -}$ RP state are compared in Figure 6.2 for the PS I complexes isolated from the *menB* single mutant and *menB rubA* double mutant at 80 K. The TR EPR spectra exhibit the same kind of overall spin polarisation pattern at both microwave frequency as the wild type, i.e. from low field to high field E/A/E at X-band and E/A/A/E/A at Q-band. The TR EPR spectra of the *menB* and *menB rubA* double mutant are nearly identical. This immediately indicates that the same quinone is present in the A_1-binding site of both mutants. It has been assigned to PQ-9 in the *menB* mutant [73]. The differences in the TR EPR spectra of the mutants compared to the wild type are evident mostly at the low and middle field ranges of the spectra as was shown in Chapter 5: i) E peak at low field is shifted to the left, particularly at Q-band; ii) absence of the prominent methyl hfc splitting of PhQ at the central shoulder of A maximum at X-band and Q-band. These features are consistent with a larger g-tensor anisotropy of PQ-9 and unresolved methyl hfc splitting of PQ-9 in the A_1-binding site of PS I, respectively. In the previous ENDOR study on the *menB* mutant, two sets of methyl hfc were resolved and assigned to the two inequivalent methyl groups of PQ-9 [73]. Both sets of methyl hfc were found smaller than those for the methyl group of PhQ.

In order to obtain information about magnetic interaction parameters of PQ-9 in the A_1-binding site of PS I, simulation of the spin polarisation patterns of the second $P_{700}^{\bullet +}A_1^{\bullet -}$ RP state were performed at both microwave frequency using the program for consecutive RP, described in Appendix I. In Figure 6.3 the simulated spin polarisation patterns at X-band (top) and Q-band (bottom) are compared to the experimental spectra of the *menB rubA* double mutant. The spin polarization pattern of the $P_{700}^{\bullet +}A_1^{\bullet -}$ RP state is known to be very sensitive to the relative orientations of the g-tensors of $P_{700}^{\bullet +}$ and $A_{1A}^{\bullet -}$ with respect to the vector ($\mathbf{z}_D$) connecting the spin density centers of the respective radical-ions $P_{700}^{\bullet +}$ and $A_{1A}^{\bullet -}$ [37]. According to high field EPR of single crystals of PS I [37], PhQ in the wild type is oriented in such way that carbonyl bonds of the PhQ head group (quinone *x*-axis) are parallel essentially to the distance vector joining $P_{700}^{\bullet +}$ and $A_{1A}^{\bullet -}$ [37]. Excellent agreement with experimental spin polarisation pattern at X- and Q-band was achieved by keeping all parameters as

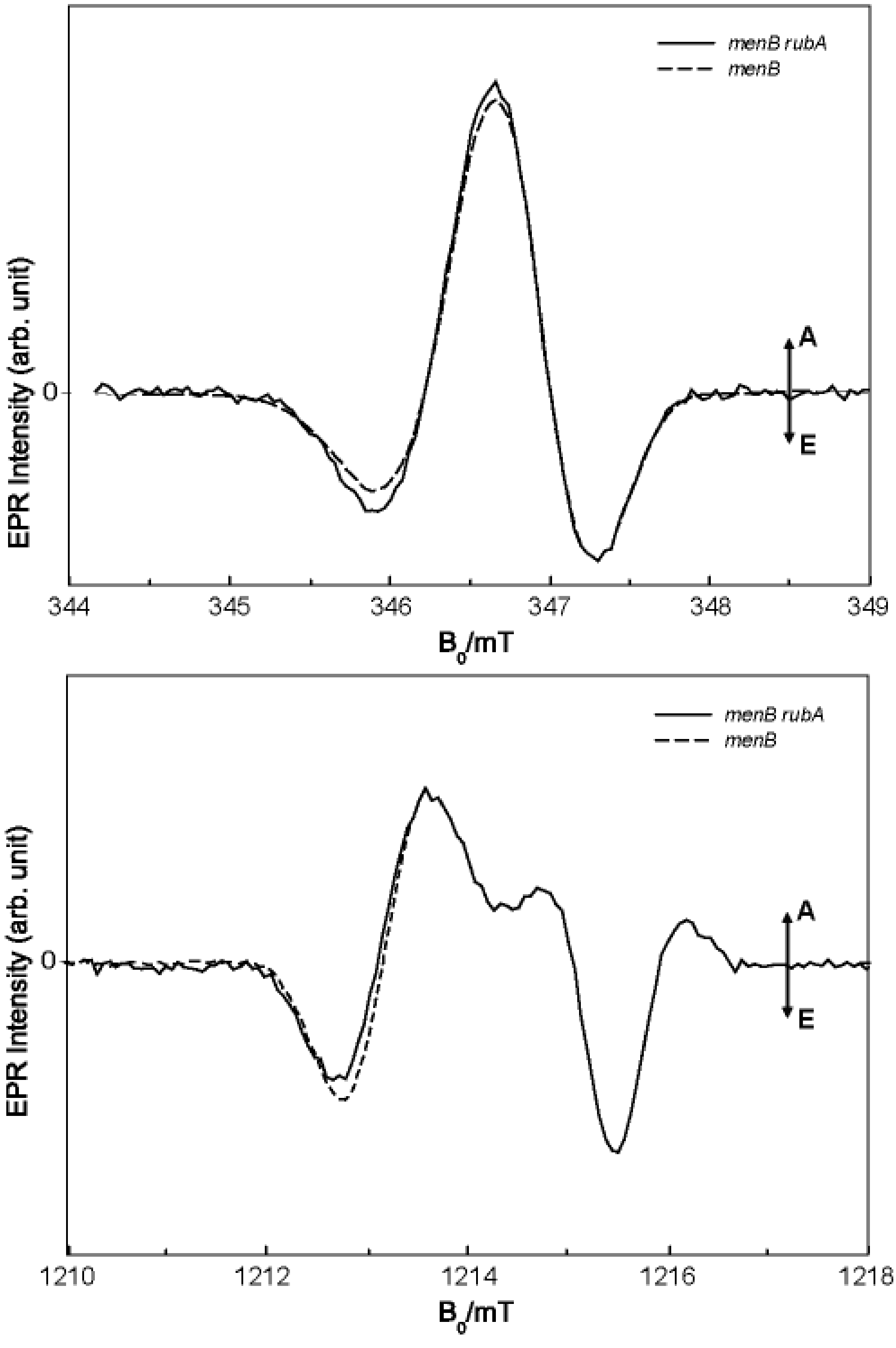

Figure 6.2. X-band (top) and Q-band (bottom) spin polarized EPR spectra of the second $P_{700}^{\bullet +}A_1^{\bullet -}$ RP state in PS I complexes from the *menB rubA* double mutant (solid line) and the *men*B mutant (broken line). The spectra were measured at 80 K and extracted from the full time/field data sets by integrating the signal intensity in a time window from 152 ns to 1520 ns following the laser flash.

established for PhQ in the wild type except that the largest g-tensor component was increased to $g_{xx} = 2.0069$ (Table 6.1). Therefore, the g-tensor of PQ-9 is more anisotropic than that of PhQ, as expected for a one ring versus two ring quinone system. In a previous ESEEM study on the *rubA* or *menB* single mutant it was demonstrated that quinones (PhQ and PQ-9, respectively) are located at the same distance from $P_{700}^{\bullet+}$ and oriented similar to PhQ in the A_1-binding site of PS I from the wild type [73]. From the similarity of the spin polarization patterns in the *menB rubA* double mutant and the *menB* single mutant it can be concluded that PQ-9 has an identical orientation in the *menB rubA* double mutant. ENDOR studies on the *menB* single mutant have identified proton hfc due to two inequivalent methyl groups (C_5 and C_6) of PQ-9 with small coupling constants (<10 MHz) Therefore, they contribute only to a slightly increased inhomogeneous line width of $A_1^{\bullet-}$ in the simulated TR EPR spectra. Nevertheless, for best agreement with the experimental spectra (particularly at X-band) the larger methyl hfc (at ring position C_6 of PQ-9) was taken into account in the simulation in addition to the aromatic C-H fragment at the high spin density ring position C_2 of PQ-9 [73].

Thus, analysis of TR EPR study on the second $P_{700}^{\bullet+}A_1^{\bullet-}$ RP state in the PS I complex isolated from the *menB rubA* double mutant allows for the following conclusions to be drawn: i) PQ-9 is the quinone in the A_1-binding site; ii) absence of the [4Fe-4S] clusters F_X, F_A, F_B and all stromal subunits PsaC, PsaD, PsaE does not disturb the A_1-binding site: the TR EPR detectable structural properties and protein-cofactor interaction features remain the same as observed for PhQ in the wild type. PQ-9 is oriented in the same way in the double mutant as PhQ in the wild type or in the *rubA* mutant and as PQ-9 in the *menB* mutant [32, 73].

In spite of indistinguishable spin polarisation patterns in the *menB rubA* and *menB* mutants, an overall lower signal-to-noise ratio was observed for the *menB rubA* double mutant. As it will be shown latter, this correlates with the appearance of a larger triplet $^3P_{700}$ contribution in the *menB rubA* double mutant (Figure 6.4). It is identified as the recombination product from the first $P_{700}^{\bullet+}A_0^{\bullet-}$ RP state, which is formed if the A_1-binding site remains empty or is otherwise blocked for forward ET from $A_0^{\bullet-}$. Several possibilities are discussed in the next section.

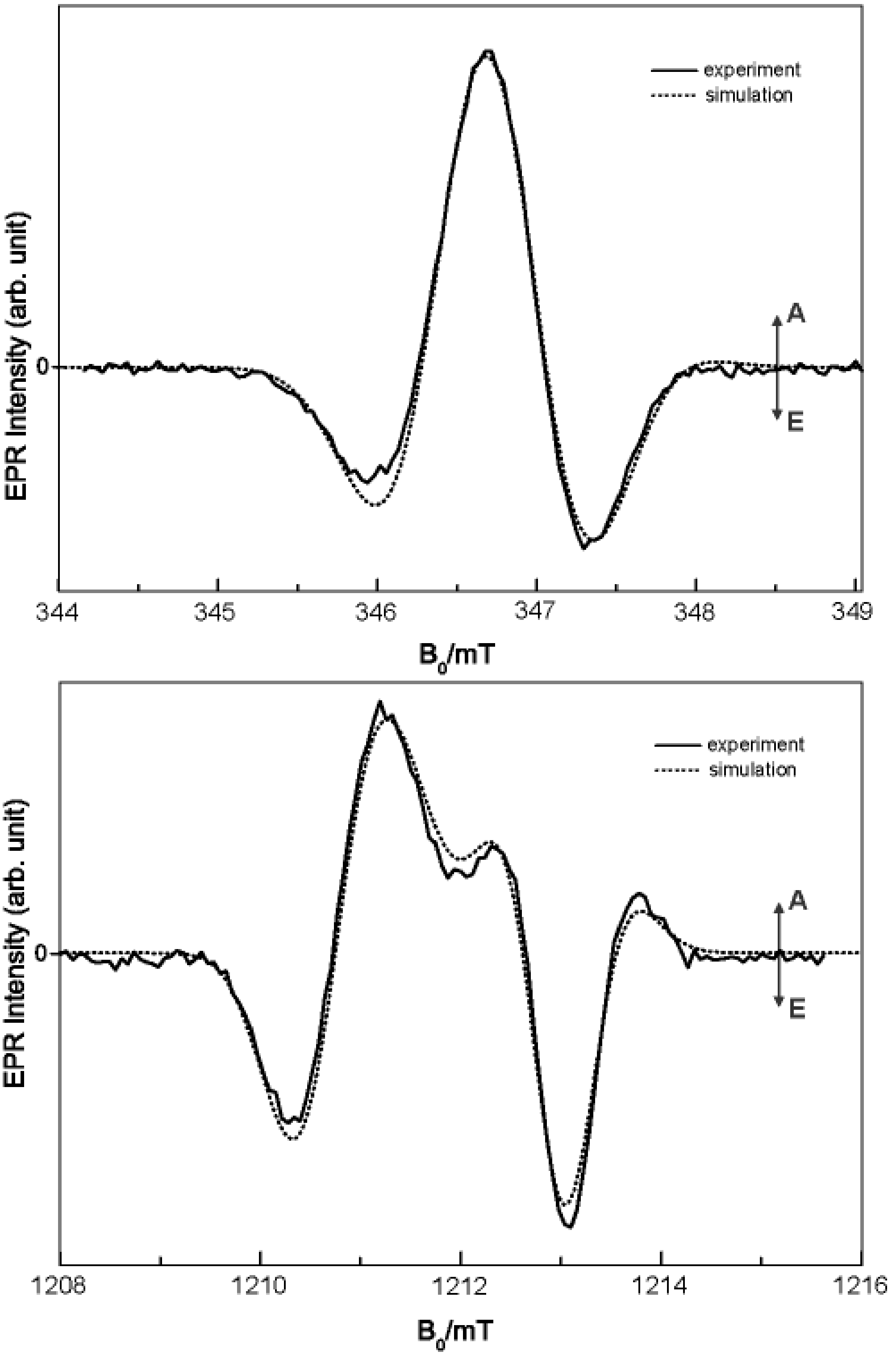

Figure 6.3. X-band (top) and Q-band (bottom) spin polarised TR EPR spectra of the second $P_{700}^{\bullet+}A_1^{\bullet-}$ RP state in PS I complexes from the *men*B *rub*A double mutant (solid line) with PQ-9 in the A_1-binding site are compared with simulations (dotted line). The structural and magnetic parameters used for the simulations are collected in Table 5.1 together with Table 6.1. The isotropic Gaussian line width parameters are: $\Delta B(P_{700}^{\bullet+})$ = 0.50 mT and $\Delta B(A_1^{\bullet-})$ = 0.60 mT.

6.2.2. Observation of $^3P_{700}$ state in the *menB rubA* double mutant as a product of charge recombination from the primary $P_{700}^{\bullet+}A_0^{\bullet-}$ RP state

X-band TR EPR spectra of PS I complexes isolated from the *menB* mutant and the *menB rubA* double mutant are compared for the wide-field sweep at 80 K in Figure 6.4 (top). A broad spectrum in the *menB rubA* double mutant with the characteristic spin polarisation pattern A/E/E/A/A/E is assigned to the $^3P_{700}$ triplet state. Such spin polarization pattern serves as a fingerprint for the $^3P_{700}$ formation by recombination from the first $P_{700}^{\bullet+}A_0^{\bullet-}$ RP state [116]. It originates from population of T_0 spin level. It cannot result from an intersystem crossing (ISC) process, which would be selective with respect to the zero-field triplet states (T_x, T_y, T_z). In case of the primary $P_{700}^{\bullet+}A_0^{\bullet-}$ RP born in the singlet (S) state only population of the T_0 spin level can recombine and lead to the observed spin polarisation pattern of the $^3P_{700}$ state. Comparable spectra of the $^3P_{700}$ state have been observed earlier for PS I complexes after extraction of native PhQ with organic solvents [13]. Under these conditions, ET beyond $A_0^{\bullet-}$ is blocked, and $^3P_{700}$ recombination becomes the predominant decay channel. Similarly, PS I complexes with either singly or doubly reduced quinone in the A_1-binding site yield the $^3P_{700}$ recombination product. Analogous triplet formation by primary $P_{700}^{\bullet+}Pheo^{\bullet-}$ RP recombination is also observed in PS II complex when quinone is missing or reduced in the Q_A-binding site [117].

Besides the wide field scan triplet contribution observed in the *menB rubA* mutant both spectra in Figure 6.4 show also the narrow signal in the center which is due to the second $P_{700}^{\bullet+}A_1^{\bullet-}$ RP state as it was already considered above and Figure 6.2. The second $P_{700}^{\bullet+}A_1^{\bullet-}$ RP is generated by forward ET from $A_0^{\bullet-}$ to A_1 in competition with recombination into the $^3P_{700}$ state. Relative to the signal amplitude of the $P_{700}^{\bullet+}A_1^{\bullet-}$ RP state, the $^3P_{700}$ state signal in Figure 6.4 (top) is large for the *menB rubA* double mutant (solid line) but negligible for the *menB* mutant (broken line). The $^3P_{700}$ state signal can serve as an indicator for the quinone occupancy of the A_1-binding site in the *menB rubA* double mutant.

In addition, the flash-induced absorbance changes in the near-IR as well as in the near-UV show for the case of the *menB rubA* double mutant that long-lived charge separation occurs in only about one half of the PS I complexes. The appearance of the $^3P_{700}$ spectrum in the transient EPR experiment of the *menB rubA* double mutant confirms that a significant part of PS I complexes follows the pathway to recombine in the $^3P_{700}$ state. In these PS I complex, the PQ-9 molecule either: i) was not incorporated into the A_1-binding site; ii) was lost from

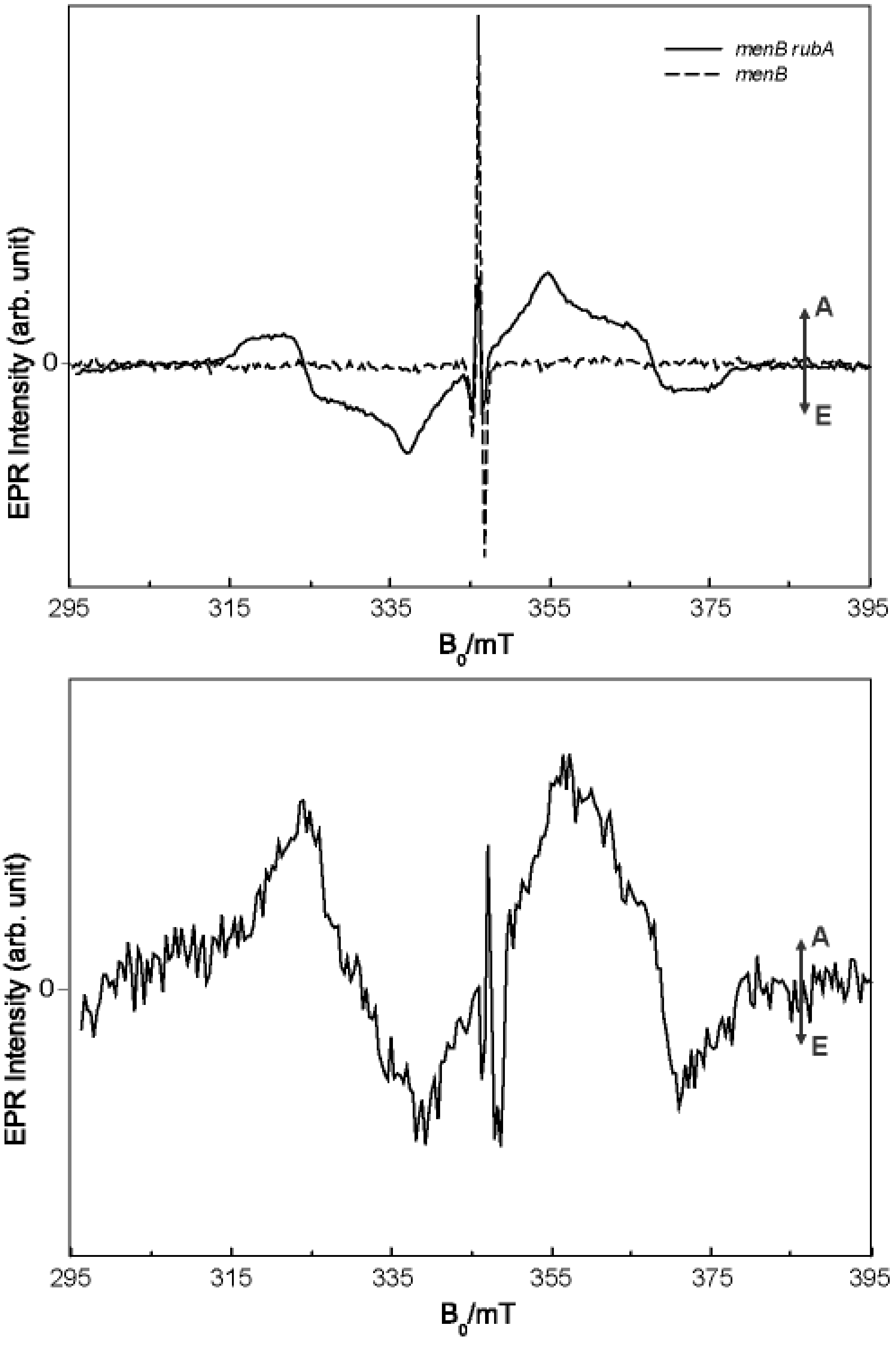

Figure 6.4. Comparison of X-band spin polarised TR EPR spectra at 80 K in the wide field mode for PS I isolated from the *men*B *rub*A (solid line) double mutant and the *men*B mutant (broken line).

Top: A sharp signal in the center corresponds to the spectrum of the second $P_{700}^{\bullet +}A_1^{\bullet -}$ RP state. A broad spectrum in the PS I complex from the *men*B *rub*A mutant is assigned to the $^3P_{700}$ state.

Bottom: The polarisation pattern changes of the “late” triplet signal in the *men*B *rub*A mutant. The signal is assigned to the ^{3}Car state populated via ISC populated ^{3}Chl.

The spectra were extracted from the complete time/field data set in an digital time integration window of 0.25 to 1.4 µs and 7 to 10 µs for early and late spectra.

the A_1-binding site during purification and sample preparation; or iii) empty or filled A_1-binding site is not functional in ET past $A_0^{\bullet -}$ due to modified properties. Under all of these conditions, the $^3P_{700}$ state would appear as a recombination product from the primary $P_{700}^{\bullet +}A_0^{\bullet -}$ RP state.

The appearance of the $^3P_{700}$ spectra in Figure 6.4 suggests that the removal of the stromal subunits and the [4Fe-4S] clusters may alter the binding affinity in the A_1-binding site. However, the empty but otherwise unmodified quinone binding sites can be distinguished from those with altered properties by additional information from quinone replacement experiments, as described below.

Figure 6.4 (bottom) demonstrates a new spectrum observed in the late time window of 8-10 μs after laser flash at 80 K. A different triplet polarization pattern is observed, with altered zero field splitting parameters and a predominantly (E)/A/E/A/E/(A) polarization pattern. Similar spin polarisation pattern have been reported previously [118, 119] and more recently for pbRC [54], and are attributed to a long-lived triplet ^{3}Car state. Such polarization pattern of the ^{3}Car state is consistent with triplet-triplet energy transfer from a preceding ^{3}Chl state populated from an excited ^{1}Chl singlet state by intersystem crossing (ISC). The characteristic spin polarization pattern of the ^{3}Chl state after ISC is (E/E/E/A/A/A) and has been observed as a transient spectrum in many cases. Additionally, in the parallel study with flash-induced absorbance changes in the near UV and visible region, kinetics with a life time of tens of microseconds was observed in PS I complex isolated from the *menB rubA* double mutant and could be assigned to the formation of the ^{3}Car state. Under certain experimental conditions, when the light intensity is near the saturation limit, excitation energy cannot be trapped anymore by the RCs. Eventually, the excitation energy stored in the antenna chlorophylls has to decay via the competing ISC channel to the ^{3}Chl state (Figure 6.5). This triplet state is then efficiently quenched by ^{3}Car as observed by optical and EPR spectroscopy [118, 119, 120, 121].

Since, under the same experimental conditions recombination to the $^3P_{700}$ state followed by ^{3}Car quenching is not observed in PS I complexes isolated from the wild type, the obvious question arises: are all A_1-binding sites functionally competent in PS I from the *menB rubA* double mutant?

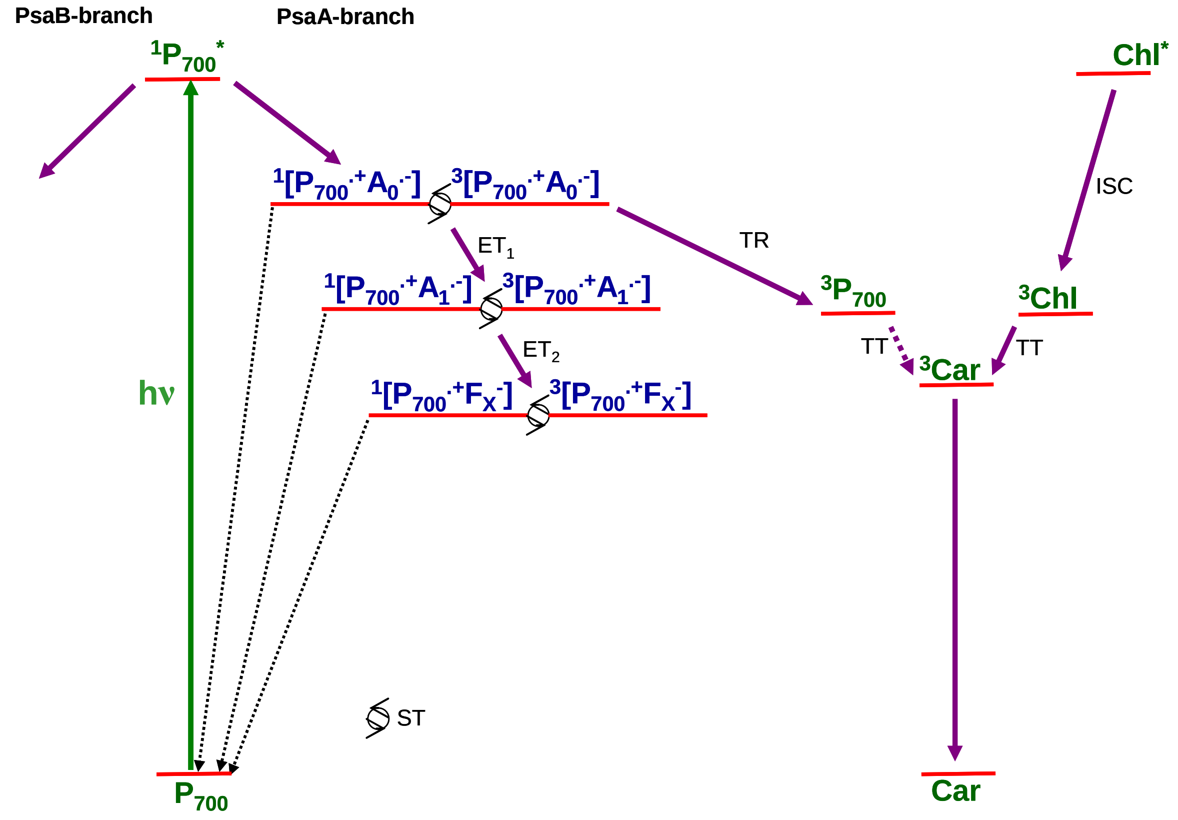

Figure 6.5. Energetic scheme of photoinduced process occurring in PS I. Scheme on the left site reflects forward ET accompanying with formation of the spin correlated RPs along a chain of electron acceptors (PsaA-branch). Scheme on the right site corresponds to the independent photocycle in the antenna system. TR - triplet RP recombination; TT - triplet-triplet transfer; ISC - intersystem crossing with zero-field spin selectivity, ST - singlet-triple mixing; ET_1/ET_2 from $A_0^{\bullet-}$ to A_1/$A_1^{\bullet-}$ to F_X (at temperature above 260 K), respectively.

6.2.3. Characterisation of the *menB rubA* double mutant as a precondition for quinone replacement studies

One possibility to explain the formation of the $^3P_{700}$ state *via* charge recombination from the primary $P_{700}^{\bullet+}A_0^{\bullet-}$ RP state of PS I complex isolated from the *menB rubA* double mutant is that a portion of the quinone binding site is empty. Hence, forward ET from A_0 is blocked. The lack of the [4Fe-4S] cluster F_X, F_A, F_B and stromal subunits PsaC, PsaD, PsaE can lead to a decrease in the binding affinity of the A_1-binding site of PS I for PQ-9. As a result, only a fraction of the A_1-binding sites contains PQ-9. In order to check this, quinone substitution experiments were carried out on the *menB rubA* double mutant using quinones with different affinity properties.

2-methyl-1,4NQ in the A_1-binding site of PS I from the menB rubA double mutant

Since NQ derivatives have higher affinity properties to the A_1-binding site of PS I than PQ-9, 2-methyl-1,4-NQ was chosen as a starting point for incorporation of artificial quinones into PS I complex isolated from the *menB rubA* double mutant [79, 80] (Chapter 5). The same *in vitro* PQ-9 replacement protocol was used as established for the *menB* single mutant [79].

Partial information about the occupancy of 2-methyl-1,4-NQ is obtained by comparison of the relative signal amplitudes of the second $P_{700}^{\bullet +}A_1^{\bullet -}$ RP and $^3P_{700}$ states at 80 K (Figure 6.6). Before commenting further on the results, it is worth mentioning that the signal amplitudes of each of the states are provided in arbitrary units. First it has to be taken into account that the signal amplitudes (of $P_{700}^{\bullet +}A_1^{\bullet -}$ RP and $^3P_{700}$ spectra) are not only proportional to the respective state population, but are also determined by the degree of spin polarisation acquired in the respective light excitation process. In addition, they have to be measured under different experimental conditions (concentration, field scan range, microwave power, cavity tuning, signal averaging conditions). Therefore, absolute spin quantisation is impossible. However, to the extent that the respective spin polarisation mechanism remains the same for the different samples studied and the experimental conditions are kept identical for all measurements of the $P_{700}^{\bullet +}A_1^{\bullet -}$ RP and the $^3P_{700}$ state the relative signal amplitudes can be analysed in terms of changes in the relative occupancy of the two states under investigation. The narrow field scan spectrum of the $P_{700}^{\bullet +}A_1^{\bullet -}$ RP state (full line), measured in a narrow magnetic field range such as the spectra in Figure 6.2, is plotted as an insert in the center of the wide field scan spectrum of the $^3P_{700}$ state (broken line). For easy comparison of the relative amplitude of the RP signal, the spectra are normalised to the same $^3P_{700}$ spectrum intensity.

Figure 6.6 compares the relative signal amplitudes of the $P_{700}^{\bullet +}A_1^{\bullet -}$ RP and $^3P_{700}$ spectra for PS I complexes isolated from the *menB rubA* double mutant with PQ-9 and 2-methyl-1,4-NQ. It is clear that the relative amplitude of the $P_{700}^{\bullet +}A_1^{\bullet -}$ RP compared to the signal intensity of $^3P_{700}$ is less for the *menB rubA* double mutant with PQ-9 and becomes higher when 2-methyl-1,4-NQ is present in the A_1-binding site. This analysis shows that within experimental accuracy all A_1-binding sites in the *menB rubA* double mutant remain functional (even if not occupied by PQ-9). They can accept electrons, if they are filled with a suitable electron acceptor as, for example, 2-methyl-1,4-NQ. Indeed, the signal amplitude of the $^3P_{700}$ spectrum becomes insignificant in comparison to the signal of the $P_{700}^{\bullet +}A_1^{\bullet -}$ RP state in PS I complexes isolated from the *menB rubA* double mutant with 2-methyl-1,4-NQ substituted in the A_1-binding site.

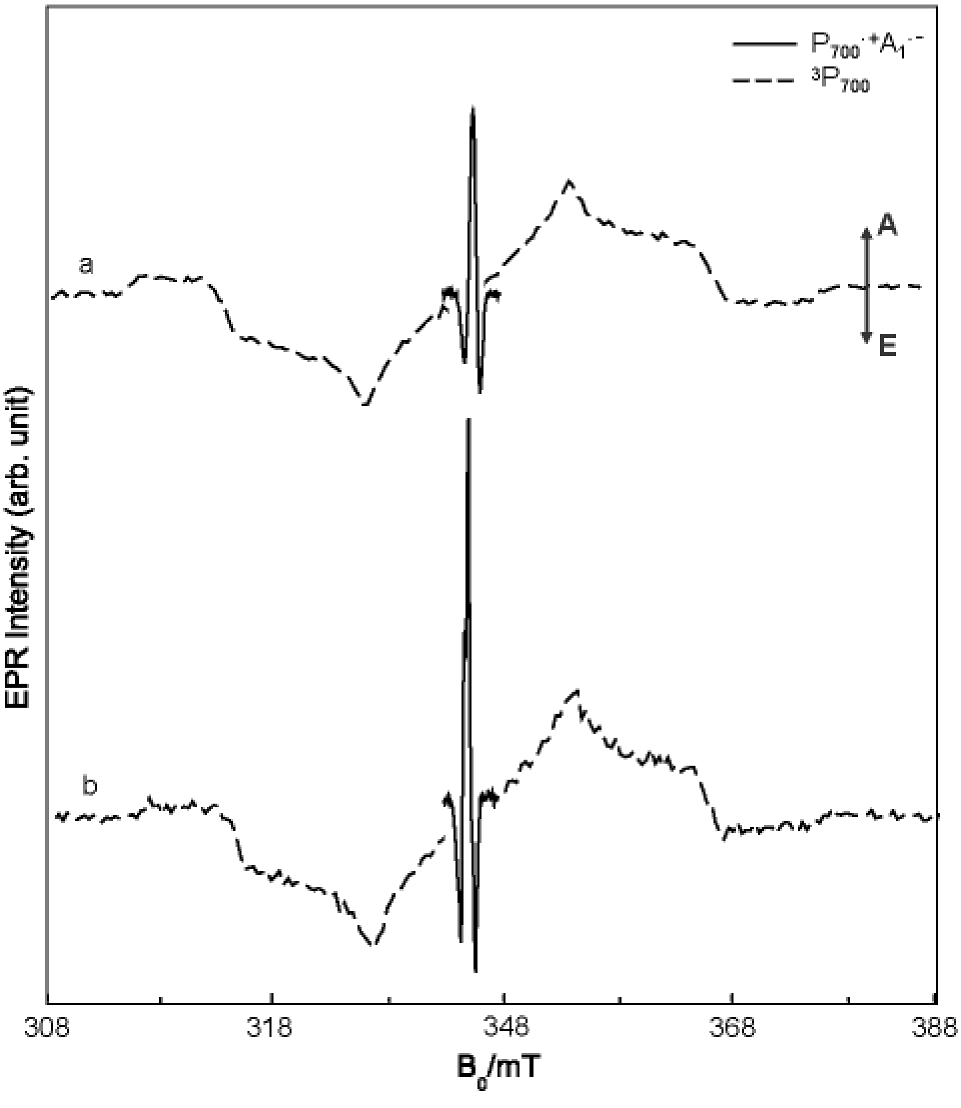

Figure 6.6. Comparison of relative amplitudes of wide field sweep spectra of the $^3P_{700}$ state (broken line) and narrow field sweep spectra of the second $P_{700}^{\bullet+}A_1^{\bullet-}$ RP state (solid line in center) of PS I isolated from the *men*B *rub*A double mutant with different quinones: (a) PQ-9 and (b) 2-methyl-1,4-NQ in the A_1-binding site at 80 K. The narrow signal of the second $P_{700}^{\bullet+}A_1^{\bullet-}$ RP state was measured under the same conditions as the spectra in Figure 6.2 and then added as central feature in the middle of the wide field sweep triplet spectra (to assure reliable amplitude determination for the both signals).

AQ in the A_1-binding site of PS I from the menB rubA double mutant

The absence of the [4Fe-4S] clusters and stromal subunits in the double mutant could cause a more accessible A_1-binding site. This would allow incorporation of a larger quinone molecule, for example AQ, with three aromatic rings (Figure 6.1), into the A_1-binding site of PS I complex isolated from *rubA menB* double mutant. The ability of AQ to bind into the A_1-binding site of PS I was checked again in terms of the relative spectral amplitudes of the

$P_{700}^{\bullet+}A_1^{\bullet-}$ RP and $^3P_{700}$ state signals at 80 K (Figure 6.7). All remarks done for Figure 6.6 applied also for Figure 6.7.

In Figure 6.7, the relative signal intensity of the corresponding $P_{700}^{\bullet+}A_1^{\bullet-}$ RP and $^3P_{700}$ spectra from various PS I samples with AQ incorporated into the A_1-binding site by different protocols are compared: (a) AQ replacement procedure into the *menB rubA* with washing, (b) AQ replacement procedure into the *menB rubA* without washing, (c) AQ reconstitution into the extracted PS I complex. Obviously, when the sample is subjected to the washing procedure after AQ replacement, the relative contribution of the $P_{700}^{\bullet+}A_1^{\bullet-}$ signal is the weakest (Figure 6.7, a). Without washing, the relative contribution of the $P_{700}^{\bullet+}A_1^{\bullet-}$ RP state increases by about a factor of 5 (Figure 6.7, b). The relative signal amplitude ratio in case (b) is the same as for PS I from the *menB rubA* double mutant with AQ (Figure 6.6, a) and as for AQ reconstituted into the A_1-binding site of the extracted PS I complex. In other words, the AQ reconstitution protocol has about the same efficiency in filling the A_1-binding sites of PS I complex from the *menB rubA* double mutant as from the extracted PS I complex. However, the washing procedure is able to remove AQ to a large extent from the A_1-binding site of PS I and it causes a decrease of the $P_{700}^{\bullet+}A_1^{\bullet-}$ RP state signal and a corresponding relative increase of the $^3P_{700}$ state signal (only the ratio of signal amplitudes is relevant). The easiness of AQ removal from the A_1-binding site reflects its low binding affinity.

In spite of AQ ability to fill the A_1-binding site of PS I and to serve as the second electron acceptor one important question remains: How does the protein-cofactor interaction participates in the direct AQ binding into the A_1-binding site of PS I? Information about the structural properties and protein-cofactor interaction in the A_1-binding site occupied with AQ can be obtained from the detailed EPR analysis of the second $P_{700}^{\bullet+}A_1^{\bullet-}$ RP state.

Figure 6.8 shows a comparison of X-band (top) and Q-band (bottom) spectra of the $P_{700}^{\bullet+}A_1^{\bullet-}$ RP state for the following set of PS I complexes isolated from the (a) wild type with PhQ, (b) *menB rubA* double mutant with PQ-9, (c) *menB* mutant with AQ incorporated *in vitro*, (d) *menB rubA* double mutant with AQ incorporated *in vitro*, and (e) the extracted PS I complex with AQ at 80 K. The TR EPR spectra of all samples exhibit the same overall polarization pattern as PS I complex from the wild type, i.e. E/A/E at X-band and E/A/A/E/A at Q-band. The total spectral width in PS I complexes containing AQ is lower compared to the wild type and the *menB* mutant because of smaller g-tensor anisotropy of AQ and absence of the partially resolved methyl hfc, which makes a considerable contribution to the spectral width. Spectral decomposition of Figure 6.8 (c) indicates that only a partial substitution (ca.

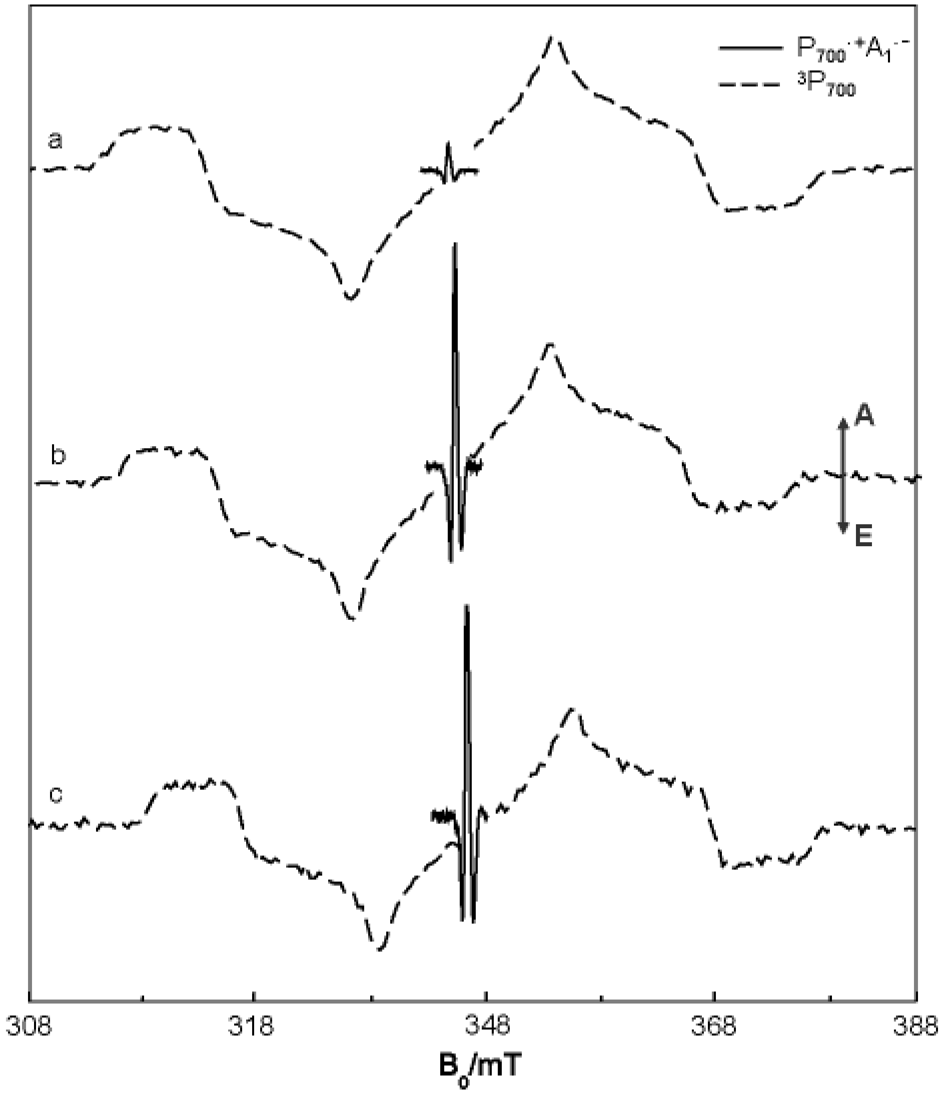

Figure 6.7. Similar comparison as in Figure 6.5 but for PS I complexes from the (a) *menB rubA* double mutant with AQ exchanged in the A_1-binding site and subsequently washed, (b) same as (a) but without washing, (c) extracted PS I with AQ reconstituted in the A_1-binding site.

30 %) of PQ-9 by AQ is achieved in the *menB* single mutant. In contrast to the *menB* single mutant, AQ is able to replace PQ-9 nearly completely in the *menB rubA* double mutant (95 %). The higher degree of AQ incorporation in the latter may be attributed to a greater accessibility of the A_1-binding site in the absence of F_X and the stromal subunits. Similar spin polarisation patterns in the *menB rubA* double mutant with AQ and the solvent-extracted PS I with AQ confirm that AQ is oriented the same way in both samples.

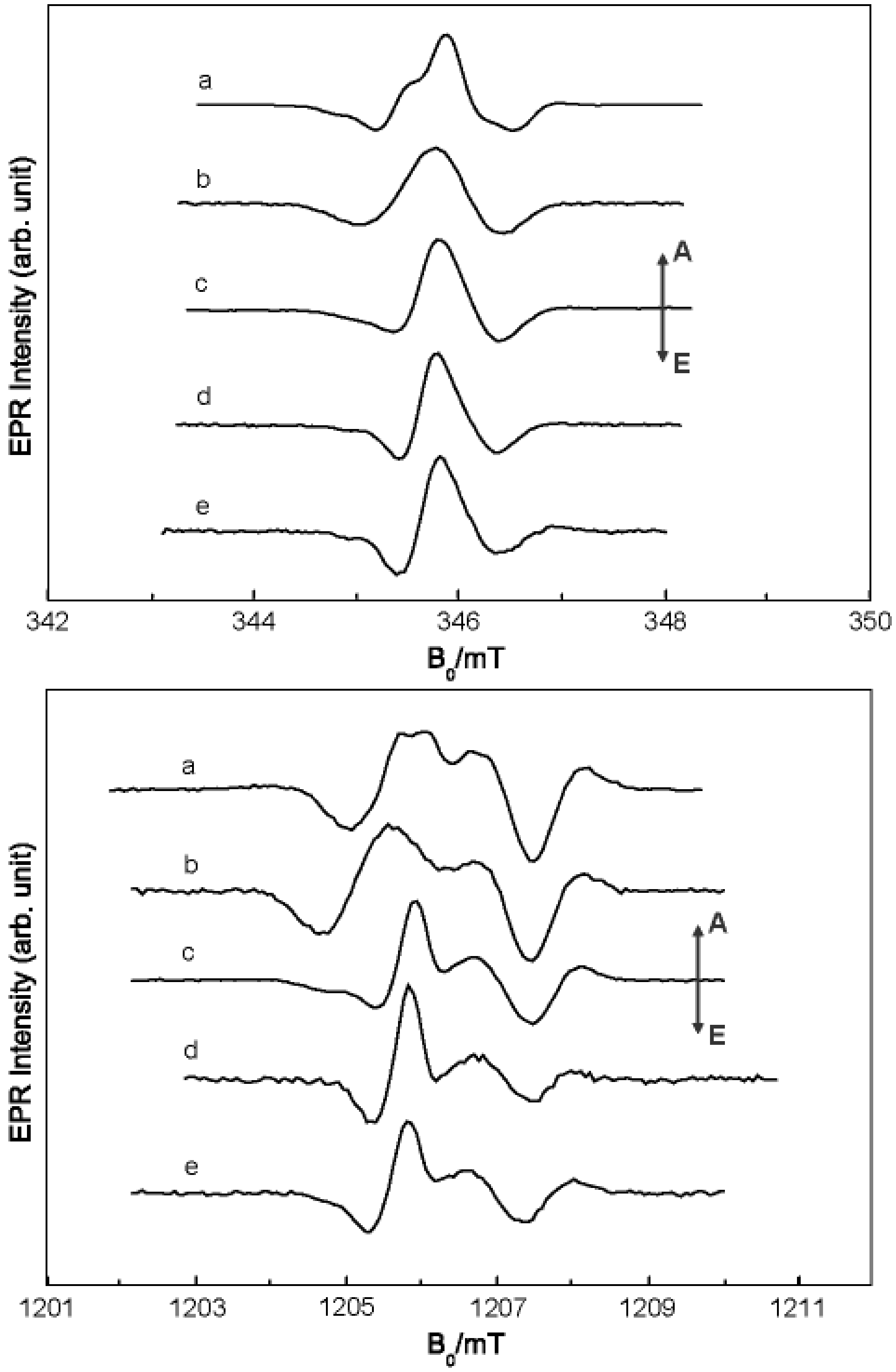

Figure 6.8. X-band (top) and at Q-band (bottom) spin polarized TR EPR spectra of the second $P_{700}^{\bullet+}A_1^{\bullet-}$ RP state in different PS I samples isolated from the (a) wild type PS I with PhQ, (b) *men*B *rub*A double mutant with PQ-9, (c) *men*B mutant with AQ partially replacing PQ-9, (d) *men*B *rub*A double mutant with incorporated AQ, (e) extracted PS I with AQ reconstituted into the A_1-binding site at 80 K. The spectra are recorded at the same experimental conditions as in Figure 6.2.

In order to derive from the spectra precise magnetic parameters of AQ in the A_1-binding site of PS I the same approach as for the simulation of spectra with PQ-9 in the *menB rubA* mutant was taken. In Figure 6.9, X-band (top) and Q-band (bottom) simulated spin polarisation patterns of the $P_{700}^{\bullet+}A_1^{\bullet-}$ RP state are compared to the experimental spectra of the *menB rubA* double mutant with AQ. Inspection of the spin polarization pattern suggests than AQ in the A_1-binding site of PS I: i) AQ has a smaller g-tensor anisotropy than PhQ (Table 6.1); ii) AQ is at the same distance from $P_{700}^{\bullet+}$ and oriented similar to PhQ in the wild type. The unresolved proton hfc of AQ was assumed to be small in simulation and can contribute only into the inhomogeneous line width of $A_1^{\bullet-}$.

The hfc splitting provides a sensitive indicator for the asymmetry in the spin density distribution induced by H-bond with the protein environment. As it was considered in Chapter 5, the single H-bond from the back bone $L722_{PsaA}$ to the carbonyl group C_4-O_4 leads to an increased the protons hfc splitting of methyl group attached at position C_2 (high spin density position). If similar H-bonding scheme for AQ is expected, the high spin density would be at ring positions of two carbon atoms apart from the H-bonded carbonyl group. The protons at these two positions have their bond axes along the molecular x-direction (Figure 6.1). The dominant hfc axis of an aromatic C-H fragment is expected to be in-plane and perpendicular to the C-H bond [37, 81]. Thus, the largest hfc splitting would be expected along the molecular y-axis. Since the proton hfc splittings for AQ are not resolved in the TR EPR spectrum conclusion about the asymmetric hydrogen bonding between the protein environment and AQ cannot be made easily. On the other hand, the quinone-protein interactions are also reflected in differences of the observed quinone g-tensor components (particular g_{xx} component) in different environments (e.g. solution, native and modified A_1-binding sites) [98, 103, 122, 123]. The H-bond formation and π-stacking lead to a rather small and sometimes opposite shift in the g-tensor anisotropy [100, 103]. Comparison of AQ g-tensor in PS I *versus* bRC shows a larger g-tensor anisotropy in PS I (Table 6.1). The same is true for other quinones in PS I *versus* bRC [124]. The analogous qualitative change in both cases indicates that protein cofactor interaction (at least one H-bond to $L722_{PsaA}$ and π-stacking with $W696_{PsaA}$) for AQ in the A_1-binding site of PS I is similar to PhQ in the wild type.

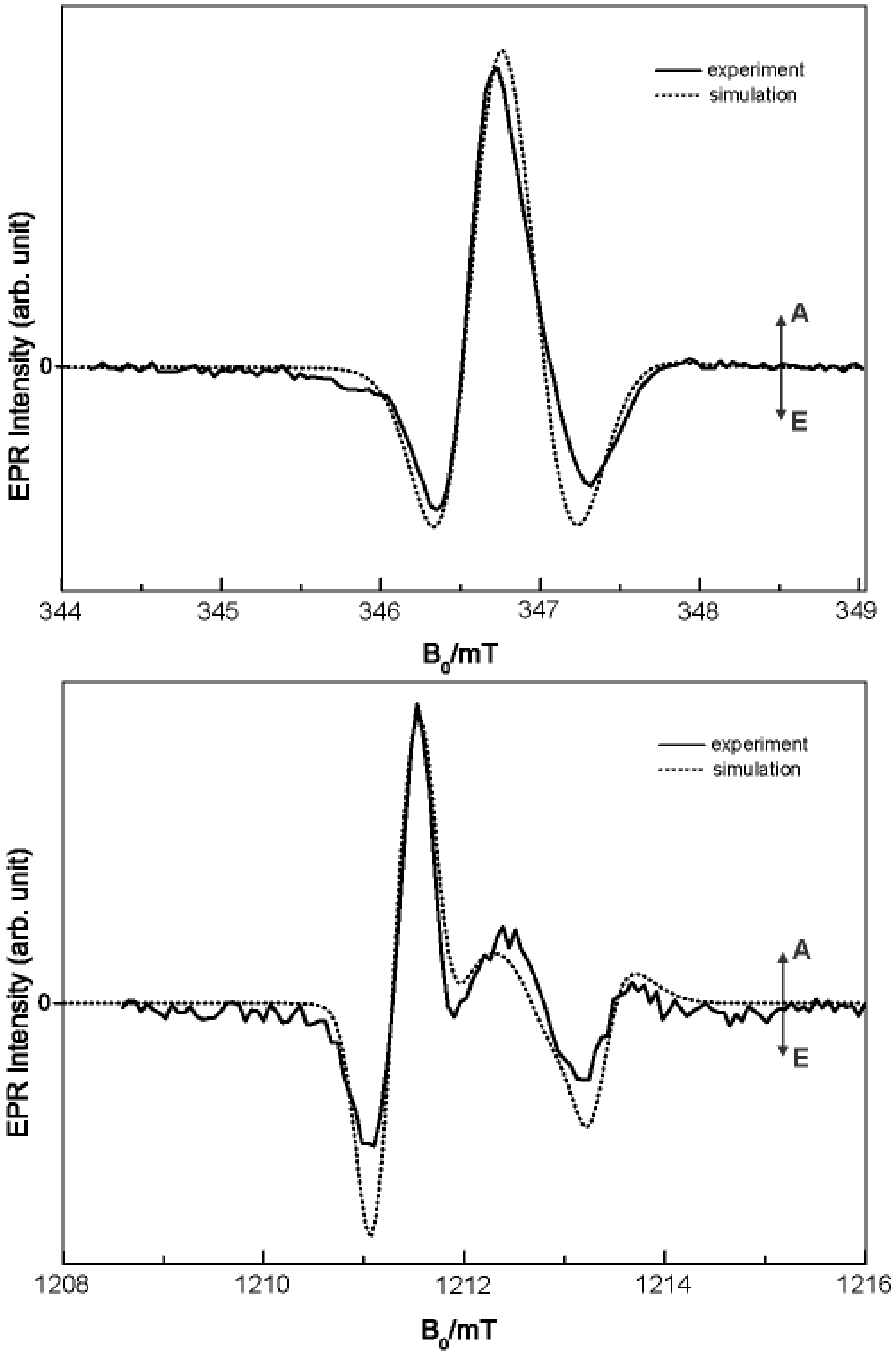

Figure 6.9. X-band (top) and Q-band (bottom) spin polarised TR EPR spectra of the second $P_{700}^{\bullet+}A_1^{\bullet-}$ RP state in PS I complexes from the *men*B *rub*A double mutant (solid line) with AQ in the A_1-binding site are compared with simulations (dotted line). The structural and magnetic parameters used for the simulations are collected in Table 5.1 and Table 6.1. The isotropic Gaussian line width parameters: $\Delta B(P_{700}^{\bullet+}) = 0.50$ mT and $\Delta B(A_1^{\bullet-}) = 0.30$ mT.

Table 6.1. Magnetic parameters used for simulations of TR EPR spectra of the second $P_{700}^{\bullet+}A_1^{\bullet-}$ RP state.

quinone	g-tensor			hfc tensor	
	g_{xx}	g_{yy}	g_{zz}	$A_\perp$ MHz	$A_{\|\|}$ MHz
PhQ (PSI)	2.0061	2.0051	2.0022	12.8	9.2
PQ-9 (PS I)	2.0069	2.0051	2.0022	9.8[a]	5.8[a]
DQ (bRC) [124]	2.0064	2.0051	2.0022	-	-
AQ (PS I)	2.0058	2.0048	2.0022	-	-
AQ (bRC) [124]	2.0056	2.0049	2.0022	-	-

Remarks

[a] The values of hfc tensor components derived from ENDOR experiment were assigned to one of the methyl groups attached at position C_6 of PQ-9 [73].

In addition, the similarity of the spin polarisation pattern of PS I complex from the *menB rubA* mutant with AQ and extracted PS I with AQ in Figure 6.9 (d and e) leads to the conclusion that, in spite of the lack of the [4Fe-4S] clusters and all stromal subunits in PS I or harsh treatment on PS I, the structural properties of the A_1-binding site are highly conserved.

6.3. Conclusions of TR EPR study of the *menB rubA* double mutant

Two key conclusions about structural features of the A_1-binding site are reached in this TR EPR study on PS I complex isolated from the *menB rubA* double mutant. The removal of the [4Fe-4S] clusters and all stromal subunits PsaC, PsaD and PsaE does not alter the structural integrity of the A_1-binding site within experimental accuracy, but influences the quinone binding affinity. The first argument, based on the analysis of spin polarization pattern, indicates that the quinones incorporated into the A_1-binding site of PS I are oriented always similar to PhQ in the wild type and its orientation is insensitive to its chemical identity (the same orientation of quinone head group). This experimental fact is consistent with previous investigation of incorporated mono-substituted NQs derivatives in PS I from the *menB* mutant, the extracted PS I and 2-phythyl-1,4-NQ in PS I from the *menG* mutant. It was demonstrated, that independently on the presence of only either methyl group or phytyl tail in the foreign quinone molecule, the methyl group of the quinone turns out at a high spin density position C_2 while the phytyl tail of the quinone is always at low spin density position C_3 [81, 93]. In case of PQ-9, high spin density position is assigned to the aromatic C – H fragment at position C_2 and to the methyl group at position C_6. Low spin density position is assigned to the methyl group at position C_5 and to the tail at position C_3 and it correlates with suggested asymmetric H-bond model for PhQ in the A_1-binding site of PS I [73] (Figure 5.1). Thus, results of PS I isolated from *menB rubA* double mutant provide evidence for highly conserved protein-cofactor interaction in the A_1-binding site of PS I such as asymmetric H-bond to the backbone nitrogen of $L722_{PsaA}$ residue in spite of the absence of the [4Fe-4S] clusters F_X, F_A, F_B and all stromal subunits PsaC, PsaD, PsaE.

One difference between the PS I complexes isolated from the *menB* single mutant and from the *menB rubA* double mutant is that the A_1-binding site is fully occupied by PQ-9 in the former whereas it is less than half are unoccupied but functionally competent in the latter. Another difference is that AQ incorporation into the A_1-binding site of PS I complexes from the *menB* mutant results in partial replacement (not more then 30 %) of PQ-9. However, the AQ incorporation into the A_1-binding site of PS I complexes from the *menB rubA* double mutant results in complete displacement (more than 95 %) of PQ-9, even though the A_1-binding sites are only partially filled after the quinone exchange. Interestingly the incorporation of the higher affinity 2-methyl-1,4-NQ into the A_1-binding site of PS I complexes from either the *menB* mutant or *menB rubA* double mutant yields a nearly complete occupancy of the quinone binding sites. How can this discrepancy be reconciled?

One possible explanation is that the removal of the [4Fe-4S] clusters and the stromal subunits leads to a decrease in the binding affinity and as a result, only a fraction of the A_1-binding sites contains PQ-9. Another possible explanation is that the removal of the stromal subunits allows the quinone binding site to be more flexible, thereby providing a greater incorporation of the larger AQ molecule. Since the A_1-binding site is located near the beginning of the A-**jk** (B-**jk**) surface helix and the return to the stromal start of the A-**k** (B-**k**) transmembrane helix which forms the ionic and hydrogen bond contact with PsaC, PsaD, PsaE subunits [2, 115], it is feasible that the removal of these stromal subunits would allow access to the external medium, and thus the greater possibility for quinone loss and/or replacement. Alternatively, the presence of empty quinone binding sites may lead to the increased AQ binding because the molecule need only to occupy an empty site and not displace a pre-existing with PQ-9, thus making the procedure similar to the quinone incorporation into the PS I particles after organic solvent extraction. Regardless of whether the A_1-binding sites are fully occupied or not, the ability to exchange AQ into the PS I isolated from the *menB rubA* double mutant indicates that the A_1-binding site is more freely accessible than for PS I complexes from either the *menB* mutant. These properties make PS I complex isolated from the *menB rubA* double mutant ideal for incorporating novel quinones, particularly AQ, into the A_1-binding site. However, it was observed the empty A_1-binding sites can be created in the *menB rubA* double mutant by washing procedure and conversely, resupplying AQ results in an increase in the occupied and a decrease in the number of the empty quinone binding sites. It is essential to emphasize that the presence of the empty quinine binding sites in the *menB rubA* double mutant after washing is a result of a relatively low AQ binding affinity to the A_1-binding rather than the result of different types or populations of the A_1-binding sites of PS I. The evidence for this is that 2-methyl-1,4-NQ with high binding affinity can fill and act in all A_1-binding sites of PS I from the *menB rubA* double mutant The attempts to incorporate AQ, which has more negative redox potential than PhQ and even more negative than PQ-9 [74], into the A_1-binding site of PS I opens another interesting aspect for study the properties of forward ET from $A_0^{\bullet -}$ to AQ to F_X. It is described in more detail in the next chapter.

7. 9,10-Anthraquinone with More Negative Redox Potential in the A_1-Binding Site of PS I

In order to investigate ET properties from $A_0^{\bullet-}$ to A_1 to F_X an attractive option is incorporation of a suitable quinone in the A_1-binding site, in particular with a more negative redox potential than native PhQ to adapt the ET kinetics to the TR EPR accessible time windows.

7.1. Background

Of particular functional significance is a huge difference in redox potentials of about 700 mV between PhQ in the A_1-binding site of PS I and PQ-9 in the Q_A-binding site of PS II. For PS I isolated from the *menB* mutant, with PQ-9 in the A_1-binding site, it was shown that forward ET from $A_1^{\bullet-}$ to F_X is slowed down only by less than an order of magnitude, hence the redox potential of PQ-9 is somewhat more positive (~ 100 meV). As a consequence the difference between the redox potentials of the same quinone (PQ-9) in the A_1-binding site of PS I and in the Q_A-binding site in PS II remains several hundreds of meV [74]. This means that the predominant contribution to the quinone redox potential comes from the protein environment and not from the molecular properties of the quinone itself.

Even though the redox potential of the quinone in RCs is largely determined by the respective protein environment, the molecular properties of the individual quinone are of particular significance. The quinone redox potential in RCs of purple bacteria has been varied systematically by introducing a variety of structurally related quinones into the Q_A-binding site of pbRC to study the influence on the forward ET kinetics to and past Q_A [125-127]. Some studies have been carried out in PS I as well. ET kinetics from $A_0^{\bullet -}$ to a series of reconstituted quinone-acceptors in the A_1-binding site of PS I were measured by absorbance difference spectroscopy as a function of the altered energy gap between A_0 and A_1 [41].

The approach presented in this chapter consists of introducing into the A_1-binding site of PS I the AQ molecule with a more negative redox potential than native PhQ (difference is about 150 meV in DMF [108, 128]). The energy gap between A_0 and A_1 is narrowed, ET from $A_0^{\bullet -}$ to A_1 may be slowed down that spin dynamics can be already developed in the $P_{700}^{\bullet +}A_0^{\bullet -}$ state and may be observable in the TR EPR accessible $P_{700}^{\bullet +}A_1^{\bullet -}$ state. Thus, the effect on the forward ET steps from $A_0^{\bullet -}$ via A_1 to the [4Fe-4S] clusters can be measured. The AQ incorporation in the A_1-binding site of PS I was realized in two ways: in either the presence or absence of the [4Fe-4S] clusters. As described before, organic solvent extraction of PhQ and reincubation were used to obtain PS I particles with AQ in the A_1-binding site in the presence of [4Fe-4S] clusters while quinone substitution in PS I isolated from the *menB rubA* double mutant yielded PS I with AQ in the A_1-binding site without [4Fe-4S] clusters (with the possibility to reconstitute the F_X afterwards). In the previous chapter it was shown that the orientation and other magnetic interaction properties of AQ in both PS I samples are the same as those of PhQ in the wild type. In order to investigate the ET kinetic properties of AQ in the A_1-binding site of PS I, TR EPR experiments were performed in the high temperature range (160 - 290 K). The correlation between the rates of the two forward ET steps from $A_0^{\bullet -}$ to A_1 to [4Fe-4S] clusters and the redox potential of AQ can be studied. Additionally, the absence of [4Fe-4S] clusters and reconstitution of F_X in the *menB rubA* double mutant gives a new possibility to investigate the predicted effect of the partial negative charge of the first [4Fe-4S] clusters F_X on the forward ET step from $A_0^{\bullet -}$ to A_1.

7.2. Results

7.2.1. Characterisation of spin polarisation pattern of the consecutive $P_{700}^{\bullet+}A_1^{\bullet-}$ and $P_{700}^{\bullet+}(FeS)^-$ RP states at 230 K

The TR EPR measurements at high temperature give access to the ET kinetics from $A_1^{\bullet-}$ to the [4Fe-4S] clusters. For native PS I, two consecutive spin polarization patterns due to the consecutive $P_{700}^{\bullet+}A_1^{\bullet-}$ and $P_{700}^{\bullet+}(FeS)^-$ RP states are observed at temperatures above 220 K [129]. Although sequential ET past $A_1^{\bullet-}$ to F_X to F_A and to F_B is well established [87, 130, 131], the kinetics of the individual ET steps are not. Therefore, the notation (FeS) leaves open which of the three [4Fe-4S] clusters is reduced while the polarisation pattern is observed in the available time window. With most non-native NQs and PQ-9 in the A_1-binding site of PS I, forward ET past the quinone is slower than the decay-limiting relaxation of the spin polarization and therefore only the first $P_{700}^{\bullet+}A_1^{\bullet-}$ RP state is observed [74]. In contrast, with AQ in the A_1-binding site of PS I, two sequential spectra are observed in the whole temperatures range from 160 to 295 K and the lifetime of the early spectrum is close to or longer than the spectrometer rise time. This is demonstrated in Figure 7.1, which shows TR EPR spectra and transients for (a) PhQ and (b) AQ in the A_1-binding site of the extracted PS I at 230 K. The spectra (top) are taken at early (solid curves) and late times (dashed curves) and are attributed to the $P_{700}^{\bullet+}A_1^{\bullet-}$ and $P_{700}^{\bullet+}(FeS)^-$ RP states, respectively. The transients (bottom) are shown for selected field positions indicated by arrows under the spectra (top). With PhQ in the A_1-binding site, the E/A/E polarization pattern of $P_{700}^{\bullet+}PhQ^{\bullet-}$ RP state dominates the spectrum at early time while at late time a mainly E spectrum due to the $P_{700}^{\bullet+}$ part of the $P_{700}^{\bullet+}$ $(FeS)^-$ RP state is observed. With AQ in the A_1-binding site, two sequential RP spectra are observed as well, but the respective spin polarization patterns have changed drastically. At early times an E/(A)/A pattern is found with a spectral width consistent with that of the $P_{700}^{\bullet+}AQ^{\bullet-}$ RP state while an E/A pattern in the $P_{700}^{\bullet+}$ region is observed at late times. These drastic changes in the spin polarisation patterns will be interpreted later as the result of spin dynamics due to the lengthened lifetime in the precursor $P_{700}^{\bullet+}A_0^{\bullet-}$ RP state. The ET kinetics from $AQ^{\bullet-}$ to F_X will be considered first.

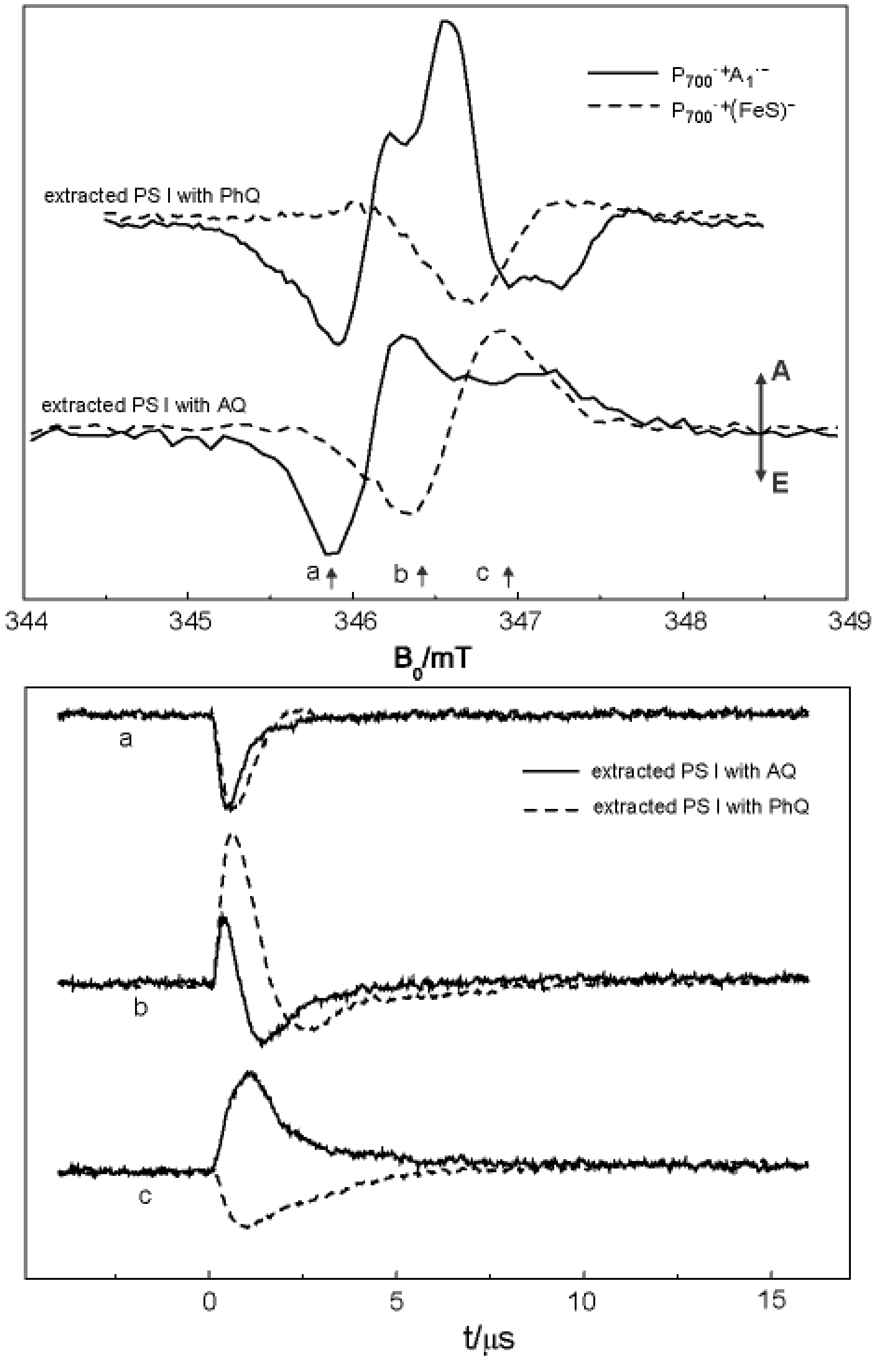

Figure 7.1. Top: X-band TR EPR spectra of the two sequential $P_{700}^{\bullet+}A_1^{\bullet-}$ (solid line) and $P_{700}^{\bullet+}(FeS)^-$ (broken line) RP states in the extracted PS I with PhQ and AQ reconstituted into the A_1-binding site at 230 K. Integration window for early and late signal: 250 – 500 ns and 2 – 2.75 μs for the extracted PS I with PhQ, 200 – 325 ns and 1.75 – 2.50 μs for the extracted PS I with AQ.

Bottom: Selected transient EPR kinetic traces of the extracted PS I with PhQ (dashed lines) and the extracted PS I with AQ (solid line) in the A_1-binding site. Field positions (a-c) at which the transients were taken are indicated by arrows labelled a, b, c below the spectra in top figure.

7.2.2. Determination of ET kinetics from $AQ^{\bullet -}$ to F_X

At the field position marked by arrow a in Figure 7.1 (top), there is no significant contribution from $P_{700}^{\bullet +}$; the transient signal is attributed to $A_1^{\bullet -}$ only. The time constants associated with the decay curves for this position shown in Figure 7.1 (bottom), are primarily due to forward ET from $A_1^{\bullet -}$ to F_X, with a possible minor contribution due to spin relaxation. The ET kinetics is also reflected in the transients at the other field positions b, c, but the behaviour is more complicated because contributions from both $P_{700}^{\bullet +}A_1^{\bullet -}$ and $P_{700}^{\bullet +}(FeS)^-$ RPs overlap. From the comparison of the transients, it is immediately evident that the decay of the quinone contribution is much faster in the extracted PS I sample reconstituted with AQ than with PhQ. A fit of all transients shown in Figure 7.1 (bottom, a), using the procedure described in Chapter 3, revealed that forward ET from $AQ^{\bullet -}$ to F_X is about 125 ns at 230 K while ET from $PhQ^{\bullet -}$ to F_X in the wild type is much slower and cannot be evaluated properly at this temperature because the decay is already dominated by spin relaxation (~ 3 µs). Since the ET from $PhQ^{\bullet -}$ to F_X in the wild type is known to be thermally activated with activation energy E_a = (220 ± 20) meV [1], the temperature dependence of ET in samples of the extracted PS I reconstituted with AQ is of interest.

7.2.3. Temperature dependence of forward ET kinetics from $AQ^{\bullet -}$ to F_X

For PS I reconstituted with AQ, the temperature dependence of forward ET from $A_1^{\bullet -}$ to F_X could be followed between 160 and 240 K. At higher temperatures it is folded with the spectrometer response function but nonetheless clearly observable in the data up to 298 K. (A complementary room temperature TR EPR experiment was performed by Prof. Art van der Est at Brock University, Canada.) Figure 7.2 shows the spectra of the $P_{700}^{\bullet +}A_1^{\bullet -}$ and $P_{700}^{\bullet +}(FeS)^-$ RPs state btained by fitting a kinetic model to the transients and plotting the field dependence of the amplitudes associated with each of the kinetic components. It was done for the whole set of temperatures between 160 and 240 K. Below 160 K, the ET rate becomes too slow to compete with the spin relaxation rate, only an upper rate limit can be given. The ET lifetimes (1/k) obtained from the fit are listed in Figure 7.2 and are plotted in Figure 7.3 (filled dots) as the natural logarithm *lnk* of the ET rate versus the inverse temperature 1/T (*Arrhenius*

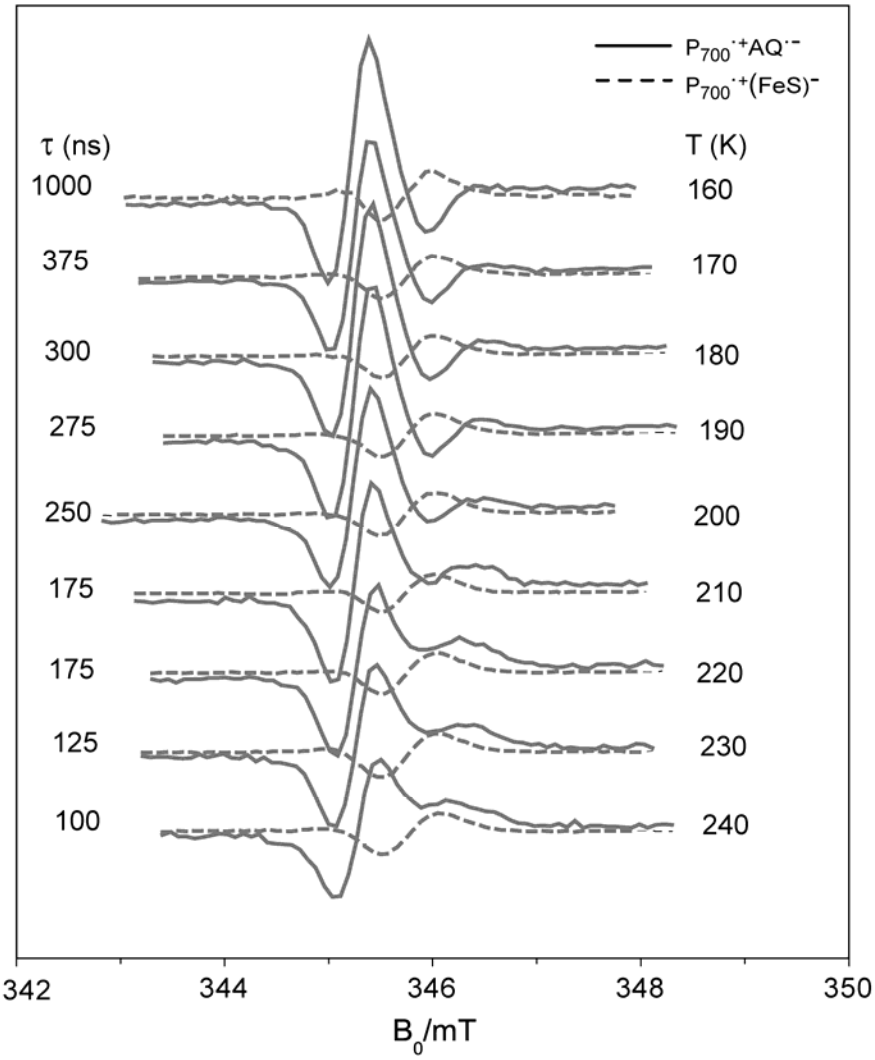

Figure 7.2. Kinetically separated TR EPR spectra of the extracted PS I with AQ reconstituted in the A_1-binding site of PS I, at different temperatures in 10 K steps between 160 (top) and 240 K (bottom). Solid line spectra correspond to the $P_{700}^{\bullet+}AQ^{\bullet-}$ RP state (early signal), dashed line spectra correspond to the $P_{700}^{\bullet+}(FeS)^{\bullet-}$ RP state (late signal).

plot). For comparison, Figure 7.3 also includes corresponding data for native PhQ (open circles at 260 and 295 K). The solid lines are the temperature dependences of the two kinetic phases observed in the transient absorption difference data for PS I complexes isolated from the wild type [1]. As can be seen in Figure 7.3, the TR EPR and optical data for native PS I agree quite well for the optical "slow" phase (open circles, lower solid line).

Concerning ET from $AQ^{\bullet-}$ to F_X, Figure 7.3 reveals two main features:

i) The ET rate is faster than the dominant "slow" component in native PS I by close to an order of magnitude.

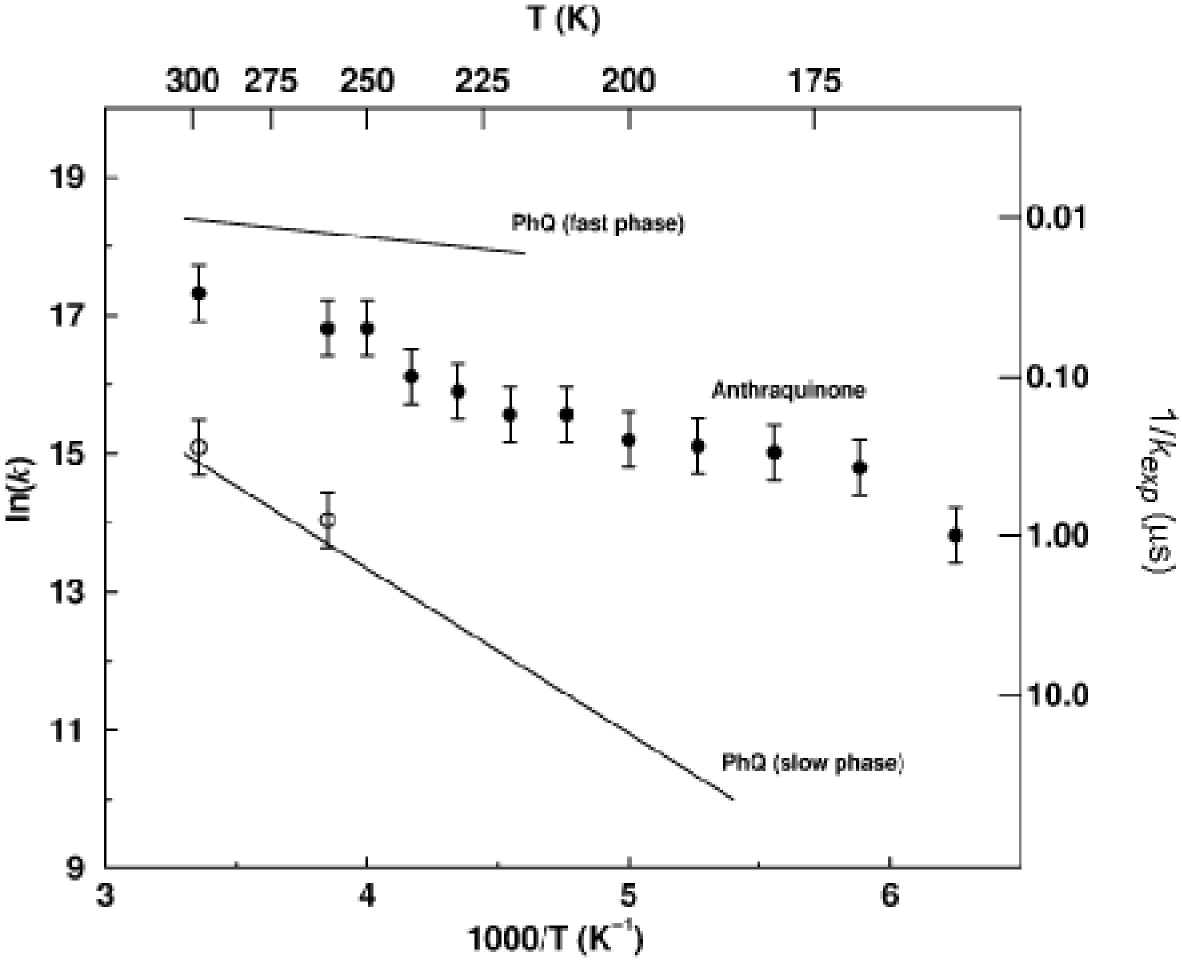

Figure 7.3. *Arrhenius plot* (ln k *versus* 1/T) of the ET rate from $AQ^{\bullet -}$ to F_X in the extracted PS I with AQ in the A_1-binding site of PS I. The rates are obtained from the kinetic separation procedure used for Figure 7.2. For comparison, data reported for the same ET step in PS I isolated from the wild type are included as straight lines based on the evaluated activation energy E_a = (220 ± 20) meV for *Thermosynechococcus elongatus*. The two solid points represent ET rates evaluated from TR EPR data for the wild type at selected temperatures (295 – 260 K).

ii) The ET can be followed down to much lower temperatures than for native PS I because the rate is faster and shows a lesser temperature dependence (at least below 240 K).

7.2.4. Evidence of altered forward ET from $A_0^{\bullet -}$ to AQ

In a series of consecutive RPs, the polarization pattern of an observed RP is sensitive to any singlet-triplet mixing and altered spin axis orientations in all proceeding RPs. Because the duration of spin dynamics evolution may depend on the lifetimes of the individual RPs, changes in the ET kinetics can be reflected in the spin polarisation pattern. Therefore, with the lifetime of the precursor $P_{700}^{\bullet +}A_0^{\bullet -}$ RP state the spectral patterns of the $P_{700}^{\bullet +}A_1^{\bullet -}$ and $P_{700}^{\bullet +}(FeS)^{-}$ RP states can be expected to change with temperature. However, in native PS I such changes are not observed because the first $P_{700}^{\bullet +}A_0^{\bullet -}$ RP state is too short-lived (less than 0.5 ns) for any significant triplet character to develop during its lifetime while $P_{700}^{\bullet +}A_1^{\bullet -}$ is long lived and full singlet-triplet mixing evolves within its lifetime. For the extracted PS I reconstituted with AQ, the spin polarisation pattern of the $P_{700}^{\bullet +}A_1^{\bullet -}$ RP state is temperature dependent, as shown in Figure 7.2. Moreover the E/A spin polarisation pattern of the third $P_{700}^{\bullet +}(FeS)^{-}$ RP state in the extracted PS I with AQ is different from the net E pattern for PS I with PhQ (Figure 7.1, top). Both of these observations suggest that singlet-triplet mixing during the lifetime of $P_{700}^{\bullet +}A_0^{\bullet -}$ RP state is likely to determine the spin polarization patterns. According to the theoretical investigation, such an effect becomes observable when the lifetime in the precursor $P_{700}^{\bullet +}A_0^{\bullet -}$ RP state is longer than 0.5 ns, i.e. comparable with the time constant associated with the inverse interaction strength responsible for singlet-triplet mixing [64, 95, 132, 133]. As it will be demonstrated in Chapter 9 more explicitly, the time constant of the first $P_{700}^{\bullet +}A_0^{\bullet -}$ RP state in the 0.5 to 5 ns time range will cause the following qualitative changes in the spin polarisation pattern of the subsequent $P_{700}^{\bullet +}A_1^{\bullet -}$ RP state: i) increased A polarization in the up-field range of a spectrum; ii) complemented by a decrease of the net absorptive peak in the center of spin polarisation pattern. Both these features are seen to become more amplified with increasing temperature (Figure 7.1). Most easily, the observed changes in the spin polarisation pattern are expected with an increase of the lifetime in the precursor $P_{700}^{\bullet +}A_0^{\bullet -}$ RP state. However, increasing lifetime with increasing temperature is highly counterintuitive. One way to explain the uncommon temperature dependence of the spin polarisation pattern is to postulate a broad distribution of the lifetimes for the $P_{700}^{\bullet +}A_0^{\bullet -}$ RP state and a width that increases with temperature. Then, for example, the polarisation determining time window (0.5 - 5.0 ns) would fall into the long-lifetime wing of the distribution and the area underneath could increase; the maximum of the distribution could even shift to shorter average lifetimes with increasing temperature. Such a model has been already employed to explain a comparable effect in the A_0 mutants of PS I [75, 134]. However, there is also evidence for such a distribution in unmodified bRC [135]. Therefore, the observed spin polarisation patterns can be approximated as the weighted sum of two limiting spectra $S(B_0)_{slow}$ and $S(B_0)_{fast}$ [134]:

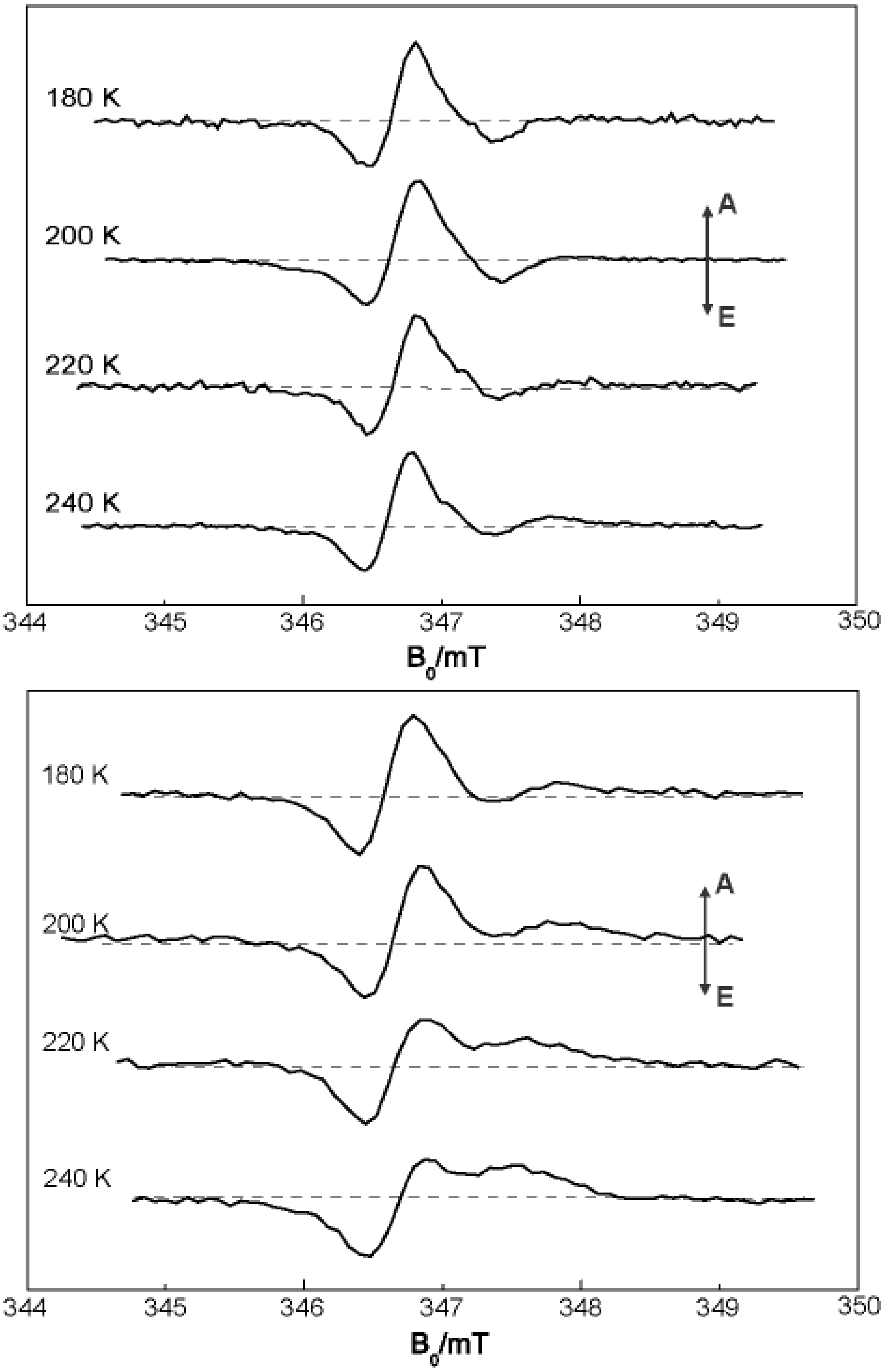

Figure 7.4. Comparison of the second $P_{700}^{\bullet +}AQ^{\bullet -}$ RP state spectra in an early time window at X-band at four temperatures in 20 K steps between 180 K and 240 K. AQ is reconstituted into the A_1-binding site of either PS I of the *menB rubA* double mutant (top) or extracted PS I (bottom). Integration window: 250 – 750 ns and 200 – 325 ns for the *menB rubA* double mutant and extracted PS I, respectively. Dashed lines indicate the baseline level and provide the reference for sign and amplitude of polarisation (A or E) across the spectrum.

$$S(B_0,T) = X(T)S(B_0)_{slow} + (1-X(T))S(B_0)_{fast} \qquad (7.1.)$$

where the weighting factor X(T) is a fraction of RCs with slow spin-mixing time in the first $P_{700}^{\bullet +}A_0^{\bullet -}$ RP. $S(B_0)_{slow}/S(B_0)_{fast}$ correspond to the limiting spectra in which the lifetime of the second $P_{700}^{\bullet +}A_0^{\bullet -}$ RP is sufficiently short/long for complete singlet-triplet mixing. Note that the parameter X(T) is temperature dependent. Therefore, the temperature is interpreted as a result of the change in the relative weighting factors of the two limiting cases.

7.2.5. Effect of negative charge of the first [4Fe-4S] cluster F_X on ET kinetics from $A_0^{\bullet -}$ to AQ

As was shown in Chapter 6, near complete AQ incorporation is also possible in PS I complex isolated from the *menB rubA* double mutant missing all [4Fe-4S] clusters. It provides an elegant way to investigate the effect of presence/absence of the [4Fe-4S] clusters on the kinetics of the $A_0^{\bullet -}$ to A_1 ET step, i.e. on the driving energy (ΔG), which is the $A_0^{\bullet -}/A_0$ and $A_1^{\bullet -}/A_1$ redox potential difference. Figure 7.4 shows a comparison of TR EPR spectra of the second $P_{700}^{\bullet +}A_1^{\bullet -}$ RP state in PS I from the *menB rubA* double mutant without [4Fe-4S] clusters substituted with AQ (top) and in the solvent extracted PS I reconstituted with AQ (bottom). Comparison of the spectra from the two samples shows that the effects attributed to singlet-triplet mixing in the precursor $P_{700}^{\bullet +}A_0^{\bullet -}$ RP state are much less pronounced in the *menB rubA* double mutant (top). Indeed, the spectrum from the *menB rubA* double mutant at 240 K (top) is comparable to the low temperature pattern at 180 K (bottom). This result implies that the slowing of forward ET through $A_0^{\bullet -}$ is more pronounced when the [4Fe-4S] clusters are present. It is important to point out that a control experiment, in which the extracted PS I is incubated with native PhQ, confirms that the quinone extraction procedure has no influence on the ET kinetics (Figure 7.1). The differences between the samples shown in Figure 7.4 would be expected if the quinone redox potential was more negative in the presence of the [4Fe-4S] clusters. This is consistent with the fact that the $[4Fe4S(SCH_3)_4]$ moiety has the formal charge 2-. Although the formal charge is most probably compensated to a large extent in the protein framework, some contribution to the local electrostatic environment is expected to remain effective and this can cause the quinone redox potentials in the A_1-binding site of PS I to be more negative than in the absence of the [4Fe-4S] clusters. Hence, the effective redox potential of AQ in the A_1-binding site of PS I is expected to be more positive (i.e. closer to that of PhQ) when the [4Fe-4S] clusters are absent.

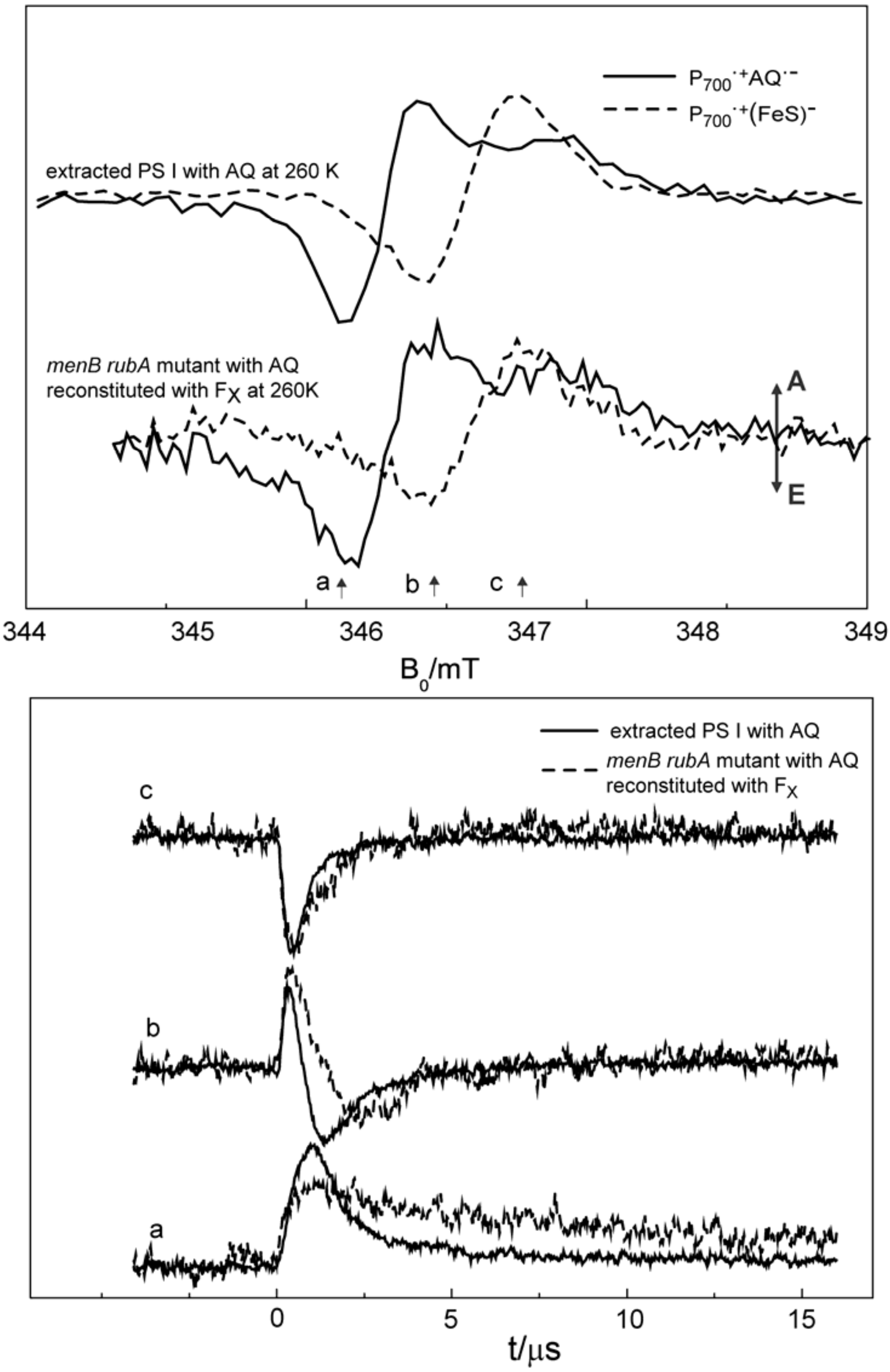

Figure 7.5. Top: X-band TR EPR spectra of the two sequential $P_{700}^{\bullet+}AQ^{\bullet-}$ (solid line) and $P_{700}^{\bullet+}(FeS)^{-}$ (broken line) RP states in the extracted PS I with and without F_X at 260 K. Integration window for early and late signal: 200 – 500 ns and 2.25 – 3.00 μs for the extracted PS I with PhQ, 200 – 325 ns and 1.75 – 2.50 μs for the extracted PS I with AQ.

Bottom: Selected transient EPR kinetic traces of the extracted PS I with PhQ (dashed lines) and AQ (solid line) in the A_1-binding site. Field positions (a-c) at which the transients were taken are indicated by arrows labelled a, b, c below the spectra in top figure.

The proposed interpretation in terms of an electrostatic contribution from the [4Fe-4S] clusters was tested experimentally by reconstituting the first [4Fe-4S] cluster F_X into the *menB rubA* double mutant. Figures 7.5 (top) shows a comparison of TR EPR spectra for the two samples at 260 K: extracted PS I with AQ and *menB rubA* double mutant with AQ in the A_1-binding site and reconstituted with F_X. The changes in the spin polarisation pattern of the early $P_{700}^{\bullet+}AQ^{\bullet-}$ and late $P_{700}^{\bullet+}(FeS)^-$ RP states show the same tendency in both samples. For comparison, they are much more different in Figure 7.1. This provides support for the notion that the spectral changes for the $P_{700}^{\bullet+}AQ^{\bullet-}$ RP state become more pronounced in the presence of F_X than in its absence. While the TR EPR spectra are similar in both samples, the transients differ substantially from each other (Figure 7.5, bottom). Such a difference can be attributed to the absence of F_X in some RCs in the F_X reconstituted sample. A partial lack of F_X in some RCs will affect the time course of the transients: in the transient section associated with the ET process, in particular at field position a and b, a longer component is expected to be observed because the ET time constant lengthens beyond the relaxation time when the F_X cluster is missing. Fitting the transients with the same time constant for ET from $AQ^{\bullet-}$ to F_X determined for the extracted PS I with AQ suggests that only about 30 % of the F_X-sites remain unoccupied in the F_X reconstituted samples. An additional experiment on the *rubA* single mutant (with PhQ in the A_1-binding site) reconstituted with F_X revealed that about 70 % of the F_X sites could be occupied with the applied reconstitution procedure. Within experimental accuracy the degree of F_X reconstitution reached about 70 % in both cases.

7.3. Conclusions of TR EPR study of PS I reconstituted with AQ

The results presented above show that when the native PhQ in PS I complex is replaced with AQ, the following effects are observed:

i) The rate of forward ET from $AQ^{\bullet-}$ to F_X is increased by about an order of magnitude.

ii) The observed changes in the spin polarization pattern of the $P_{700}^{\bullet+}AQ^{\bullet-}$ RP state are consistent with the expectation that significant triplet character can evolve during the lifetime of the primary $P_{700}^{\bullet+}A_0^{\bullet-}$ RP state.

Assuming that singlet-triplet mixing can evolve in the primary $P_{700}^{\bullet+}A_0^{\bullet-}$ RP , it is clear that ET from $A_0^{\bullet-}$ to AQ has to be slower (1 – 2 ns) than from $A_0^{\bullet-}$ to PhQ (50 ps) in native PS I. All results are consistent with idea that a shift of the quinone redox potential to a more negative value results in a slowing of the first ET step from $A_0^{\bullet-}$ to AQ while the second step from $AQ^{\bullet -}$ to F_X is accelerated. It can be easily rationalized by application of Marcus theory.

7.4. Application of Marcus theory for qualitative estimation of the altered quinone redox potential

Marcus theory expresses the rate *k* of a non-adiabatic ET reaction as [136]:

$$k = \frac{2\pi |V|^2}{\hbar\sqrt{4\pi\lambda k_B T}} exp\left[\frac{-(\Delta G + \lambda)^2}{4\lambda k_B T}\right] \tag{7.2}$$

where *V* is the electronic coupling between the initial electron donor and final acceptor state. In general, it is assumed that *V* decreases exponentially ($|V|^2 \sim e^{-2\beta R}$) with the edge-to-edge distance *R* between the reactants, weighted by an empirical β-factor. λ is the reorganisation energy and ΔG is the standard Gibbs free energy (driving force) of the ET reaction. A plot of *log k* versus ΔG gives an inverted parabola with its maximum at $-\Delta G = \lambda$. In PS I, the most extensive set of data from which the *Marcus curve* has been constructed is for the ET process from $A_0^{\bullet -}$ to A_1. Itoh and co-workers incorporated a series of acceptors into PhQ extracted PS I complexes and followed the kinetics using absorbance difference spectroscopy [41]. In order to determine the free energy ΔG between A_0 and A_1 in PS I, redox potential of A_0 was fixed the same for each acceptor and redox potential of the acceptors in the A_1-binding site was calculated by the same shift from their values in DMF [42]. The acceptors were chosen so that the ΔG values would cover a range of about 600 meV above and below the value estimated for native PS I [42]. Consistent with Eqn. (7.2), the experimental plot of log *k* vs. ΔG gave an inverted parabolic shape and the optimal barrier-free rate of about $(25 \text{ ps})^{-1}$ was found for native PhQ in the A_1-binding site of PS I. The redox potential of AQ is estimated to be about 100 meV more negative than PhQ. However, based on this result a shift of about 100 meV in ΔG from the value for PhQ would not result in a significant change in the rate. Furthermore, the effect of a change in ΔG on the rate depends critically on the shape of the *Marcus curve* and a shift of about 350 meV slows the rate by nearly three orders of magnitude. At the steepest point on the *Marcus curve* in [41, 42] a change of 70 meV in ΔG results in a 260-fold change in the rate. From this, it can be seen that a relatively narrow distribution of ΔG values around that expected for AQ could indeed lead to the very broad distribution of rates proposed to explain the temperature dependence of the observed spin polarization patterns. Such distribution would also reconcile the optical [41, 42] and EPR data which show picosecond and nanosecond $P_{700}^{\bullet+}A_0^{\bullet-}$ lifetimes, respectively for acceptors with redox potentials similar to AQ.

One way to understand the observed faster ET rate from $AQ^{\bullet-}$ to F_X is as resulting from the lowering of the quinone redox potential. The following approach was taken: i) the absolute rates were calculated for selected temperature according to the Eqn. 7.2; ii) corresponding ΔG values were compared with ΔG values of the wild type. Before calculating the absolute rates, the optimal rate is required. Based on reasonable parameter ranges, the experimentally determined $A_1^{\bullet-}$ to F_X ET rate of $(250\ \text{ns})^{-1}$ at room temperature (295 K) and the activation energy $E_a = (220 \pm 20)$ meV, the reorganisation energy was evaluated to be in the range from 0.8 to 1.1 eV, which corresponds to the optimal rate of $k_{opt} \sim 2\cdot10^{10}\ \text{s}^{-1}$ [120]. Note, this result (temperature dependence of $PhQ^{\bullet-}$ to F_X ET rate) does not depend strongly on the ΔG value since it is small (in the range from +0.06 to -0.11 eV) compared to reorganisation energy (Table 7.1). Using the empirical relation $\log k_{opt} = 15 - 0.6R$ the optimal rate corresponds to the edge-to edge distance $R \sim 8$ Å, which is in satisfactory agreement with the distance evaluated from the X-ray model [4]. The ΔG value required to reproduce the observed rates for the $AQ^{\bullet-}$ to F_X ET between 240 and 260 K was estimated to be in the range from -0.09 to 0.28 eV for reorganisation energy between 0.8 and 1.1 eV, respectively (Table 8.1). This can be compared with ΔG value of the $PhQ^{\bullet-}$ to F_X ET rate in wild type from 0.06 to 0.12 eV (Table 8.1). Thus, this calculation is in good agreement with the expected value of approximately -0.15 eV based on the redox potential difference of AQ and PhQ in DMF [42, 108, 128].

Qualitatively the change in the quinone redox potential is demonstrated in the Figure 7.6. Also, with the range of values for the reorganisation energy given in Table 7.1, the estimate of ΔG values leads to the activation energy E_a in the range of 80 - 180 meV, which is compatible with the *Arrhenius slope* above 240 K. However, careful examination of Figure 7.3 shows that the slope of AQ data is probably smaller below 240 K than above. Such behaviour is not surprising, since PS I in aqueous solution undergoes a transition to a disordered solid at approximately this temperature, depending on the composition of the medium [1]. For glass point T_g it is around 190 K in a 50 %/50 % mixture and is lower for higher glycerol concentration. For the wild type, it is not clear whether a change in slope occurs below the glass point, because there are not any optical and EPR data available for this

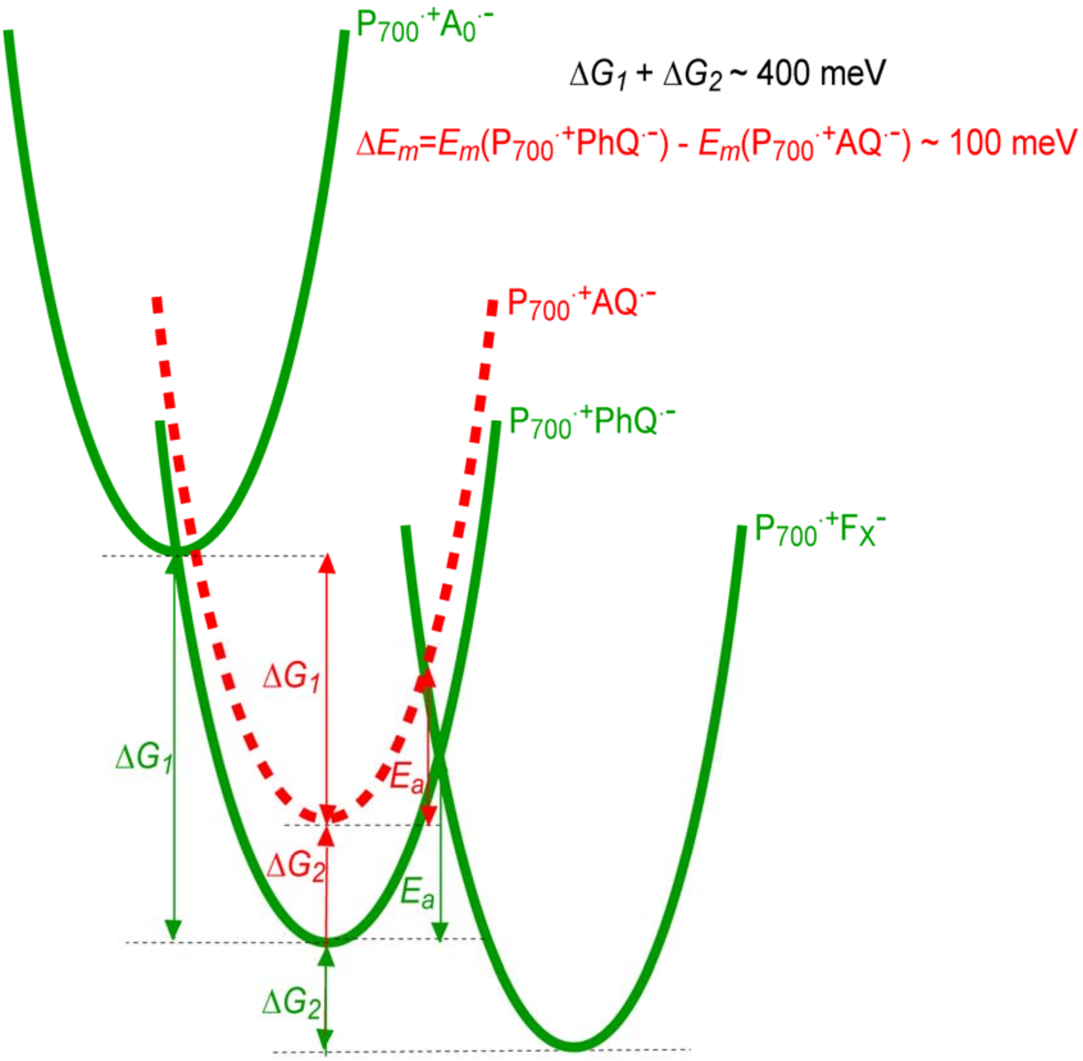

Figure 7.6. The scheme of parabolic redox potential curves along the reaction coordinate (according to Marcus theory) is used to illustrate the predominant potential down-shift due to the more negative redox of AQ.

Table 7.1. ET parameters in PS I.

ET step	ΔG (eV)	λ (eV)	V (eV)	$(k_{opt})^{-1}$	$(k_{exp})^{-1}$	
					295 K	260 K
$A_0^{\bullet -}$ to A_1	-0.34	0.34 eV	0.0017	~25 ps [42]	-	-
$PhQ^{\bullet -}$ to F_x	+0.06 – -0.12	0.8-1.1	0.001	~50 ps [1]	280 ns	840 ns
$AQ^{\bullet -}$ to F_x	-0.09 – -0.28	0.8-1.1	0.001	-	< 50 ns	~ 50 ns

region. For AQ, the lower slop below 240 K is consistent with the expectation that the reorganisation energy should be lower in a more rigid medium.

In summary, this is the first example where the transient EPR signal of the $P_{700}{}^{\bullet+}AQ^{\bullet-}$ state carries information on the two consecutive ET steps from $A_0{}^{\bullet-}$ to AQ to F_X. The kinetic behaviour from $A_0{}^{\bullet-}$ via AQ to F_X can be rationalized in terms of classical Marcus theory and a shift of the quinone redox potential by about 100 meV to more negative value.

8. Contributions of the Distant Protein Environment to the Redox Potential of Phylloquinone and the First [4Fe-4S] Cluster in PS I

The object of this study is to investigate the contributions of the distant electrostatic protein environment to the redox potential of PhQ and the first [4Fe-4S] cluster F_X. Electrostatic calculations predict that the partial negative charges associated with a particular aspartate residue play a significant role in modulating the redox potentials of A_{1A}, A_{1B} and F_X [110]. To test this prediction, the aspartate $D575_{PsaB}$ and $D566_{PsaB}$ residues were targeted for mutation. The negatively charged aspartate was replaced with neutral alanine (A) and positively charged lysine (K). Multifrequency TR EPR was applied to measure the ET kinetics from $A_1^{\bullet -}$ to F_X in these variants.

8.1. Motivation

In the previous chapters, the central question concerns the origin of the highly negative quinone redox potential in the A_1-binding site of PS I. Quinone substitution studies as described in Chapter 7 and [74] show that the molecular properties of the quinone (one or multiple rings, different derivatives and etc.) contribute to a minor extent to their redox in the

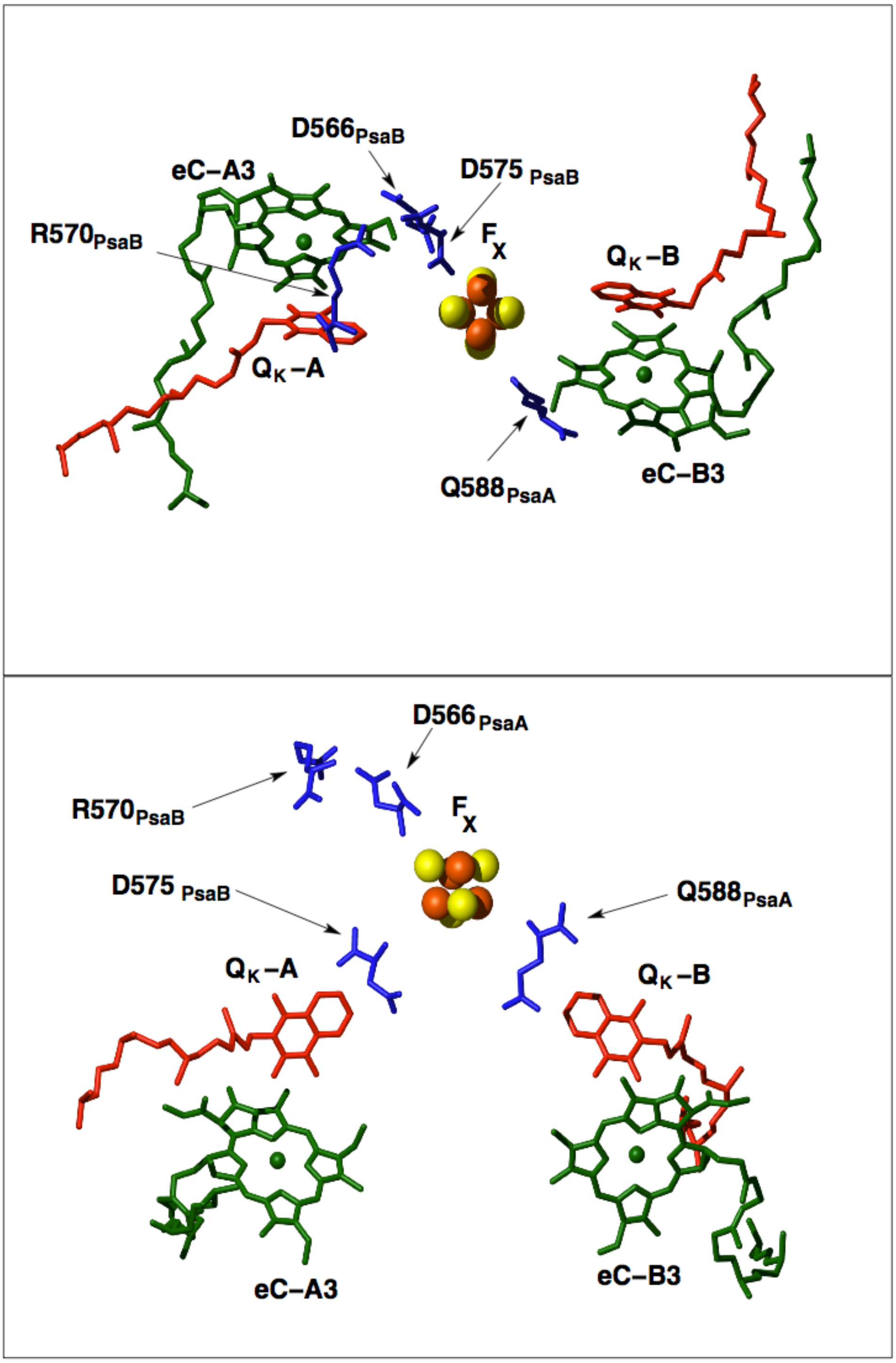

Figure 8.1. The arrangement of the cofactors in PS I in the region of the electron acceptors A_{1A}, A_{1B} and F_X shown from two perspectives. The location of the residues D575$_{\text{PsaB}}$, D566$_{\text{PsaB}}$, R570$_{\text{PsaB}}$ and Q588$_{\text{PsaA}}$ are also indicated. The first two of these residues were targeted for mutation while Q588$_{\text{PsaA}}$ is the residue in PsaA that is analogous to D575$_{\text{PsaB}}$ in PsaB. The top panel is a view from the stromal side of the complex along the membrane normal. The bottom panel is a view along a direction approximately perpendicular to the membrane normal. In both cases the PsaA-branch of cofactors is on the left and the PsaB-branch is on the right. Here A_{1A}, A_{1B} are denoted as O_K-A, O_K-B, and A_{0A}, A_{0B} as eC-A3, eC-B3, respectively.

A_1-binding site of PS I. This is a clear indication that the main contributions to the quinone redox potential come from the protein environment. Several spectroscopic techniques including TR EPR and TR optical spectroscopy have been used to study the influence of specific amino acids which are directly involved in protein-cofactor interactions along the putative ET pathway from $A_0^{\bullet-}$ through A_1 to F_X [34, 137-140]. The striking result with such site-specific mutations was that alteration of the supposedly critical amino acids had only a modest effect on the ET rate from $A_{1A}^{\bullet-}$ (“slow” kinetic phase) and $A_{1B}^{\bullet-}$ (“fast” kinetic phase) to F_X [35, 138, 139], despite the fact that their side groups are in direct van-der-Waals contact with PhQ.

The main goal of this study is to test the hypotheses from electrostatic calculation, the role of the PsaB-specific aspartate $D575_{PsaB}$ residue in the modulating of redox potential of A_1. It is expected that the changes in the identity of the side chain must affect the driving force (or redox potential difference between A_1 to F_X) of the $A_1^{\bullet-}$ to F_X ET. As the consequence the change in the $A_1^{\bullet-}$ to F_X ET rate can be seen by TR EPR. To generate the largest possible range of differences, the aspartate residue has been changed to alanine with a neutral side chain and to lysine with a side chain that is positively charged at the appropriate pH. In addition, the aspartate $D566_{PsaB}$ residue was also targeted for mutagenesis. The $D566_{PsaB}$ residue is involved in salt-bridges to $R65_{PsaC}$ and $K51_{PsaC}$ and hence its negative charge is compensated in the wild type [115]. Its replacement with alanine and lysine residues is expected to leave uncompensated positive charges on both $R65_{PsaC}$ and $K51_{PsaC}$. Because $D566_{PsaB}$ is located at the stromal surface and at a considerable distance from either A_{1A} or A_{1B}, the uncovering of these positive charges should affect primarily the redox potential of F_X. The positions of the $D575_{PsaB}$ and $D566_{PsaB}$ residues with respect to the ET acceptor A_{1A}/A_{1B} and F_X are shown in Figure 8.1 as suggested in the X-ray structure model (pdb entry 1JB0) [3, 4]. The experimental kinetics results will be compared with more detailed electrostatic calculations that take into account the influence of $D575_{PsaB}$ and $D566_{PsaB}$ on the redox potential of F_X as well as A_{1A} and A_{1B}.

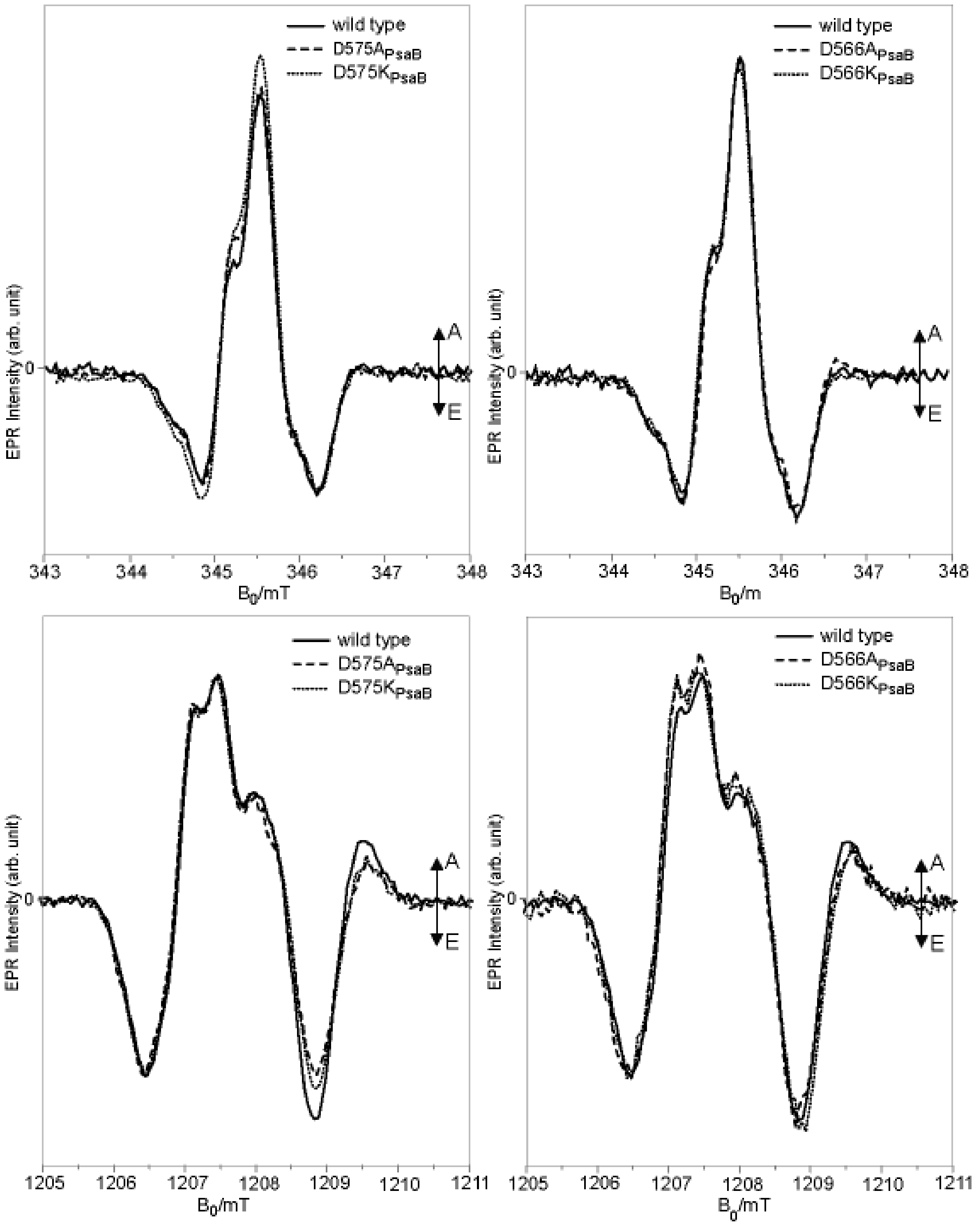

Figure 8.2. Comparison of TR EPR spectra at X-band (top) and Q-band (bottom) for the second $P_{700}^{\bullet+}A_1^{\bullet-}$ RP state of PS I isolated from the wild type, D575$_{PsaB}$ (left) and D566$_{PsaB}$ (right) mutants in frozen solution at 80 K. The spectra were integrated in the time windows 200 –1500 ns (X-band) and 500-1500 ns (Q-band). Left: PS I trimers isolated from the wild type (solid line), D575A$_{PsaB}$ (broken line) and D575K$_{PsaB}$ (dotted line) mutants. Right: PS I trimers isolated from the wild type (solid line), the D566A$_{PsaB}$ (broken line) and D566K$_{PsaB}$ (dotted line) mutants.

8.2. Results

8.2.1. Characterisation of X- and Q-band spin polarised TR EPR spectra of the second $P_{700}^{\bullet+}A_1^{\bullet-}$ RP state in the aspartate variants at 80 K

Since the spin polarization pattern of the $P_{700}^{\bullet+}A_1^{\bullet-}$ RP state is sensitive to the orientation and spin density distribution of the quinone radical-ion [37, 61, 129], it provides a good test of the structural integrity of the A_{1A}-binding site after a change has been introduced in the environment. Because the Asp residues targeted for mutation are located sufficiently distant from A_1 (~ 9 Å or more), only minor alterations are expected in the structural integrity of the A_1-binding sites. Figure 8.2 shows X- and Q-band TR EPR spectra of the second $P_{700}^{\bullet+}A_1^{\bullet-}$ RP state for PS I isolated from the $D575A_{PsaB}$, $D575K_{PsaB}$, $D566A_{PsaB}$, $D566K_{PsaB}$ mutants as well as the corresponding wild type spectra taken in frozen solution at 80 K. The overall spin polarization patterns for both sets of variants are highly similar to the wild type. Thus, changes in the nature of the side chain at position 575_{PsaB} and 566_{PsaB} do not induce any significant alterations in either the orientation of the quinone or in the spin density distribution over the quinone ring.

8.2.2. Analysis of ET rate from $A_1^{\bullet-}$ to F_X in the aspartate variants at 260 K

As it was shown in Chapter 7, TR EPR measurements at high temperature give access to the ET kinetics from $A_1^{\bullet-}$ to F_X. Figure 8.3 compares TR EPR spectra and transients at 260 K of PS I isolated from the wild type with those from the two sets of mutants: $D575A_{PsaB}$, $D575K_{PsaB}$ (top) and $D566A_{PsaB}$, $D566K_{PsaB}$ (bottom). The transients are shown for selected field positions as indicated in the spectra at the left in Figure 8.3. As the electron is transferred from $A_1^{\bullet-}$ to F_X, the E/A/E spin polarization pattern of $P_{700}^{\bullet+}A_1^{\bullet-}$ changes to one with the net E, which results from the $P_{700}^{\bullet+}$ contribution in the $P_{700}^{\bullet+}(FeS)^-$ spectrum. The spin polarization patterns of the $P_{700}^{\bullet+}A_1^{\bullet-}$ and $P_{700}^{\bullet+}(FeS)^-$ RP states in the variants are almost identical to those in the wild type. As is evident from the kinetic traces, the $A_1^{\bullet-}$ to F_X ET kinetics in the $D575_{PsaB}$ and $D566_{PsaB}$ variants are not much different from the wild type (Figure 8.3, top). The overall trend is most clearly evident at position b: the slowing of the

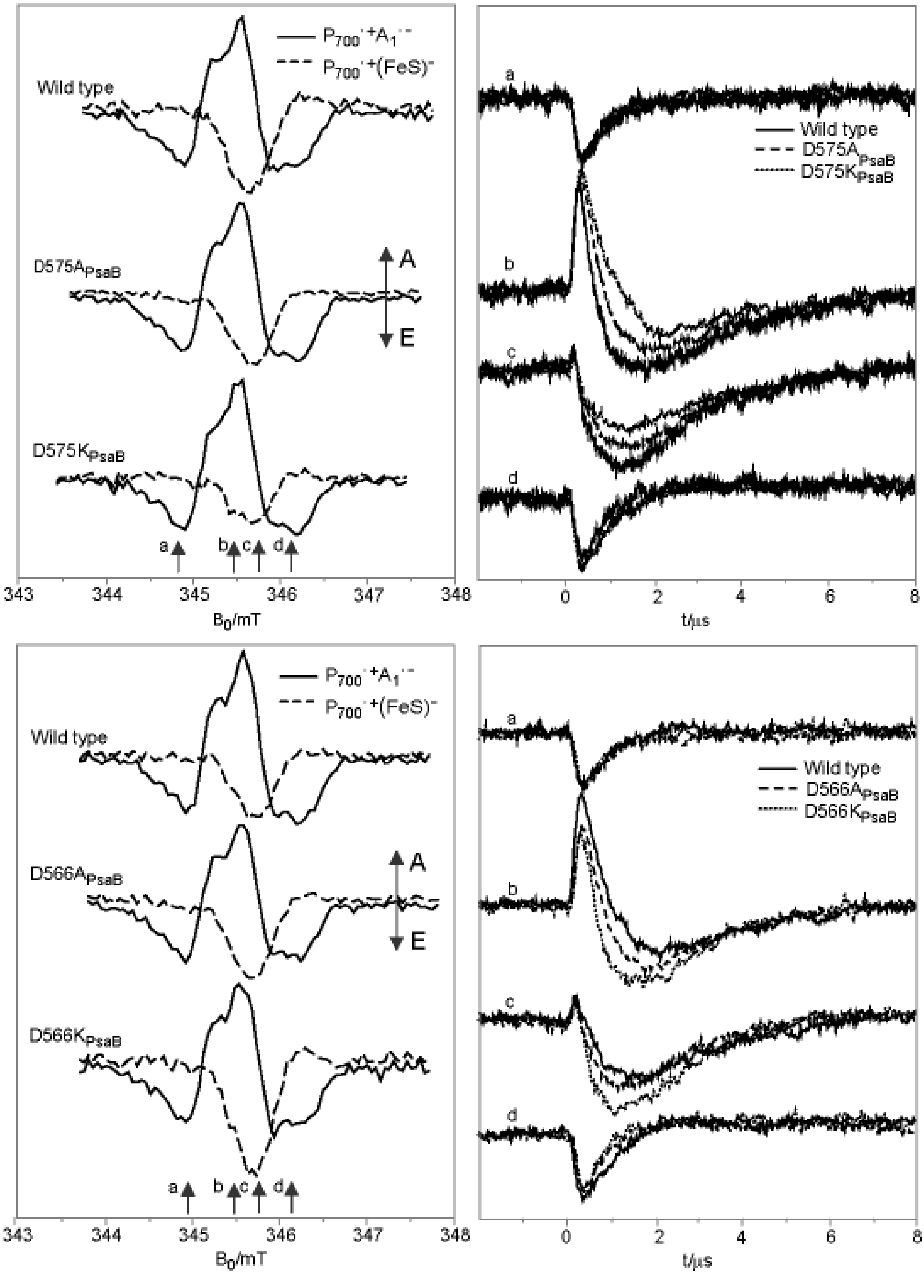

Figure 8.3. Left: X-band TR EPR spectra of the two sequential $P_{700}^{\bullet+}A_1^{\bullet-}$ (solid line) and $P_{700}^{\bullet+}(FeS)^-$ (broken line) RP states in PS complexes isolated from the wild type and D575$_{PsaB}$ (top), D566$_{PsaB}$ (bottom) mutants at 260 K. Integration window for early and late signal are 200 – 400 ns and 1.75 – 2.25 μs, respectively.

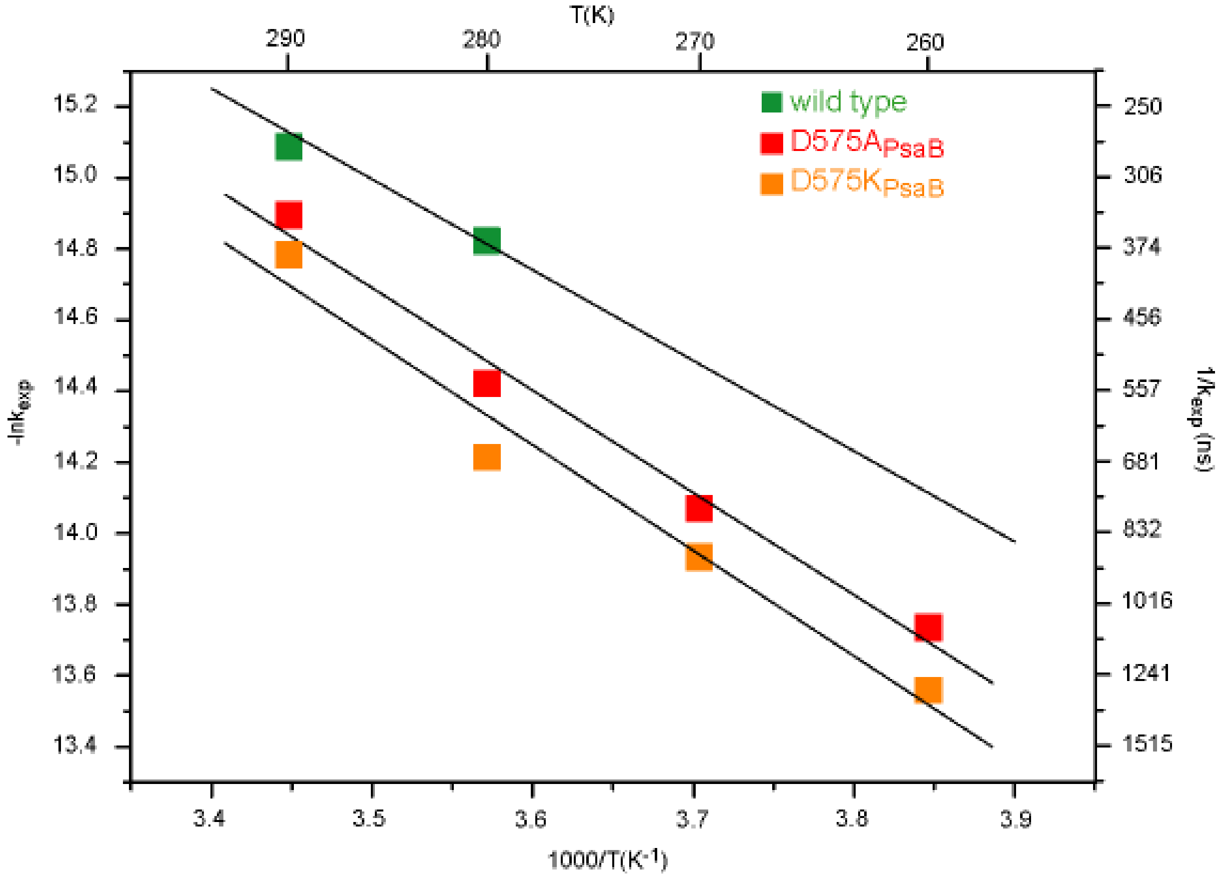

Figure 8.4. *Arrhenius plot* (ln*k versus* 1/T) of the forward ET from $A_1^{\bullet-}$ to F_X in PS I complexes isolated from the wild type (green square), $D575A_{PsaB}$ (red square) and $D575K_{PsaB}$ (orange square) mutants. The slope of wild type corresponds to the activation energy E_a = (220 ± 20) meV as it was evaluated from the optical data in the *Thermosynechococcus elongatus* [1]. From extrapolation of TR EPR data the activation energy was determined in the $D575_{PsaB}$ variants: $E_a(D575A_{PsaB})$ = (245 ± 20) meV and $E_a(D575K_{PsaB})$ = (255 ± 20) meV.

$A_1^{\bullet-}$ to F_X ET rate in the lysine variant (dotted curve) is nearly doubled compared to that in the alanine variant (dashed curve). In contrast, alteration of $D566_{PasB}$ (Figure 8, bottom) leads to an opposite effect: the $A_1^{\bullet-}$ to F_X ET in the $D566_{PsaB}$ variants is faster than in the wild-type. Again, the lysine variant shows a larger effect than does the alanine variant. Using the procedure described in Chapter 4 the transients of two sets of variants were fit and the numbers of the evaluated ET rate are collected in Table 8.1. This table includes ET rates obtained from room temperature TR EPR and TR optical spectroscopy. TR EPR data on the D575 variants at room temperature were provided by Prof. Art van der Est (Brock University, Canada). In this experiment also the slight slowing in the forward ET kinetics from $P_{700}^{\bullet+}A_1^{\bullet-}$ to $P_{700}^{\bullet+}F_X^{-}$. is observed, although weaker than at 260 K.

Table 8.1. Evaluated time constants (k^{-1}) for ET from $A_1^{\bullet -}$ to F_X at 295 K and 260 K.

	TR EPR		Time-Resolved Optical Spectroscopy				
	Slow phase k^{-1} (ns)		Stretched exponential fit		Double exponential fit		
			k^{-1} (ns)	Stretch factor (β)	Slow phase k^{-1} (ns)	Fast phase k^{-1} (ns)	Fast phase relative amplitude
295K							
WT	280	-	239	0.86	259	15	20%
D575A$_{PsaB}$	320	360*	232	0.81	239	12	13%
D575K$_{PsaB}$	340	410*	371	0.73	340	13	20%
D566A$_{PsaB}$	-	245*	116	0.79	149	10	20%
D566K$_{PsaB}$		210*	106	0.74	122	10	20%
R570E$_{PsaB}$	-	-	222	0.81	255	20	22%
260K			-		-	-	-
WT	785						
D575A$_{PsaB}$	1070		-		-	-	-
D575K$_{PsaB}$	1280						
D566A$_{PsaB}$	685		-		-	-	-
D566K$_{PsaB}$	590						

Remarks

The time constants are evaluated from EPR data by fitting an appropriate model function of time to the experimental transients as described in the text. The optical transients were fit with either a mono-exponential or bi-exponential decay function. Time constants marked by * are not measured but extrapolated using the *Arrhenius plots* shown in Figure 8.4. The activation energy of the wild type was set to 220 ± 20 meV [1]. From the limited data set at four temperatures between 290 and 260 K the activation energies are evaluated to be 245 meV and 255 meV for the D575A$_{PsaB}$ and D575K$_{PsaB}$ variants, respectively. Within the larger error margins these values do not differ from the wild type value 220 ± 20 meV. The latter has been taken for extrapolation of the data for the D566A$_{PsaB}$ and D566K$_{PsaB}$ variants.

Two sets of D575$_{PsaB}$ and D566$_{PsaB}$ variants were also investigated by optical absorption difference spectroscopy by Dr. Rufat Agalarov (Pennsylvania State University, USA). Again, in the TR optical study the lifetime is lengthened for the D575K$_{PsaB}$ and the D566$_{PsaB}$ variants show the opposite change, Table 8.1. In both types of experiment the lysine variant has a larger effect on the ET kinetics than alanine. Therefore, these room temperature results are fully consistent with TR EPR study measured at 260 K.

Manifestation of a temperature dependence in the forward ET kinetics from $A_1^{\bullet-}$ to F_X

The temperature dependence of the $A_1^{\bullet-}$ to F_X ET rate constant (*Arrhenius plot*) for the $D575_{PsaB}$ variants compared to the wild type are shown in Figure 8.4. The data for the $D575_{PsaB}$ variants were obtained from TR EPR measurements using the same fitting procedure as for 260 K. The data for PhQ in the wild type include only two data points (295 and 260 K) and were extrapolated with an activation energy of E_a = 220 meV ± 20 meV evaluated from TR absorbance difference optical data [1]. Within experimental uncertainty, no significant change is observed in the activation energy (nearly the same *Arrhenius plot*) for the variants and wild type. The activation energy was estimated to be about E_a = 245 ± 20 meV and E_a = 255 ± 20 meV in the $D575A_{PsaB}$ and $D575K_{PsaB}$ variants, respectively.

8.3. Conclusions of TR EPR study of the $D575K_{PsaB}$, $D575A_{PsaB}$ and $D566K_{PsaB}$, $D566A_{PsaB}$ variants

The results of the ET kinetic studies of the alanine and lysine variants of $D575_{PsaB}$ and $D566_{PsaB}$ can be summarized as follows:

i) In both sets of variants only small changes of less than a factor of two are observed in the $A_1^{\bullet-}$ to F_X ET rates; the rates decrease for the $D575_{PsaB}$ variants but increase for the $D566_{PsaB}$ variants.

(ii) There are systematic trends in the kinetics such that introducing lysine generally causes a larger effect than introducing alanine.

Moreover, the decrease in the $A_1^{\bullet-}$ to F_X ET rate induced by alteration of $D575_{PsaB}$ residue is less than what was observed when residues in direct van-der-Waals contact with the quinone are altered, e.g. $W696_{PsaA}$, which is π-stacked with the quinone, or $S692_{PsaA}$, which is connected by H-bonds to $W696_{PsaA}$ and $R694_{PsaA}$ as part of an H-bond network between A_0 to A_1 to F_X [34, 35].

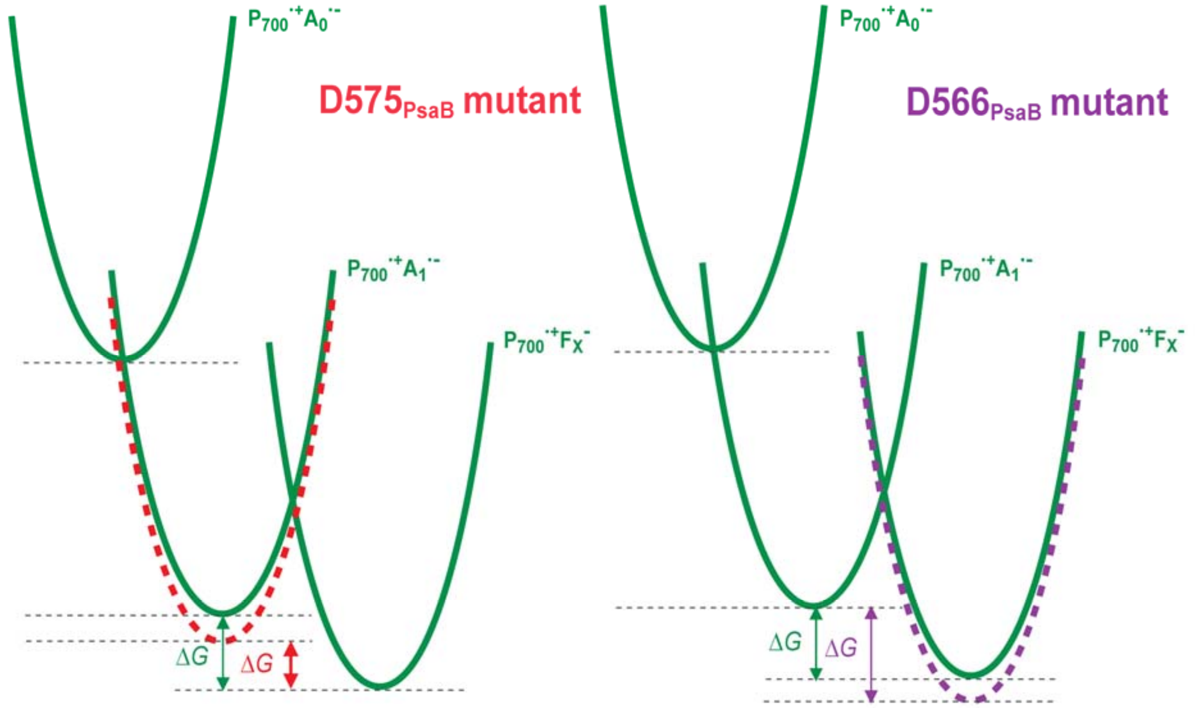

Figure 8.5. The scheme of parabolic redox potential curves along the reaction coordinate (according to Marcus theory) is used to illustrate the predominant potential down-shift due to the aspartate mutation to alanine or lysine.
Left: The D575$_{PsaB}$ variant affects predominantly the redox potential of A_1; for simplicity its down-shift is indicated alone.
Right: The D566$_{PsaB}$ variant affects predominantly the redox potential of F_X; for simplicity its down-shift is indicated alone.
The respective down-shifts lead to opposite changes of the redox potential difference *ΔG* between A_1 and F_X. Therefore opposite changes of the driving force for the $A_1^{\bullet-}$ to F_X ET, in agreement with the observed changes of time constants.

8.4. Application of Marcus theory for qualitative explanation of redox potential changes of A_1 and F_X

A possible explanation for the systematic slow-down and acceleration of the $A_1^{\bullet-}$ to F_X ET in the D575$_{PsaB}$ and D566$_{PsaB}$ variants can be a specific change of the redox potential of the respective cofactors. For simplicity it is assumed that variation in the position D575$_{PsaB}$/D566$_{PsaB}$ has a predominant effect on the A_{1A}/F_X cofactor, respectively. Since only differences matter, the observed effect can be assigned to a redox potential change of one cofactor only. These preconditions lead us to the following conclusions:

i) According to the electrostatic calculation, the D575$_{PsaB}$ residue changes its protonation state from fully ionized to nearly fully protonated with charge-separation and hence formation of the reduced $A_1^{\bullet -}$ state [110]. A change in the protonation state of $D575_{PsaB}$ residue influences most strongly the redox potential of A_{1A} in PS I [110]. Therefore, all changes can be due to a change in the redox potential of A_{1A} only.

ii) The $D566_{PsaB}$ residue is located closer to F_X than to A_{1A}, the positive charge on PsaC exposed by the removal of salt bridges to $D566_{PsaB}$ will influence the redox potential of F_X more than that of A_{1A}. Again it is sufficient to consider a change in redox potential of F_X only.

Therefore, a neutral or more positive charge instead of the negatively charged aspartate side chain in position $D575_{PsaB}$/$D566_{PsaB}$ will drive the redox potential of A_{1A}/F_X more positive. The corresponding decrease/increase in driving energy between A_{1A} and F_X will slow down/speed up the $A_{1A}^{\bullet -}$ to F_X ET as observed in the experiment. The predicted changes in the driving energy $\Delta\Delta G$ for the variants compared to the wild type can be estimated from the rate expression of classical Markus theory given in Chapter 7 (Eqn. 7.2). Setting the reorganisation energy λ between 0.8 and 1.1 eV and the electronic coupling value V to 1.12 meV [1], the experimentally observed changes in ET rate at 260 K in the aspartate variants correspond to a very small shift in the driving energy ($\Delta\Delta G \approx -0.02$ eV) for the $D575A_{PsaB}$ variants and twice the amount for the $D575K_{PsaB}$ variant. Shifts of similar magnitude, but of opposite sign ($\Delta\Delta G \approx +0.02$ eV), are obtained for the $D566_{PsaB}$ variants relative to the wild type. Figure 8.5 illustrates the effect of a small shift to more positive redox potential of either A_{1A} or F_X by the $D575_{PsaB}$/$D566_{PsaB}$ mutation. It is also evident that small variations in the driving energy ΔG will not influence the activation energy much when the reorganisation energy λ is much bigger than ΔG. Indeed, the activation energy E_a remains almost unaffected in the $D575_{PsaB}$ variants (Figure 8.5).

8.5. Comparison with electrostatic calculations

The experimentally determined changes in driving energy (~ 20 meV) turn out to be quite small. Particularly, if it is compared with the ~ 200 mV contribution of the negative charge of $D575_{PsaB}$ (fully ionized) to the redox potential of A_{1A} as predicted by the electrostatic calculations [110, 141]. To rationalize the observed small changes in the ET rates Dr. Hiroshi Ishikita (University of Southern California, Los Angeles) extended the previous computational studies and calculated the shifts in the redox potential of F_X as well as of A_{1A}

Table 8.2. Calculated shifts (ΔE_m) in the redox potential (E_m) and driving energy for the $A_1^{\bullet -}$ to F_X electron transfer ($\Delta\Delta G$)) relative to the wild type E_m in meV.

	ΔE_m [a]			**$\Delta(\Delta G)$ [a]**	
	A_{1A}	**A_{1B}**	**F_X**	**$A_{1A} \rightarrow F_X$**	**$A_{1B} \rightarrow F_X$**
D575A$_{\text{PsaB}}$	+119	+136	+123	–4	+13
D575K$_{\text{PsaB}}$	+125	+144	+132	–7	+12
D566A$_{\text{PsaB}}$	–19	+8	+53	–72	–45
D566K$_{\text{PsaB}}$	–20	+8	+54	–74	–46

[a] Calculated values with the native crystal structure for the native PS I complex from *Thermosynechococcus elongatus* [4].

and A_{1B} for the D575$_{\text{PsaB}}$ and D566$_{\text{PsaB}}$ variants. The values listed in Table 8.2 indicate the following features:

i) Removal of the negative charge at position D575$_{\text{PsaB}}$ (or appearance of uncompensated positive charge) leads to a significant up-shift of redox potential not only of A_{1A} and A_{1B} but also of F_X. For the two D575$_{\text{PsaB}}$ variants, these shifts (from the wild type) are very similar for A_{1A}, A_{1B} and F_X, thus in general agreement with the observed small changes on the $A_{1A}^{\bullet -}$ to F_X ET rates. However, the calculated up-shifts do not reproduce well the slowing down of the ET rates (positive ΔG). In fact, the up-shift is even slightly larger for F_X than for A_{1A}. In addition, ΔG for the $A_{1A}^{\bullet -}$ to F_X ET remains nearly unchanged for the D575A$_{\text{PsaB}}$ and D575K$_{\text{PsaB}}$ variant, because the calculations only set the partial charge associated with the protonation state of the aspartate side chain at position D575$_{\text{PsaB}}$ to zero and do not account for possible uncompensated positive charges.

ii) For the D566$_{\text{PsaB}}$ variants the calculated up-shift in redox potential concerns mainly F_X while it is marginal for A_{1A} and A_{1B}. Correspondingly, the driving energy ΔG for the $A_{1A}^{\bullet -}$ to F_X ET is predicted to increase, as indeed observed. However, the calculated driving energy is higher than observed and again remains about the same for the $A_{1A}^{\bullet -}$ to F_X ET in the D566A$_{\text{PsaB}}$ and D566K$_{\text{PsaB}}$ variants.

Note that the available TR EPR time window allows detection of the “slow” ET kinetics attributed to the $A_{1A}^{\bullet -}$ to F_X ET step. It will not be able to resolve the “fast” ET kinetics past A_{1B} if ET is about (or less) than 30 % in PsaB-branch [132], as determined from optical data for the “fast” phase of $A_1^{\bullet -}$ reoxidation in cyanobacterial PS I.

8.6. Proposal for an altered bound-water network between $A_{1A/B}$ and F_X

The calculated redox potentials for A_{1A} and A_{1B} indicate a strong influence of the bound-water molecules [110, 141], in particular water W37 (1JB0) with an H-bond to the side chain of $D575_{PsaB}$. This water is also part of a larger bound-water network, located on the PsaB side of the complex between A_{1B} and F_X. There is a corresponding network of water molecules on the PsaA side located between A_{1A} and F_X. However, the number and arrangement of the water molecules in the two networks are different (Figure 8.6 and Table 8.3). The network on the PsaA side is composed of five water molecules in a roughly linear arrangement while on the PsaB side five of six waters are interconnected in a pentagonal arrangement [6]. Previous electrostatic calculations have shown that the redox potentials for the quinones are influenced strongly by these water molecules and were shown to vary significantly for the three cases: no water molecules, only W37 and all bound waters included [110]. The calculated corresponding redox potentials are for A_{1A}: -438, -531 and -629 mV and for A_{1B}: -604, -686 and -776 mV. Significant shifts due to the bound-water molecules occur not only for the individual redox potentials values of A_{1A}, A_{1B} and F_X but also show up in the respective A_{1A}/A_{1B} asymmetry ($\Delta_{A/B}$: -166, -155 and -147 mV). Accordingly, the driving energy ΔG for the $A_{1A}^{\bullet-}$ and $A_{1B}^{\bullet-}$ to F_X ET processes may depend on the details of the bound water networks. Variation of $D575_{PsaB}$ to either alanine or lysine will remove the H-bond between W37 and the aspartate residue, which is likely to induce other changes in the B-side water network. Inspection of the structure in Figure 8.6 suggests that the loss of the H-bond between W37 and $D575_{PsaB}$ leads to a repositioning of W37, e.g. with the possible formation of two new hydrogen bonds, e.g. to the side chain of $R712_{PsaB}$ and to W160 water molecule. As a consequence of these rearrangements, water molecule W162 may be lost. Without W162 and W37 repositioned, the water networks on both PsaA and PsaB sides would become essentially the same. Therefore, doubling the bound-water network of the PsaA side to the PsaB side is a specific proposal for calculation of a change in the redox potential of A_{1A}, A_{1B} and F_X due to $D575_{PsaB}$ variation. In addition, different adaptations of the bound-water network in case of the $D575A_{PsaB}$ and $D575K_{PsaB}$ variant could be considered as origin for the observed changes in the respective $A_1^{\bullet-}$ to F_X ET rate.

In summary, only minor but systematic shifts in the redox potential difference between A_{1A} and F_X are observed in the $D575_{PsaB}$ and $D566_{PsaB}$ variants. This is in qualitative agreement with electrostatic calculations, as they indicate a general trend that the redox potentials of A_{1A} and F_X are altered in a similar way in the investigated variants. Possible rearrangements in the protein environment cannot be easily included in the electrostatic calculation in the absence of independent structural information. However, reasonable suggestions such as proposed change in the bound-water network can be tested.

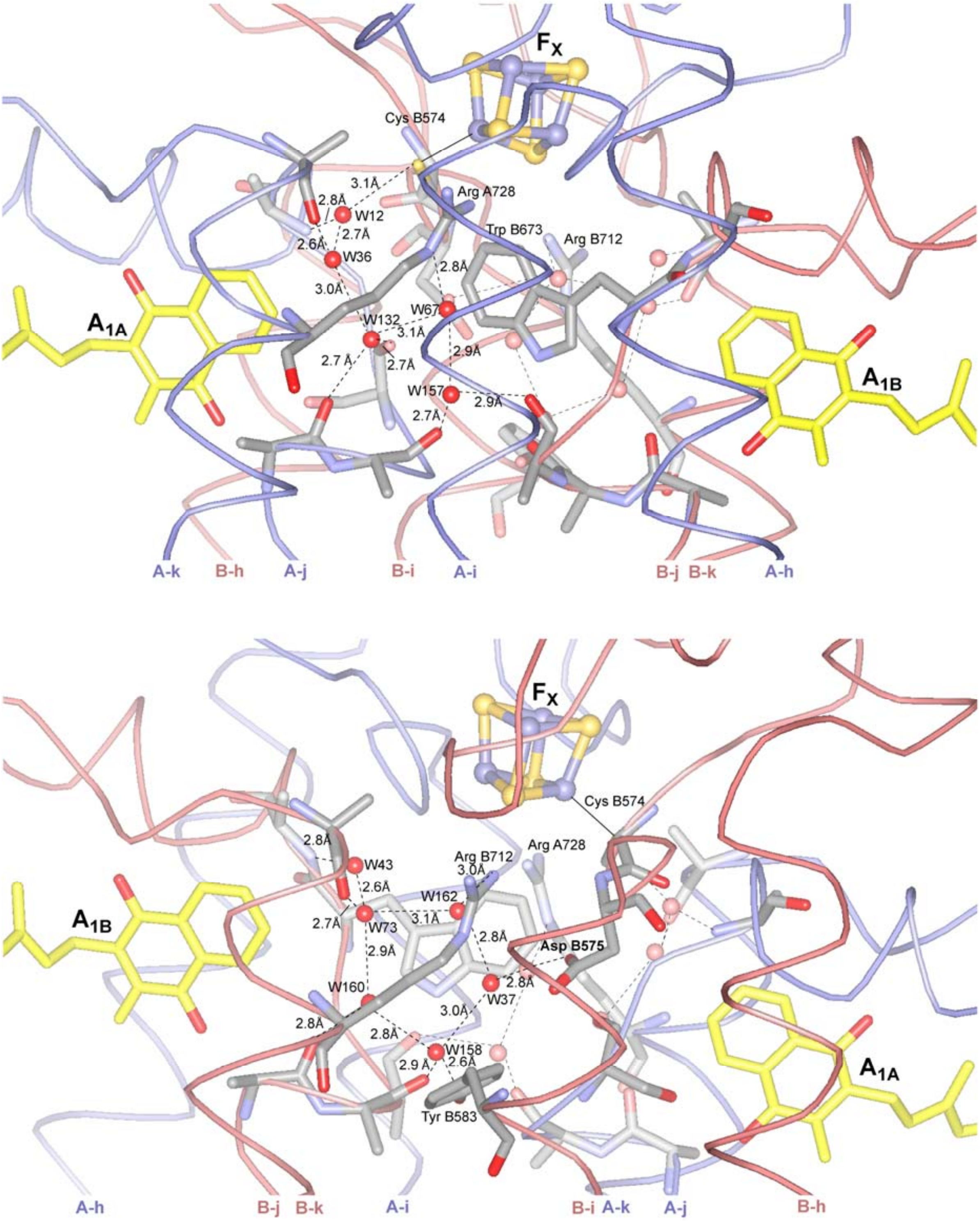

Figure 8.6. Details of the structural model of PS I (pdb entry 1JB0) representing the environment of the acceptors A_{1A}, A_{1B} and F_X. The view projection is approximately parallel to the membrane surface and onto to plane of the acceptor centers from opposite directions. The two inequivalent networks of bound water molecules located between PhQ and the first [4Fe-4S] cluster F_X. Possible H-bonds between the water molecules and the backbone and/or side chains of amino acids in the protein environment are indicated by thin lines. While the PsaA-side bound water network has 5 members in an approximately linear arrangement, the PsaB-side one has 6 members of which five are arranged in a pentagon arrangement.

Table 8.3. Two sets of bound water networks connected to the PsaA and PsaB subunits of PsaA/PsaB heterodimer.

Subunits	Water molecule	Distance, Å	Type	Amino residue or water molecule
PsaA	W12	3.1	S	S^{γ} Cys B574
		2.8	B	N Arg A694
		2.7	I	W36
PsaA	W36	2.6	B	O Ile A724
		2.7	I	W12
		3.0	I	W132
PsaA	W67	2.8	S	N^{ε} Arg A728
		3.1	I	W132
		2.9	I	W157
PsaA	W132	2.7	B	O Phe A689
		2.7	B	O Ser A692
		3.0	I	W36
		3.1	I	W67
PsaA	W157	2.7	B	O Leu A690
		2.9	B	O Ile B671
		2.9	I	W67
PsaB	W37	2.8	S	$O^{\delta 1}$ Asp B575
		3.0	I	W158
		2.8	I	W162
PsaB	W43	2.8	S	N Arg B674
		2.6	I	W73
PsaB	W73	2.7	B	O Ile B708
		2.9	I	W160
		3.1	I	W162
PsaB	W158	2.9	B	O Leu B670
		2.6	B	O^{η} Tyr B583
		3.0	I	W37
		2.8	I	W160
PsaB	W160	2.8	B	O Phe B669
		2.9	I	W73
		2.8	I	W158
PsaB	W162	3.0	S	$N^{\eta 1}$ Arg B712
		2.8	I	W37
		3.1	I	W73

Remarks

S – H-bond to side chain of amino residue

B – H-bond to back bone of amino residue

I – intra-molecular H-bond

9. Mutants in the Vicinity of the Primary Electron Acceptor A_0 of PS I: Methionine to Asparagine Mutation of the Ligand to the Central Metal Ion of A_0 Chlorophyll *a*

A question in this Chapter addresses the role of the primary electron acceptor A_0 in forward ET of PS I. To probe this issue, the axial ligand to the primary electron acceptor A_0, which is a methionine (M) residue in the wild type, has been substituted with a leucine (L) residue which has an inert side chain and with an asparagine (N) residue which has an dipolar side chain in either the PsaA- or PsaB-branch [134]. As demonstrated for the ML variants, the MN mutations are expected to alter the redox potential of A_0 in either branch and to influence the ET kinetics from $A_0^{\bullet-}$ to A_1. Multifrequency TR EPR techniques were used to investigate this effect on spin polarisation pattern of the second $P_{700}^{\bullet+}A_1^{\bullet-}$ and third $P_{700}^{\bullet+}(FeS)^-$ RP states.

9.1. Motivation

According to the X-ray structure model the binding pocket of the primary acceptor, A_0, has a number of unique features that may explain the function of this *Chl a* as cofactor at a relative low redox potential. The axial ligand to the central Mg^{2+} of each chlorophyll (A_{0A}/A_{0B}) in the

PsaA- and PsaB-branch respectively is provided by the sulphur of the methionine side chain $M688_{PsaA}/M668_{PsaB}$. This coordination is highly unusual since interaction between acid Mg^{2+} and the soft base sulphur is expected to be very weak. The lack of a strong fifth bond may account for the relatively low redox potential of A_{0A}/A_{0B} (E_m = -1050 meV in PS I [15] compared to Chl *a* in solution E_m = -900 meV [142]). This Chapter focuses on the investigation of variants with the methionine residue changed to asparagine either in the PsaA- or PsaB-branch of PS I from *Synechocystis sp*. PCC 6803. These mutations are expected to influence the ET properties at the A_0 (and possibly A_1) level of charge separation.

It should be noted that site-directed mutations in either the PsaA or PsaB protein subunit may also affect the directionality of charge separation. The highly symmetric arrangement of the chlorophylls in each of the ET chains raises the question to what extent both branches are active in ET, i.e. if both chlorophylls A_{0A} and A_{0B} are involved in the forward ET? Majority of the published results concerns PS I from *Chlamydomonas reinhardtii* (eukaryotes). Site-directed mutants with the methionine $M684_{PsaA}/M664_{PsaB}$ residue (corresponds to $M688_{PsaA}$/ $M668_{PsaB}$ in the X-ray structural model (pdb entry 1JB0)) mutated to histidine, leucine and serine were studied with pulsed EPR and ultrafast pump-probe experiments and indicated blockage or severe slowing of the forward $A_0^{\bullet-}$ to A_1 ET [138, 143]. However, blockage of ET past $A_0^{\bullet-}$ for these MH variants was challenged with recent TR EPR studies at ambient temperatures [2]. Another variant concerns site-directed mutation of the tyrosine to phenylalanine ($Y696P_{PsaA}/Y676P_{PsaB}$ or “tickling” mutants) with the loss of a H-bond from the tyrosine C-O group to the outer ring of the A_0 chlorophyll. The ET kinetics from $A_0^{\bullet-}$ to A_1 to F_X were observed to remain unchanged. However, the initial branching ratio was claimed to change in the favour of ET along the B-branch [144].

In contrast, mutation of the methionine $M688_{PsaA}/M668_{PsaB}$ residue to leucine ($M688L_{PsaA}/M668L_{PsaB}$ variants) in *Synechocystis sp*. PCC 6803 (prokaryotes) provided strong evidence for asymmetric ET predominantly along PsaA-branch [134]. TR EPR observation of the $P_{700}^{\bullet+}A_1^{\bullet-}$ state of PS I isolated from the $M688L_{PsaA}$ mutant showed a sizeable decrease in the forward $A_0^{\bullet-}$ to A_1 ET rate, whereas in the PsaB variant no change from the wild type was found [75, 134]. This was confirmed by optical pump-probe studies of the $A_0^{\bullet-}$ lifetime [145].

In this work, the methionine $M688_{PsaA}$ and $M668_{PsaB}$ residues (pdb entry 1JB0) were changed in *Synechocystis sp*. PCC 6803 to asparagine ($M688N_{PsaA}/M668N_{PsaB}$ variants). The idea behind the choice of asparagine for mutation of methionine is not only to remove the specific sulphur ligand to the central Mg^{2+} of A_0 as in the case of the $M688L_{PsaA}/M668L_{PsaB}$

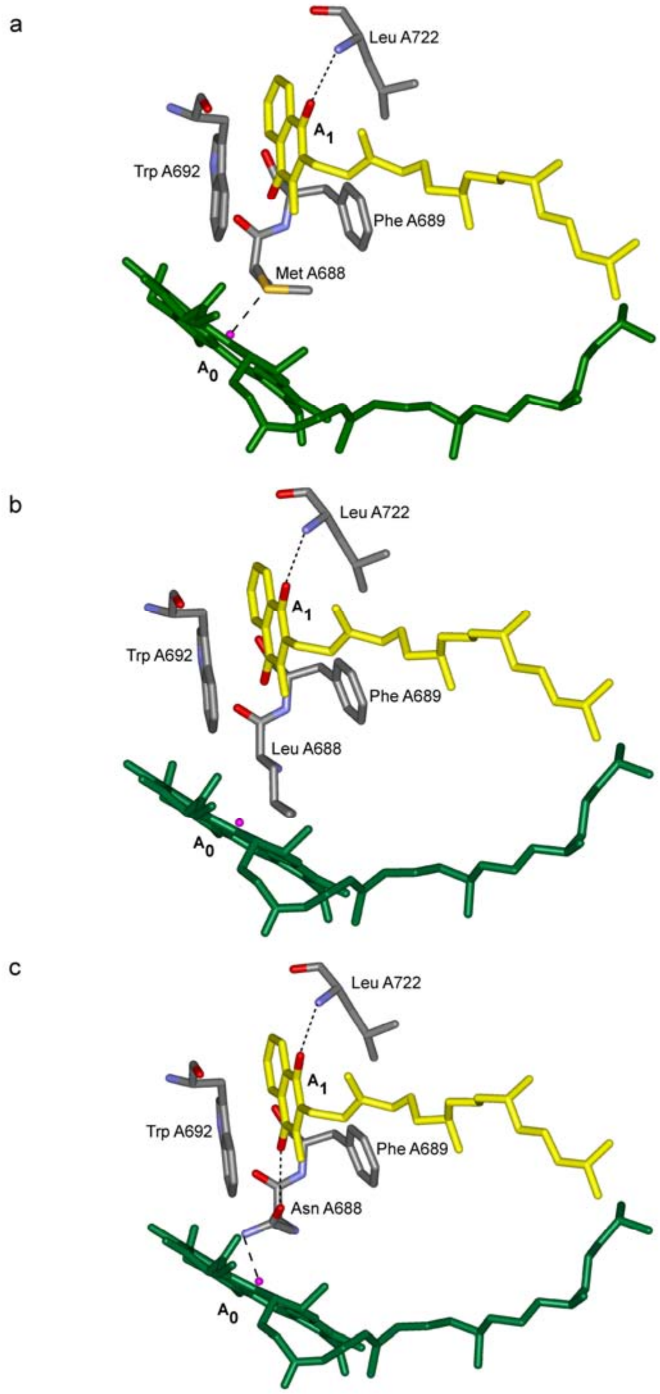

Figure 9.1. View of the protein environment between A_0 and A_1 in the PsaA heterodimer. The backbone amide proton of $L722_{PsaA}$ provides a single H-bond to the carbonyl group of PhQ. The amide ring of $W697_{PsaA}$ is π-stacked with the second ring of PhQ. Side chain –OH group of $S692_{PsaA}$ is involved in a H-bonded network that connects to the $W697_{PsaA}$ and to the backbone oxygen of the $M688_{PsaA}$. A_0 is ligated to the protein via the amino residue (a) $M688_{PsaA}$ which provides S as a ligand to the central ion Mg^{2+} of chlorophyll-A_0. In case of the mutations, (b) $L688_{PsaA}$ doesn't provide any ligand bond to the A_0 while N of (c) $N688_{PsaA}$ can be a ligand to A_0 as well as O of $N688_{PsaA}$ is H-bonded to the second carbonyl group of quinone (C_1 position).

variants with inert side chains but to offer a possible nitrogen ligand instead (Figure 9.1). The previous TR EPR study can be extended in two ways: i) The previous results for the M688L$_{PsaA}$/M668L$_{PsaB}$ variants concerning the observed changes of the $A_0^{\bullet -}$ to A_1 ET kinetics can be confirmed for the new variants. ii) The effect of a possible alternative ligand to the A_0 central metal ion can be tested.

9.2. Results

9.2.1. X-, Q- and W-band spin polarisation patterns of the second $P_{700}^{\bullet +}A_1^{\bullet -}$ RP state in the M668N$_{PsaB}$ and M688N$_{PsaA}$ variants at low temperature

X-band (top) and Q-band (bottom) TR EPR spectra of the second $P_{700}^{\bullet +}A_1^{\bullet -}$ RP state in PS I isolated from the wild type (dotted line), M668N$_{PsaB}$ (solid line) and M688N$_{PsaA}$ (broken line) mutants at 80 K are compared in Figure 9.2. All spectra are normalized to the same low-field E peak amplitude. The spectrum in the M668N$_{PsaB}$ variant is essentially the same as that of the wild type. Whereas the spin polarization pattern in the M688N$_{PsaA}$ variant shows significant differences from that of the wild type. For example, the negative amplitude of the up-field E peak and the positive amplitude of the mid-field A peak are substantially decreased.

Nearly the same change of spin polarization pattern was observed before in the M688L$_{PsaA}$ variant [95] (Figure 9.3). The change in the spin polarization pattern can be attributed to lengthening the effective lifetime in the primary $P_{700}^{\bullet +}A_0^{\bullet -}$ RP state. Using the SCRP model, Salikhov et. al. performed numerical simulations and demonstrated how an increase of the lifetime of the primary $P_{700}^{\bullet +}A_0^{\bullet -}$ RP state modifies the spin polarization pattern of the observed $P_{700}^{\bullet +}A_1^{\bullet -}$ RP state [95]. An effective lifetime of the precursor $P_{700}^{\bullet +}A_0^{\bullet -}$ RP state of 1 - 2 ns was able to reproduce satisfactorily the observed spin polarisation patterns at X- and Q-band for the M688L$_{PsaA}$ variant.

W-band TR EPR spectra of the second $P_{700}^{\bullet +}A_1^{\bullet -}$ RP state in the M688N$_{PsaA}$ (solid line) and M668N$_{PsaB}$ (broken line) variants are compared at 120 K in Figure 9.4. Note that at W-band the contributions of the individual radical-ion partners $P_{700}^{\bullet +}$ and $A_1^{\bullet -}$ are separated quite well but not yet at Q-band. The up-field part of the spectrum is associated mostly with

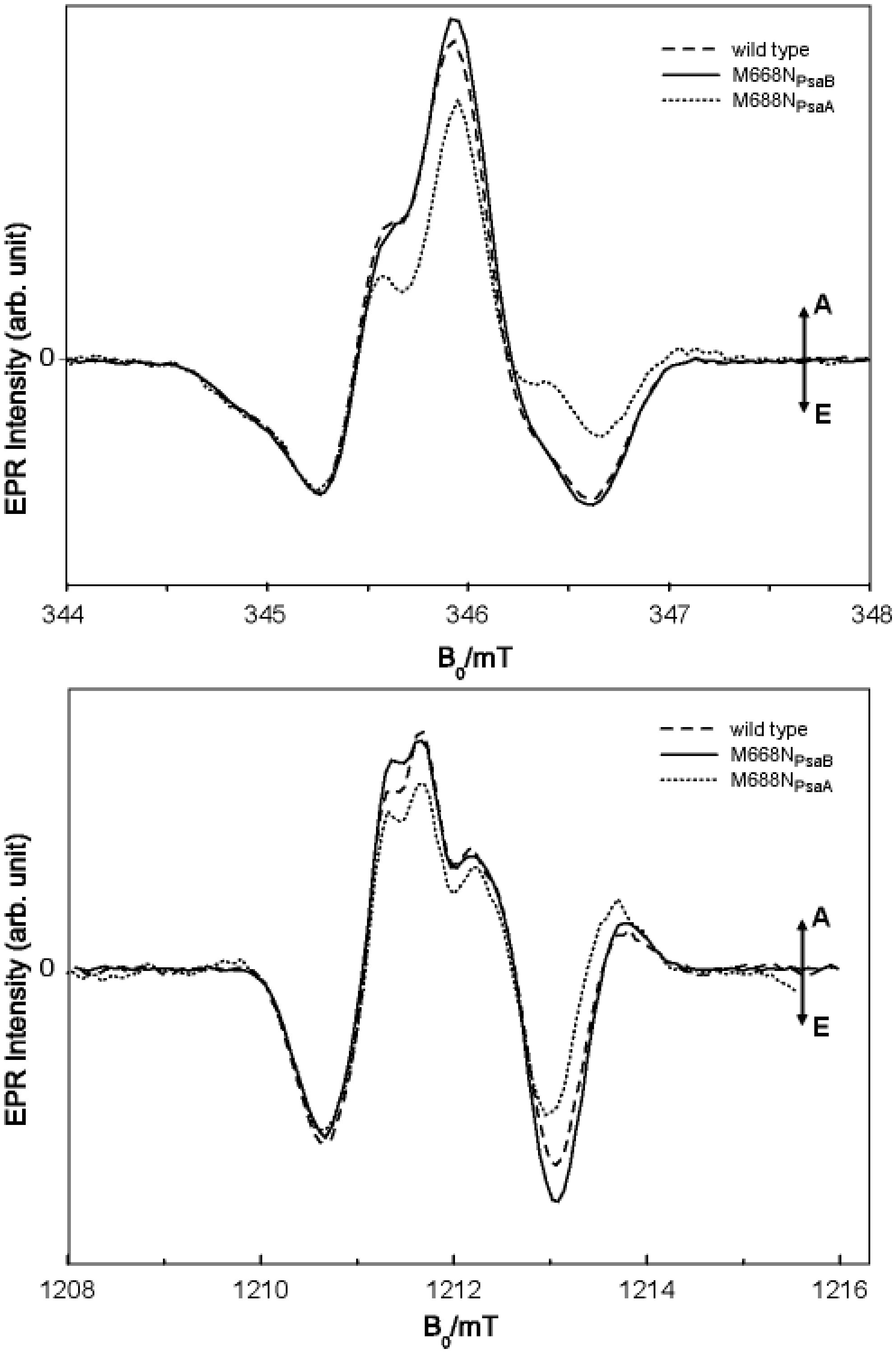

Figure 9.2. Comparison of X-band and Q-band TR EPR spectra of the second $P_{700}^{\bullet+}A_1^{\bullet-}$ RP state of PS I complexes isolated from the wild type (broken line), M668N$_{PsaB}$ (solid line) and M688N$_{PsaA}$ (dotted line) mutants at 80 K.

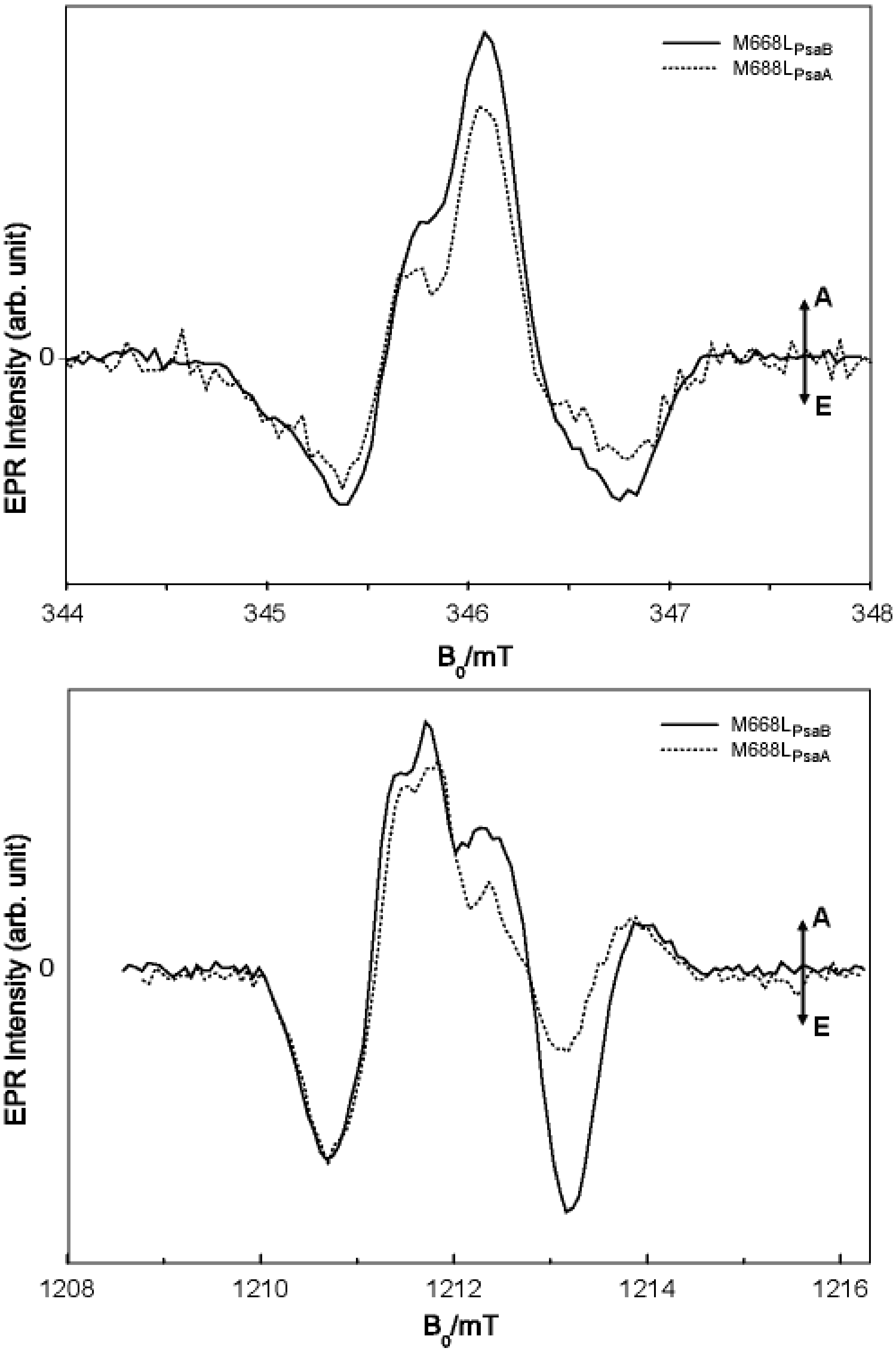

Figure 9.3. Comparison of X-band and Q-band TR EPR spectra of the second $P_{700}^{\bullet +}A_1^{\bullet -}$ RP state of PS I complexes isolated from the M668L$_{PsaB}$ (solid line) and M688L$_{PsaA}$ (dotted line) mutants at 80 K.

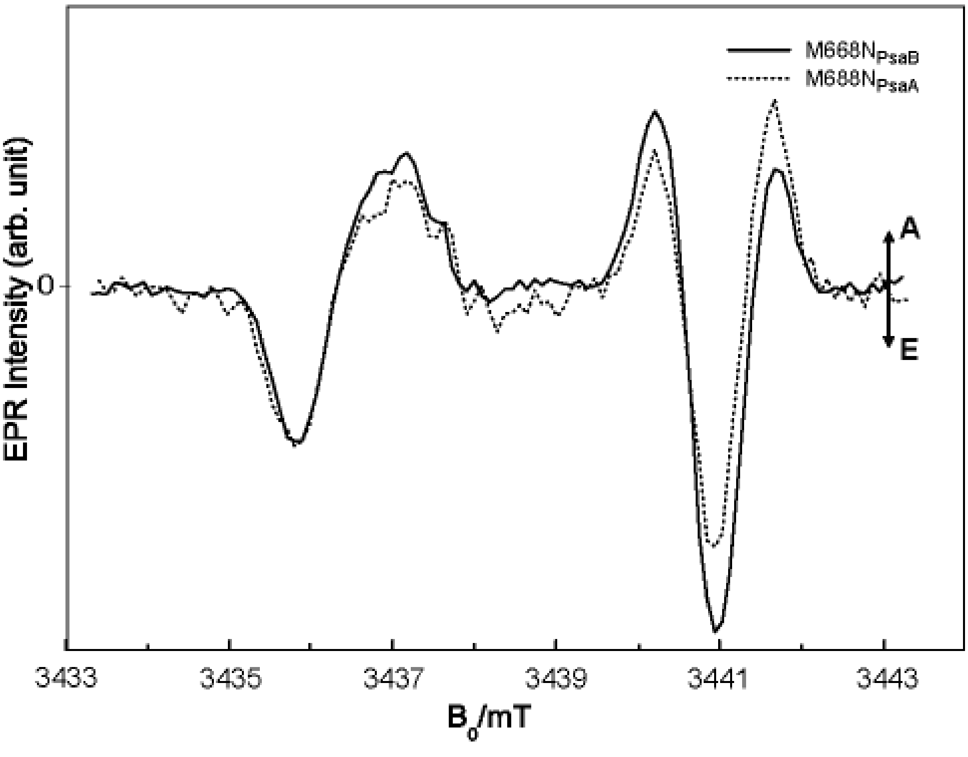

Figure 9.4. Comparison of W-band TR EPR spectra of the second $P_{700}^{\bullet+}A_1^{\bullet-}$ RP state of PS I complexes isolated from the M668N$_{PsaB}$ (solid line) and M688N$_{PsaA}$ (dotted line) mutants at 120 K.

the contribution of the $P_{700}^{\bullet+}$ radical-ion while the spectral part in the mid- and down-field range is due to the contribution from $A_1^{\bullet-}$ radical-ion. Again, the spectra are normalized to the same amplitude of the down-field E peak. They exhibit the same overall spin polarization pattern E/A/E/A. The spin polarization pattern in the M668N$_{PsaB}$ is very similar to that measured in the wild type [73]. Again, the spin polarization pattern for the M688N$_{PsaA}$ differs significantly from that of M668N$_{PsaB}$ variant, in particular in the up-field range with a decrease in the dominant E/A features an increase in most up-field A amplitude. As it will be shown in the next section these changes of spin polarization pattern are consistent with an increase of the effective lifetime of the precursor $P_{700}^{\bullet+}A_0^{\bullet-}$ RP state.

9.2.2. Effect of lengthening the life time of the precursor $P_{700}^{\bullet+}A_0^{\bullet-}$ RP state on the spin polarisation pattern of the second $P_{700}^{\bullet+}A_1^{\bullet-}$ RP state at W-band

Qualitatively, the change in the spin polarization pattern in the M688L$_{PsaA}$ and M688N$_{PsaA}$ variants can be explained as a result of spin-dynamics in the primary $P_{700}^{\bullet+}A_0^{\bullet-}$ RP state. In

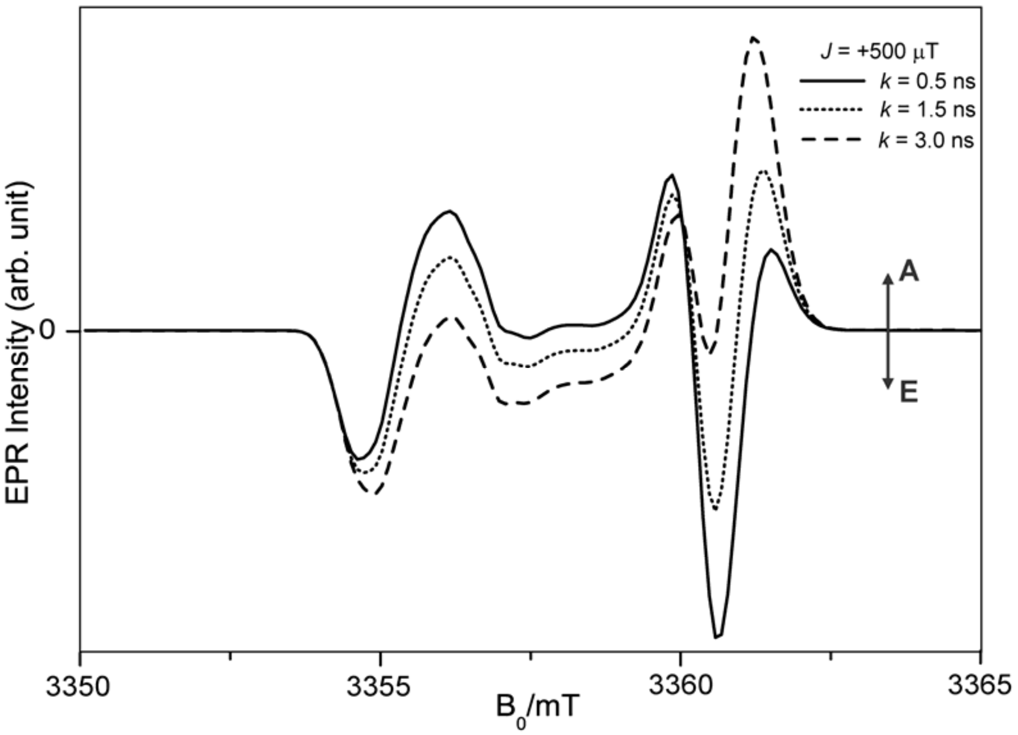

Figure 9.5. Simulations are shown for W-band spin-polarized EPR spectra of the $P_{700}^{\bullet +}A_1^{\bullet -}$ RP state. The life time *k* of the precursor state $P_{700}^{\bullet +}A_0^{\bullet -}$ is varied as indicated in the figure. The exchange coupling *J* was positive.

the wild type, the lifetime of the precursor $P_{700}^{\bullet +}A_0^{\bullet -}$ RP (~ 50 ps) is too short for spin dynamics (> 0.5 ns). If the lifetime of the $P_{700}^{\bullet +}A_0^{\bullet -}$ RP is increased to more than 0.5 ns, singlet-triplet mixing can occur. Therefore, following spin projection during the ET step to the subsequent $P_{700}^{\bullet +}A_1^{\bullet -}$ RP state as superposition of S and T_0 states will be populated, but not the S state only as is the case for the $P_{700}^{\bullet +}A_1^{\bullet -}$ RP in the wild type. The degree of singlet-triplet mixing in the precursor $P_{700}^{\bullet +}A_0^{\bullet -}$ RP state depends on its lifetime and on the spin coupling parameters. An approximate treatment is presented in [64, 132]. In accordance with these and other studies of spin dynamics in the primary RP born in the singlet state, the $P_{700}^{\bullet +}$ radical-ion of the secondary $P_{700}^{\bullet +}A_1^{\bullet -}$ RP state will inherit a partial net A polarisation while $A_1^{\bullet -}$ inherits corresponding a net E polarisation [64, 132].

Here, the effect of the lifetime of the precursor $P_{700}^{\bullet +}A_0^{\bullet -}$ PR state on the observed spin polarization pattern of the $P_{700}^{\bullet +}A_1^{\bullet -}$ PR state was evaluated quantitatively using the full solution of the time dependent spin density equations for the case of consecutive RPs as in [95]. Simulations of the spectra at W-band are presented in Figure 9.5. The magnetic and orientation parameters of $P_{700}^{\bullet +}$, $A_0^{\bullet -}$, $A_1^{\bullet -}$ used in the simulation are collected in

Table 9.1. Structural and magnetic interaction parameters of the primary $A_0^{\bullet -}$ radical used for simulations of TR EPR spectra of the $P_{700}^{\bullet +}A_1^{\bullet -}$ RP state. Parameters of the $P_{700}^{\bullet +}$ and $A_1^{\bullet -}$ are collected in Table 5.1.

		g-tensor			
	g_{xx}	g_{yy}	g_{zz}		
$A_{0A}^{\bullet -}$	2.0031	2.0031	2.0031		
	Euler angle relating g-tensors			dipolar axis in g($A_{0A}^{\bullet -}$)	
	α	β	γ	θ	φ
$P_{700}^{\bullet +}A_{0A}^{\bullet -}$	0°	0°	0°	17.9°	153.2°
				spin-spin coupling	
			D (dipole coupling)	*J* (exchange coupling)	
$P_{700}^{\bullet +}A_{0A}^{\bullet -}$			-340 µT	500 µT	
		relaxation and recombination			
	$T_1 = 100$ µs			$K_S = (20\text{ ns})^{-1}$	
	$T_2 = 1.3$ µs			$K_T = (2\text{ ns})^{-1}$	
		residual inhomogeneous linewidth			
		$\Delta B(A_{0A}^{\bullet -}) = 0.50$ mT			

Table 9.1 together with Table 5.1. As the lifetime of the primary $P_{700}^{\bullet +}A_0^{\bullet -}$ RP state is varied between 0.5 - 3 ns, the high-field A/E/A amplitude is reduced/reduced/increased (exchange coupling between $P_{700}^{\bullet +}$ and $A_0^{\bullet -}$ set positive). The correlated effect in the down-field region is also clearly shown: The E/A amplitude increases/decreases with increasing lifetime of the precursor $P_{700}^{\bullet +}A_0^{\bullet -}$ RP state. From the comparison of simulated and experimental spectra the lifetime is evaluated to fall in the range of 1 - 1.5 ns for the primary $P_{700}^{\bullet +}A_0^{\bullet -}$ RP in PS I from $M688N_{PsaA}$, compared to ~ 50 ps in the wild type.

9.2.3. TR EPR study of consecutive forward ET from $A_0^{\bullet -}$ through A_1 to F_X

Temperature dependence of spin polarisation patterns of the $P_{700}^{\bullet +}A_1^{\bullet -}$ and $P_{700}^{\bullet +}(FeS)^-$ RP states in the $M688N_{PsaA}$ variant

As it was demonstrated in Chapter 7, for specific time windows TR EPR spectroscopy permits evaluation of the kinetics of consecutive forward ET steps from $A_0^{\bullet -}$ via A_1 to the [4Fe-4S] clusters. Note that the first $A_0^{\bullet -}$ to A_1 ET step cannot be resolved directly, but the

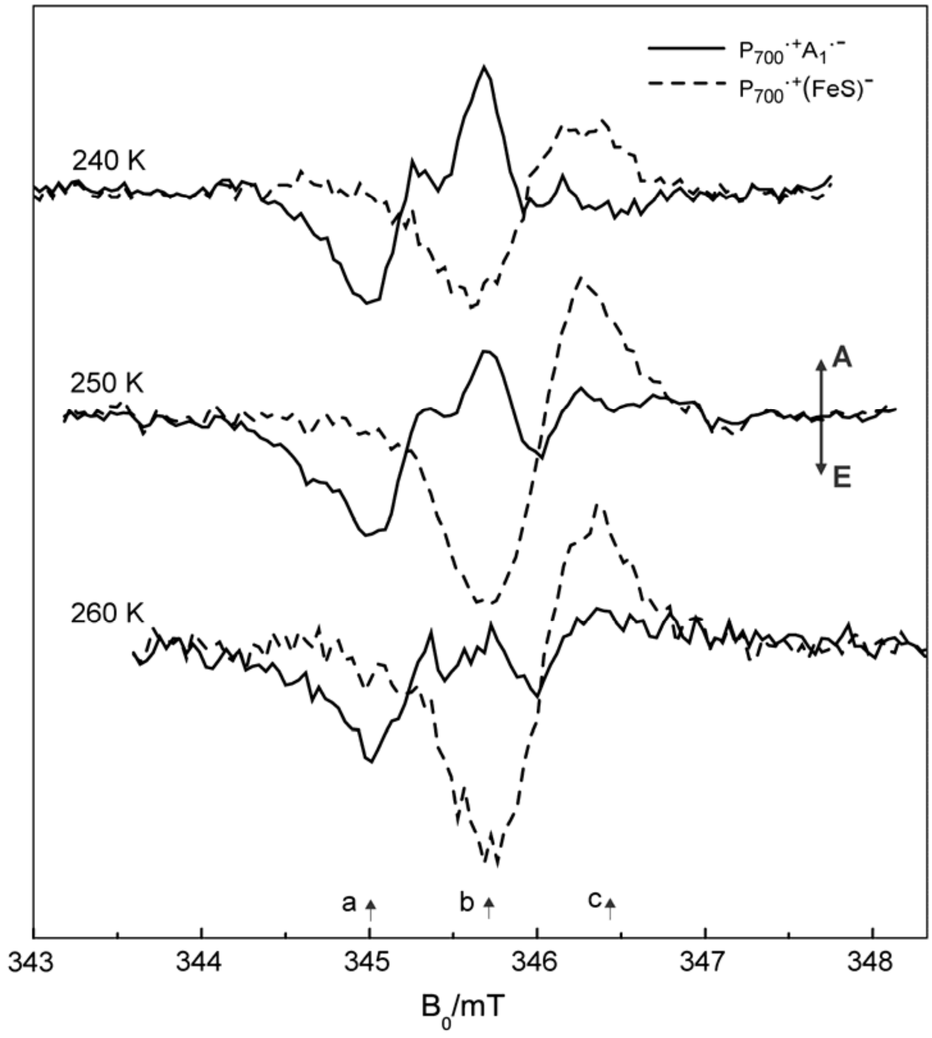

Figure 9.6. TR EPR spectra of the two sequential $P_{700}^{\bullet+}A_1^{\bullet-}$ (solid lines) and $P_{700}^{\bullet+}(FeS)^-$ (broken lines) RP states of PS I isolated from $M688N_{PsaA}$ mutants at temperatures 240 K (top), 250 K (middle) and 260 K (bottom). Spectra are integrated in the following time windows: early signal 200 – 400 ns and late signal 1.75 – 2.25 µs.

spin polarization patterns of both subsequent $P_{700}^{\bullet+}A_1^{\bullet-}$ and $P_{700}^{\bullet+}(FeS)^-$ RP states depend on the spin evolution in all previous RPs. Thus, the lifetime of the primary $P_{700}^{\bullet+}A_0^{\bullet-}$ RP state can be determined from the spin polarization pattern of the $P_{700}^{\bullet+}A_1^{\bullet-}$ and $P_{700}^{\bullet+}(FeS)^-$ RP polarisation patterns. For the wild type and $M688N_{PsaA}$ variant the spin polarization patterns of the $P_{700}^{\bullet+}A_1^{\bullet-}$ and $P_{700}^{\bullet+}(FeS)^-$ RP states were observed to be temperature independent. X-band TR EPR spectra in PS I isolated from the $M688N_{PsaA}$ mutant at three temperatures 240, 250 and 260 K are presented in Figure 9.6. The solid/broken lines belong to the $P_{700}^{\bullet+}A_1^{\bullet-}/P_{700}^{\bullet+}(FeS)^-$ RP states, respectively. Obviously, the spin polarization patterns of both RP states change with temperature. The mainly E/A spin polarisation pattern of $P_{700}^{\bullet+}(FeS)^-$ RP state of the $M688N_{PsaA}$ variant differs clearly from the mostly net E pattern from the wild type as well as M668N$_{PsaB}$ variant (Figure 9.7, top). The difference even increases with increasing temperature. Together with the changes observed in the spectrum of the $P_{700}^{\bullet+}A_1^{\bullet-}$ RP state this is considered the main evidence for effective spin-dynamics developing in the precursor $P_{700}^{\bullet+}A_0^{\bullet-}$ RP state. Similar changes in the spin polarisation pattern of the $P_{700}^{\bullet+}A_1^{\bullet-}$ and $P_{700}^{\bullet+}(FeS)^{-}$ RP states were observed earlier for the M688L$_{PsaA}$ variant as well as for PS I with AQ in the A_1-binding site (Chapter 7). To varying degree in all cases, e.g. the up-field E feature decreases with increasing temperature in amplitude and becomes more A for the observed secondary $P_{700}^{\bullet+}A_1^{\bullet-}$ RP state. This is consistent with a lengthening of the $A_0^{\bullet-}$ to A_1 ET time constant with increasing temperature. In order to explain such counter intuitive behaviour a possible explanation has been suggested for the M688L$_{PsaA}$ variant [134], as also described in Chapter 7. Assuming that the ML and MN mutation have similar influence on the properties of the A_0-binding site, the spin polarisation pattern can be considered as sum of contributions of two limiting cases (“slow” and “fast” spin-mixing time, i.e. short-lived and long-lived $P_{700}^{\bullet+}A_0^{\bullet-}$ RP with respect to the given spin-mixing time, Eqn. 7.1). The observed temperature dependence can be evaluated in terms of a temperature dependent relative weighting factor for the two limiting spectra. This way, the observations can be interpreted as an increasing weight for the long-lived $P_{700}^{\bullet+}A_0^{\bullet-}$ RP spectrum with increasing temperature. However, this remains equivalent to the result of an effective lifetime of the long-lived $P_{700}^{\bullet+}A_0^{\bullet-}$ state increasing with increasing temperature, in contrast to the normal situation of decay time shortening with increasing temperature. A possible way was offered in Chapter 7 with suggestion of a broad lifetime distribution for the $P_{700}^{\bullet+}A_0^{\bullet-}$ RP state, which broadens with increasing temperature such that the relative contribution of the limiting case (long-lived $P_{700}^{\bullet+}A_0^{\bullet-}$ RP) increases even though the average lifetime may remain constant or even slightly shorten with increasing temperature.

Forward ET from $A_1^{\bullet-}$ *to* F_X *at 260 K*

X-band TR EPR spectra and transients in PS I isolated from the wild type, M668N$_{PsaB}$ and M688N$_{PsaA}$ mutants at 260 K are compared in Figure 9.7. The transients are shown for selected field positions as indicated below the spectra (top). The spin polarization patterns of the $P_{700}^{\bullet+}A_1^{\bullet-}$ and $P_{700}^{\bullet+}(FeS)^{-}$ RP states in the M668N$_{PsaB}$ variant are very similar to those in the wild type: the E/A/E polarization pattern of the early RP state changes to a pattern with the net E for the late RP state (Figure 9.6, top). As it was expected the transients of the M668N$_{PsaB}$ variant do not show any significant differences to those of the wild type (Figure 9.7, bottom). In contrast, significant changes are observed for the transients of the

M688N$_{PsaA}$ variant (Figure 9.6, bottom). The $A_1^{\bullet -}$ to F_X forward ET decay at field positions a and b field is clearly faster in the M688N$_{PsaA}$ variant than in the wild type (and M668N$_{PsaB}$ variant).Using the same procedure as it was applied or the kinetic evaluation in Chapter 7 and Chapter 8, the ET rate approximately doubles. In addition, this result correlates with optical data at room temperature from Dr. Rufat Agalarov (Pennsylvania State University, USA). It shows that the forward $A_1^{\bullet -}$ to F_X ET rate is increased by factor of two in the M688N$_{PsaA}$ variant.

The experimental observations due to an increase of the $A_1^{\bullet -}$ to F_X ET rate was more clearly demonstrated in Chapter 7, where ET rate is 10 times faster than in the wild type. This acceleration correlates quite well with a more negative redox potential of AQ compared to native PhQ in the A_1-binding site of PS I. For the MN A_0 mutant, a significant change in the quinone redox potential is not expected. However, the asparagine with dipole side chain groups can introduce some contribution to the redox potential of A_1 as well.

9.3. Conclusions of TR EPR study of the M668N$_{PsaB}$ and M688N$_{PsaA}$ variants

The most important conclusions from TR EPR study on the M668N$_{PsaB}$ and M688N$_{PsaA}$ variants can be summarized as following:

i) Substantial changes in the spectroscopic and ET properties are observed only for the PsaA polypeptide variant while none of these changes are observed for PsaB polypeptide variant. This corresponds to the fact, that TR EPR observes only the transient RP state of the PsaA-branch.

ii) The observed change in the spin polarisation patterns of the sequential $P_{700}^{\bullet +}A_1^{\bullet -}$ and $P_{700}^{\bullet +}(FeS)^-$ RP states in the M688N$_{PsaA}$ variant can be interpreted as lengthening the effective lifetime of the precursor $P_{700}^{\bullet +}A_0^{\bullet -}$ RP state. The effect is quite similar to those observed for the M688L$_{PsaA}$ variant. Note that the forward ET rate from A_{0A} to A_{1A} is lengthened from about 50 ps in the wild type to 1 - 2 ns for M688N$_{PsaA}$ and M688L$_{PsaA}$ variants. As a consequence there will be increased competition with other decay processes (like $^3P_{700}$ recombination) but not blockage of forward ET as claimed for MH (and other variants) in *Chlamydomonas reinhardtii*.

iii) In addition, a faster forward $A_1^{\bullet -}$ to F_X ET was observed in the M688N$_{PsaA}$ variant, about twice faster than in the wild type.

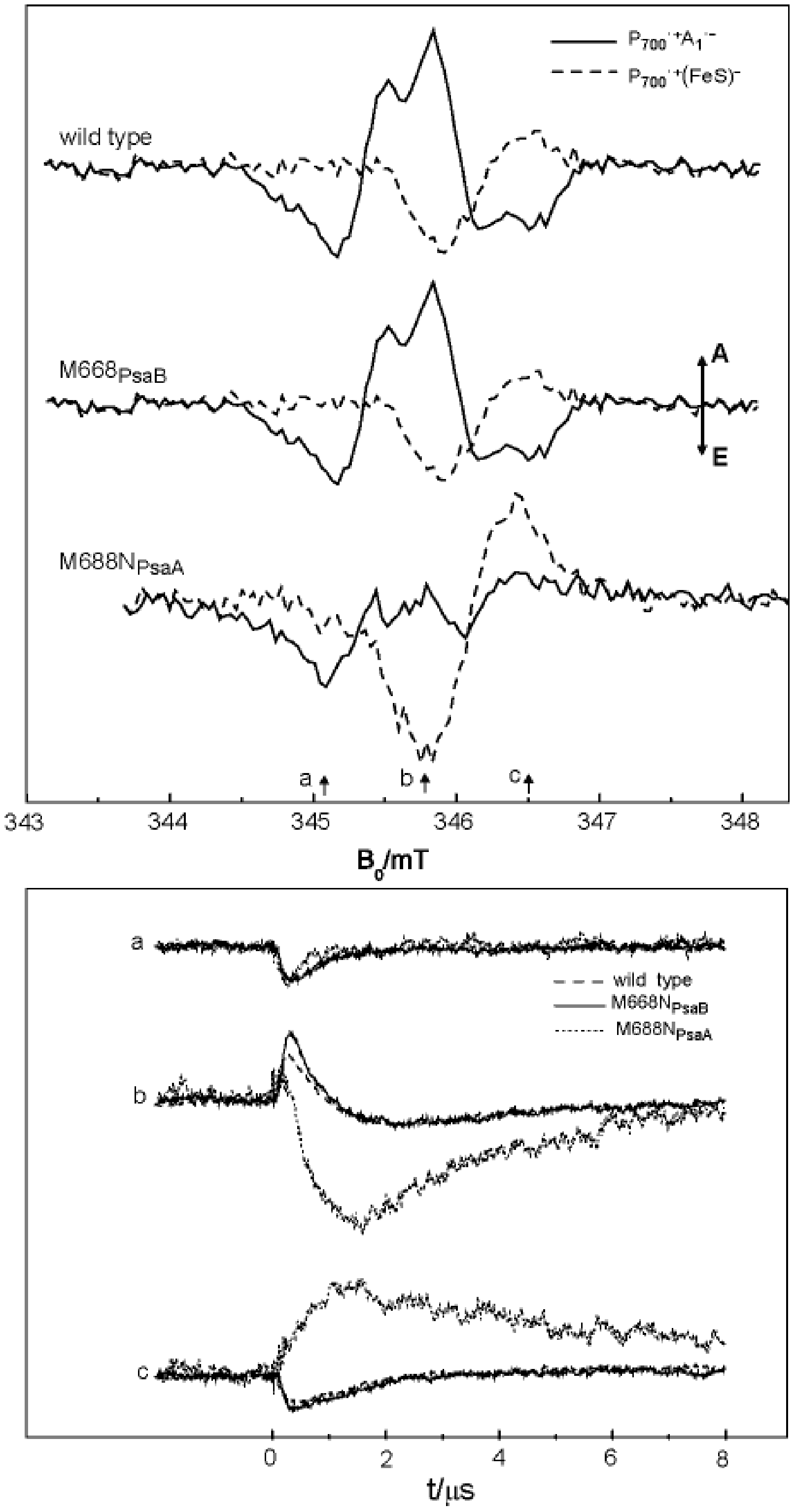

Figure 9.7. Top: TR EPR spectra of the two sequential $P_{700}^{\bullet +}A_1^{\bullet -}$ and $P_{700}^{\bullet +}(FeS)^-$ RP states of PS I isolated from the wild type, $M668N_{PsaB}$ and $M688N_{PsaA}$ mutants at 260 K. Spectra are integrated in the following time windows: early signal 200 – 400 ns and late signal 1.75 – 2.25 µs.

Bottom: EPR transient traces of PS I complexes from the wild type (broken line), $M668N_{PsaB}$ (solid line), $M688N_{PsaA}$ (dotted line) mutants. The field positions are indicated by arrows labeled a – c below the spectra in top.

9.4. Asymmetry ET in the cyanobacterial PS I

Although functionally not really significant, a really major debate occupies the recent literature as to which extent the two quasi-symmetric branches of cofactors are active in forward ET processes following light-induced primary charge separation. The final inner-membrane ET step from $A_1^{\bullet-}$ to F_X is more easily accessible to measurement and has thus provided the majority of data related to the issue of directionality in PS I. As it was mentioned, at room temperature the rate of $A_1^{\bullet-}$ re-oxidation is found to be biexponential with a “fast” (20 ns) and “slow” (200 ns) phase [29]. Studies of site-directed mutants in the local environment of PhQ in PS I from *Chlamydomonas reinhardtii* clearly identify the “slow” phase associated with ET via the PsaA-branch and similarly the fast phase to PsaB-branch ET [29]. Optical and TR EPR studies on analogous cyanobacterial PS I variants (*Synechocystis sp*. PCC 6803) clearly confirm the assignment of the “slow” phase to the PsaA-branch ET but have to leave undecided the origin of the minor fast phase [34, 35]. Optical data together with EPR data on the photoaccumulated quinone radical-ion in the site directed mutants of PS I from *Chlamydomonas reinhardtii* indicated that mutations in the PsaB polypeptide change the kinetics of the “fast” phase [140, 146-148].

In this study, the $M668N_{PsaB}$ variant does not lead to any TR EPR observations associated with forward ET along the PsaB-branch while the $M688N_{PsaA}$ variant shows significant changes as compared to the wild type. Both these results are consistent with previous study on the $M688L_{PsaA}$ and $M668L_{PsaB}$ variants, where the effect in the $M688L_{PsaA}$ variant was only observed. Since the environments of the two A_0 chlorophyll molecules in the PsaA- and PsaB-branches are nearly identical, these results correlate with highly asymmetric ET along the PsaA-branch in cyanobacterial PS I. Interpretation of the spectral changes in the $M688N_{PsaA}$ and $M688L_{PsaB}$ variants is based on the fact that mutation of the MN either ML causes significant changes in the electric and possibly other properties of the primary acceptor A_0 site which alter the kinetics of ET along the PsaA-branch.

10. Summary

The work presented in this dissertation focuses on the better understanding of the specific electron transfer properties in Photosystem I. Multifrequency TR EPR spectroscopy was applied to characterise spin polarisation pattern of the functional light-induced intermediate states of the sequential $P_{700}^{\bullet +}A_1^{\bullet -}$ and $P_{700}^{\bullet +}(FeS)^-$ RP states created during charge separation in Photosystem I. The primary task of my study was to determine the specific protein-cofactor interactions allowing quinone to serve as an efficient secondary acceptor in the A_1-binding site of Photosystem I. Part A is devoted to the investigations of structural and functional properties of selected quinones in the A_1-binding site of Photosystem I. Part B addresses the question how specific properties of the protein environment control the electron transfer properties of the individual acceptors (A_0, A_1, F_X)?

The first specific protein-cofactor interaction of the quinone cofactor is hydrogen-bonding. The X-ray structure model of Photosystem I at 2.5 Å resolution identifies for the ground state a single hydrogen bond from the backbone leucine residue to one of the carbonyl groups of the quinone acceptor in the A_1-binding site. Experimental evidence obtained in Chapter 5 indicates that the motif of a single-sided hydrogen bond applies also to the functional charge separated state $P_{700}^{\bullet +}A_1^{\bullet -}$ as well. The valence model suggests a highly asymmetric spin density distribution over the quinone ring induced by the single hydrogen bond. The spin densities are probed for the most sensitive ring carbon positions (C_1 and C_4) by introducing selectively ^{13}C isotope labelled 2-methyl-1,4-naphthoquinone in the A_1-binding site of Photosystem I. The spin densities are evaluated from the measured ^{13}C

hyperfine tensor components. Comparison to the ^{13}C hyperfine tensor components of other well studied quinone-binding sites reveals the uniqueness of the A_1-binding site in terms of the highest asymmetry realized in Photosystem I.

In order to investigate the role of the terminal acceptors, three iron-sulphur clusters, on the A_1-binding site properties, the *menB rubA* double mutant was available. In this double mutant the more weakly bound plastoquinone-9 replaces the native phylloquinone acceptor and all iron-sulphur clusters together with the PsaC, PsaE, PsaD protein subunits are missing. It was established that these modifications do not change the structural integrity of the A_1-binding site (Chapter 6). All essential protein-quinone interactions such as the single hydrogen bond from the backbone protein and π-staking with tryptophan residue are conserved. Plastoquinone-9 is oriented in a similar fashion as phylloquinone in the wild type (the same orientation of the quinone head group). However, observation of a significant triplet $^3P_{700}$ spectra contribution as a recombination product from the precursor $P_{700}^{\bullet+}A_0^{\bullet-}$ radical pair indicates that a part of the A_1-binding sites remains empty. In order to check the integrity of the unoccupied A_1-binding sites, quinones with different binding affinity were incorporated into the A_1-binding site of Photosystem I isolated from the *menB rubA* double mutant. Plastoquinone-9 can readily be replaced by 2-methyl-1,4-naphthoquinone. Moreover, 2-methyl-1,4-naphthoquinone can occupy nearly all of the empty A_1-binding sites. Thus, the *menB rubA* double mutant is well suited for quinone replacement studies.

In particular, 9,10-anthraquinone was selected for incorporation into the A_1-binding site of Photosystem I, because it is expected to provide an even more negative redox potential in the A_1-binding site than native phylloquinone (Chapter 7). One of the key features of the A_1-binding site in Photosystem I is its highly negative redox potential between -750 and -810 meV. Other well studied quinone binding sites have much more positive redox potential like the Q_A-binding in bacterial reaction center with -130 meV. Incorporation of 9,10-anthraquinone with the more negative redox potential than native phylloquinone is expected to increase the redox potential difference between A_1 and F_X. The consequence is an acceleration of the corresponding electron transfer step. Correspondingly, the redox potential difference between A_0 and A_1 will decrease and electron transfer slows down. This would be the first example where the transient signals of the sequential $P_{700}^{\bullet+}A_1^{\bullet-}$ and $P_{700}^{\bullet+}F_X^-$ radical pair states carry simultaneously information on the two consecutive electron transfer steps from $A_0^{\bullet-}$ to A_1 and from $A_1^{\bullet-}$ to F_X and can be investigated within the same TR EPR study. The observed changes in the electron transfer kinetics from $A_0^{\bullet-}$ to A_1 to F_X correspond to the expected shift of the redox potential of 9,10-anthraquinone to the more negative value by about 100 meV. Indeed, the kinetics of both electron transfer processes $A_0^{\bullet-}$ to A_1 to F_X become TR EPR accessible in this case. Moreover, a comparison of spin polarisation patterns of the $P_{700}^{\bullet+}A_1^{\bullet-}$ radical pair state in the presence and absence of the iron-sulphur clusters indicates that the $A_0^{\bullet-}$ to A_1 electron transfer process is slower and the redox potential of 9,10-anthraquinone in the A_1-binding site of Photosystem I is more negative in the presence of the first iron-sulphur clusters F_X. This is consistent with the fact that the partial negative charge of the $[Fe_4S_4(SH_3)_4]^{2-}$ state associated with F_X contributes to the redox potential of A_1. However, the effect is much smaller than predicted by electrostatic calculations.

The main contribution to the redox potential of cofactors is expected to come from electrostatic interactions between partial charges of the protein environment and the electron cofactors. Electrostatic calculations predicted that partial negative charges associated with specific aspartate residues play a significant role in modulating the redox potentials of A_1 and F_X. To test this prediction, the side chains of the specific B-side residues 575_{PsaB} and 566_{PsaB} were changed from negatively charged aspartate (D) to neutral alanine (A) and to positively charged lysine (K). As described in Chapter 8, for the $D575_{PsaB}$ variants the rate of electron transfer from $A_1^{\bullet-}$ to F_X is observed to decrease slightly according to the sequence D/A/K. In the $D566_{PsaB}$ variants, the small but clearly opposite effect of a slight increase in the rate is observed following the same sequence D/A/K. These results are consistent with the expectation that by changing these residues the redox potential of nearby cofactors will be shifted to more positive values and that the magnitude of this shift will depend on the distance between the cofactors and the residues being changed. Thus, the redox potential of A_1 experiences a larger shift than F_X for the $D575_{PsaB}$ variants while F_X will experience a larger shift than A_1 for the $D566_{PsaB}$ variants. As a result, the driving energy for the electron transfer step from $A_1^{\bullet-}$ to F_X will be diminished in the former and increased in the latter by about 20 meV. Therefore, the observed contributions from the electrostatic protein environment turn out to go in the right direction but to be very small, in line with the expectation that individual changes by point mutants will be compensated by an adjustment in the rest of the protein lattice. Each of the specific changes is expected to contribute very little to the highly negative quinone redox potential in the A_1-binding site of Photosystem I versus the Q_A site in type II reaction centers. However, the results are consistent with the expectation that the negative redox potential is made up from the sum of many small contributions.

One part of this study addresses the directionality issue. Presence of two quasi C_2-symmetric chains of cofactors the PsaA- and PsaB-branches raises the question whether two branches are active in electron transfer. The possibility to study the directionality of electron transfer was a scenario for side-directed mutations on the level of the primary electron acceptor A_0. In this work, the axial methionine ligands to the central Mg^{2+} atoms of A_{0A} and A_{0B} are replaced by asparagines (N) or leucine (L) in *Synechocystis* sp. PCC 6803. In comparison to the wild type, the PsaA-branch mutant shows increase in the effective lifetime of the precursor $P_{700}^{\bullet+}A_0^{\bullet-}$ radical pair state from 50 ps to the 1-2 ns. As a consequence spin dynamics (singlet-triplet mixing) occurs and causes the observed changes in spin polarisation patterns of the subsequent $P_{700}^{\bullet+}A_1^{\bullet-}$ radical pair state. While the PsaB-branch mutant does not show any effects on the spin polarisation pattern relative to the wild type. These results are consistent with asymmetric electron transfer along PsaA-branch as was confirmed in several previous studies for the cyanobacterial Photosystem I.

Appendix I

Theoretical Approach for Simulation of TR EPR Spectra

The spin density matrix obeys the kinetic equation in frequency units [64, 96, 132]:

$$\begin{aligned}\frac{\partial \hat{\rho}(t)}{\partial t} &= -i\left[\hat{H}, \hat{\rho}(t)\right] + \Gamma \hat{\rho}(t) - \\ &- \frac{1}{2}K_S(\hat{\Pi}_S \hat{\rho}(t) + \hat{\rho}(t)\hat{\Pi}_S) - \frac{1}{2}K_T(\hat{\Pi}_T \hat{\rho}(t) + \hat{\rho}(t)\hat{\Pi}_T) - K_{ET}\hat{\rho}(t)\end{aligned} \qquad (I.1)$$

Here the first term displays the spin dynamic induced by $\hat{H}_0'$ and EPR transition by $\hat{H}_{mw}$ as was considered in details in 3.1.1. The second term describes relaxation process. The third and fourth terms are contributions from recombination of RP with the rate constant K_S and K_T from either the singlet or the triplet state, respectively. The final terms describes ET to the next acceptor with the rate constant K_{ET}. $\hat{\Pi}$ corresponds to the projection operator to the singlet or triplet state of the spin.

In the Liouville representation the kinetics equation of the spin density matrix of RP can be rewritten in the following form:

$$\frac{\partial \hat{\rho}(t)}{\partial t} = \hat{L}\hat{\rho}(t) \qquad (I.2)$$

where $\hat{L}$ is the Liouville operator comprising all terms in equation (3.32).

Thus, the spin density matrix $\hat{\rho}_1(t)$ of the first $P_{700}{}^{\bullet+}A_0{}^{\bullet-}$ RP obeys the equation [95]:

$$\frac{\partial \hat{\rho}_1(t)}{\partial t} = \hat{L}_1 \hat{\rho}_1(t) \tag{I.3}$$

L_1 is the Liouville operator of the primary $P_{700}{}^{\bullet+}A_0{}^{\bullet-}$ RP.

The spin dynamics in the second $P_{700}{}^{\bullet+}A_1{}^{\bullet-}$ RP are treated in the same way:

$$\frac{\partial \hat{\rho}_2(t)}{\partial t} = L_2 \hat{\rho}_2(t) + k_1 \hat{\rho}_1(t) \tag{I.4}$$

where $\hat{\rho}_2(t)$ and L_2 represent the spin density matrix and the Liouville operator of the secondary $P_{700}{}^{\bullet+}A_1{}^{\bullet-}$ RP. The first term in equation (I.4) described the spin dynamic in the second $P_{700}{}^{\bullet+}A_1{}^{\bullet-}$ RP is similar to equation (I.3) while the last term is the flux of the density matrix from the primary $P_{700}{}^{\bullet+}A_0{}^{\bullet-}$ RP. The form of this term implies that the ET is non-adiabatic process. As a result, immediately after ET from the primary acceptor $A_0{}^{\bullet-}$ to the secondary acceptor A_1 the spin density matrix of the secondary $P_{700}{}^{\bullet+}A_1{}^{\bullet-}$ RP inherits the density matrix of the precursor $P_{700}{}^{\bullet+}A_0{}^{\bullet-}$ RP. Thus the last term in equation (I.4) represents the polarisation transfer from the primary $P_{700}{}^{\bullet+}A_0{}^{\bullet-}$ RP to the secondary $P_{700}{}^{\bullet+}A_1{}^{\bullet-}$ RP [95].

The intensity of the time dependent EPR signal is proportional to [95]:

$$I(EPR) = Tr\left[\hat{\rho}_1(t)(\hat{S}_{Py} + \hat{S}_{A0y})\right] + Tr\left[\hat{\rho}_2(t)(\hat{S}_{Py} + \hat{S}_{A1y})\right] \tag{I.5}$$

Here the first and the second terms correspond to the EPR signals of the $P_{700}{}^{\bullet+}A_0{}^{\bullet-}$ primary and secondary $P_{700}{}^{\bullet+}A_0{}^{\bullet-}$ RPs.

Spin polarized EPR spectrum should be calculated by solving of equations (I.3), (I.4) together with (I.5) for an appropriate number of field steps. Polarized TR EPR spectrum is recorded as a digital boxcar spectrum. To model this, the theoretical EPR spectrum should be calculated by integration in the some time window τ_a [95, 96]:

$$
\begin{aligned}
&\hat{\rho}_1(0) = -i\left[\hat{H}_0 + \hat{H}(t)_{mw}, \langle\hat{\rho}_1(t)\rangle\right] + \hat{\Gamma}\langle\hat{\rho}_1(t)\rangle - \\
&-\frac{1}{2}K_S(\hat{\Pi}_S\langle\hat{\rho}_1(t)\rangle + \langle\hat{\rho}_1(t)\rangle\hat{\Pi}_S) - \frac{1}{2}K_T(\hat{\Pi}_T\langle\hat{\rho}_1(t)\rangle + \langle\hat{\rho}_1(t)\rangle\hat{\Pi}_T) - (k_1 + \frac{1}{\tau_a})\langle\hat{\rho}_1(t)\rangle \\
&-k_1\langle\hat{\rho}_1(t)\rangle = -i\left[\hat{H}_0 + \hat{H}(t)_{mw}, \langle\hat{\rho}_2(t)\rangle\right] + \hat{\Gamma}\langle\hat{\rho}_2(t)\rangle - \\
&-\frac{1}{2}K_S(\hat{\Pi}_S\langle\hat{\rho}_2(t)\rangle + \langle\hat{\rho}_2(t)\rangle\hat{\Pi}_S) - \frac{1}{2}K_T(\hat{\Pi}_T\langle\hat{\rho}_2(t)\rangle + \langle\hat{\rho}_2(t)\rangle\hat{\Pi}_T) - (k_2 + \frac{1}{\tau_a})\langle\hat{\rho}_2(t)\rangle
\end{aligned}
\tag{I.6}
$$

with $\langle\hat{\rho}_1(t)\rangle = \int \exp(-\frac{t}{\tau_a})\hat{\rho}_1(t)dt$ and $\langle\hat{\rho}_2(t)\rangle = \int \exp(-\frac{t}{\tau_a})\hat{\rho}_2(t)dt$. k_1, k_2 are the ET constant from the first to the second RP ($P_{700}{}^{\bullet+}A_0{}^{\bullet-}$ to $P_{700}{}^{\bullet+}A_1{}^{\bullet-}$) and from the second to the third RP ($P_{700}{}^{\bullet+}A_1{}^{\bullet-}$ to $P_{700}{}^{\bullet+}F_X{}^{\bullet-}$), respectively.

Then intensity of the EPR spectra are calculated as [95]:

$$
\begin{aligned}
I_1(P_{700}^{+\cdot}A_0^{-\cdot}) &= Tr\left[\langle\hat{\rho}_1(t)\rangle(\hat{S}_{Py} + \hat{S}_{A0y})\right] \\
I_2(P_{700}^{+\cdot}A_1^{-\cdot}) &= Tr\left[\langle\hat{\rho}_2(t)\rangle(\hat{S}_{Py} + \hat{S}_{A1y})\right]
\end{aligned}
\tag{I.7}
$$

The program for the spin correlated RP was written in Mathlab by Prof. Kev Salikhov (Zavoiskiy Physical-Technical Institute, Kazan, Russia).

Powder EPR spectrum is calculated by adding up the contributions of all evenly distributed orientations relative to the external magnetic field B_0 (a spiral sampling algorithms was used [44]). Additionally, in order to take into account all small (<9 MHz) hfc interactions of paramagnetic particles $P_{700}{}^{\bullet+}$, $A_0{}^{\bullet-}$, $A_1{}^{\bullet-}$ in the spectra an inhomogeneous broadenings of the EPR transition were added by two procedures. In the first procedure, inhomogeneous broadening was generated by adding to the Zeeman frequency of paramagnetic particle ($P_{700}{}^{\bullet+}$, $A_0{}^{\bullet-}$, $A_1{}^{\bullet-}$) a random term distributed according to a Gaussian [95, 96]. In the second procedure, intensities of the EPR signal calculated for a chosen magnetic field B_0 in (3.42) were modelled with a line shape corresponding to a Gaussian distribution of the hfc interaction induced by local magnetic fields for each paramagnetic particle [95, 96]. Moreover, inhomogeneous width parameter was different for each paramagnetic particle ($P_{700}{}^{\bullet+}$, $A_0{}^{\bullet-}$, $A_1{}^{\bullet-}$).

Relaxation

The relaxation of each individual spin in the basis of the eigenfunctions of $\hat{S}_z$ operator ($\hat{S}_{Pz}, \hat{S}_{Az}$) is represented by the following equations:

$$\begin{aligned}
\frac{d\rho_{1/2,-1/2}}{dt} &= -W_2\rho_{1/2,-1/2} \\
\frac{d\rho_{-1/2,1/2}}{dt} &= -W_2\rho_{-1/2,1/2} \\
\frac{d\rho_{1/2,1/2}}{dt} &= -W_1(\rho_{1/2,1/2} - p\rho_{-1/2,-1/2}) \\
\frac{d\rho_{-1/2,-1/2}}{dt} &= W_1(\rho_{1/2,1/2} - p\rho_{-1/2,-1/2})
\end{aligned} \tag{I.8}$$

The quantity p serves to describe the populations of the states in equilibrium and is determined by the Boltzman distribution over the Zeeman states of each individual spin:

$$p = exp(-\frac{\hbar\omega}{kT}) \tag{I.9}$$

The transverse relaxation is characterised by the time $T_2 = \frac{1}{W_2}$ and the longitudinal relaxation time by $\mathrm{T}_1 = \frac{1}{\mathrm{W}_1(1+\mathrm{p})}$.

The relaxation super operator $\hat{\Gamma}_i$ for a single spin *i* can be rewritten in the form:

$$\frac{d\rho_i}{dt} = \hat{\Gamma}_i\,\rho_i$$

with

$$\hat{\Gamma}_i = \begin{pmatrix} -W_{1i} & 0 & 0 & pW_{1i} \\ 0 & -\frac{1}{T_{2i}} & 0 & 0 \\ 0 & 0 & -\frac{1}{T_{2i}} & 0 \\ W_{1i} & 0 & 0 & -pW_{1i} \end{pmatrix} \tag{I.10}$$

For the two-spin systems, the relaxation super operator $\hat{\Gamma}_i$ as:

$$\hat{\Gamma}_i = \hat{\Gamma}_P \otimes 1 + 1 \otimes \hat{\Gamma}_A \tag{I.11}$$

References

1. Schlodder E., Falkenberg K., Gergeleit M., Brettel K. *Biochemistry*, 37. **1998**, 9466-9476.
2. Golbeck J. H. *Photosystem I: the Light-Driven Plastocyanin:Ferredoxin Oxidoreductase.* Springer. **2006**.
3. Fromme P., Jordan P., Krauß N. *Biochim. Biophys. Acta*, 1507. **2001**, *1-3*, 5-31.
4. Jordan P., Fromme P., Witt T.H., Klukas O., Saenger W., Krauss N. *Nature*, 411. **2001**, 909-917.
5. Ben-Shem A., Frolow F., Nelson N. *Nature*, 426. **2003**, 630-635.
6. Jordan P., *Doctoral Thesis*. 2001, Free University Berlin, Germany.
7. Byrdin M., Jordan P., Krauss N., Fromme P., Stehlik D., Schlodder E. *Biophys. J.*, 83. **2002**, *1*, 433-457.
8. Breton J., Naberdryk E., Leibl W. *Biochemistry*, 38. **1999**, 11585-11592.
9. Breton J., Xu W., Diner B. A., Chitnis P. R. *Biochemistry*, 41. **2002**, 11200-11210.
10. Kass H., Bittersmannweidlich E., Andreasson L. E., Bonigk B., Lubitz W. *Chem. Phys.*, 194. **1995**, 419-432.
11. Kass H., Fromme P., Witt T.H., Lubitz W. *J. Phys. Chem. B*, 105. **2001**, 1225-1239.
12. Pantelidou M., Chitnis P., Breton J. *Biochemistry*, 43. **2004**, 8380-8390.
13. Sieckman I., van der Est A., Bottin H., Setif P., Stehlik D. *FEB Lett.* **1991**, *284*, 98-102.
14. Plato M., Krauß N., Fromme P., Lubitz W. *Chem. Phys.*, 294. **2003**, 483-499.
15. Brettel K. *Biochim. Biophys. Acta Bioenergetics*, 1318. **1997**, 322-273.
16. Hasting G., Kleinherenbrink F. A., Lin S., Blankenship R.E. *Biochemistry*. **1994**, *33*, 3185-3192.
17. Kumazaki S., Iwaki M., Ikegami I., Kandori H., Yoshihara K., Itoh S. *J. Phys. Chem.*, 98. **1994**, 200-206.
18. Kumazaki S., Kandori H., Petek H., Yoshihara K., Ikegami I. *J. Phys. Chem.*, 98. **1994**, 10335-10342.
19. Gibasiewicz K., Ramesh V. M., Lin S., Redding K., Woodbury N. W., Webber A. N. *Biophys. J.*, 85. **2003**, 2547-2559.
20. Hasting G., Hoshina S., Webber A. N., Blankenship R.E. *Biochemistry*. **1995**, *34*, 15512-15522.
21. Muller M. G., Niklas J., Lubitz W., Holzwarth A. R. *Biophys. J.*, 85. **2003**, 3899-3922.
22. Brettel K., and Vos M.H. *FEBS Lett.*, 447. **1999**, *2-3*, 315-317.
23. Mi D. H., Lin S., Blankenship R. E. *Biochemistry*, 38. **1999**, 15231-15237.
24. Savikhin S., Xu W., Martinsson P., Chitnis P., Struve W. S. *Biochemistry*, 40. **2001**, 9282-9290.
25. Brettel K. *FEBS Lett.*, 239. **1988**, *1*, 93-98.
26. Bock C.H., van der Est A., Brettel K., Stehlik D. *FEBS Lett.*, 247. **1989**, 91-96.
27. Sétif P., and Brettel K. *Biochemistry*, 32. **1993**, 7846-7854.
28. Leibl W., Toupance B., Breton J. *Biochemistry*, 34. **1995**, 10235-10237.
29. Joliot P., and Joliot A., in *Biochemistry*. 1999. p. 11130-11136.
30. Brettel K., and Leibl W. *Biochim. Biophys. Acta*, 1507. **2001**, *1-3*, 100-114.
31. van der Est A., Bock. C., Golbeck J. H., Brettel K., Sétif P., Stehlik D. *Biochemistry*, 33. **1994**, 11789-11797.

32. Shen G., Antonkine M. L., van der Est A., Vassiliev I. R., Brettel K., Bittl R., Zech S., Zhao J., Stehlik D., Bryant D. A., Golbeck J. H. *J. Biol. Chem.*, 277. **2002**, 20355-20366.
33. Shen G., Zhao J., Reimer S. K., Antonkine M. L., Cai Q., Weiland S. M., Golbeck J. H., Bryant D. A. *J. Biol. Chem.*, 277. **2002**, 20343-20354.
34. Xu W., Chitnis P., Valieva A., van der Est A., Pushkar Y. N., Krzystyniak M., Teutloff C., Zech S., Bittl R., Stehlik D., Zybailov B., Shen G., Golbeck J. H. *J. Biol. Chem.*, 278. **2003**, 27864-27875.
35. Xu W., Parag R. R., Valieva A., van der Est A., Brettel K., Guergova-Kuras M., Pushkar Y. N., Zech S. G., Stehlik D., Shen G., Zybailov B., Golbeck J. H. *J. Biol. Chem.*, 278. **2003**, 27876-27887.
36. Bittl R., and Zech S. *J. Phys. Chem. B*, 101. **1997**, 1429-1436.
37. Zech S. G., Hofbauer W., Kamlowski A., Fromme P., Stehlik D., Lubitz W., Bittl R. *J. Phys. Chem.*, 104. **2000**, 9728-9739.
38. Fischer N., Boundreau E., Hippler M., Drepper F., Haehnel W., Rochaix J.D. *Biochemistry*, 38. **1999**, 5546-5532.
39. Fischer N., Sétif P., Rochaix J.D. *J. Biol. Chem.*, 274. **1999**, 23333-23340.
40. Lakshimi K. V., Jung Y. S., Golbeck J. H., Brudvig G. W. *Biochemistry*, 38. **1999**, 13210-13215.
41. Itoh S., Iwaki M., Ikegami I. *Biochim. Biophys. Acta*, 1507. **2001**, 115-138.
42. Iwaki M., Kumazaki S., Yoshihara K., Erabi T., Itoh S. *J. Phys. Chem.*, 100. **1996**, 10802-10809.
43. Zavoisky E. *J. of Physics USSR*. **1945**, *9*, 211-216.
44. Weil J. A., Bolton J. R., Wertz J. E., *Electron Paramagnetic Resonance. Elementary Theory and Practical Applications*. 1994: Willey J. & Sons, New York.
45. Abragam A., *The Principles of Nuclear Magnetims*. 1961: Oxford University Press, New York.
46. Atherton N. M. 1993: Ellis Horwood Ltd. and RTR Printice Hall, New York.
47. Carrigton A., and Mclachlan A. D. *Introduction to Magnetic Resonance.* Harper and Row, New York. **1967**.
48. Gordy W., *Theory and Applications of Electron Spin Resonance*. 1979: Willey J. & Sons, New York.
49. Gendel J., Freed J. H., Fraenkel G. K. *J. Chem. Phys.*, 37. **1962**, 1832-2841.
50. Karplus M., and Fraenkel G. K. *J. Chem. Phys.*, 35. **1961**, 1312-1323.
51. Bargon J., Fischer H., Johnsen U. *Zeitschrift für Naturforschung, Teil A: Astrophysik, Physik und Physikalische Chemie* 10. **1967**, *22*, 1551-1555.
52. Kaptein R., Dijkstra K., Nicolay K. *Nature*, 274. **1978**, 293-294.
53. Muus L. T., Atkins P. W., Mclauchlan K.A., Pedersen J. B., *Chemical induced magnetic polarisation*. 1977: ed. Reidel, Dordrecht.
54. Bittl R., and Kothe G. *Chem. Phys. Lett.*, 177. **1991**, *6*, 547-553.
55. Salikhov K. M. *10 Lextures of Spin Chemistry. UNIPRESS, Kazan*. **2000**.
56. Tang J., Thurnauer M. C., Norris J. R. *Chem. Phys. Lett.*, 219. **1994**, 283-290.
57. Salikhov K. M., Bock C. H., Stehlik D. *Appl. Magn. Reson.*, 1. **1990**, 195-211.
58. Buckley C. D., Hunter, D. A., Hore P. J., Mclauchlan K. A. *Chem. Phys. Lett.*, 135. **1987**, 307-312.
59. Hoff A. J., *Advanced EPR. Aplication in Biology and Biochemistry*. 1989: Elsevier, Amsterdam.
60. Hore P. J., Hunter D. A., Mckie C.D., Hoff. A. J. *Chem. Phys. Lett.* , 137. **1987**, *6*, 495-500.
61. Stehlik D., Bock C., Petersen J. *Phys. Chem*, 93. **1989**, 1612.

62. Hore P. J. *European EPR Summer School and COST Training School.* 2005. Universität Frankfurt am Main, Wiesbaden, Germany.
63. Carrigton A., and Mclachlan A. D. *Introduction to Magnetic Resonance.* Harper and Row, New York. **1961**.
64. Kandrashkin Yu. E., Salikhov K. M., Stehlik D. *Appl. Magn. Reson.*, 12. **1997**, 141-166.
65. Zwanenburg G., and Hore P. J. *Chem. Phys. Lett.*, 203. **1993**, 65-74.
66. Kothe G., Weber S., Ohmes E., Thurnauer M. C., Norris J. R. *Chem. Phys. Lett.*, 177. **1991**, 547-553.
67. Kothe G., Weber S., Ohmes E., Thurnauer M. C., Norris J. R. *J. Am. Chem. Soc.*, 116. **1994**, 7729-7734.
68. Kothe G., Weber S., Ohmes E., Thurnauer M. C., Norris J. R. *J. Phys. Chem.*, 98. **1994**, 2706-2712.
69. *Org. Reaction.* **1942**, *I*, 251.
70. Bathi A., and Kale N. *Angew. Chem.*, 79. **1967**, 1100.
71. Premasagar V., Palaniswamy V. A., Eisenbraun E. J. *J. Org. Chem.*, 46. **1981**, 2974-2976.
72. Biggins J., and Mathis P., in *Biochemistry*. 1988. p. 1494-1500.
73. Zybailov B., van der Est A., Zech S. G., Teutloff C., Wade Johnson T., Shen G., Bittl R., Stehlik D., Chitnis P. R, Golbeck J.H. *J. Biol. Chem.*, 275. **2000**, *12*, 8531-8539.
74. Semenov A.Y., Vassiliev I. R., van der Est A., Mamedov M.D., Zybailov B., Shen G., Stehlik D., Diner B. A., Chitnis P. R., Golbeck J. H. *J. Biol. Chem.*, 275. **2000**, 23429-23438.
75. Cohen R., *Doctoral Thesis*. 2004, Pennsylvania State University, USA.
76. Vassiliev I. R., Yu J. P., Jung Y. S., Schulz R., Ganago A. O., Mcintosh L., Golbeck J. H. *J. Biol. Chem.*, 274. **1999**, 9993-10001.
77. van der Est A., Bock. C., Golbeck J. H., Brettel K., Setif P., Stehlik D. *Biochemistry*. **1994**, *33*, 11789-11797.
78. Bock C.H., van der Est A., Brettel K., Stehlik D. *FEBS Lett.* **1989**, *247*, 91-96.
79. Pushkar Y. N., Golbeck J. H., Stehlik D., Zimmermann H. *J. Phys. Chem.*, 108. **2004**, 9439-9448.
80. Wade Johnson T., Zybailov B., Daniel Jones A., Bittl R., Stehlik D., Golbeck J. H., Chitnis P. R. *J. Biol. Chem.*, 276. **2001**, 39512-39521.
81. Sakuragi Y., Zybailov B., Shen G., Daniel Jones A., Chitnis P. R., van der Est A., Bittl R., Zech S., Stehlik D., Golbeck J. H., Bryant D. A. *Biochemistry*, 41. **2002**, 394-395.
82. Deligiannakis Y., and Rutherford A. W. *Biochim. Biophys. Acta*, 1507. **2001**, 226-246.
83. Hanley J., Deligiannakis Y., Macmillan F., Bottin H., Rutherford A. W. *Biochemistry*, 36. **1997**, 11543-11549.
84. Kamlowski A., Altenberg-Greulich B., van der Est A., Zech S. G., Bittl R., Fromme P., Lubitz W., Stehlik D. *J. Phys. Chem. B*, 102. **1998**, 8278-8287.
85. Fursman K., Teutloff C., Bittl R. *J. Phys. Chem. B*, 106. **2002**, 9679-9686.
86. Lubitz W., and Feher G. *Appl. Magn. Reson.*, 17. **1999**, 1-48.
87. van den Brink J. S., Spoyalov A. P., Gast P., Van Liemt W. B. S., Raap J., Lugtenburg J., Hoff A. J. *FEBS Lett.*, 353. **1994**, 273.
88. Grimaldi S., Ostermann T., Weiden N., Mogi T., Miyoshi H., Ludwig B., Michel H., Prisner T., Macmillan F. *Biochemistry*, 42. **2003**, 5632-5639.
89. Kacprzak S., Kaupp M., Macmillan F. *J. Am. Chem. Soc.*, 128. **2006**, 5659-5671.
90. Flores M., Isaacson R., Abresch E., Calvo R., Lubitz W., Feher G. *Biophys. J.*, 90. **2006**, 3356-3362.
91. Pushkar Y. N., Ayzatulin O., Stehlik D. *Appl. Magn. Reson.*, 28. **2005**, 195-211.

92. Reiter R.C., Stevenson G.R., Wang Z. Y. *J. Phys. Chem.*, 94. **1990**, 5717-5720.
93. Pushkar Y. N., Zech S. G., Stehlik D., Brown S., van der Est A., Zimmermann H. *J. Phys. Chem.*, 106. **2002**, 12052-12058.
94. Rigby S. E., Evans M. C., Heathcote R. *Biochemistry*, 35. **1996**, 6651-6656.
95. Salikhov K. M., Pushkar Y. N., Golbeck J. H., Stehlik D. *Appl. Magn. Reson.*, 24. **2003**, 467-482.
96. Salikhov K. M., Zech S. G., Stehlik D. *Mol. Phys.*, 100. **2002**, 1311-1321.
97. O'Malley P. J. *Biochim. Biophys. Acta*, 1411. **1999**, 101-113.
98. Epel B., Niklas J., Sinnecker S., Zimmermann H., Lubitz W. *J. Phys. Chem. B*, 110. **2006**, 11549-11560.
99. van den Brink J. S., Spoyalov A. P., Gat P., Vamliemt W. B. S., Raap J., Lugtenburg J., Hoff A. J. *FEBS Lett.*, 353. **1994**, 273-276.
100. Kacprzak S., and Kaupp M. *J. Phys. Chem. B*, 108. **2004**, 2464-2469.
101. Sinnecker S., Reijerse E., Neese F., Lubitz W. *J. Am. Chem. Soc.*, 126. **2004**, 3280-3290.
102. Fritscher J., Prisner T., Macmillan F. *App. Mag. Res.* **2006**, in press.
103. Kaupp M. *Biochemistry*, 41. **2002**, 2985-2900.
104. Teutloff C., *Doctoral Thesis*. 2003, Technische Universität Berlin, Germany.
105. Teutloff C., Hofbauer W., Zech S. G., Stein D., Bittl R., Lubitz W. *Appl. Magn. Res.*, 21. **2001**, 363-379.
106. Rohrer M., Gast P., Möbius K., Prisner T. F. *Chem. Phys. Lett.*, 259. **1998**, 523-530.
107. Schnegg A., Fuhs M., Rohrer M., Lubitz W., Prisner T. F., Möbius K. *J. Phys. Chem. B*, 106. **2002**, 9454-9462.
108. Ashnagar A., Bruce J. M., Dutton P. L., Prince R. C. *Biochim. Biophys. Acta*, 801. **1984**, *3*, 351-359.
109. Swallow A. J., *Function of Quinones in Energy Conserving Systems*. 1982: Academic Press, New York. 59-72.
110. Ishikita H., and Knapp E. W. *J. Biol. Chem.*, 278. **2003**, 52002-52011.
111. Stowell M. H., Mcphillips T M., Rees D. C., Soltis S. M., Abresch E., Feher G. *Science* 276. **1997**, 812.
112. Pushkar Y. N., Stehlik D., van Gastel M., Lubitz W. *J. Mol. Struct.*, 700. **2004**, 233-241.
113. Flores M., Asaacson R., Abresch E., Calvo R., Lubitz W. *Chem. Phys.*, 294. **2003**, 401-413.
114. Niklas J., *Doctoral Thesis*. 2006, Technische Universität Berlin, Germany.
115. Antonkine M. L., Jordan P., Fromme P., Golbeck J. H., Stehlik D. *J. Mol. Biol.*, 327. **2003**, *3*, 671-697.
116. Budil D. E., and Thurnauer M. C. *Biochim. Biophys. Acta*, 1057. **1991**, *1*, 1-41.
117. Kamlowski A., Frankemöller L., van der Est A., Stehlik D., Holzwarth A. R. *Ber. Bunsenges Phys. Chem.*, 100. **1996**, 2045-2051.
118. Frank H. A., and Cogdell R. J. *Photochem. Photobiol.*, 63. **1996**, 257-264.
119. Frank H. A., Mclean M. B., Sauer K. *Proc. Natl. Acad. Sci. U. S. A*, 76. **1979**, 5124-5128.
120. Schlodder E., Paul A., Cetin M. in *PS 2001 Proceedings, 12th International Congress on Photosynthesis*. 2001. Brisbane, Australia.
121. Bittl R., Schlodder E., Geisenheimer I., Lubitz W., Cogdell R. J. *J. Phys. Chem. B*, 105. **2001**, 5525-5535.
122. Burghaus O., Plato M., Rohrer M., Möbius K., Lubitz W. *J. Phys. Chem.*, 97. **1993**, 7639-7647.
123. van der Est A., Sieckmann I., Lubitz W., Stehlik D. *Chem. Phys.*, 194. **1995**, 349-359.

124. Hulsebosch R. J., Borovykh I. V., Paschenko S. V., Gast P., Hoff A. J. *J. Phys. Chem. B*, 103. **1999**, 6815-6823.
125. Gunner M .R., and Dutton P. L. *J. Am. Chem. Soc.*, 111. **1989**, 3400-3412.
126. Xu Q., Baciou L., Sebban P., Gunner M. R. *Biochemistry*, 41. **2002**, 10021.
127. Xu Q., and Gunner M .R. *J. Phys. Chem. B*, 104. **2000**, 8035.
128. Prince R. C., Dutton P. L., Bruce J. M. *FEBS Lett.*, 160. **1983**, 273-276.
129. van der Est A. *Biochim. Biophys. Acta*, 1507. **2001**, 212-225.
130. Lueneberg J., Fromme P., Jekow P., Schlodder E. *FEBS Lett.*, 338. **1994**, 197-202.
131. Moenne-Loccoz P., Heathcote P., Mclachlan D. J., Berry M. C., Davis I. H., Evans M. C. *Biochemistry*, 33. **1994**, 10037-10042.
132. Kandrashkin Yu. E., Salikhov K. M., van der Est A., S. D. *Appl. Magn. Reson.*, 15. **1998**, 417-447.
133. Kandrashkin Yu. E., Vollmann W., Stehlik D., Salikhov K. M., van der Est A. *Mol. Phys.*, 100. **2002**, 1431-1443.
134. Cohen R., Shen G., Golbeck J. H., Xu W., Chitnis P. R., Valieva A., van der Est A., Pushkar Y. N., Stehlik D. *Biochemistry*, 43. **2004**, 4741-4754.
135. Hartwitch G., Lossau H., Michel-Beyerle M. E., Orgodnik A. *J. Phys. Chem. B*, 102. **1998**, 3815-3820.
136. Marcus R. A., and Sutin N. *Biochim. Biophys. Acta*, 811. **1985**, 265-322.
137. Boudereaux B., Macmillan F., Teutloff C., Agalarov R., Gu F. F., Grimaldi, S., Bittl R., Brettel K., Redding K. *J. Biol. Chem.*, 276. **2001**, *306*, 37299-37306.
138. Fairclough W. V., Forsuth A., Evans M. C., Rigby S. E., Purton S., Heathcote P. *Biochim. Biophys. Acta*, 1606. **2003**, 43-55.
139. Guergova-Kuras M., Boudreaux B., Joliot A., Joliot P., Redding K. *Proc. Natl. Acad. Sci. U. S. A*, 98. **2001**, 4437-4442.
140. Purton S., Stevens D. R., Muhiuddin I. P., Evans M. C., Carter S., Rigby S. E., Heathcote P. *Biochemistry*. **2001**, 2167-2175.
141. Ivashin N., and Larsson S. *Chem. Phys. Lett.*, 375. **2003**, 383-387.
142. Fuijta I., Davis M. S., Fajer J. *J. Am. Chem. Soc.* **1978**, *1978*, 6280-6282.
143. Ramesh V. M., Gibasiewicz K., Lin S., Bingham S. E., Webber A. N. *Biochemistry*, 43. **2004**, 1369-1375.
144. Yajing Li., van der Est A., Lucas M. G., Ramesh V. M., Gu F., Petrenko A., Lin S., Webber A. N., Rappaport F., Redding K. *PNAS*, 14. **2006**, 2144-2149.
145. Dashdorj N., Xu W., Cohen R., Golbeck J. H., Savikhin S. *Biophys. J.*, 88. **2005**, 1238-1249.
146. Muhiuddin I. P., Heathcote P., Carter S., Purton S., Rigby S. E., Evans M. C. *FEBS Lett.*, 503. **2001**, 56-60.
147. Rigby S. E., Muhiuddin I. P., Evans M. C., Purton S., Heathcote P. *Biochim. Biophys. Acta*, 1556. **2002**, 13-20.
148. Poluektov O. G., Pashenko S. V., Utschig L. M., Lakshimi K. V., Thurnauer M. C. *J. Am. Chem. Soc.*, 127. **2005**, 11910-11911.

List of own Publications

1. Y. Sakuragi, B. Zybailov, G. Shen, D. A. Bryant, J. H. Golbeck, B. A. Diner, I. Karyagina, J. Pushkar, and D. Stehlik. Recruitment of a Foreign Quinone into the A_1 Site of Photosystem I. Characterization of a *menB rubA* Double Deletion Mutant in *Synochococcus* sp. PCC 7002 Devoid of F_X, F_A, F_B and containing Plastoquinone or Exchanged 9,10-Anthraquinone. *J. Biol. Chem.* 280. **2005**, 12371-12381.

2. Y. N. Pushkar, I. Karyagina, D. Stehlik, S. Brown, and A. van der Est. Recruitment of a Foreign Quinone into the A_1 Site of Photosystem I. Consecutive Forward Electron Transfer from A_0 to A_1 to F_X with Anthraquinone in the A_1 Site as studied by Transient EPR. *J. Biol. Chem.* 280. **2005**, 12382-12390.

3. I. Karyagina, J. H. Golbeck, N. Srinivasan, D. Stehlik and, and H. Zimmermann. Single-Sided Hydrogen-Bonding to the Quinone Cofactor in Photosystem I Probed by Selective ^{13}C-Labelled Naphthoquinones and Transient EPR. *Appl. Mag. Reson.* 30. **2006**, 287-310.

4. I. Karyagina, Y. Pushkar, D. Stehlik, A. van der Est, H. Ishikita, B. Jagannathan, R. Agalarov, and J. H. Golbeck. Contributions of the Distant Protein Environment to the Redox Potentials of the Electron Acceptor A_1 Phylloquinones and the F_X Iron-Sulphur Cluster in Photosystem I. *Biochemistry* 46. **2007**, 10804-10816.

5. I. Karyagina, R. O. Cohen, A. van der Est, J. Golbeck and D. Stehlik. Time Resolved EPR study of the Methionine to Asparagine Mutation of the Ligand to the Electron Acceptor A_0 in *Cyanobacterial* Photosystem I. (in preparation)

Conference Contributions

1. I. Karyagina, Y. N. Pushkar, D. Stehlik. *TR-EPR Study of the Electron-Transfer Properties in Photosytem I with Anthraquinone in the* A_1 *Electron Acceptor Binding Site.* International Symposium of Protein-Cofactor Interactions in Biological Processes, Caputh, May 13-15, 2004.

2. D. Stehlik, Y. Pushkar, I. Karyagina, S. Brown, A. van der Est, D. Bryant, J. H. Golbeck. *Control of Function by Protein-Cofactor Interaction in the Electron Transfer Chain of Photosytem I.* Proceedings of the 13th International Congress of Photosyntesis, Monréal, eds. A. v. d. Est and D.Bruce.1, 25-27, 2005.

3. I. Karyagina, Y. N. Pushkar, D. Stehlik. *TR-EPR Study of the Electron Transfer Properties in Photosytem I with Anthraquinone as Secondary Acceptor.* International Conference of Modern Development of Magnetic Resonance, Kazan, Russia, August 15-20, 2004.

4. I. Karyagina, Y. N. Pushkar, D. Stehlik. *TR-EPR Study of the Electron Transfer Properties in Photosytem I with Anthraquinone in the* A_1*-Binding Site.* VII International Youth Scientific School of Actual Problems of Magnetic Resonance and its Application, Kazan, Russia, August 15-19, 2004.

5. I. Karyagina, R. O. Cohen, A. van der Est, J. H. Golbeck, D. Stehlik *TR EPR Study of Methionine to Asparagine Mutation of the Ligand to the Primary Electron Acceptor* A_0. EUROMAR 2005/EENC 2005, Veldhoven, the Netherlands, July 3-8, 2005.

6. I. Karyagina, R. O. Cohen, A. van der Est, J. H. Golbeck, D. Stehlik *Control of Asymmetric Electron Transfer Kinetics in Cyanobacterial Photosystem I: TR EPR Study of Methionine to Asparagine Mutation of the Ligand to the Primary Electron Acceptor* A_0. European EPR Summer School and COST Training School, Wiesbaden, Germany, July 17-24, 2005.

7. I. Karygina, R. O. Cohen, A. van der Est, J. H. Golbeck, D. Stehlik. *Directionality of Electron Transfer in Cyanobacterial Photosystem I: TR EPR Study of the Methionine to*

Asparagine/Leucine Mutation of the Ligand to the Primary Electron Acceptor A_0. 9th International Symposium on Spin and Magnetic Field Effects in Chemistry and Related Phenomena, Oxford, UK, September 11-17, 2005.

8. I. Karyagina, J. H. Golbeck, A. van der Est, D. Stehlik. *TR EPR Study of Mutations of Asp residues* $D575_{PsaB}$ *and* $D566_{PsaB}$ *to Ala and Lys*. ICMRBC, Göttingen, Germany, August 20-25, 2006.

9. I. Karyagina, J. H. Golbeck, A. van der Est, D. Stehlik *Control of Electron Transfer in Cyanobacterial Photosystem I: TR EPR Study of Asp Mutations of* $D575_{PsaB}$ *and* $D566_{PsaB}$ *to Ala and Lys*. EFEPR-06, Madrid, Spain, September 5-8, 2006.

Abbreviations

A_{xx}, A_{yy}, A_{zz} – principal components of hfc tensor $\tilde{A}$

a_{iso} – isotropic hfc constant

A – absorptive signal

A_0, A_1 – electron acceptor cofactors in Photosystem I

AQ – 9,10- anthraquinone

bo_3-QOX – bo_3-type quinol oxidase

bRC – bacterial reaction center

Chl a – chlorophyll *a* molecule

^{3}Chl *a* – triplet state of chlorophyll *a* molecule from antenna

Car – carotenoid molecule

^{3}Car – triplet state of carotenoid molecule

DFT – density functional theory

DMF – dimethyl formamide

ΔG – Gibbs free energy

E – emissive signal

E_m – midpoint potential

ENDOR – electron nuclear double resonance

EPR – electron paramagnetic resonance

ESEEM – electron spin echo envelope modulation

ET – electron transfer

[4Fe-4S], F_X, F_A, F_B – iron sulphur clusters as terminal electron acceptors in Photosystem I

FTIR – Fourier transform infrared spectroscopy

hfc – hyperfine coupling

IP – isopropanol

NQ – naphthoquinone

Q_A – one-electron quinone acceptor site in bRC

Q_H – second quinone acceptor site in bo_3-type quinol oxidase

ρ_π – unpaired π electron spin density

P_{700} – primary donor in Photosystem I

P_{680} – primary donor in Photosystem II

$^3P_{700}$ – triplet state primary donor in Photosystem I

pbRC- purple bacterial reaction center

PhQ – phylloquinone

PQ-9 – plastoquinone-9

PS I, PS II – Photosystem I, Photosystem II

PsaA, PsaB, PsaC, PsaD, PsaE – protein subunits in Photosystem I

RC – reaction center

RP – radical pair

SCRP – spin correlated radical pair concept

TR EPR – time resolved electron or transient paramagnetic resonance

UQ-2 – ubiquinone-2

UQ-3 – ubiquinone-3

UQ-10 – ubiquinone-10

ΔB – residual Gaussian linewidth

Acknowledgement

I wish to thank all people who contributed to my PhD work. First of all, I'm deeply grateful to Prof. Dr. Dietmar Stehlik for providing me the opportunity to work in his group and for his support during my PhD. I want to say "Thank you" to him many times for the fruitful scientific discussions, for his motivation and for his constant attention. My special thanks to Prof. Dr. Kev Salikhov for providing me with the possibility to do my diploma work in the group of Prof. Dr. Dietmar Stehlik. Also, I acknowledge him for providing us with the program of consecutive radical pairs. I would like to express my special gratitude to Prof. Dr. John Golbeck for his innovative ideas and providing us with interesting mutants, without which no chapter of this thesis would have been possible to write. I would like to thank Prof. Dr. Art van der Est for his helpful discussions and for his program to evaluate electron transfer parameters. I want to thank Dr. Yulia Pushkar for introducing me into the TR EPR method. I thank all colleagues from the lab of Prof. Dr. John Golbeck who participated in the preparation and characterisation of all samples, particular, Dr. Rachel Cohen for the preparation of the A_0-mutants, Dr. Gaozhong Shen and Yumiko Sakuragi for the *menB rubA* double mutant, Nithya Srinivasan for the preparations of the *menB* mutant, and Dr. Rufat Agalarov for conducting optical experiments. Many thanks to Herbert Zimmermann for synthesizing the ^{13}C labelled quinones. I appreciate the constant support of Prof. Dr. Robert Bittl's group. I thank Dr. Christian Teutloff for the kind attention and useful discussions during my entire PhD. I am grateful to Dr. Yuriy Grishin for helping me to understand some tricks in the EPR technique.

I would like to thank Prof. Hans-Heinrich Limbach for agreeing to be my second supervisor. The meeting with the members of the Graduate School GKK "*Hydrogen Bond and Hydrogen Transfer*" helped me a lot in the general presentation of science.

I would like to take the opportunity to thank all members of AG Stehlik/Vieth Sabine, Roswitha, Sergey, Alexey, Karsten and Talea for the friendly attitude and the nice atmosphere. I am grateful to Prof. Dr. Alexandra Yurkovskaya, Dr. Konstantin Ivanov, Dr. Mathias Krzystyniak for the critical reading of some sections of my thesis.

Finally, I want to deeply thank Viktor, my parents and Marina for their love and their great support.